

Position-controlled selective area growth of Ga-polar  
GaN nanocolumns by molecular beam epitaxy:  
*A versatile approach towards semipolar GaN and  
the characterization of single nanocolumns*

Dissertation

zur Erlangung des mathematisch-naturwissenschaftlichen Doktorgrades

"Doctor rerum naturalium"

der Georg-August-Universität Göttingen

-

im Promotionsprogramm ProPhys

der Georg-August University School of Science (GAUSS)

vorgelegt von

Arne Urban

aus Bremen

Göttingen, 2013

### Betreuungsausschuss

Prof. Dr. Angela Rizzi, IV. Physikalisches Institut, Georg-August Universität Göttingen

Prof. Dr. Hans-Ulrich Krebs, Institut für Materialphysik, Georg-August Universität Göttingen

Prof. Dr. Michael Seibt, IV. Physikalisches Institut, Georg-August Universität Göttingen

### Mitglieder der Prüfungskommission

Referentin: Prof. Dr. Angela Rizzi, IV. Physikalisches Institut, Georg-August Universität Göttingen

Korreferent: Dr. Bruno Daudin, Nanophysique et Semiconducteurs, CEA-Grenoble/INAC/SP2M/NPSC

2. Korreferent: Prof. Dr. Hans-Ulrich Krebs, Institut für Materialphysik, Georg-August Universität Göttingen

### Weitere Mitglieder der Prüfungskommission

Prof. Dr. Michael Seibt, IV. Physikalisches Institut, Georg-August Universität Göttingen

Prof. Dr. Hans Hofsäss, II. Physikalisches Institut, Georg-August Universität Göttingen

Prof. Dr. Tim Salditt, Institut für Röntgenphysik, Georg-August Universität Göttingen

Prof. Dr. Claus Ropers, Courant Forschungszentrum IV. Physikalisches Institut, Georg-August Universität Göttingen

Tag der mündlichen Prüfung: 29. November 2013

---

## CONTENTS

---

1	INTRODUCTION	1
1.1	Outline of this thesis . . . . .	2
<b>I REVIEW</b>		
2	THE MATERIAL SYSTEM: GALLIUM NITRIDE	
2.1	Basic physical properties . . . . .	7
2.1.1	Crystal structure . . . . .	7
2.1.2	Dislocations and extended defects . . . . .	10
2.1.3	Electronic band structure . . . . .	12
2.1.4	Optical transitions . . . . .	13
2.1.5	Polarization effects . . . . .	16
2.1.6	Thermal stability . . . . .	20
2.2	Growth methods of gallium nitride . . . . .	21
3	MOLECULAR BEAM EPITAXY OF GALLIUM NITRIDE	
3.1	Molecular beam epitaxy . . . . .	23
3.2	Thermodynamic description . . . . .	25
3.2.1	Supersaturation . . . . .	25
3.2.2	Crystal surface energies . . . . .	27
3.2.3	Size effects . . . . .	30
3.3	Kinetic description . . . . .	34
4	MOLECULAR BEAM EPITAXY OF GALLIUM NITRIDE NANOCOLUMNS	
4.1	Self-induced growth . . . . .	37
4.2	Selective area growth . . . . .	41
4.3	Polarity of GaN nanocolumns . . . . .	44
5	EXPERIMENTAL TECHNIQUES	
5.1	Patterning techniques . . . . .	47
5.1.1	Electron beam lithography . . . . .	47
5.1.2	Focused ion beam . . . . .	48
5.1.3	Pulsed laser ablation . . . . .	49
5.2	Characterization techniques . . . . .	49
5.2.1	Reflection high energy electron diffraction . . . . .	49
5.2.2	Atomic force microscopy . . . . .	50
5.2.3	Scanning electron microscopy . . . . .	51
5.2.4	Transmission electron microscopy . . . . .	52
5.2.5	Raman spectroscopy . . . . .	54
<b>II RESULTS</b>		
6	TOWARDS SELECTIVE AREA GROWTH	
6.1	Patterning of SAG arrays . . . . .	59

6.1.1	Electron beam lithography . . . . .	61
6.1.2	Pulsed laser ablation . . . . .	62
6.2	Flux calibration . . . . .	63
6.3	Standard selective area growth conditions . . . . .	66
7	SELECTIVE AREA GROWTH OF GAN NANOCOLUMNS BY MBE	
7.1	Kinetic description . . . . .	69
7.1.1	Ga adatom surface processes . . . . .	69
7.1.2	Towards arrayed, semipolar GaN templates . . . . .	75
7.1.3	Dynamical growth conditions . . . . .	81
7.2	Excursus: Morphology and polarity . . . . .	85
7.2.1	Semipolar surfaces at the nanocolumn tip . . . . .	85
7.2.2	Polarity determination and control of SAG GaN NCs . . . . .	89
7.3	Thermodynamic description . . . . .	99
8	STRUCTURAL PROPERTIES OF SAG GAN NANOCOLUMNS	
8.1	Dislocations and extended defects . . . . .	107
8.1.1	Threading dislocations . . . . .	107
8.1.2	Extended defects . . . . .	111
8.2	Raman spectroscopy . . . . .	115
8.3	Towards semipolar III nitride heterostructures . . . . .	118
9	CORRELATION OF OPTICAL AND STRUCTURAL PROPERTIES	
9.1	Single SAG nanocolumns . . . . .	124
9.1.1	Defect-free nanocolumn . . . . .	125
9.1.2	Low defect density nanocolumns . . . . .	127
9.1.3	High defect density nanocolumn . . . . .	130
9.2	Ensembles of SAG nanocolumns . . . . .	132
III CONCLUSION		
10	SUMMARY AND OUTLOOK	141
10.1	Outlook . . . . .	144
A	APPENDIX	
A.1	Experimental setups, routines, and procedures . . . . .	145
A.2	Electron beam lithography . . . . .	148
A.3	Nitrogen flux calibration . . . . .	151
A.4	Incubation time during SAG . . . . .	151
A.5	Shadowing effects . . . . .	154
A.6	Wet chemical etching of Mo . . . . .	155
A.7	Optimized cross sectional focused ion beam preparation . . . . .	155
A.8	Transmission electron microscopy . . . . .	157
A.9	Photoluminescence . . . . .	158
A.10	Hooke's law for wurtzite symmetry . . . . .	159
BIBLIOGRAPHY		161



---

## INTRODUCTION

---

Gallium nitride (GaN) is a binary compound semiconductor which belongs to the group III nitrides (III–N). GaN crystallizes typically in the wurtzite structure and has a direct band gap of 3.4 eV. Other members of the III nitrides are indium nitride (InN) and aluminum nitride (AlN), which likewise are of wurtzite crystal phase. The direct band gaps are 0.7 and 6.2 eV, respectively. The GaN-based ternary alloys  $\text{In}_x\text{Ga}_{1-x}\text{N}$  and  $\text{Al}_y\text{Ga}_{1-y}\text{N}$  theoretically allow to tailor the fundamental band gap from the near infrared (InN) to the far ultraviolet (AlN) parts of the electromagnetic spectrum. No other materials system offers this range of direct band gaps<sup>[1]</sup>. In fact, GaN-based optoelectronic devices are firmly established in everyday life: Solid-state lighting for illumination applications such as full color displays, automotive headlights and ambient lighting<sup>[2]</sup> utilize GaN-based light emitting diodes (LEDs). High definition optical data storage devices such as Blu-ray players which operate at a wavelength of 405 nm are based on InGaN laser diodes (LDs).

The outstanding properties of the III nitrides in general<sup>[1,3]</sup>, the possibility to continuously tune the band gap, and especially the high melting temperature and the wide band gap of GaN and AlN, allow to envision a variety of GaN-based (high power) optoelectronic applications. These comprise for example photovoltaics, full visible spectrum LEDs, blue and green LDs for projectors (InGaN), and ultraviolet LDs for photolithography, chemical analysis, and medical, as well as environmental applications (AlGaN)<sup>[4,5]</sup>.

Despite the overwhelming application versatility various problems have to be encountered and overcome to pave the way towards this bright future. One of them is related to the growth direction: The III nitrides are subject to polarization effects which cause internal electric fields. In conventional III–N devices, the growth surface is the polar  $c$ -plane which is described by the Miller-Bravais indices (0001). The growth direction perpendicular to this plane is  $[0001]$ . For this specific geometry, the built-in electric fields are aligned along the growth direction of the light emitting region, which is detrimental to the performance of these devices. A possibility to circumvent or at least reduce these fields is the growth on nonpolar or semipolar surfaces. The former  $\{1\bar{1}00\}$   $m$ - and  $\{11\bar{2}0\}$   $a$ -surfaces are perpendicular to the  $c$ -plane. The latter are identified by  $\{hkil\}$  with nonzero  $h$ ,  $k$ ,  $i$  indices and

nonzero  $l$  index. The inclination of these semipolar surfaces varies between the polar and nonpolar surfaces. In fact, already today, devices which have been grown on such surfaces can compete with the conventional  $c$ -plane devices<sup>[2]</sup>. This is astonishing due to the fact that the research on nonpolar or semipolar GaN-based LDs and LEDs started only about 10 years ago<sup>[6]</sup>. However, the growth of non- or semipolar GaN substrates or templates is challenging<sup>[6]</sup>. One method to obtain nonpolar or semipolar GaN is to slice true bulk GaN substrates—which only recently (2006) became commercially available<sup>[3]</sup>—to expose these surfaces<sup>[7]</sup>. However, this approach is expensive and the size of the substrates limited to some millimeters. Another strategy is to use patterned substrates to take advantage of the excellent growth behavior of GaN along the  $c$ -direction<sup>[6]</sup>. If the GaN  $c$ -direction is inclined with respect to the substrate normal during growth, this allows to grow large area semipolar GaN layers<sup>[6]</sup>. On the other hand, perfectly ordered GaN columns can be grown when the GaN  $c$ -direction is aligned parallel to the substrate normal during growth. These columns may form stable semipolar surfaces at the tip<sup>[8–11]</sup>.

In addition, the position-controlled selective area growth of GaN nano- or sub- $\mu\text{m}$  columns gained a great deal of attention as building blocks for the realization of nanoscale optoelectronic or photonic applications<sup>[12]</sup>. Such columns are characterized by a high aspect ratio and diameters in the range of a few to 100 nm (nano-) and smaller than 1  $\mu\text{m}$  (sub- $\mu\text{m}$ ). The selective area growth process allows to control both the size and the position of the columns. On the one hand, this is prerequisite for column-based device processing<sup>[12]</sup>, on the other hand, the homogenization of the column dimensions—as compared to self-induced column ensembles with dispersive size distribution—is expected to reflect the homogenization of other properties, such as the optical emission characteristics. Owing to the excellent position control, the selective area growth takes a step forward towards the characterization of individual nano- or sub- $\mu\text{m}$  sized objects. This is of major importance, since physical properties of such columns may be altered as compared to layers due to surface-induced effects which gain importance with increasing surface area and decreasing column diameter<sup>[12,13]</sup>. In addition, variation of the array design for selective area growth helps to elucidate the growth mechanism of the columns, which is not explained in full detail up to the present date<sup>[12]</sup>.

The aim of this work is the selective area growth of GaN nano- or sub- $\mu\text{m}$  columns by molecular beam epitaxy on prepatterned GaN(0001) templates.

## 1.1 OUTLINE OF THIS THESIS

Part I of this thesis reviews the theoretical background which is considered to be vital for the understanding of this thesis. Furthermore, the performed research will be motivated in detail. [Chapter 2](#) summarizes important ba-

sis physical properties of GaN. General aspects which are of importance concerning the growth of GaN by molecular beam epitaxy are discussed in [Chapter 3](#). The growth of GaN nanocolumns by molecular beam epitaxy will be topic of discussion in [Chapter 4](#). The last chapter of this part ([Chapter 5](#)) summarizes the patterning and characterization techniques which have been used in this thesis.

Part II presents results on the selective area growth of GaN nanocolumns, as well as on the structural and optical properties of these columns. [Chapter 6](#) describes the route towards successful selective area growth in detail and summarizes optimized growth conditions. In the following [Chapter 7](#), the selective area growth is investigated. First, a kinetic description, with focus on Ga adatom surface processes which have a strong impact on the nanocolumn axial growth rate, will be used. In addition, it will be shown that the approach of selective area growth is indeed suited to obtain arrayed, semipolar GaN templates. The second section of this chapter presents results on the morphology of the nanocolumns and the polarity, i.e. whether the crystallographic growth direction is along  $[0001]$  or antiparallel to this direction along  $[000\bar{1}]$ . The last section of this chapter discusses the distinct morphology of the GaN columns in the framework of equilibrium thermodynamics. [Chapter 8](#) presents results on the structural properties of the columns. These comprise the crystal quality in general, and the presence of dislocations and extended defects. In addition, the growth of III–N semipolar multi-quantum wells will be presented. The optical properties of the selectively grown GaN nanocolumns will be assessed in [Chapter 9](#) and furthermore correlated with the structural properties. Single GaN nanocolumns are subject of investigation, as well as ensembles of nanocolumns.

Part III summarizes the main achievements and conclusions of this work. Based on the results of this thesis, an outlook provides proposals on the future research on selective area growth of GaN nanocolumns by molecular beam epitaxy.



Part I

REVIEW



---

## THE MATERIAL SYSTEM: GALLIUM NITRIDE

---

*This chapter will review the material system gallium nitride which is investigated in this thesis. First, basic physical properties will be discussed which are vital for the understanding of this thesis. In addition, this discussion further motivates the performed research. Growth methods of gallium nitride different to molecular beam epitaxy will be briefly summarized in the second part. Most parts of this chapter are written according to the books of Morkoç<sup>[14,15]</sup>.*

### 2.1 BASIC PHYSICAL PROPERTIES

#### 2.1.1 Crystal structure

The group III nitrides (this term will always refer to the group III elements Al, Ga, or In) exist in the wurtzite (hexagonal), zinc blende, and rock salt (both cubic) crystal structures. Since the wurtzite (wz) phase is the thermodynamically stable structure under ambient conditions, it will be focus of attention. A ball-and-stick model of wurtzite GaN is shown in [Figure 2.1](#). However, the zinc blende (zb) phase shows some crystallographic similarities to the wurtzite phase and the relative energy difference between these phases is in general small for the III nitrides; especially only  $\Delta E_{wz-zb} = -9.88$  meV/atom for GaN<sup>[16]</sup>. This may be detrimental to the crystal quality due to the ease of the incorporation of crystal phase changes, e.g. basal plane stacking faults (see [Section 2.1.2](#)). Therefore, this crystal polytype will be also topic of discussion. The rock salt phase can only be induced in the III nitrides under very high pressures (hundreds of kbar). Since this phase is not relevant for epitaxial growth, the interested reader may refer to Refs.<sup>[14,15]</sup> and references therein.

The space group of the wurtzite structure in the Hermann-Mauguin notation is  $P6_3mc$ . The unit cell is hexagonal and characterized by the

two lattice constants  $a$  and  $c$ . The primitive lattice vectors in the Cartesian coordinate system are

$$\mathbf{a}_1 = a \begin{pmatrix} 1/2 \\ \sqrt{3}/2 \\ 0 \end{pmatrix}, \quad \mathbf{a}_2 = a \begin{pmatrix} 1/2 \\ -\sqrt{3}/2 \\ 0 \end{pmatrix}, \quad \mathbf{c} = c \begin{pmatrix} 0 \\ 0 \\ 1 \end{pmatrix}. \quad (2.1)$$

The direction along the primitive  $c$  lattice vector is by convention defined as the  $c$ -axis. The internal parameter  $u$  describes the interatomic distance of III and N atoms along the  $c$ -axis. For an ideal wurtzite structure this value is  $u = 3/8 = 0.375$  in terms of the lattice constant  $c$ , and furthermore,  $c/a = \sqrt{8/3}$ . The lattice parameters of the III nitrides are listed in [Table 2.1](#).

Material	$a$ (Å)	$c$ (Å)	Comment	$u$ ( $c$ )
GaN	3.189	5.185	Platelets	0.376
AlN	3.111	4.979 – 4.982	Bulk	0.377
InN	3.530 – 3.548	5.704 – 5.960	Powder	0.380

**Table 2.1:** Lattice parameters of the III nitrides at room temperature according to Ref.<sup>[14]</sup>. The internal parameter is according to Ref.<sup>[17]</sup>.

The structure is described by two interpenetrating hexagonal close-packed sublattices for the group III and N atoms. These are offset along the  $c$ -axis ideally by  $5c/8$ . Thus, each species is tetrahedrally surrounded by 4 atoms of the other species and vice versa. The unit cell contains six atoms of each type.

In the hexagonal system, Miller-Bravais indices in the form  $(hkil)$ , with  $i = -(h + k)$  define crystallographic planes. The directions of the plane normal vectors are given by  $[hki l/\lambda^2]$ , where  $\lambda = \sqrt{2/3} \cdot c/a$ <sup>[18]</sup>. For sake of clarity, it is pointed out that  $[hki l]$  is not necessarily perpendicular to the corresponding plane  $(hkil)$ .

A prominent, in crystal growth commonly used plane is the basal  $(0001)$   $c$ -plane. Consequently,  $a$  is the in-plane lattice constant and  $c$  the out-of-plane lattice constant of the basal plane. The stacking sequence along the  $c$ -direction is given by alternating close-packed  $(0001)$  planes of group III or N atoms. This sequence can be reduced to AaBbAa..., where upper- and lowercase letters represent the different constituents and different letters represent projected positions onto the  $c$ -plane. Since the Ga-N dimer which corresponds to e.g. Aa is oriented perpendicular to the  $c$ -plane, one can further reduce this stacking scheme to ABA..., referring only to the projection of the Ga-N dimer onto the basal plane. This is shown in [Figure 2.1\(f\)](#).

Other prominent planes are the  $\{11\bar{2}0\}$   $a$ - and the prismatic  $\{1\bar{1}00\}$   $m$ -plane. The  $c$ -plane is referred to as being polar, while the latter are termed nonpolar. Arbitrary planes in between, with nonzero  $h$ ,  $k$ , and  $i$  indices



and nonzero  $l$  index are termed semipolar. The reason will be discussed in [Section 2.1.5](#). Important crystallographic planes of the wurtzite system are shown in [Figure 2.1\(d, e\)](#). The theoretical inclination angles of some semipolar planes with respect to the  $c$ -plane are listed in [Table 2.2](#).

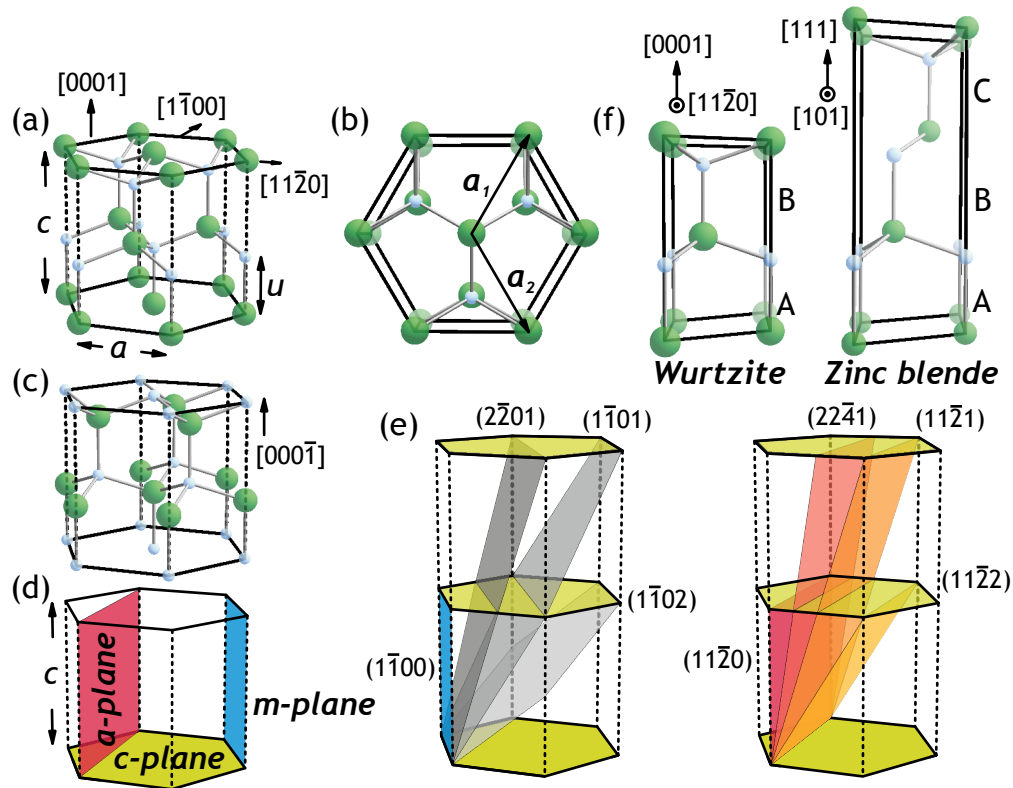


**Figure 2.1:** Model of the wurtzite crystal structure, exemplarily shown for GaN. Big and small spheres denote Ga and N atoms, respectively. (a) Ga-polar GaN. (b) Top-view projection of (a) along the  $c$ -axis. The N-polar case is shown in (c). Polar, nonpolar (d), and low-indexed semipolar (e) planes are shown. (f) Stacking sequence for wurtzite along  $[0001]$ , and for zinc blende along  $[111]$ . A perspective view has been used for these figures.

The wurtzite crystal structure is non-centrosymmetric: For an arbitrary point  $(x, y, z)$  in the unit cell, no equivalent point at  $(-x, -y, -z)$  is found. The crystal structure is lacking inversion symmetry along the  $c$ -direction and therefore,  $[0001]$  and  $[000\bar{1}]$  are non-equivalent. The III nitrides are therefore termed polar, i.e. the Ga-N dimer which is described by the vector pointing from Ga to N can be aligned parallel or antiparallel with respect to the  $c$ -direction. The first case corresponds to Ga-polarity, the latter to N-polarity. The corresponding notations for the basal plane are  $(0001)$  and  $(000\bar{1})$ , respectively. The lack of inversion symmetry has major consequences for the optical properties of III nitride heterostructures. This will be discussed in [Section 2.1.5](#).

The space group of the zinc blende structure in the Hermann-Mauguin notation is  $F\bar{4}3m$ . The unit cell is cubic and is formed by two interpenetrating

Miller-Bravais index ( <i>hkil</i> )	$\angle((0001), (hkil))$ ( $^\circ$ )	Nomenclature
( $2\bar{2}01$ )	75.1	
( $1\bar{1}01$ )	62.0	<i>s</i> -plane
( $1\bar{1}02$ )	43.2	<i>r</i> -plane
( $22\bar{4}1$ )	81.3	
( $11\bar{2}1$ )	72.9	
( $11\bar{2}2$ )	58.4	
( $11\bar{2}3$ )	47.3	<i>n</i> -plane

**Table 2.2:** Examples of semipolar planes in GaN.

face-centered cubic sublattices, which are offset by  $\sqrt{3}a/4$  along a body diagonal, e.g.  $[111]$ . The cubic lattice constant is given by  $a$ . Identical to the wurtzite structure, each atom is coordinated tetrahedrally by the other species. However, the stacking sequence of the (111) close-packed planes along  $\{111\}$  is ABCA..., following the reduced stacking scheme. A ball-and-stick model of the zinc blende stacking sequence is shown in [Figure 2.1\(f\)](#).

### 2.1.2 Dislocations and extended defects

Dislocations are one-dimensional imperfections in the crystallographic arrangement with respect to a perfect crystal. Generally, dislocations can be grouped into misfit and threading dislocations (TDs). The former are generated due to strain accommodation in heteroepitaxy, while the latter are discussed to be related to crystallographic misorientation<sup>[19]</sup>. Since in this work homoepitaxial growth was carried out, only threading dislocations will be discussed.

Threading dislocations originate at the interface of the epilayer and propagate through the crystal. They are terminated if they reach the crystal surface or annihilate each other. TDs may be formed at coalescence boundaries due to slight deviations of the crystal orientation of one island with respect to the other<sup>[19]</sup>. Since TDs typically run perpendicular to the interface where they are created, they do not accommodate strain<sup>[19]</sup>. Dislocations are characterized by their Burgers vector  $\mathbf{b}$  and the line direction  $\mathbf{u}$ . For screw dislocations,  $\mathbf{b} \parallel \mathbf{u}$ , while  $\mathbf{b} \perp \mathbf{u}$  for edge dislocations. The type of the TDs can be edge ( $\mathbf{a}$ -type), screw ( $\mathbf{c}$ -type) or mixed ( $\mathbf{a} + \mathbf{c}$ -type) with Burgers vectors  $\mathbf{b} = \frac{1}{3} \langle 11\bar{2}0 \rangle$ ,  $\mathbf{b} = \langle 0001 \rangle$  and  $\mathbf{b} = \frac{1}{3} \langle 11\bar{2}3 \rangle$ , respectively. Threading dislocations can bend towards the crystal surface and are annihilated at the surface<sup>[20]</sup>. Especially in the case of nanostructures with a larger surface-to-

volume ratio as compared to bulk material, this mechanism is effective for the reduction of threading dislocations<sup>[10,21–23]</sup>. The underlying mechanism is discussed to be due to image forces of free surfaces, which force the dislocation out of the crystal<sup>[22]</sup> or due to total line energy minimization of the dislocations<sup>[20,23]</sup>. Furthermore bending of TDs has been attributed to changes in the growth mode<sup>[24]</sup>.

Stacking faults are irregularities in the ordering of complete layers of atoms, that do not necessitate breaking of bonds. Stacking faults are characterized by the displacement vector  $\mathbf{R}$  which corresponds to the displacement of two crystal regions—which are in contact—with respect to each other<sup>[25]</sup>. Basal plane stacking faults (BSFs) are stacking irregularities in the basal (0001) plane and transform the wurtzite stacking locally into the zinc blende stacking. Prismatic stacking faults (PSFs) are found in the  $\{11\bar{2}0\}$  system. BSFs are terminated at the crystal surface or are bound by partial dislocations. For this thesis, the majority of stacking faults were extended BSFs. Therefore, the PSFs, as well as the partial dislocations will not be discussed here. For completeness, the reader may refer to Ref.<sup>[25]</sup>. Four types of BSFs are considered for GaN, the intrinsic types  $I_1$ ,  $I_2$ , and  $I_3$  and the extrinsic type  $E$ <sup>[25,26]</sup>. The classification is according to the number of violations of the stacking rule.

Crystallographically,  $I_1$  results from removal of one basal plane, e.g. A or B, followed by shearing the crystal above the fault by  $\frac{1}{3}\langle 1\bar{1}00 \rangle$ . The displacement vector is  $\mathbf{R} = \frac{1}{6}\langle 2\bar{2}03 \rangle$ . The stacking sequence then reads ...ABABACAC...; the cubic inclusion is underlined. Note, that  $I_1$  faults for which the fault starts in A or B are equivalent. The  $I_1$  stacking fault cannot be formed by a single glide motion which is required for strain relaxation and is thus exclusively related to growth<sup>[25]</sup>.

Type  $I_2$  corresponds to a shear of one crystal half by  $\frac{1}{3}\langle 1\bar{1}00 \rangle$ , and thus,  $\mathbf{R} = \frac{1}{3}\langle 1\bar{1}00 \rangle$ . The stacking sequence contains two violations of the stacking rule: ...ABABCACAC... Besides the formation during growth, deformation during or after growth may create type-II faults<sup>[25]</sup>.

The extrinsic type follows immediately from an insertion of one basal C-layer into the crystal. The stacking sequence and the displacement vector are ...ABABCABAB... and  $\mathbf{R} = \frac{1}{2}[0001]$ , respectively. Following the arguments from Ref.<sup>[25]</sup>, the BSF type  $E$  is related to growth.

The intrinsic type  $I_3$  was theoretically predicted<sup>[26]</sup> and is created by one basal layer (A or B) which occupies a C-position. This leads to a stacking sequence ...ABABACABAB... Experimental verification of the type-III BSF by transmission electron microscopy is scarcely reported to the present date<sup>[27]</sup>.

*Ab initio* calculations<sup>[26]</sup> of these BSFs in wurtzite III nitrides generally predict formation energies which increase in the order GaN, InN, AlN. The BSF of type  $I_1$  always has the lowest formation energy. In the case of GaN,

this value is 10 meV per unit cell area, which translates to  $1.12 \text{ meV \AA}^{-2}$ . The formation energy of the other types increases in the order  $I_3$ ,  $I_2$ ,  $E$ . The BSFs of type  $I_1$  and  $I_2$  are commonly observed in GaN. The extrinsic type has the highest formation energy and can be transformed into the energetically more favorable BSF of type  $I_1$  by a  $R = \frac{1}{3} \langle 1\bar{1}00 \rangle$  shear<sup>[25]</sup>. Accordingly, it is less common observed in GaN<sup>[14]</sup>. The crystallographic arrangement of the BSFs is shown in Figure 2.2.

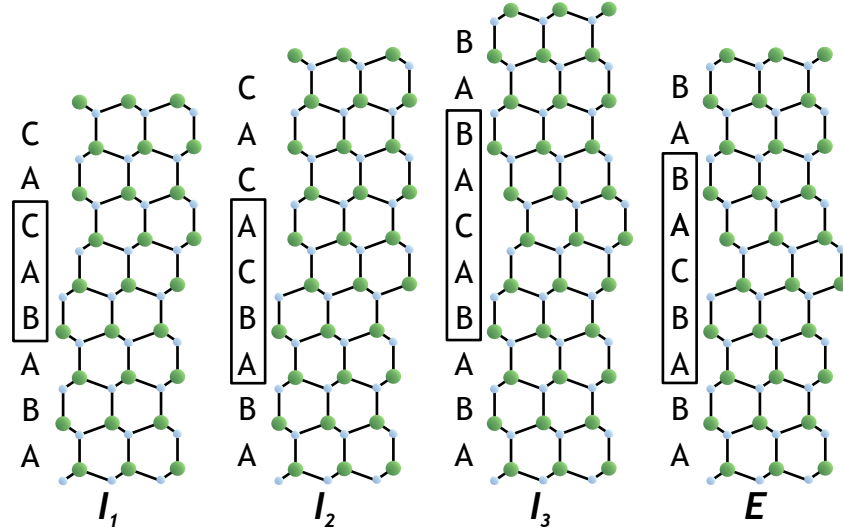


**Figure 2.2:** Atomic structure of basal plane stacking faults in Ga-polar GaN projected along  $[11\bar{2}0]$ . The reduced stacking sequence is indicated and the fault region marked by rectangles. Big and small spheres denote Ga and N atoms, respectively.

A theoretical investigation of the electronic structure of BSFs revealed no defect-induced localized states in the band gap of the III–N host<sup>[26]</sup>. Nevertheless, a slight narrowing of the band gap was calculated, which is due to the local formation of zinc blende within the wurtzite phase. This may give rise to a crystal phase quantum well with type-II band alignment<sup>1</sup>. In fact, in luminescence experiments on BSFs in GaN, a luminescence line below the wurtzite band gap is observed<sup>[28–31]</sup>. The electronic band structure of GaN will be discussed in the next section, the optical properties are summarized in Section 2.1.4.

### 2.1.3 Electronic band structure

The fundamental aspects of the electronic band structure of GaN will be summarized in the following.

<sup>1</sup> The electron wave function is localized in the zinc blende region, whereas the hole wave function is localized within the surrounding wurtzite regions.

GaN is a direct semiconductor with a band gap  $E_g$  at  $\Gamma$  ( $k=0$ ) between 3.42 eV (300 K) and 3.505 eV (1.6 K). The wave vector is denoted by  $k$ . The temperature dependence of the band gap follows the equation

$$E_g(T) = E_g(0) - \alpha T^2 / (\beta + T). \quad (2.2)$$

$E_g(T)$  denotes the fundamental band gap at temperature  $T$ . Parameter values for  $\alpha$  and  $\beta$  are for example summarized in Ref.<sup>[14]</sup>. In GaN, the character of the conduction band minimum is mainly formed by the gallium  $s$  orbitals, and thus described as  $s$ -like, showing a parabolic dispersion. The character of the valence band maximum is  $p$ -like, due to the nitrogen  $p$  orbitals. In the wurtzite system, the (sixfold) degeneracy of the upper valence band level at  $k=0$  is lifted due to the crystal field splitting as compared to zinc blende crystals. Taking also into account spin-orbit interaction, the upper valence bands split into three bands, which are designated as heavy hole (HH), light hole (LH), and crystal field split hole (CH) bands. In terms of optics nomenclature, these are termed A, B, and C, respectively (see Section 2.1.4).

The lifting of the degeneracy of the upper valence bands for wurtzite crystals is shown schematically in Figure 2.3.

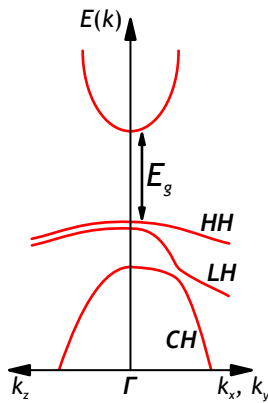


Figure 2.3: Schematic representation of the  $\Gamma$  point valence and conduction bands in crystals with wurtzite symmetry, such as GaN. Figure adapted from Ref.<sup>[14]</sup>.

#### 2.1.4 Optical transitions

Electrons in semiconductors may be excited from the valence band to the conduction band, provided that the excitation energy is larger than the fundamental band gap. The excitation can be e.g. due to irradiation by photons (photoluminescence) or electrons (cathodoluminescence) and leaves behind a hole in the valence band. Electrons and holes thermalize to conduction band minimum and valence band maximum, respectively, by inelastic scattering processes. In direct semiconductors, recombination across the band gap ( $\Delta k \approx 0$ ) mostly occurs radiatively via emission of photons. For indirect semiconductors, the position of conduction band minimum and valence band maximum is at different  $k$ -values. The momentum of the emitted

photon is negligible and momentum conservation requires absorption or emission of a phonon for this band-to-band transition. The probability of this scattering process is low and electron-hole pair recombination is mainly non-radiative in indirect semiconductors.

In the following, only radiative recombination will be considered. The electron and hole are attracted due to (statically screened) Coulomb interaction. The bound state is termed Wannier exciton with a binding energy of

$$E_X = -\frac{1}{n^2} \frac{\mu^*}{m_e^* \epsilon^2} \cdot 13.6 \text{ eV}. \quad (2.3)$$

This formula is derived from the hydrogenic model within the effective-mass approximation. The reduced effective mass of the electron-hole system is denoted by  $\mu^*$ , the effective electron mass by  $m_e^*$ , the dielectric constant of the semiconductor by  $\epsilon$ , and the integer  $n$  is the principal quantum number. The exciton ground state corresponds to  $n = 1$ . Recombination of the electron-hole pair results in the emission of a photon with an energy corresponding to the band gap reduced by the exciton binding energy. Due to the lifting of the degeneracy in the wurtzite symmetry at  $\Gamma$ , three free excitons A (HH), B (LH), and C (CH) exist in GaN. (Un)intentional doping of semiconductors will introduce donor- and acceptor-related levels in the energy gap and excitons may interact with these dopants. The terminology for excitons bound to neutral donors or acceptors, is  $D^0X$  and  $A^0X$ , respectively. The corresponding donor-bound state related for example to the A exciton is denoted by  $D^0X_A$ . If no band is specified the nomenclature is simply  $D^0X$ . For such exciton complexes, the photon energy will be lowered further according to the binding energy of the exciton-impurity-complex:

$$h\nu = E_g - |E_X| - |E_{BX}| \quad (2.4)$$

The term  $E_{BX}$  denotes the binding energy of the bound exciton,  $h$  and  $\nu$  are the Planck constant and photon frequency, respectively. Additional emission peaks at lower energy may be observed due to the emission of optical phonons. The related peaks are termed phonon replica.

The growth of high-quality GaN results in unintentional n-type doping which is discussed to be related to silicon or oxygen impurities<sup>[32]</sup>. The dominant emission line in high-quality n-type GaN with low background donor and acceptor concentrations is typically  $D^0X_A$ . GaN layers which are grown in the molecular beam epitaxy system of this work show typical electron concentrations of about  $2 \cdot 10^{17} \text{ cm}^{-3}$ . Also for undoped GaN nanocolumns grown by molecular beam epitaxy, electron concentrations of mid  $10^{17} \text{ cm}^{-3}$  were reported<sup>[33]</sup>. The optical properties of the GaN nanocolumns which were grown for this thesis are therefore expected to be dominated by donor-related transitions. This argument is supported by the fact, that the used molecular beam epitaxy system never contained any Mg which is attributed

Peak position (eV)	Nomenclature, description	Comment
3.478	$X_A$ , Free exciton A	
3.471 – 3.472	$D^0X_A$ , Donor-bound exciton	Si, O impurity
3.44 – 3.46	TES, Two-electron-satellite of $D^0X$	
3.41 – 3.42	$Y_2$ , Structurally related	BSF $I_1$ : 3.41 – 3.42 eV <sup>[28,31]</sup>
3.35 – 3.36	$Y_4$ , Structurally related	BSF $I_2$ : 3.35 eV <sup>[31]</sup>
3.34	$Y_5$ , Structurally related	BSF $I_2$ : 3.32 – 3.33 eV <sup>[29,30]</sup>
3.30 – 3.32	$Y_6$ , Structurally related	
3.28	UVL, Electron-Acceptor	BSF $E$ : 3.29 eV <sup>[31]</sup>
3.27	DBX, Donor-bound exciton	Zinc blende GaN
3.26	UVL, Donor-Acceptor Pair	Si impurity
3.21 – 3.23	$Y_7$ , Structurally related	
3.16	Donor-Acceptor Pair (DAP)	Zinc blende GaN
2.2 – 2.3	YL, Yellow luminescence	Ga vacancy <sup>[34]</sup> , C impurity <sup>[35]</sup>
$\Delta E = -91$ meV	LO, Phonon replica	Wurtzite GaN

**Table 2.3:** Luminescence characteristics of GaN at low temperature according to Ref.<sup>[15]</sup> and references therein. If the zinc blende phase instead of the wurtzite phase is considered, this is explicitly mentioned.

to a common acceptor-bound transition in GaN. Table 2.3 summarizes the optical transition energies in GaN which are relevant for this thesis.

Considering confinement due to a reduction of the dimensionality of the system by e.g. quantum wells (QWs), optical transition energies are notably modified (blueshift) if the size of the well, i.e. the confining potential, is of comparable size to the exciton Bohr radius:

$$a_{B,X} = \frac{\epsilon h^2}{\pi q^2 \mu^*} \quad (2.5)$$

The elementary charge is denoted by  $q$ . The Bohr radius for a free exciton in GaN is about 30 Å. This shows that quantization effects in GaN are only relevant for very small quantum structures. The dimensions of the nanostructures (except for QWs) which are investigated in this thesis are much larger than the calculated value. Therefore, confinement effects do not have to be considered for this thesis. It is worth to note, that in nanocolumns, besides confinement effects, also surface-induced effects may become important<sup>[13]</sup>. In fact, for undoped GaN nanocolumns with diameters significantly larger than this confinement limit, a blueshift of donor-bound exciton transition energies was observed<sup>[36]</sup>. This was attributed to the decreasing binding

energy of the exciton complex if the donor is located close to the surface of the nanocolumn. An effect which reduces exciton transition energies in QWs is the quantum-confined Stark effect (QCSE). It is related to polarization effects which tilt the conduction and valence band profiles. This leads to an effectively smaller band gap. These effects will be discussed in the following.

### 2.1.5 Polarization effects

The III nitrides are subject to polarization effects due to their partly ionic nature, the lack of inversion symmetry in the wurtzite crystal structure, and the arrangement of the GaN tetrahedra in the wurtzite structure. In classical electromagnetism, the macroscopic polarization  $\mathbf{P}$  is caused by the presence of electric dipole moments in a dielectric. If without an external field persistent polarization exists, one speaks of spontaneous polarization  $\mathbf{P}_0$ . Piezoelectric polarization  $\mathbf{P}_{PE}$  is induced by strain. This classical description is however only applicable in the case of a dielectric solid which can be described as an assembly of well separated and independently polarizable units, as in the case of ionic crystals<sup>[37]</sup>. In covalent materials, for which the electronic charge is delocalized and bonding requires a quantum mechanical description, such local-dipole picture is oversimplified. Furthermore, it is not the polarization which is the accessible quantity in experiment but the variations  $\Delta\mathbf{P}$  with respect to a (typically unknown) reference polarization<sup>[37]</sup>. Nevertheless, one can show that in the case of the III nitrides an interface of wurtzite and zinc blende symmetry is the key to calculate the absolute value of spontaneous polarization for the wurtzite system. This is because the zinc blende reference structure has zero spontaneous polarization<sup>[17]</sup>.

The importance of interfaces or surfaces considering polarization effects is further emphasized applying the Maxwell's equations in matter. A macroscopic bound volume charge density  $\rho_b = -\nabla \cdot \mathbf{P}$  is caused by spatial variations of the polarization. For abrupt changes in polarization, e.g. at an interface of a heterostructure of materials with polarizations  $\mathbf{P}_1$  and  $\mathbf{P}_2$ , this reduces to a bound sheet charge density<sup>[38]</sup>

$$\sigma_b = -\mathbf{n}_{12} \cdot (\mathbf{P}_2 - \mathbf{P}_1). \quad (2.6)$$

The surface or interface normal vector pointing from material 1 to material 2 is given by  $\mathbf{n}_{12}$ . An internal electric field will be induced, which can tilt and manipulate the engineered heterostructure band profile to a large extent. This is the quantum-confined Stark effect which leads to a spatial separation of the electrons and holes inside the confining potential. The reduced wave function overlap integral results in a decrease of the radiative recombination efficiency.

For all cation-polar III nitrides, calculations show that the spontaneous polarization is negative (pointing along  $[000\bar{1}]$ ) and follows the trend of the crystal nonideality<sup>[17,39]</sup>.



Although the classical picture of polarization caused by the presence of local dipole moments is oversimplified, one can dare to use the classical approach to illustrate polarization effects. On the one hand, this is due to the relatively large electronegativity of Ga, In, and Al as compared to N (about half the value of nitrogen on the Pauling scale). On the other hand, the spontaneous polarization follows the trend of the crystal nonideality. This reflects the geometric (classical) effect of the bonding configuration.

As shown in Figure 2.4(a), the vector which points from N to Ga along  $[000\bar{1}]$  has the length  $u$  (in units of  $c$ ). The cumulative component of the triple bonded Ga atom points along  $[0001]$ , with a length  $3(1/2 - u)$ . Using the ideal value of the wurtzite structure,  $u = 0.375$ , the net dipole moment for the GaN tetrahedron is canceled. However, for nonideal values (see Table 2.1), a net dipole moment results. Due to the arrangement of the GaN tetrahedra in the wurtzite structure (see Figure 2.1(a)), a macroscopic spontaneous polarization which points along  $[000\bar{1}]$  occurs for the III nitrides. For N-polarity, the same direction for the spontaneous polarization results. Applying tensile strain to the tetrahedron, the cumulative out-of-plane polarization component of the triple bonded Ga or N atom (Ga- and N-polar, respectively) decreases. This gives rise to the additional piezoelectric polarization  $P_{PE}$  which points along  $[000\bar{1}]$ . For compressive strain, the cumulative out-of-plane polarization component increases and results in  $P_{PE}$  to point along  $[0001]$ , thus opposite to the spontaneous polarization. Since the polarization discontinuity at an interface induces a bound charge density, it is clear that the polarity of the sample determines the sign of the charge density. Figure 2.4(b) shows the cases of tensile and compressive strain.

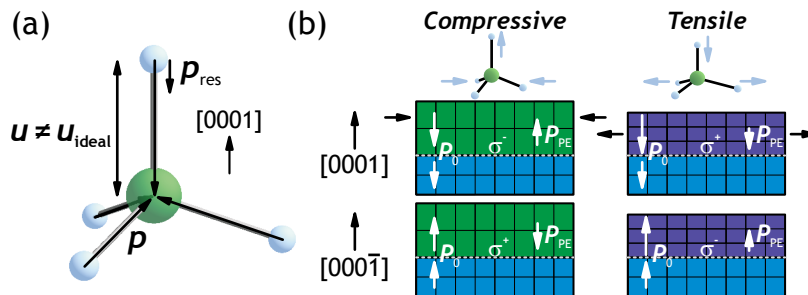


**Figure 2.4:** (a) GaN tetrahedron (big: Ga, small: N) in the classical dipole moment picture (N negatively charged, Ga positively charged). The resulting net electric dipole moment is given by  $p_{res}$ . Adapted from Ref.<sup>[14]</sup>. (b) Direction of spontaneous and piezoelectric polarization for GaN-based heterostructures with different polarity and strain state. Compressive strain applies e.g. for  $\text{In}_x\text{Ga}_{1-x}\text{N}$  on GaN, tensile strain e.g. for  $\text{Al}_y\text{Ga}_{1-y}\text{N}$  on GaN. The arrows at the GaN tetrahedra indicate atomic displacements with respect to the unstrained state. Positive and negative induced interface charges are denoted by  $\sigma^+$  and  $\sigma^-$ , respectively.

In the absence of external electric fields, the total macroscopic polarization is the sum of spontaneous and piezoelectric polarization,

$$\mathbf{P} = \mathbf{P}_0 + \mathbf{P}_{\text{PE}}. \quad (2.7)$$

For ternaries or quaternaries  $\text{Al}_x\text{In}_y\text{Ga}_{1-x-y}\text{N}(0001)$  layers, modeling of the alloy according to Vegard's law can be used to calculate the spontaneous polarization<sup>[40]</sup>:

$$\mathbf{P}_0(x, y) = x\mathbf{P}_0^{\text{AlN}} + y\mathbf{P}_0^{\text{InN}} + (1 - x - y)\mathbf{P}_0^{\text{GaN}} \quad (2.8)$$

For arbitrary alloy concentrations, the spontaneous polarization is thus easily calculated for the III nitrides. On the other hand, the piezoelectric polarization is related to strain. Before one can give a general form for the piezoelectric polarization, one first has to deal with the deformations  $\varepsilon_{kl}$  of a crystal due to stresses  $\sigma_{ij}$  which can be described by Hooke's law:

$$\sigma_{ij} = \sum_{k,l} c_{ijkl}\varepsilon_{kl}, \quad i, j, k, l = 1, 2, 3. \quad (2.9)$$

The elastic stiffness coefficients of the crystal along different directions are given by the fourth ranked elastic tensor  $c_{ijkl}$  (see [Section A.10](#)). In wurtzite symmetry, the piezoelectric polarization is now related to strain via

$$\mathbf{P}_{\text{PE}} = \begin{pmatrix} 0 & 0 & 0 & 0 & e_{15} & 0 \\ 0 & 0 & 0 & e_{15} & 0 & 0 \\ e_{31} & e_{31} & e_{33} & 0 & 0 & 0 \end{pmatrix} \begin{pmatrix} \varepsilon_{xx} \\ \varepsilon_{yy} \\ \varepsilon_{zz} \\ \varepsilon_{yz} \\ \varepsilon_{xz} \\ \varepsilon_{xy} \end{pmatrix} = \begin{pmatrix} e_{15}\varepsilon_{xz} \\ e_{15}\varepsilon_{yz} \\ e_{31}(\varepsilon_{xx} + \varepsilon_{yy}) + e_{33}\varepsilon_{zz} \end{pmatrix},$$

with the components  $e_{ij}$  of the piezoelectric tensor<sup>2</sup> in Voigt notation<sup>[41,43]</sup>. This equation can be used to discuss polarization effects in the most convenient cases: *a*-, *m*- and *c*-plane heterostructures.

First, the nonpolar cases will be discussed. Without shear ( $\varepsilon_{yz}, \varepsilon_{xz}, \varepsilon_{xy} = 0$ ), the piezoelectric polarization is zero both along  $[11\bar{2}0]$  (*x*-axis), and  $[1\bar{1}00]$  (*y*-axis). The spontaneous polarization is directed along  $[000\bar{1}]$ . The normal vectors of the *a*- and *m*-interfaces are perpendicular to the *c*-axis. Consequently, according to [Equation 2.6](#), no interface charges occur. The engineered band profile of the heterostructure is not affected. This is shown in [Figure 2.5\(a\)](#).

For heterostructures grown along the *c*-direction, only biaxial strain is present. The piezoelectric polarization—and thus the total polarization—is aligned perpendicular to the heterostructure interface. Consequently, the

<sup>2</sup> Note, that in the early literature, the piezoelectric tensor appears in the form  $d_{ij}$ <sup>[41]</sup>, which is however related to  $e_{ij}$  through a tensor relationship<sup>[42]</sup>.

product of interface normal vector and difference in total polarization is nonzero. The resulting interface charges give rise to an electric field inside the heterostructure, which is aligned along the growth direction. Consequently, the conduction and valence bands are tilted. This is shown in Figure 2.5(b).

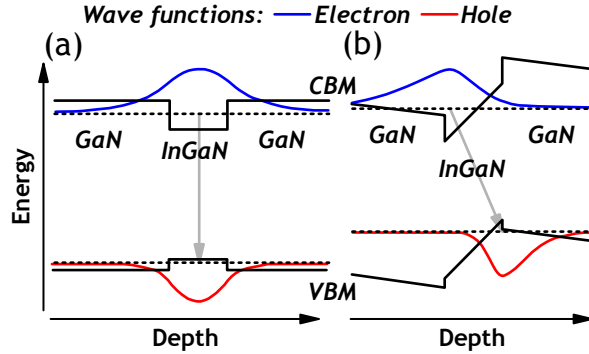


**Figure 2.5:** Conduction band minimum (CBM) and valence band maximum (VBM) profile for GaN/In<sub>0.1</sub>Ga<sub>0.9</sub>N(25 Å)/GaN quantum wells grown along a nonpolar direction (a) and along the polar [0001] direction (b). The quantum-confined Stark effect spatially separates (gray arrows) the electron and hole wave functions. The ground state energy levels of the confined carriers are indicated by dashed lines. Adapted from Ref.<sup>[1]</sup>.

If we now investigate semipolar heterostructures, the discussed equations hold. However, the strain components  $\varepsilon_{ij}$  are not as trivial as in the (non)polar case. Romanov *et al.* theoretically considered GaN-based layers grown pseudomorphically on semipolar GaN templates<sup>[43]</sup>. The  $c$ -axis of the template is inclined by an angle  $\vartheta$  with respect to the template surface normal vector  $z'$ , as schematically shown in Figure 2.6(a).

If layer and template have the same crystal structure, this situation can be described by only two misfit parameters<sup>3</sup>, which depend only on the lattice constants of layer and template, and the inclination angle  $\vartheta$ <sup>[43]</sup>. The polarization discontinuity  $\Delta P_{z'}$ , perpendicular to the heterostructure interface can be calculated by

$$\Delta P_{z'} = P_{PE,L,z'} + (P_{0,L} - P_{0,T}) \cos \vartheta. \quad (2.10)$$

The subscripts T and L denote the template and layer, respectively. The strain-induced piezoelectric polarization component  $P_{PE,L,z'}$  perpendicular to the heterostructure interface is only function of  $\vartheta$ , the elastic stiffness coefficients, the piezoelectric coefficients, and the two misfit parameters and is thus easily calculated.

The main results obtained in Ref.<sup>[43]</sup> indicate that besides for the nonpolar orientations, the total polarization discontinuity becomes zero for semipolar In <sub>$x$</sub> Ga<sub>1- $x$</sub> N/GaN and Al <sub>$y$</sub> Ga<sub>1- $y$</sub> N/GaN heterostructures with inclinations of about 45° and 70°, respectively. The actual alloy content is influencing

<sup>3</sup> The lattice parameters of the layer are assumed to behave according to Vegard's law.

this crossover in both cases only weakly. This is shown exemplarily for  $\text{In}_x\text{Ga}_{1-x}\text{N}$  in Figure 2.6(b).

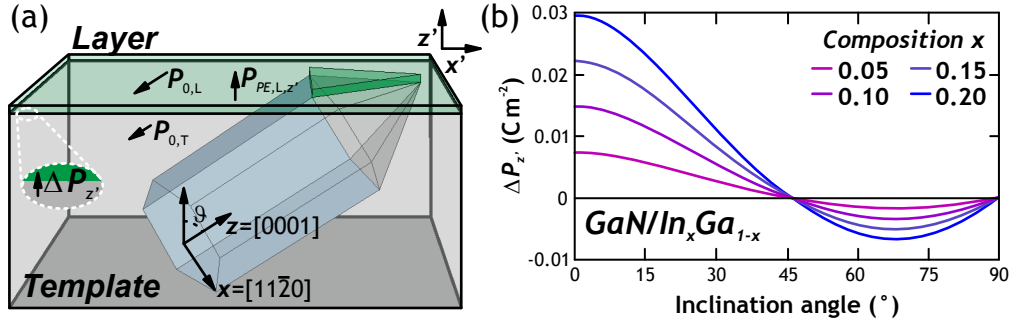


**Figure 2.6:** (a) Scheme of the coordinate system for the semipolar GaN-based layer/template heterostructure according to Ref.<sup>[43]</sup>, exemplarily shown for an  $\text{In}_x\text{Ga}_{1-x}\text{N}/\text{GaN}$  heterostructure. A nanocolumn with semipolar faceted tip and growth direction along  $[0001]$  is depicted, to illustrate the situation in the case of GaN-based heterostructures grown at the tip of such nanocolumns. (b) Total polarization discontinuity as function of inclination angle at a semipolar  $\text{In}_x\text{Ga}_{1-x}\text{N}/\text{GaN}$  interface under biaxial compression. Adapted from Ref.<sup>[43]</sup>.

Another important result is the fact, that  $\epsilon_{zz}$  and  $\epsilon_{yz}$ , i.e. uniaxial strain along the  $z$ -direction ( $[0001]$ ) and shear strain in the  $y$ -plane ( $m$ -plane) along  $z$ , are nonzero for such semipolar GaN-based layers. For large alloy concentrations, the resulting nonzero strain components are expected to be sources for the introduction of defects in GaN-based semipolar heterostructures.

### 2.1.6 Thermal stability

Growth temperatures in the range of  $1/2$  to  $2/3$  of the semiconductor melting temperature  $T_m$  are considered as rule of thumb for high-quality compound semiconductor growth. However, in the case of the III–N system, the nitrogen equilibrium vapor pressure over the crystal at such elevated temperatures is higher than the typical background pressure during molecular beam epitaxy (around  $10^{-5}$  mbar due to nitrogen) as shown in Figure 2.7(a).

Despite the existing discrepancy between the reported values of the nitrogen equilibrium vapor pressure over the III nitrides<sup>[44,47]</sup>, it becomes clear that a compensation of such high pressures is not possible at  $1/2 \cdot T_m$ . A significant lowering of substrate temperatures is required to overcome decomposition rates.

Annealing experiments by Ambacher *et al.* on epitaxial thin III–N films in vacuum suggest growth temperatures below 630, 850 and 1040 °C for InN, GaN and AlN, respectively<sup>[47]</sup>. In the case of GaN, different experimental approaches confirmed this behavior, claiming the GaN decomposition temperature under vacuum to be about 800 °C<sup>[46,48]</sup>. It is worth to note, that the

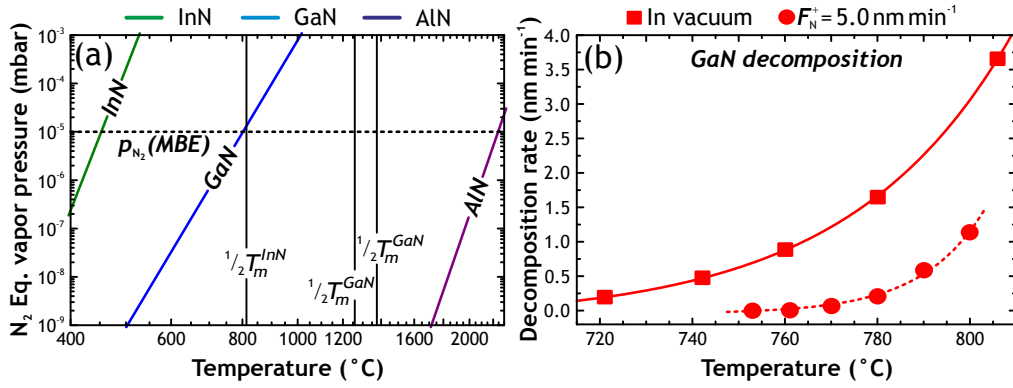


**Figure 2.7:** (a) Equilibrium  $N_2$  vapor pressure between vapor and solid phases in the III–N system as function of temperature. Adapted from Ref.<sup>[44]</sup>. Vertical lines denote half the melting temperatures of the III nitrides<sup>[45]</sup>. The dashed line indicates the background pressure during molecular beam epitaxy due to nitrogen. (b) GaN decomposition rate as determined by quadrupole mass spectrometry for different substrate temperatures in vacuum or under active nitrogen exposure. The incoming nitrogen flux is given by  $F_N^+$  and calibrated in  $\text{nm min}^{-1}$ . Lines guide the eye. Adapted from Ref.<sup>[46]</sup>.

decomposition rate is function of the chemical environment. GaN decomposition is significantly reduced under N-rich conditions (see [Figure 2.7\(b\)](#)), as compared to decomposition in vacuum or under excess Ga supply<sup>[46]</sup>.

## 2.2 GROWTH METHODS OF GALLIUM NITRIDE

Molecular beam epitaxy is the growth technique of choice for this thesis and will be discussed in the next chapter in detail. However, this thesis will also refer to different growth techniques of GaN; be it for comparison with results from literature or for classification of different templates or substrates which have been used. This section will therefore briefly discuss the epitaxial approach by vapor phase epitaxy (VPE), as well as the true bulk approaches by the high nitrogen pressure solution technique (HPS) and the ammonothermal method according to reviews<sup>[49,50]</sup>.

The VPE method is categorized according to the used gas sources. If a hydride source is used to supply nitrogen, the term hydride vapor phase epitaxy (HVPE) is used; if any organic precursor gas is used, the term metal-organic vapor phase epitaxy (MOVPE) applies. Both methods base on thermal cracking (pyrolysis) of gaseous precursors at the sample surface.

In HVPE, Ga metal and HCl are pre-reacted to form the group III precursor GaCl which is transported to the growth zone by a carrier gas. The source for nitrogen is ammonia  $NH_3$  and growth takes place at around  $1030^{\circ}C$ . Sapphire(0001) substrates are used for heteroepitaxial growth of GaN. The growth rates are in the range of several ten up to  $100 \mu\text{m h}^{-1}$ . Such high growth rates are sufficient to grow thick GaN layers, for which the sapphire

substrate can be sacrificed after growth. This approach yields free-standing GaN substrates.

In the case of MOVPE, trimethylgallium or triethylgallium and ammonia are used for group III and N precursors, respectively. Note, that in some cases the term MOVPE is strictly preserved for homoepitaxial growth, i.e. GaN epitaxially grown on GaN templates or substrates, while metal-organic chemical vapor deposition (MOCVD) is used for heteroepitaxial growth. The carrier gases are typically hydrogen or nitrogen, or a mixture of both. The growth temperatures are similar to HVPE, however the growth rates are in the range of a few  $\mu\text{m h}^{-1}$ . Such rates are too low for the quasi-bulk approach of HVPE. Therefore, MOCVD is only capable of growing GaN quasi-substrates, so-called templates. Standard GaN templates are about  $3\mu\text{m}$  thick GaN layers heteroepitaxially grown on  $\text{Al}_2\text{O}_3$  (0001).

True bulk GaN is grown by HPS in the form of hexagonal platelets. In this approach, liquid Ga is saturated with 1 at% nitrogen at elevated temperatures up to  $1700^\circ\text{C}$  and nitrogen pressures of 20 kbar. Temperature gradients in the range of several  $^\circ\text{C cm}^{-1}$  along the crucible allow the crystallization of GaN at the cooler end. The growth rate is highly anisotropic with growth rates of about  $1 - 2\mu\text{m h}^{-1}$  along  $\langle 0001 \rangle$  and  $50 - 100\mu\text{m h}^{-1}$  along  $\langle 1\bar{1}00 \rangle$ .

The ammonothermal method is based on the mineralizer-assisted seeded growth of bulk GaN. Liquid or polycrystalline GaN is mixed in autoclaves with the mineralizer (catalyst). Reaction occurs with ammonia at temperatures in the range of  $500$  to  $700^\circ\text{C}$  and pressures of several kbar. The GaN seeds are fed at a growth rate of about  $4\mu\text{m h}^{-1}$ . This growth rate is significantly lower as compared to HPS, however, a large number of seeds can be fed simultaneously and growth can be sustained for several days. This overcomes the drawback of the low growth rate and today, truly bulk GaN  $c$ -plane 2-inch wafers are commercially available.

# 3

---

## MOLECULAR BEAM EPITAXY OF GALLIUM NITRIDE

---

*This chapter provides the theoretical background of crystal growth. First, the general idea behind molecular beam epitaxy will be discussed. In the following parts, GaN crystal growth by molecular beam epitaxy will be considered; first, in the framework of equilibrium thermodynamics and afterwards, in a kinetic approach. Big parts of this chapter are written following the books by Markov<sup>[51]</sup> and Herman, Richter, and Sitter<sup>[52]</sup>.*

### 3.1 MOLECULAR BEAM EPITAXY

Molecular beam epitaxy (MBE) is a deposition technique for thin epitaxial films or nanostructures on a crystalline substrate in vacuum. The constituents for growth are supplied in the form of molecular beams. On the one hand, this is due to the vacuum conditions, for which the mean free path (i.e. the average distance an atom travels through vacuum without colliding with another atom) is larger than the distance between the constituent sources and the substrate. On the other hand, this is due to the use of effusion cells which allow a directed irradiation of the sample by the constituents. Therefore, interaction of the constituents occurs directly at the sample surface. The latter is heated to allow for surface migration of the atoms.

In MBE, typical source-to-substrate distances are around 30 cm. A background pressure of about  $10^{-3}$  mbar would already be sufficient for the mean free path to overcome this distance. However, MBE is an ultra-high vacuum (UHV) technique, in order to reduce impurity incorporation during growth. Typical layer growth rates in MBE are around  $1 \text{ MLs}^{-1}$  (monolayer per second), which translates to about  $1 \mu\text{m h}^{-1}$ . Such growth rates are low enough to allow for sufficient surface migration of the impinging atoms to produce high-quality epitaxial structures. Furthermore, such low growth rates and residual vapor pressures of around  $10^{-12}$  mbar allow for the growth of crystals with impurity concentrations below one part per million. In the case



of GaN, typical layer growth rates of about  $3 - 4 \text{ nm min}^{-1}$  are even lower by a factor of about 5.

In this thesis, a commercial Veeco GEN II MBE system (shown in [Figure 3.1](#)) was used. A combination of cryo and ion getter pumps, as well as liquid  $\text{N}_2$  cryo shroud cooling allows to reach background pressures of  $10^{-11}$  mbar prior to growth and  $10^{-5}$  mbar during growth. The latter value is due to the presence of nitrogen in the chamber, which is no source of contamination.

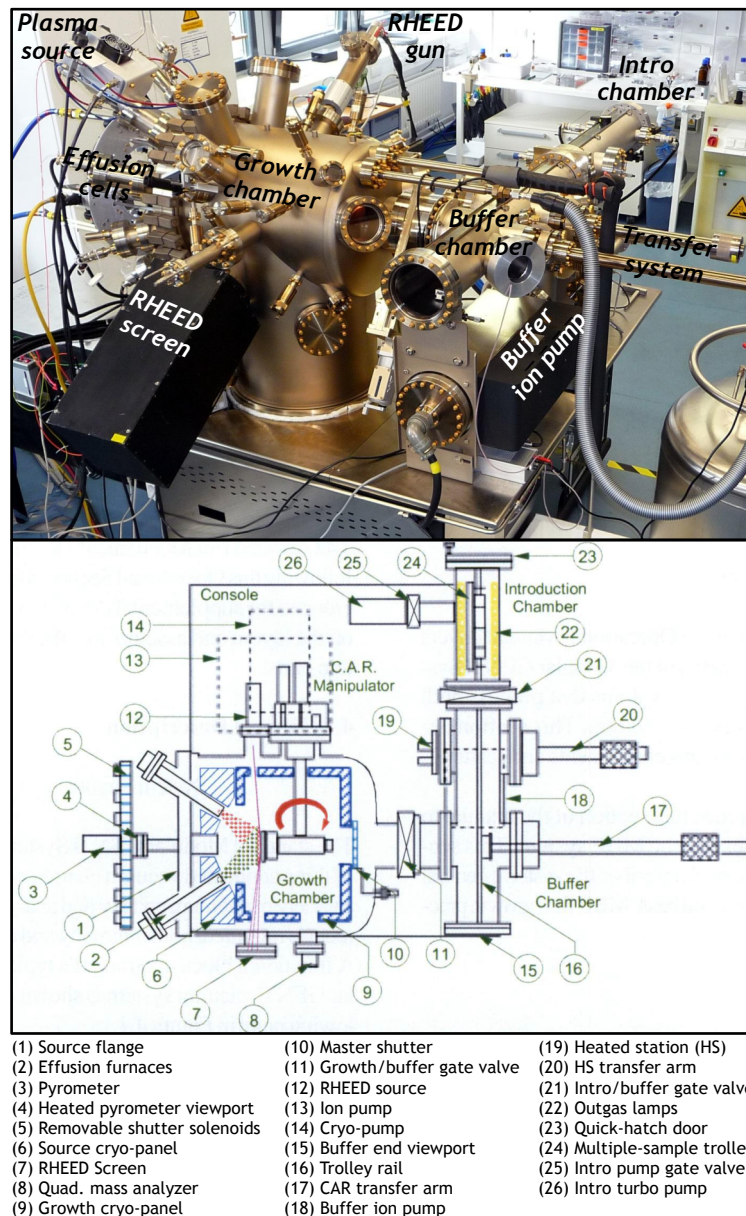


Figure 3.1: Photograph<sup>[53]</sup> and block diagram<sup>[54]</sup> of the Veeco GEN II MBE system.

The metal constituents are thermally evaporated inside inert ceramic crucibles which are heated by a filament. The crucibles are held in effusion cells which can be mechanically opened or closed by shutters which are



positioned in front of the cell. The effusion rate is controlled by the filament temperature and depends on the geometry of the cell, the filling, and the vapor pressure inside the cell. Nitrogen is a very inert gas and has to be dissociated for reaction to occur. Due to the high binding energy (9.8 eV per  $N_2$  molecule) this is thermally not possible. Therefore, a radio frequency (RF) plasma source is used to excite the nitrogen to the plasma state. Ultra-pure (6N) gaseous nitrogen is excited via a high frequency (13.56 MHz) electric field inside a resonator. Nitrogen flow rate and plasma excitation power can be regulated, which allows for changing plasma composition, i.e. the ratio of atomic and molecular nitrogen<sup>[55]</sup>.

Due to the UHV conditions and the beam nature of the constituents, the supply fluxes can be controlled precisely. Therefore, high-purity epitaxial structures with abrupt interfaces on the atomic monolayer scale can be grown by MBE. Furthermore, the UHV conditions allow for *in situ* monitoring and characterization techniques, such as reflection high energy electron diffraction (see Section 5.2.1). The procedure for substrate cleaning prior to growth and the exact growth procedure is summarized in Section 6.3. A schematic of an MBE growth chamber is shown in Figure 3.2.

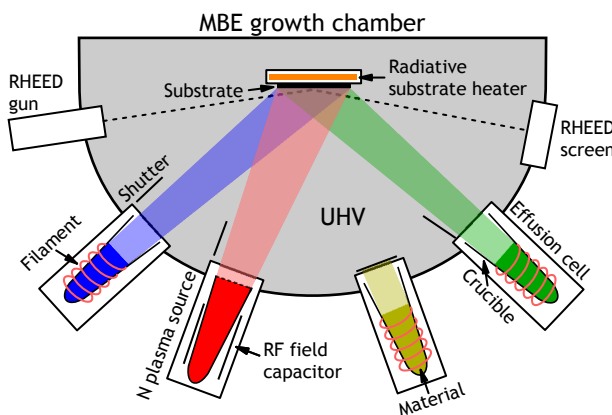


**Figure 3.2:** Schematic of an MBE growth chamber as described in the text. The gun and screen of the reflection high energy electron diffraction (RHEED) system is shown, which is used for *in situ* monitoring of growth. Adapted from Ref.<sup>[53]</sup>.

Generally, film growth is understood in the framework of thermodynamics. However, in the case of MBE, kinetics may play an important role in the description of the growth process<sup>[14]</sup>. Nevertheless, the knowledge of thermodynamic equilibrium surface structures is the starting point for the understanding of crystal growth<sup>[56]</sup>. Thus, the following sections will discuss the MBE process according to these two complementary approaches.

## 3.2 THERMODYNAMIC DESCRIPTION

### 3.2.1 Supersaturation

A thermodynamic description of the MBE process requires a thermodynamic potential which describes the constraints of the system in an appropriate

manner. Since MBE proceeds in good approximation at constant pressure  $p$  and constant temperature  $T$ , the Gibbs free energy

$$G = U + pV - TS \quad (3.1)$$

with the natural variables  $T$ ,  $p$ , and  $N$  is used. The internal energy is given by  $U$ ,  $V$  denotes the volume,  $S$  the entropy, and  $N$  the number of particles. Thermodynamic equilibrium condition for two infinitely large phases in contact is given by minimization of the Gibbs free energy and can be described by the equality of their chemical potentials  $\mu_i$ . This value is defined by the derivative of the Gibbs free energy with respect to the number of particles  $N_i$  in the system,

$$\mu_i = \left( \partial G / \partial N_i \right)_{T,p,N}, \quad (3.2)$$

and describes the work which has to be done to change the particle number of the considered phase by unity. The index  $i$  describes the type of particles, e.g. different atomic species or different phases. For a single component system with two phases  $A$  and  $B$ , the condition for thermodynamic equilibrium reads

$$\mu_A = \mu_B. \quad (3.3)$$

Crystal growth is per definition not thermodynamic equilibrium. Nevertheless, the concept of chemical potential is absolutely essential to understand crystal growth, since the difference of the chemical potentials is the *thermodynamic driving force* for phase transition. In the following, crystallization of an ideal solid from an ideal vapor will be considered. The supersaturation is the difference of chemical potentials and reads<sup>[51]</sup>

$$\Delta\mu = \mu_c(T) - \mu_v(p, T) = k_B T \ln \frac{p}{p_0}. \quad (3.4)$$

Pressure and equilibrium vapor pressure of the vapor are denoted by  $p$  and  $p_0$ , respectively. The crystal and vapor phase are denoted by  $c$  and  $v$ , respectively.

The driving force for crystallization from a vapor is thus related to pressures. Since the discussion of pressures in the case of solids may lead to misunderstandings, some extra lines will be devoted to this topic.

A crystal in the MBE chamber is held at constant temperature and is irradiated by atoms which are evaporated from an effusion cell. The vapor pressure  $p_v$  inside the effusion cell will result in a specific pressure  $p$  at the sample surface. Due to the UHV conditions the vapor can be treated as an ideal gas,  $pV = Nk_B T_v$ , where  $k_B$  is the Boltzmann constant and  $T_v$  the absolute temperature of the vapor. The pressure is related to a flux of atoms which impinge on the unit surface area:<sup>[52]</sup>

$$F = \frac{p}{\sqrt{2\pi m k_B T_v}} \quad (3.5)$$

The atomic mass is given by  $m$ . The crystal surface which is in contact with the vapor of pressure  $p$  will thus be subject to an incoming flux  $F^+$  of atoms according to Equation 3.5. Vice versa, atoms will evaporate from the crystal surface, which can be understood as negative flux. Crystal and vapor are under equilibrium pressure  $p_0$ , when the evaporating flux  $-F_0$  is counterbalanced by the impinging flux  $F_0$  from the vapor. The equilibrium flux  $F_0$  is related to  $p_0$  according to Equation 3.5. Taking into account Equation 3.4, crystallization occurs when at the sample surface  $p > p_0$  ( $F^+ > F_0$ ), and sublimation in the opposite case.

### 3.2.2 Crystal surface energies

In the following, it is assumed that the crystal phase is thermodynamically stable with respect to the vapor. In addition, not an infinitely extended crystal, but a small crystallite in contact with the surrounding vapor will be considered. As discussed, the chemical potential describes the work which has to be done to change the particle number of the phases by unity. By transferring atoms from the vapor to the crystallite, the system gains energy proportional to the product of supersaturation and number of transferred atoms. This term is therefore proportional to the volume of the crystallite. However, a phase-dividing surface between crystal and vapor has to be created, which requires energy. This is the total surface energy which is given by the product of surface energy<sup>1</sup>  $\sigma$  and total surface area  $S$ . For a crystallite with constant volume, the total surface energy depends only on the shape of the crystallite. Taking into account the difference between bulk crystal and small crystallite by its total surface energy (assumed to be isotropic), the thermodynamic equilibrium condition at constant pressure and temperature reads according to Equation 3.1<sup>[51]</sup>

$$\Delta G = \mu_c dN_c + \mu_v dN_v + \sigma dS = 0. \quad (3.6)$$

The number of atoms in the crystallite and in the vapor is given by  $N_c$  and  $N_v$ , respectively. Thus, for a closed system,  $N_c + N_v = \text{const}$  and  $dN_c + dN_v = 0$ , and the above condition for thermodynamic equilibrium reduces to the minimum in total surface energy.

In this thermodynamic framework, the surface morphology of a crystallite does not depend on the specific reaction path (kinetics), but only on the surface energy. The latter is commonly understood as the energy required to cut a crystal at some plane to obtain a new surface<sup>[56]</sup>. A method for the determination of surface energies for all crystal systems based on slab calculations is reported in Ref.<sup>[57]</sup>. However, without going into detail, within

<sup>1</sup> Note, that this is actually an energy density given in energy per unit area. However, in literature the term surface energy rather than surface energy density is used. To be congruent with literature, in the following the former term will be used.

this computational method the surface energies can only be calculated absolutely, when the two surfaces which are created by cutting a crystal are crystallographically identical<sup>[57]</sup>. For non-equivalent surfaces, only the sum of the two surface energies is absolutely defined. For individual surfaces, only relative surface energies can be calculated.

Absolute surface energies can be calculated for the nonpolar  $\{1\bar{1}00\}$  and  $\{11\bar{2}0\}$  GaN surfaces. These calculations also relate to specific GaN growth conditions which influence the atomic surface termination and surface reconstructions. The growth conditions can be fully expressed by the chemical potentials of Ga and N. The nitrogen chemical potential is typically expressed by the Ga chemical potential—this is possible due to the assumption of thermodynamic equilibrium—and the surface energies are calculated as function of the difference of the chemical potentials  $\mu_{\text{Ga}} - \mu_{\text{Ga}}^{\text{bulk}}$ <sup>[58]</sup>. The latter value is the chemical potential of the infinitely extended Ga bulk phase. The most negative boundary of this expression corresponds to N-rich growth conditions, while the origin corresponds to Ga-rich conditions. Going beyond these boundaries, liquid Ga formation (towards positive values) and GaN dissociation (towards negative values) occurs. The results for GaN  $m$ - and  $a$ -surfaces are shown as surface energy phase diagrams in [Figure 3.3](#).

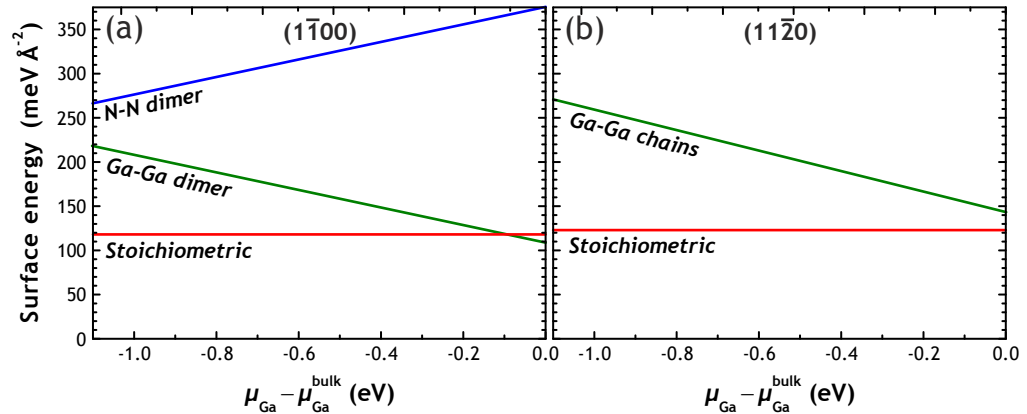


**Figure 3.3:** Surface energies for clean GaN  $m$ - (a) and  $a$ -surfaces (b) as function of the Ga chemical potential. Only the thermodynamically allowed range is shown (see text). Furthermore, surface terminations of the very first surface layer are indicated (see text). Adapted from Ref.<sup>[59]</sup>.

The surface energies of stoichiometric  $m$ - and  $a$ -surfaces are reported to be 118 and 123 meV Å<sup>-2</sup>, respectively<sup>[59]</sup>. Furthermore, non-stoichiometric surfaces which may occur during epitaxial growth, i.e. rather Ga- or N-terminated, have been studied. In the case of  $m$ -plane GaN ([Figure 3.3\(a\)](#)), this is achieved by replacing Ga (N) atoms by N (Ga) atoms in the outermost Ga-N dimer configuration of the unit cell. For stoichiometric  $a$ -plane GaN ([b](#)), the outermost surface layer shows a Ga-N chain configuration. Again, the surface termination is changed by replacing Ga (N) atoms by N (Ga) within the chain. For both surfaces, a nitrogen termination is thermodynamically not

stable. A Ga-terminated surface in the case of the  $m$ -surface, is expected to be stable only under Ga-rich growth conditions. The stoichiometric surfaces are stable for a wide range of Ga chemical potential.

Relative surface energies have been calculated for semipolar<sup>[60–65]</sup> or polar<sup>[66]</sup> GaN surfaces. However, these calculations are not suited for quantitative comparison among surfaces of different crystallographic families. Nevertheless, these calculations provide valuable predictions on the thermodynamic stability of specific surface configurations for the considered surfaces. In general, the cleaved ideal surfaces are thermodynamically unstable and cation adatom or adlayer(s) stabilized surface reconstructions are favored for a wide range of Ga chemical potential. An exception are the polar GaN surfaces, for which under N-rich conditions a  $2 \times 2$  N adatom stabilized GaN(0001) surface reconstruction is expected. For GaN(000 $\bar{1}$ ), a  $2 \times 2$  Ga adatom reconstructed surface is predicted to be stabilized under N-rich conditions. It has to be noted, that although N adatoms on such surfaces are in general thermodynamically unstable, kinetic stabilization of those adatoms may occur under specific growth conditions<sup>[67]</sup>. This will be discussed in [Section 3.3](#).

The equilibrium crystal shape of the considered crystallite is only function of total surface energy, and the calculated absolute surface energies for GaN  $a$ - and  $m$ -surfaces can thus be used to predict this shape. The equilibrium shape of a crystal surrounded<sup>2</sup> by a homogeneous vapor follows the condition<sup>[51]</sup>

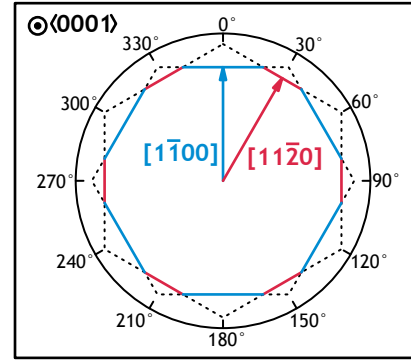
$$\frac{\sigma_j}{h_j} = \text{const.} \quad (3.7)$$

Constant temperature and volume of the system have been assumed. The surface energies of the  $j$  non-equivalent surfaces are denoted by  $\sigma_j$ . The parameter  $h_j$  gives the distance of the corresponding crystal faces to an arbitrary reference point within the crystal. The geometrical interpretation of this equation is known as Wulff construction<sup>[68]</sup>: The distance of a crystal face from a point within the crystal is proportional to the corresponding surface energy. By drawing vectors along  $\langle 11\bar{2}0 \rangle$  and  $\langle 1\bar{1}00 \rangle$  with magnitudes proportional to  $\sigma_a$  and  $\sigma_m$ , respectively, the inner polygon which is defined by the vectors normal intersections, provides the GaN equilibrium crystal shape in  $\langle 0001 \rangle$  projection. This construction is shown in [Figure 3.4](#), using the reported surface energies of the nonpolar surfaces.

The theoretical value of the segment length ratio of stoichiometric GaN  $m$ - and  $a$ -surfaces is 1.8. GaN crystallites which exhibit the equilibrium crystal shape will always show this shape, no matter at what stage of growth, i.e. for short or long growth times. Note, that a necessary prerequisite for the

<sup>2</sup> An analogous approach treats a crystal on a foreign substrate<sup>[51]</sup>. Besides surface energies, also interfacial energies have to be taken into account. However, since this thesis treats the homoepitaxial growth of GaN, the omission of interface contributions is justified.

**Figure 3.4:** Polar Wulff construction to determine the GaN equilibrium crystal shape in projection along  $\langle 0001 \rangle$ . The magnitude of the vectors along  $a$ - and  $m$ -directions are proportional to the corresponding absolute surface energies. Dotted lines show vector normals, the equilibrium crystal shape corresponds to the inner polygon which is indicated by solid lines.



equilibrium shape is the condition of constant supersaturation all over the crystal surface. Due to the non-existence of reliable surface energies for GaN(0001) and GaN(000 $\bar{1}$ ) surfaces, the equilibrium shapes in  $[11\bar{2}0]$  and  $[\bar{1}\bar{1}00]$  projection are not predictable.

### 3.2.3 Size effects

The preceding section pointed out the importance of surfaces, if non-infinitely extended systems are considered. This section will discuss the effect of variable particle size on the equilibrium vapor pressure over the particle and its consequences for growth. Again, surface energies will be shown to be of major importance.

For simplicity, first a liquid in contact with vapor will be discussed. The discussion will then be extended to a crystallite which is surrounded by vapor.

A single molecule inside the liquid will experience a net cohesive force due to the average molecule density. If this molecule is placed in contact with the flat surface of the liquid, the net cohesive force will be reduced due to the reduced average molecule density at the surface. Evaporation of molecules at the very surface thus requires less energy as compared to molecules inside the liquid. An equilibrium vapor pressure over the liquid will result. If the same molecule is now located at the surface of a droplet with a diameter comparable to only several molecules, the net cohesive force will be further reduced and the molecule is evaporated even more easily. Thus, a higher equilibrium vapor pressure over such a small liquid droplet occurs.

Treating this problem theoretically, a liquid droplet at constant temperature  $T$ , which is in contact with a vapor, and enclosed in a constant volume is considered. One then obtains the equation of Thomson-Gibbs<sup>[51]</sup> which relates supersaturation to droplet size:

$$\mu_v - \mu_l = \frac{2\sigma\Omega}{r} \quad (3.8)$$

The chemical potential and surface tension of the liquid are given by  $\mu_l$  and  $\sigma$ , respectively. The average volume of a molecule or atom inside the droplet of radius  $r$  is denoted by  $\Omega$ . Derivation of Equation 3.8 requires the calculation of  $dS/dV = 2r^{-1}$  for a spherical particle with surface area  $S$  and volume  $V$ . With the result from Equation 3.8, Equation 3.4 can be rewritten in terms of a size-dependent equilibrium vapor pressure  $p(r)$  of the droplet

$$p(r) = p_0 \exp\left(\frac{2\sigma\Omega}{rk_B T}\right). \quad (3.9)$$

The equilibrium vapor pressure over the infinitely extended liquid with flat surface is  $p_0$ . Thus, with decreasing droplet size the equilibrium vapor pressure over the droplet will increase.

Equation 3.9 is still valid if a small crystallite of spherical shape and with isotropic surface energy  $\sigma$  is considered<sup>[51]</sup>. The atomic volume  $\Omega$  inside the crystal replaces the average volume of an atom or molecule inside the liquid. Figure 3.5 illustrates a cubic model crystal for a pictorial discussion.

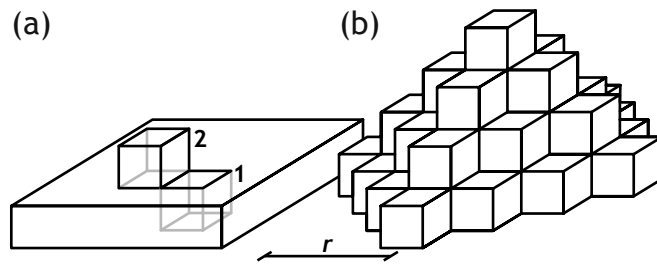


**Figure 3.5:** Cubic model crystal with flat surface (a) and a particle with finite radius (b). Atomic positions 1 and 2 correspond to sites which require highest and lowest energy for removal of these surface atoms, respectively.

In the case of the flat surface in Figure 3.5(a), the atomic position 1 which is embedded in the crystal will have five bonds with the crystal. The position 2 forms only one bond. Separation of the atoms from the crystal thus requires breaking different numbers of bonds, and the removal of the atom at position 2 requires less energy. In Figure 3.5(b), a particle with finite radius is considered. The average atomic coordination number (nearest neighbors) of the surface atoms varies with the particle radius  $r$ . For an infinite radius, the flat surface of (a) is obtained. For smaller radii, the two extremal positions which occur are 1 and 2. Therefore, the number of bonds which have to be broken to remove a surface atom will be in the range of five to one. For crystallites small enough to significantly change the average coordination number of the surface atoms as compared to the flat surface, the equilibrium vapor pressure over the surface will be thus larger. Note, that as a first approximation the surface energy is equal to the sum of energies of the broken bonds per unit area<sup>[51]</sup>. Consequently, the same conclusion follows, if Figure 3.5 is discussed in terms of the surface energy.

In the following, a spherical GaN particle on a flat surface will be considered. Using Equation 3.9 and revisiting Equation 3.5, the corresponding equilibrium evaporation rate  $F^-$  of atoms from such a small crystallite with isotropic surface energy is given by

$$F^-(r) = -F_0 \exp\left(\frac{2\sigma\Omega}{rk_B T}\right). \quad (3.10)$$

The equilibrium evaporation rate  $-F_0$  corresponds to  $p_0$ . In thermodynamic equilibrium, the evaporation flux is counterbalanced by the incoming flux  $F^+$ . If however the vapor pressure around the crystallite is changed, the net flux  $F_{\text{tot}}$  from the vapor to the crystallite (or vice versa for negative values) is given by

$$F_{\text{tot}}(r) = F^+ + F^-(r) = F^+ - F_0 \exp\left(\frac{2\sigma\Omega}{rk_B T}\right). \quad (3.11)$$

The following paragraph will discuss whether size-dependent evaporation rates (Equation 3.10) are expected to influence growth rates of GaN during MBE.

The Ga flux from a GaN crystal, which corresponds to equilibrium vapor pressure is difficult to determine, since phase diagrams of the GaN(s) + Ga(g) system are limited<sup>[69]</sup>. The solid and gaseous phases are denoted by s and g, respectively. Instead, one can use experimental data obtained from GaN decomposition experiments<sup>[46]</sup> under conditions similar to typical MBE growth conditions. The authors measured the Ga desorption flux  $F_{\text{Ga}}^-$  (calibrated in  $\text{nm min}^{-1}$ ) from a decomposing GaN(0001) surface for various chemical environments (see Figure 2.7(b)). To counterbalance decomposition, at least  $F_0 \geq |F_{\text{Ga}}^-|$  is required. The experimentally obtained value for  $|F_{\text{Ga}}^-|$  is thus estimated as lower limit for  $F_0$ . Note, that a real crystal surface is never atomically smooth and the reported value is thus not related to a perfectly smooth crystal surface. However, the authors point out that their GaN(0001) layer was regrown under slightly Ga-rich conditions before experiments. These conditions are known to provide very smooth surfaces<sup>[70]</sup>. For a substrate temperature of  $780^\circ\text{C}$  and an incoming active nitrogen flux of  $5.0 \text{ nm min}^{-1}$ , the desorbing Ga flux was around  $F_{\text{Ga}}^- = -0.2 \text{ nm min}^{-1}$ . These conditions resemble the typically used growth conditions of this thesis (substrate temperature of  $780^\circ\text{C}$  and N flux of  $6.2 \text{ nm min}^{-1}$ ).

To calculate the magnitude of the size-dependent evaporation rates, in addition, assumptions concerning the GaN surface energy have to be done. Exemplarily the value of  $123 \text{ meV \AA}^{-2}$  for the stoichiometric  $a$ -surface was chosen. Since any three-dimensional particle requires various surfaces, e.g.  $a$ -,  $m$ -, and  $c$ -surfaces, the surface energy was varied between factors  $1/2$  and  $3/2$  to understand the effect of surface energy variation. The calculation of Equation 3.10 for the discussed values is shown in Figure 3.6.

The size-dependent Ga evaporation rate is predicted to exceed the Ga equilibrium evaporation rate even for particle radii as large as 100 nm. The



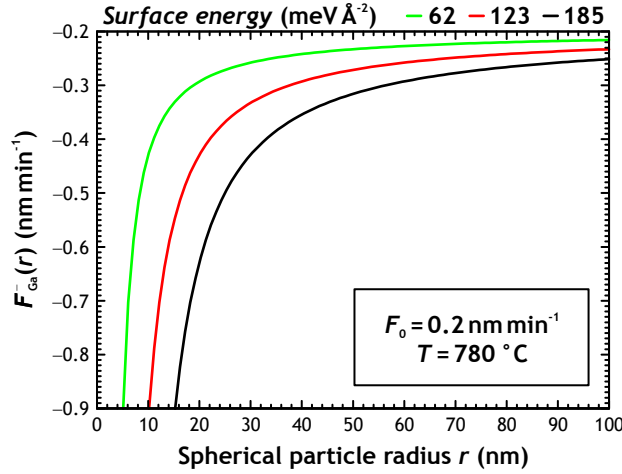


**Figure 3.6:** Calculation of the Ga evaporation rate from (indicated by minus sign) a spherical GaN particle with isotropic surface energy as function of particle radius. The surface energy is varied. The atomic volume of Ga in GaN is  $\Omega_{\text{Ga}} = 1/2 \cdot 11.24 \text{ \AA}^3$ . The substrate temperature is given, as well as the assumption for the Ga equilibrium evaporation rate from a GaN(0001) surface under a nitrogen supply of  $5 \text{ nm min}^{-1}$ .

magnitude of these deviations increases for increasing surface energy. For decreasing particle size, the Ga evaporation rate becomes more negative, indicating enhanced Ga evaporation. In this thesis, an effective Ga flux at the sample surface of  $0.7 \text{ nm min}^{-1}$  was used. This value explicitly includes desorption (see Section 6.2). Assuming, that the incoming flux was larger by  $F_0$ , a value of  $F_{\text{Ga}}^+ = 0.9 \text{ nm min}^{-1}$  is obtained. According to Figure 3.6 and Equation 3.11, for a spherical GaN particle with an isotropic surface energy which corresponds to the  $\alpha$ -surface, the total flux is counterbalanced for a particle radius of about 10 nm. A decrease or increase of the surface energy will shift the radius for flux counterbalance to smaller and larger radii, respectively.

The increase of the total flux with increasing particle size is commonly referred to as *Gibbs-Thomson effect* and the effect on the growth rates, i.e. a higher growth rate for larger particle radii, is known as *Ostwald ripening*. These effects are used to explain nanocolumn growth rates which increase for increasing nanocolumn diameter of nanocolumns grown by the vapor-liquid-solid (VLS) approach<sup>[71-74]</sup>. For GaN nanocolumns, which are grown by the vapor-solid (VS) approach, this effect was scarcely reported<sup>[75]</sup> or hypothesized<sup>[76]</sup> to influence the nanocolumn axial growth rates. Nevertheless, it is suggested that this effect may influence the growth rates of GaN nanostructures due to size-dependent equilibrium vapor pressures. The mechanism which is expected to result in the opposite behavior, namely increasing axial growth rates with decreasing diameter is due to diffusion, and is treated in the next section. For nanocolumn growth by the VLS

approach the reader is referred to Ref.<sup>[77]</sup>, the VS growth mechanism of GaN nanocolumns will be discussed in [Chapter 4](#).

### 3.3 KINETIC DESCRIPTION

Growth of the III nitrides by MBE proceeds at relatively low temperatures as compared to conventional III–V semiconductors. Therefore, the MBE process is often discussed to be rather governed by kinetics than by thermodynamic equilibrium<sup>[14]</sup>. In the kinetic description, energy barriers prevent atoms from occupying configurations which are related to (absolute) potential energy minimum. Thus, growth rates will depend on constituent arrival rates, and surface morphologies may depend on the specific reaction path.

The impinging constituents are adsorbed on the substrate surface at first. Surface migration via diffusion allows the atoms to sample the crystal for energetically favorable crystal positions, where they may be incorporated into the crystal lattice. Also nucleation on the crystal surface may occur. If no incorporation occurs, the constituents will thermally desorb into the gas phase<sup>3</sup>; furthermore, thermal decomposition of the crystal may take place by breaking of bonds. These processes are competing with each other and the kinetic approach of crystal growth uses rates and activation energies. The following paragraph will discuss these atomistic processes.

The impinging constituents have to overcome an activation barrier in order to be adsorbed at the substrate surface. The adsorbed atoms can be bound weakly (neutral adsorbate) to the surface or strongly (binding energies in the range of several eV) due to electron transfer between adsorbate and surface<sup>[78]</sup>. In the case of Ga, weak adsorption on GaN(0001) is observed<sup>[78]</sup>, which suggests that the Ga adatoms are sufficiently mobile for subsequent diffusion. For this, the atoms have to overcome an activation barrier which is due to the surrounding lattice potential. In a random walk with a diffusion length

$$\lambda = \sqrt{D\tau} = \sqrt{D_0 \exp(-E_d / (k_B T)) \tau}. \quad (3.12)$$

they will diffuse on the substrate surface effectively preferentially along potential minimum pathways.  $D$  and  $D_0$  are diffusion coefficients, with the latter being temperature-independent. The lifetime of the diffusion event and the activation energy are given by  $\tau$  and  $E_d$ , respectively. Limiting values for  $\tau$  can be the lifetime before desorption or incorporation. For the latter event, the lifetime depends inversely on the growth rate. Therefore, the diffusion length on a given surface may not only be function of temperature according to [Equation 3.12](#), but of growth rate as well. Such a behavior was exemplarily calculated for Ga diffusion on cubic GaN(001) based on experimentally determined diffusion coefficients<sup>[79]</sup>. Under the assumption that the lifetime

<sup>3</sup> This process can also take place immediately after adsorption.

of the diffusion event is limited by the growth rate, an increase of the Ga adatom surface diffusion length was calculated for decreasing growth rate, as well as for an increase of temperature. If however the limiting factor for the diffusion lifetime is a high desorption rate (i.e. high temperature), the counterintuitive result is obtained, that an increase of temperature further decreases the Ga adatom diffusion length. This implies, that diffusion lengths at typical growth conditions have to be assessed and cannot be simply extrapolated using [Equation 3.12](#).

The potential energy surface (PES) for Ga and N adatom diffusion on GaN(0001) and GaN(000 $\bar{1}$ ) was studied by *ab initio* calculations<sup>[67]</sup>. The results show lowest barriers for Ga diffusion on Ga- and N-polar GaN to be 0.4 and 0.2 eV, respectively. In the case of N, significantly higher barriers of 1.4 and 0.9 eV are obtained. This shows, that Ga adatoms are more mobile on GaN(0001) and GaN(000 $\bar{1}$ ) as compared to N by orders of magnitude at typical growth temperatures. Under excess N, the lowest diffusion barriers for Ga increase by a factor of about 5. This is typically attributed to rough surface morphologies of GaN(0001) layers grown under such conditions.

N and Ga adatom diffusion barriers on nonpolar GaN surfaces were also studied<sup>[80]</sup>. In the case of Ga adatom diffusion, a strong in-plane anisotropy was found. On the *m*-surface, lowest diffusion barriers of around 0.2 and 0.9 eV were calculated for Ga adatom diffusion along  $[11\bar{2}0]$  and  $[0001]$ , respectively. In case of the *a*-surface, the lowest diffusion barriers are about 0.6 and 0.3 eV along  $[1\bar{1}00]$  and  $[0001]$ , respectively. These results indicate that Ga adatom diffusion along the *c*-axis is favored for the *a*-surface as compared to the *m*-surface. In the case of N adatoms, an instability of the nonpolar surfaces against atomic N is reported. This indicates, that once an N adatom diffuses on these surfaces close to another N atom from the crystal or close to another N adatom on the surface, the formation of N<sub>2</sub> is favored.

When the constituents are incorporated into the crystal a chemical bond (between Ga and N) is formed. Under typical GaN synthesis environment in MBE, liquid (l) Ga and gaseous (g) molecular nitrogen have the lowest free energy<sup>[81]</sup>. Therefore, the forward reaction  $2\text{Ga}(\text{l}) + \text{N}_2(\text{g}) \rightarrow 2\text{GaN}(\text{s})$  requires energy which may be provided by various excited nitrogen species. The crystal phase (which may be thermodynamically unstable, see [Figure 2.7](#)) is stabilized by a kinetic energy barrier for decomposition (cohesive energy of about 2.2 eV per Ga–N bond), such that the rate of backward reaction is exceeded by the forward reaction which allows for growth of GaN<sup>[81]</sup>. The growth rate is thus given by the differences of forward (incorporation) and backward (decomposition) rates.

Nucleation is a random process caused by density fluctuations within the homogenous mother phase (e.g. vapor). The rate of nucleation can be calculated in the kinetic approach. However, the exact rates are not of interest in this thesis, and therefore a thermodynamic approach is used to explain the

phenomenon of nucleation qualitatively: Homogenous nucleation is driven by the competition of the magnitudes of the thermodynamic potential of a cluster and the same amount of material in the mother phase. In the case of cluster formation, the increase of total energy due to the formation of a surface has to be compensated by the energy gain which originates from the volume formation. This criterion leads to a critical radius for nucleation; below this value the nucleus is thermodynamically unstable and the probability of decay will overcome the probability of growth. The opposite effect, i.e. formation of a stable nucleus and subsequent growth occurs for nuclei with radii larger than the critical radius. If impurities, defects and foreign surfaces are present, heterogeneous nucleation furthermore requires the consideration of interface energies.

During desorption the adsorbed atoms overcome the attractive adsorption potential and are re-evaporated. The rate of desorption is therefore proportional to a Boltzmann factor  $\propto \exp(-E_{\text{des}}/(k_B T))$ , with the corresponding activation energy  $E_{\text{des}}$ . Since the lifetime between adsorption and desorption event  $\tau_{\text{des}} \propto \tau_0 \exp(E_{\text{des}}/(k_B T))$ <sup>[82]</sup>, the desorption process is very sensitive to temperature.  $\tau_0$  denotes a constant. Gallium desorption occurs in the atomic form, i.e. Ga atoms. For nitrogen however, desorption occurs in the molecular form  $\text{N}_2$ . This is due to the large binding energy of the  $\text{N}_2$  molecule (9.8 eV per molecule) and the exothermic nature of the reaction. Thus, desorption of  $\text{N}_2$  is expected, once an N adatom diffuses close to another N atom. In this case, surface diffusion may limit the  $\text{N}_2$  desorption rate. An important consequence of this is the prediction that various N adatom terminated GaN surfaces are thermodynamically unstable against atomic nitrogen<sup>[62,64,65,67,80,83]</sup>. In the case of the polar GaN surfaces, the thermodynamically unstable N adatom configuration may be kinetically stabilized under excess nitrogen growth conditions. This is due to the relatively large N diffusion barriers<sup>[67]</sup>. The nonpolar surfaces are in contrast discussed to be unstable against atomic N even for stoichiometric surface termination<sup>[80]</sup>.

# 4

---

## MOLECULAR BEAM EPITAXY OF GALLIUM NITRIDE NANOCOLUMNS

---

*This chapter will review two complementary approaches for the non-catalytic growth of GaN nanocolumns by molecular beam epitaxy. First, the self-induced growth and the underlying growth mechanism will be discussed. Building on the understanding of the self-induced growth mechanism, general aspects which also apply in the selective area growth will then be discussed in the second part. The last section is devoted to the discussion on the polarity of MBE-grown GaN nanocolumns.*

### 4.1 SELF-INDUCED GROWTH

Catalyst-free, self-induced (SI) growth of GaN nanocolumns (NCs) by MBE was reported first in 1997 by the group of K. Kishino at Sophia University, Tokyo, Japan<sup>[84]</sup>, and shortly after at the Universidad Politécnica de Madrid, Madrid, Spain<sup>[85]</sup>. The term nanocolumn describes columnar crystallites for which the height exceeds the diameter several times, and the latter is typically in the range of some hundred nanometers. Several terms are used in literature such as nanowire, nanocolumn, and nanorod, or even sub- $\mu\text{m}$  columns. The first term is typically used when the diameter is below 100 nm. Nanocolumns or -rods refer to columnar structures with diameters above 100 nm, however, significantly smaller than one micron. Sub- $\mu\text{m}$  columns refer to columnar crystallites with diameters in the range close to one micron. For convenience, the term nanocolumn will be used throughout this thesis, even though the diameter of the columns of this thesis is in the range of 100 nm to 1  $\mu\text{m}$ . Furthermore, these structures grow in a defined direction with respect to the substrate, in most cases perpendicular. The term self-induced refers to the formation of these structures without the use of a foreign catalyst material. Many experiments have been conducted to study the underlying growth mechanism since the publication of the first reports. These experiments cover a wide parameter window such as the flux

ratio  $F_{\text{N}}^+ / F_{\text{Ga}}^+$ , inclination of the cell ports in the MBE chamber, growth time, substrate temperature, polarity and thickness of buffer layers, as well as different substrate materials. The most common substrate is Si. For a complete overview, the reader is referred to Refs.<sup>[12,86]</sup>. The growth mechanism of self-induced GaN NCs has been studied in detail and general concepts which also apply in the case of selective area growth will be summarized here.

The growth of self-induced NCs proceeds under nominally nitrogen-rich ( $F_{\text{N}}^+ / F_{\text{Ga}}^+ > 1$ ) growth conditions at high growth temperatures in the range of the GaN decomposition temperature (800 °C) or above. In general, the growth can be divided into two stages.

In the first stage, nucleation of stable GaN nuclei occurs<sup>[87–91]</sup>. The nucleation may be delayed by an incubation time  $t_{\text{inc}}$ <sup>[88,90,92,93]</sup>. For self-induced GaN NCs on  $\text{Si}_x\text{N}_y/\text{Si}(111)$ , it was shown that the incubation time can easily reach several tens of minutes and increases with a reduction of Ga flux<sup>[93,94]</sup> or a raise of substrate temperature<sup>[93]</sup>. For heterogeneous nucleation ( $\text{AlN}(0001)/\text{Si}(111)$ <sup>[88,90]</sup> and  $\text{Si}_x\text{N}_y/\text{Si}(111)$ <sup>[93]</sup>), the subsequent elongation of the NC is initiated by a shape transition (plastic relaxation) of the GaN nuclei from spherical cap-shaped to the typically observed hexagonal NC shape with flat  $c$ -plane tip and  $m$ -plane sidewalls. It was argued, that the driving force for the shape transition is an anisotropy of surface energy of the involved polar, nonpolar and semipolar GaN surfaces<sup>[90]</sup>. This led to the conclusion that the nucleation stage is rather governed by thermodynamics than kinetics.

The second stage of growth, the elongation phase, is generally accepted to be driven by Ga diffusion towards the NC tip<sup>[87,92,95–107]</sup>. In this kinetic description, the axial growth rate is given by the direct impingement of Ga and N on the tip area and Ga diffusion on the substrate and the NC sidewalls towards the tip. Note, that in the following always *experimental*<sup>1</sup> diffusion lengths are considered. These conclusions were drawn from *ex situ* growth rate investigations. The average axial growth rate was shown to be larger than the nominal Ga supply and increased with the latter<sup>[99,104,106]</sup>. Comparison of the axial growth rate with the nominal N supply showed, that the latter exceeded the axial growth rate. Monitoring the *in situ* NC axial growth rate as function of NC height by AlN marker insertions<sup>[92,105]</sup>, consolidated these observations. Furthermore, a radius-dependent axial growth rate  $\propto r^{-1}$  was reported<sup>[98]</sup>, which is predicted according to NC growth models which take into account mass transport due to diffusion<sup>[74,98,106–110]</sup>. Note however, that also deviating<sup>[87]</sup> or opposing<sup>[75]</sup> diameter-dependent axial growth rates were reported. In the latter case, an increase of the NC axial growth rate with NC radius was observed. From theoretical side, a NC growth mechanism assisted by Ga adatom diffusion is supported: The potential energy surface

<sup>1</sup> These experimentally assessed diffusion lengths are expected to differ from theoretical calculations in which perfect surfaces are considered.

for Ga adatom diffusion on GaN  $m$ - and  $a$ -surfaces was calculated (see Section 3.3). The calculations indicate that Ga adatom diffusion along the  $c$ -axis (typical growth direction of MBE-grown GaN NCs) is favored for the  $a$ -surface as compared to the  $m$ -surface. Since the sidewalls of SI NCs are typically  $m$ -surfaces<sup>[106,111,112]</sup>, one can conclude that enhanced diffusion towards the tip either occurs at sidewall edges, where  $a$ -plane facets are formed, or that Ga adatoms have to be adsorbed on the  $m$ -surfaces in close proximity to the NC tip to contribute to axial growth<sup>[80]</sup>. In addition, one could consider the adsorption on a  $m$ -surface, diffusion along  $[11\bar{2}0]$  to an  $a$ -surface—which may include a diffusion barrier—and subsequent diffusion along  $[0001]$ . The Ga diffusion length on GaN NC sidewalls along the  $c$ -axis was estimated from experiment, and a value of about 40 – 45 nm was found<sup>[92,98,106]</sup>. This value is much smaller than the typical NC height which is in the range of some hundred nanometers to a few microns. For NC heights smaller than this diffusion length, in addition Ga diffusion from the substrate has to be taken into account. Ga adatoms which are diffusing from the substrate to the NC sidewalls are expected to have to overcome a diffusion barrier, and thus, both diffusion lengths may be rate limiting. A contribution to growth due to diffusion of N on the NC sidewalls was ruled out theoretically<sup>[80]</sup>.

The phase of the NC tip was found to be solid after growth and a vapor-solid growth mechanism was concluded. This interpretation was supported by further experiments<sup>[100,102,113]</sup>, which included Ga predeposition<sup>2</sup>, growth interruptions<sup>3</sup>, as well as ramping the grown samples down to ambient temperature under Ga flux<sup>4</sup>.

Taking into account major key points which govern the growth of SI GaN NCs by MBE, theoretical models to predict the axial growth rate were developed. In the following, one of the latest models by Dubrovskii *et al.*<sup>[106]</sup> will be discussed. An isolated, hexagonal NC with variable height  $h$  and constant radius  $r$  is impinged by N and Ga ( $F_{\text{Ga}}^+$ ) at the  $c$ -plane tip and the vertical sidewalls. Mass transport from the substrate and the NC sidewalls to the tip is considered, taking into account stationary diffusion equations for the Ga adatom concentrations. Furthermore, Ga desorption from the tip ( $F_{\text{Ga}}^-$ ) is taken into account. The details of the model can be found in the mentioned reference. In the following, only the two asymptotic regimes of the axial growth rate  $dh/dt$  will be discussed:

- 
- 2 This suppressed the growth of self-induced NCs on the predeposited Ga droplet region.
  - 3 The size of a liquid Ga droplet at the NC tip should change due to desorption or diffusion. A kink or step would be observed along the NC growth axis after growth continuation.
  - 4 No liquid Ga droplet at the tip of the nanocolumns was observed.

**Regime I:**

$$\frac{dh}{dt} = F_{\text{Ga}}^+ \left( 1 - \frac{F_{\text{Ga}}^-}{F_{\text{Ga}}^+} + \frac{1}{r} \left( \frac{\lambda_s^2}{h} \cdot A + h \cdot B \right) \right), \text{ for } h \ll \lambda_f. \quad (4.1)$$

**Regime II:**

$$\frac{dh}{dt} = F_{\text{Ga}}^+ \left( 1 - \frac{F_{\text{Ga}}^-}{F_{\text{Ga}}^+} + \frac{\lambda_f}{r} \cdot C \right), \text{ for } h \gg \lambda_f. \quad (4.2)$$

The growth time is denoted by  $t$ . The effective diffusion lengths on NC sidewalls and substrate are given by  $\lambda_f$  and  $\lambda_s$ , respectively. The parameters  $A$ ,  $B$ , and  $C$  contain geometric considerations, the driving forces for the Ga adatom diffusion towards the tip<sup>[106,114]</sup> and diffusion coefficients on substrate and NC sidewalls. Figure 4.1 shows the calculated NC axial growth rates for the two regimes.

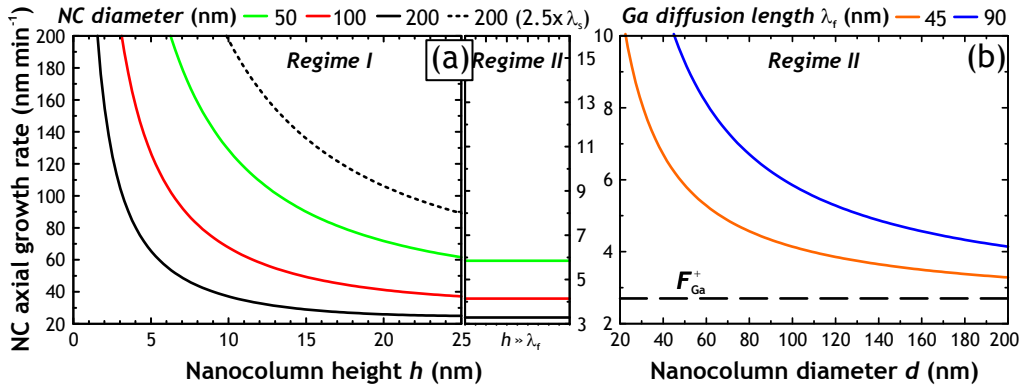


**Figure 4.1:** Calculation of the NC axial growth rate for *regimes I* and *II* as function of NC height (a) and NC diameter (b). All parameters were taken according to Ref.<sup>[106]</sup>. For (a) the Ga diffusion length on the substrate  $\lambda_s$  is about 100 nm. NC diameter and  $\lambda_s$  are exemplarily varied. For (b),  $\lambda_f$  is varied. The dashed line in (b) denotes the incoming Ga flux of 2.7 nm min<sup>-1</sup>.

For both regimes, the direct impingement/desorption term  $\left( F_{\text{Ga}}^+ \left( 1 - \frac{F_{\text{Ga}}^-}{F_{\text{Ga}}^+} \right) \right)$  contributes to growth in a constant manner.

For *regime I* ( $h \ll \lambda_f$ ), the axial growth rate is independent on  $\lambda_f$ . The term reciprocal in  $h$  is due to Ga diffusion on the substrate. The magnitude of this term decreases with increasing NC height. However, it is quadratic in  $\lambda_s$  and may therefore strongly influence the growth rate, as shown in Figure 4.1(a). The term linear in  $h$  is due to Ga diffusion on the sidewalls and gains weight with increasing NC height. The total diffusion term shows a reciprocal radius dependence, i.e. a higher growth rate is predicted for thinner NCs as compared to thicker NCs. Note, that the growth rate may easily be enhanced by two orders of magnitude as compared to the incoming flux according to this model. However, this enhancement is significantly



reduced, once the NC height becomes comparable to the Ga diffusion length on the NC sidewalls.

For *regime II* ( $h \gg \lambda_f$ ), the Ga adatoms which diffuse on the substrate are not contributing to axial growth; only diffusion on the sidewalls has to be considered. Again, the diffusion term shows a reciprocal radius dependence and depends linearly on  $\lambda_f$ . Interestingly, the growth rate is no function of NC height. Thus, stationary growth conditions at the tip are predicted for NCs with constant diameter.

The model was successfully applied to describe the self-induced growth of GaN NCs by MBE on Si(111)<sup>[106]</sup>.

## 4.2 SELECTIVE AREA GROWTH

Selective area growth (SAG) is a catalyst-free epitaxial growth technique which combines a bottom-up (epitaxy) and a top-down (lithography) approach. A substrate is covered with a thin functional layer which is lithographically patterned. This layer is chemically inert and acts as mask where nucleation during growth is strongly suppressed. The regions where the layer has been removed act as nucleation centers. For sufficiently small apertures in the functional layer, this leads to position-controlled epitaxial growth of nanostructures on the substrate. A detailed overview on the SAG of GaN NCs by MBE and MOVPE and their potential for solid state lighting can be found in Ref.<sup>[12]</sup>. A diversified overview on the SAG of III–V NCs by MOVPE and their possible applications is reviewed in Ref.<sup>[115]</sup>. The following paragraph will review the development of SAG of GaN NCs in chronological order and conclusions concerning the understanding of the growth mechanism will be drawn.

The earliest approach towards the achievement of catalyst-free position-controlled growth of single GaN NCs by MBE was reported at Sophia University, Tokyo, Japan<sup>[116,117]</sup> in 2008. Thin Al dots were deposited on Si(111) and AlN islands were formed by nitridation. On or at the edge of these islands, the growth of GaN NCs perpendicular to the substrate was achieved. Similar to the SI case, N-rich conditions and a high growth temperature around 970 °C were used. Nucleation of GaN was suppressed on the bare Si substrate. This is understood to be due to the formation of a thin  $\text{Si}_x\text{N}_y$  layer during nitridation<sup>[87,101,102,118,119]</sup>, which acts as inert layer at such temperatures. When the growth of GaN on  $\text{Si}_x\text{N}_y/\text{Si}(111)$  was not completely suppressed (for lower temperatures), a denuded area around the AlN pattern was observed, where no growth of GaN occurred. The authors concluded that the growth was suppressed due to Ga adatom surface diffusion from the substrate towards the NCs. The Ga diffusion length on the substrate was estimated from the width of the denuded zone. This approach showed that the key towards the selective area growth of single

GaN nanocolumns is a thin functional layer different from the substrate on which the GaN NCs epitaxially grow.

In a following experiment, thin stripes of Ti were deposited onto Si(111)<sup>[120]</sup> and irradiated by atomic nitrogen. This resulted in the formation of TiN and  $\text{Si}_x\text{N}_y$ . At lower growth temperatures (around 880 °C), growth of GaN occurred on the mask, as well as on the substrate in between the TiN stripes. Raising the temperature above 935 °C, the nucleation of GaN on the TiN stripes was suppressed. This was attributed to the enhanced surface diffusion of Ga adatoms from the substrate towards the unpatterned areas. On the substrate, dense growth of non-ordered GaN NCs occurred. Decreasing the width of the uncovered  $\text{Si}_x\text{N}_y/\text{Si}(111)$  stripes down to 120 nm, a row of single GaN NCs was grown, while the growth on the TiN mask was suppressed. It was suggested, that these growth conditions and a regularly patterned TiN layer with aperture diameters less than several hundred nanometers is suited for SAG of single GaN NCs. This approach was realized by the group of K. Kishino using GaN templates for the homoepitaxial SAG of single GaN NCs with aperture diameters of around 170 nm<sup>[121,122]</sup>. Well-aligned GaN NCs with  $\{1\bar{1}00\}$  sidewalls and a pyramidal tip geometry were obtained at a growth temperature around 900 °C. By raising the growth temperature from 900 to 925 °C, the denuded zone around the SAG NCs was enlarged and the Ga adatom diffusion length on the TiN was estimated to increase from 92 to 495 nm. Furthermore, a decrease of the axial growth rate was observed, which was interpreted to be due to accelerated desorption of Ga adatoms from the TiN surface. For increasing nitrogen flux, an increase of the axial growth rate was observed. This led to the conclusion that the SAG occurred under the nitrogen supply limitation scheme<sup>[122]</sup>.

Similar to the previous results, Bertness *et al.* reported of SAG GaN NCs with pyramidal tip region and  $\{1\bar{1}00\}$  sidewalls on AlN buffer layers on Si(111). A  $\text{Si}_x\text{N}_y$  mask was used and growth occurred in the N-rich regime at a growth temperature around 840 °C. The authors however pointed out, that the selectivity mechanism was rather due to Ga evaporation from the mask, than diffusion on the mask. This was concluded from the observation that the NC axial growth rate was independent of aperture diameter and pitch. The pitch denotes the nearest neighbor distance of apertures for regularly patterned arrays. When growth conditions were altered, such that GaN nucleated on the mask, no denuded zone around the NCs was observed. Although Ga diffusion on the mask was ruled out, it was suggested that Ga diffusion on the NC tip facets has to be considered. This was concluded from the fact, that the pyramidal tip geometry was only observed for aperture diameters < 500 nm. For larger NC diameters, the tip showed multiple random facets. This was attributed to insufficient Ga diffusion.

Gotscke *et al.* investigated Si<sup>[123]</sup> and  $\text{Si}_x\text{O}_y$ <sup>[124]</sup> masks on AlN buffer layers on Si(111) for the SAG process under nitrogen-rich conditions at 800 °C. For sufficiently small apertures (diameter around 60 nm), single

GaN NCs with  $c$ -plane tip and  $m$ -plane sidewalls have been grown. In the first publication the authors presented a quantitative approach to explain average radial and axial growth rates in a Ga diffusion assisted growth model with material contribution from direct impingement on the NC surface area and impingement on the substrate. The Ga diffusion length on the  $\text{Si}_x\text{N}_y$  layer was estimated to be around 400 nm, the Ga diffusion length on the sidewalls was not reported. Although a Ga diffusion assisted growth mechanism was concluded, NC axial growth rates in contradiction to the expected  $r^{-1}$  behavior were reported in the later publication.

The latest reports on the growth mechanism of SAG GaN NCs by MBE are given by Bengoechea-Encabo *et al.*<sup>[11]</sup>. Similar to the approach of Kishino *et al.*, GaN templates and patterned, nitridated Ti masks were used. At untypical high growth temperatures (960 °C) and high fluxes in the nominally slightly Ga-rich regime (16 and 13 nm min<sup>-1</sup> for  $F_{\text{Ga}}^+$  and  $F_{\text{N}}^+$ , respectively)<sup>5</sup>, a hexagonal pyramidal GaN crystal morphology ( $r$ -planes) was observed for aperture diameters of about 200 nm. The axial growth was inhibited, which was discussed to be due to a decomposition rate of these facets comparable to the growth rate on them. For smaller apertures (diameter around 50 nm), NCs with  $c$ -plane tips were observed. This change in morphology was attributed to a change of the local N/Ga ratio within the aperture due to Ga adatom diffusion on the TiN layer. This explanation was supported by growth experiments at different substrate temperatures, while keeping the nominal Ga and N supply constant. At a substrate temperature of 860 °C, NCs with  $c$ -plane tips were observed. For growth temperatures above 900 °C, for which Ga desorption is expected to be enhanced, NCs with pyramidal tips were observed<sup>[125]</sup>. A step towards the SAG of nonpolar GaN NCs was shown in 2012 by the use of  $a$ -plane GaN templates and TiN masks, which resulted in the selective area growth of GaN NCs along the  $a$ -direction<sup>[126]</sup>.

In summary, SAG of GaN NCs by MBE typically occurs under nominally nitrogen-rich growth conditions close or above the GaN decomposition temperature (under vacuum). The dominant physical processes have been suggested to be either Ga adatom surface diffusion on the functional layer towards the NCs or Ga adatom desorption from the functional layer.

However, the growth of SI and SAG NCs proceeds under nominally similar growth conditions and the NC sidewall morphology is comparable. It is thus concluded, that conceptual aspects which are valid for the growth of SI NCs also have to be taken into account for the selective area growth. This includes incubation times for the nucleation of GaN, limited Ga diffusion lengths on the NC sidewalls and dynamical growth conditions due to Ga diffusion towards the apertures and the NC tip, including changes in the magnitude of these contributions due to the evolving NC height (*regimes I*

5 The authors pointed out, that due to the high growth temperature the actual N/Ga ratio was much larger than the nominal one.

and *II*). This implies, that in the case of ordered arrays with pitch  $p$ , two different cases have to be considered: When the array pitch is smaller than  $2\lambda_s$ , the NCs compete for the Ga adatoms which diffuse on the substrate. If the pitch is larger than  $2\lambda_s$ , the NCs can be treated as isolated and do not compete for material<sup>[127]</sup>. The classification of these regimes is vital for the understanding of the SAG mechanism. Since these regimes will be used repeatedly throughout this thesis, they will be termed

1. *competitive regime* ( $p < 2\lambda_s$ ) and
2. *isolated regime* ( $p > 2\lambda_s$ ).

In addition, the growth *regimes I* and *II* which were described in [Section 4.1](#) will be of importance.

[Chapter 7](#) presents the results on the homoepitaxial selective area growth of GaN nanocolumns which have been grown for this thesis, and is intended to gain deeper insight into the SAG mechanism.

### 4.3 POLARITY OF GAN NANOCOLUMNS

For future NC-based optoelectronic devices, the NC polarity is of great interest since it determines the direction of spontaneous and piezoelectric polarization (see [Section 2.1.5](#)). Furthermore, the incorporation behavior of In differs for thin GaN films of different polarity<sup>[128,129]</sup>, and higher achievable In concentrations are predicted for N-polar GaN as compared to Ga-polarity<sup>[129]</sup>. Besides, dopant and impurity incorporation, as well as the formation of native point defects was found to be related to the polarity of GaN films<sup>[130–135]</sup>.

Therefore, the polarity of GaN NCs is frequently discussed in literature, however, no satisfying consensus is achieved. The influence of substrate or buffer layer polarity on the NC polarity was discussed<sup>[136–140]</sup>. Recently, it has been argued that MBE-grown self-induced NCs can only show N-polarity<sup>[139]</sup>. Furthermore, specific NC morphologies and different axial growth rates were related to Ga- or N-polarity<sup>[136,137,141,142]</sup>. Correlation of NC polarity and defects, such as high and low basal plane stacking fault densities which indicate either N- or Ga-polarity, was proposed<sup>[142]</sup>.

Despite the discrepancies among the mentioned reports, most results suggest N-polarity for heteroepitaxial self-induced MBE GaN NCs which show a  $c$ -plane tip facet<sup>[138,139,143,144]</sup>. In the case of SAG GaN NCs by MBE, reports on the polarity are rare. Nevertheless, the homoepitaxial growth of NCs on Ga-polar GaN templates was shown to provide Ga-polar SAG NCs. These showed a pyramidal tip morphology<sup>[121,122,145]</sup>. Using N-polar GaN templates, N-polar GaN NCs have been obtained, which showed  $c$ -plane tips<sup>[145]</sup>. This morphology is consistent with the reports of N-polar SI NCs. Furthermore, these results are in agreement with homoepitaxial SAG GaN

NCs obtained by MOVPE. A pyramidal geometry was attributed to Ga-polarity<sup>[136,146–148]</sup>, while N-polar NCs showed flat *c*-plane tips<sup>[136,146,147]</sup>. However, the correlation of NC polarity and NC morphology for the MOVPE technique has to be taken with care, since the used carrier gases can strongly affect the shape of the NCs<sup>[10,147,149]</sup>. The same is true for MBE, as the variation of the N/Ga flux ratio was shown to affect the NC morphology<sup>[11,125]</sup> (the NC polarity was however not reported in these publications).

The polarity of the SAG NCs which have been grown for this thesis will be investigated in [Section 7.2.2](#).



# 5

---

## EXPERIMENTAL TECHNIQUES

---

*This chapter will briefly introduce patterning techniques which have been utilized for the fabrication of functional mask arrays for the SAG of NCs in this thesis. Furthermore, relevant techniques for the characterization of the SAG arrays and of the SAG NCs will be described. Details on the exact experimental conditions will be given in the corresponding chapters which summarize the results or in [Appendix A](#).*

### 5.1 PATTERNING TECHNIQUES

#### 5.1.1 *Electron beam lithography*

Electron beam lithography (EBL) can be considered as the carthorse for nanolithography on a laboratory scale. The reasons are the excellent spatial resolution due to the small electron de Broglie wavelength, the small diameter of the focused electron beam, and especially the versatility to vary lithography design parameters almost without any restriction. However, EBL is a time-consuming serial writing technique which requires several processing steps. Furthermore, the obtained results depend sensitively on the precise parameters before, during and after lithography. Achieving features of around 30 nm is quite straight forward; if the reader however intends to work towards ultimate resolution, the experimental requirements to achieve sub-20 nm resolution are reviewed in Ref.<sup>[150]</sup>. A general overview of EBL in nanoscale fabrication can be found in Ref.<sup>[151]</sup>.

In the following, a short description of the EBL process will be given, the precise experimental procedure is summarized in [Section A.2](#). In the first step, an EBL resist (typically polymethylmethacrylat, PMMA) dissolved in organic solvent is spin coated onto a clean substrate. Subsequent electron beam irradiation causes chemical changes of the resist, which changes the solubility of the exposed resist with respect to a developing solvent. Low beam currents in the picoampere range and high acceleration voltages

around 20 kV are required to reduce Coulomb interaction at the surface of the specimen in order to obtain a spatial resolution of a few ten nanometers. Incident electrons can be backscattered (elastic Rutherford scattering) from regions deep in the substrate back to the resist or excite secondary electrons (inelastic scattering). Therefore, also the unpatterned resist regions will be partly exposed. This is especially pronounced for closely spaced features. To correct this proximity effect, the electron beam dwell time has to be adjusted for lithography designs which show varying feature spacings (see [Section A.2](#)). In the next step, the resist is dissolved in the developing solvent. Depending on whether exposed or unexposed regions are removed, the resist is termed positive or negative, respectively. The obtained pattern is then transferred to the substrate by etching techniques (wet chemical or reactive ion etching). On the other hand, the patterned resist can be used as mask for subsequent film deposition. In this case, the desired pattern is obtained after stripping the resist (and the deposited film on top) in a remover solvent. To remove resist residues, this step also applies in the etching approach. For final cleaning, the sample can be exposed to an oxygen plasma.

### 5.1.2 *Focused ion beam*

Focused ion beam (FIB) is a technology based on focusing a high energy (5 – 30 keV) ion beam (typically  $\text{Ga}^+$ ) onto the specimen and subsequent interaction of the ions with the specimen atoms at the very surface. Due to the small probe size and the comparable masses of ions and specimen atoms, features with a spatial resolution of a few tens of nanometers can be milled into virtually any material. The processes behind milling are physical sputtering, material redeposition and amorphization. The concept of milling can be used for the preparation of lamellae for transmission electron microscopy (see [Section A.7](#)), as well as for the resist-free patterning of SAG arrays<sup>[121]</sup>. Furthermore, functional materials such as Pt can be deposited onto the sample for protection of the specimen surface, writing of circuits for electrical contacting or catalyst deposition. This is achieved by introducing metal-organic precursors into the beam path. These are dissociated and a part of the precursor is deposited on the surface. Modern FIB machines are equipped with an additional electron beam, the so-called dual-beam setup. This allows real-time monitoring of the milling process (like in conventional scanning electron microscopes, see [Section 5.2.3](#)). Furthermore, the electron beam can be used for electron beam-assisted precursor deposition, which is less invasive as compared to the ion beam-assisted deposition technique. Similar to EBL, FIB patterning is a time-consuming serial writing technique. However, the possibility of position-controlled milling of specimens with high spatial resolution is worth the expenditure of time. For a complete overview of the capability of the FIB technique, the reader is referred to Refs.<sup>[152,153]</sup>.



### 5.1.3 Pulsed laser ablation

Laser nanomanufacturing is based on light-matter interaction and covers a wide range of potential applications. An extensive overview can be found in Ref.<sup>[154]</sup>. In principle, a focused laser beam is collimated onto the specimen surface to ablate material, where electrons of the specimen absorb the incident photon energy and transfer it to the lattice. This results in a temperature rise on the picosecond timescale and the surface temperature can reach melting, vaporization or even ionization temperature. By the use of pulsed lasers with short pulse duration and small light absorption depth, this heat-affected zone can be limited to small volumes. Between the pulses, the material is supercooled to ambient temperature to its initial phase and the modified surface morphology is left behind. In order to transfer a pattern onto the specimen, a mask with the desired pattern geometry can be projected onto the surface or an intensity pattern with the desired geometry is created by multiple beam interference<sup>[155]</sup>. Furthermore, the focused laser can be scanned over the sample.

## 5.2 CHARACTERIZATION TECHNIQUES

### 5.2.1 Reflection high energy electron diffraction

Reflection high energy electron diffraction (RHEED) is a versatile *in situ* characterization technique to examine for example crystal structure, epitaxial morphology, and growth rates during MBE.

A focused, high energy (several keV) electron beam irradiates the sample surface in grazing incidence, under angles typically smaller than  $3^\circ$ . Due to the small incident angles, the electrons mainly interact with the surface atoms of the sample. Generally, constructive interference due to diffraction by a crystal lattice is described according to the Laue condition, i.e.  $k_0 - k' = K$ .  $k_0$ ,  $k'$ , and  $K$  are the wave vectors of the incoming electrons, the diffracted electrons, and a reciprocal lattice vector, respectively. Due to the small penetration depth of the electrons into the crystal, the reciprocal lattice points degenerate to infinitely extended reciprocal lattice rods perpendicular to the two-dimensional surface. Considering elastic scattering  $k_0 = k'$ , the Ewald sphere construction can be used to graphically describe satisfaction of the Laue condition: The origin of  $k$ -space ( $k_x = k_y = k_z = 0$ ) coincides with the electron beam incident position on the sample surface. A sphere with radius  $k_0$  is then centered around  $k_0$ . Constructive interference occurs, where the reciprocal lattice rods cut the Ewald sphere. The diffraction pattern is projected onto a screen which is positioned in reflection geometry with respect to the incident electron beam. The reflex positions follow so-called Laue rings. This is due to the intersection of the reciprocal lattice rods with the Ewald sphere at different values of  $k_z$ .

For a perfectly flat layer, one would expect a diffraction pattern composed out of spots. However, for two-dimensional layers, a streaky pattern is observed, while a spotty pattern is observed for rough layers or nanostructures. This is due to several factors: The high energy of the electrons (14 keV in this thesis) causes the radius of the Ewald sphere to be large in comparison with the in-plane reciprocal lattice constant ( $630 \text{ nm}^{-1}$  and  $23 \text{ nm}^{-1}$ , respectively, for the used conditions and considering a GaN(0001) surface<sup>1</sup>). Furthermore, the electron beam is not fully monochromatic, which results in a broadening of the Ewald sphere shell. In addition, crystal imperfections and lattice vibrations will cause broadening of the reciprocal lattice rods. For a layer, the intersection of Ewald sphere and reciprocal lattice rods will be elongated to streaks due to the enlarged cross section. In the case of rough layers or nanostructures, the electron beam is also transmitted through the crystal. Thus, the reciprocal lattice of a three-dimensional crystal will intersect the Ewald sphere and the observed reflexes will show a spotty pattern. Both cases are illustrated in [Figure A.4](#).

The shape of the reflexes therefore provides information on the surface morphology. Geometry and distance of the reflexes are related to crystal structure, additional reflexes are due to surface reconstructions or adsorbates at the surface. The specular spot in the pattern due to the directly reflected electron beam is typically most intense and sensitive to surface morphology. The intensity evolution of this spot allows to monitor growth rates (see [Section 6.2](#)) or surface coverage by liquid or amorphous films. In the former case, the intensity of the spot oscillates due to varying surface roughness during the deposition of one crystalline monolayer; i.e. an intensity maximum corresponds to a smooth surface, an intensity minimum to maximal surface roughness, caused by the deposition of half a monolayer. In the latter case, deposition and desorption of thin liquid films correlate with intensity transients. This is due to the amorphous structure of liquid films, for which only a diffuse diffraction pattern can be observed. During deposition, the intensity will decrease due to an increasing contribution of diffuse scattering. The intensity will remain constant once the film thickness exceeds the electron penetration depth. The opposite transient is observed during desorption.

### 5.2.2 Atomic force microscopy

Atomic force microscopy (AFM) is a very sensitive method to probe the surface morphology of semiconductor epilayers or nanostructures. The basic principle is the interaction between a sharp tip and the sample surface. The tip is mounted to a cantilever which can be moved up and down with respect to the specimen surface. Depending on the material of tip and sample, as

<sup>1</sup> The magnitude of the incoming wave vector is related to the electron wavelength  $\lambda$  by  $k_0 = 2\pi/\lambda$ . The reciprocal lattice constant  $a^*$  is given by  $a^* = 4\pi/\sqrt{3} a^{-1}$ .

well as their relative distance, the forces may be attractive or repulsive. The deflection of the cantilever, which is caused by the interaction of tip and sample is measured by a laser spot reflection from the cantilever. This reflection is detected by a photodiode. The distance of the tip to the sample surface is adjusted through a feedback loop which controls a piezoelectric tube on which the cantilever is mounted. During measurement, constant force conditions are maintained. In this way, the specimen topography is probed. To reduce the damage of surface and tip, often the tapping mode (non-contact) is used. In this mode, the cantilever is driven to oscillate close to its resonant frequency. Interaction with the sample reduces the oscillation amplitude which is detected by the laser spot deflection on the photodiode.

In the case of smooth GaN epilayers, AFM with the use of standard tips (tip radius of around  $< 10$  nm) is suited to detect sub-nm features, such as monoatomic steps with a step height of  $c/2 = 2.6 \text{ \AA}$ .

### 5.2.3 *Scanning electron microscopy*

In a scanning electron microscope (SEM), the sample is investigated by scanning a focused electron beam over the surface. The electrons with energies  $E_0$  in the range of 1 to 20 keV interact with the sample. Depending on the nature of the scattering processes, i.e. elastic or inelastic, various physical processes can be detected for characterization of the specimen.

Inelastic scattering for topographical contrast is made use of by detecting low energetic secondary electrons, i.e. electrons emitted from the outer shells of the specimen atoms due to interaction with the incident electrons. The energy range of these secondary electrons is in the range of several eV. Therefore, only electrons emitted close to the sample surface are visualized. This implies, that especially positions for which the electrons can escape easily, such as edges and kinks, contribute to the signal. Thus, mainly topographical contrast is obtained at a spatial resolution of several nanometers.

Furthermore, the incident electrons can scatter inelastically with the electrons from the inner shell of the specimen atoms. The shell electrons are emitted, leaving a hole in the inner shell. During recapture of an electron from the outer shell, an X-ray photon may be emitted (otherwise an Auger electron is emitted). The energy and intensity of the X-rays is characteristic for the involved atomic species and concentration, respectively, such that energy dispersive X-ray spectroscopy (EDX) yields quantitative information of chemical composition of the specimen in the excited volume.

In semiconductor samples, the incident electrons can further excite electrons deep from the valence band into the conduction band, leaving behind a hole in the valence band. The carriers thermalize to the conduction band minimum (electrons) and valence band maximum (holes) and can recombine radiatively, given that the semiconductor is direct (see [Section 2.1.4](#)). This

process is termed cathodoluminescence (CL) and provides information about the optical and electronic properties of the sample. In SEM-CL, the resolution is mainly limited by the penetration depth of the electrons into the material, which is proportional to  $E_0^{1.67}$ <sup>[156]</sup>. Thus, low acceleration voltages are favored to increase the spatial resolution.

#### 5.2.4 *Transmission electron microscopy*

In transmission electron microscopy (TEM), a sample thin enough to be transparent for electrons with energies in the range of 80 to 300 keV is illuminated by the latter. Due to the high acceleration voltage, the electron wavelength is much smaller than typical semiconductor lattice constants (e.g. around 2.5 pm for  $E_0 = 200$  keV). TEM thus allows to study the structural properties of the specimen on the very nanoscale. Actually, it is not the electron wavelength which is limiting the spatial resolution, but aberrations of the electromagnetic lenses which are used for deflection of the electron beam. Nevertheless, sub-nm resolution is achieved even for standard TEMs, while greatly enhanced resolution is obtained for aberration corrected microscopes<sup>[157]</sup>.

The basic principle—as for all electron microscopes—is electron scattering of the incident electrons within the sample. This changes the spatial and angular distribution of the transmitted electrons, with both distributions being profound for TEM characterization. The basic operation modes are the diffraction and image mode, i.e. projecting a diffraction pattern and an image of the specimen onto a screen, respectively. This is achieved by a set of apertures and electromagnetic lenses. Without going into detail, several imaging techniques which have been applied in this thesis will be discussed. For an in-depth description of transmission electron microscopy and technical aspects, the reader is referred to Ref.<sup>[158]</sup>.

Transmission electron microscopy is best understood in reciprocal space. Considering a crystalline specimen, the incident electrons are subject to diffraction, i.e. constructive interference of the electron plane wave occurs according to the Laue condition. This gives rise to a diffraction pattern of the specimen, which can be projected onto the TEM viewing screen. The spots within the diffraction pattern correspond to reciprocal lattice vectors which are referred to as diffraction vectors  $\mathbf{g}$ . Taking Bragg's law into account, these diffraction vectors correspond to specific diffraction angles. Analyzing the diffraction pattern with respect to geometry and magnitude of reciprocal lattice vectors allows to study the crystalline structure of the sample. Furthermore, it allows to orient crystallographic directions of the specimen lattice with respect to the incident beam direction which is termed as selection of a zone axis.

The most basic real space imaging technique is the acquisition of bright and dark field images. By an aperture, one selects the direct beam, i.e.

the central spot in the diffraction pattern, and switches to the image mode, thus obtaining a bright field image. Repeating the same procedure with the selection of a specific diffraction vector, a dark field image is obtained, which is characterized by the selected vector  $\mathbf{g}$ . The latter imaging condition results in diffraction contrast: Only such electrons are visualized, which are Bragg scattered according to the selected diffraction condition.

Phase contrast imaging, often referred to as high resolution transmission electron microscopy (HRTEM), requires ultra-thin samples (in the range of a few nanometers) and is simply spoken achieved by using several diffraction vectors for imaging. The latter correspond to lattice planes, thus, the projection of the crystal structure is imaged via a superposition of lattice planes. Note however, that the spatial intensity of the electron wave corresponding to  $\mathbf{g}$ , shows a sinusoidal oscillatory behavior which depends on the sample thickness, the exact beam incident direction, and the beam energy. The observed lattice fringes in the real space image therefore do not necessarily correspond to atomic planes. Furthermore, the manner in which spatial frequencies of the specimen are transferred to the viewing screen is not trivial. These frequencies show oscillatory behavior which depends mainly (for constant acceleration voltage) on defocus conditions and the spherical aberration  $C_s$ . For conventional high resolution transmission electron microscopy, typically Scherzer defocus condition (specific microscope-dependent defocus value) is used, which is characterized by a relatively broad spatial frequency band which is transferred with constant phase. This allows rather intuitive image interpretation. This condition was used for all HRTEM images throughout this thesis, if not stated otherwise. In the case of  $C_s$  correction, the oscillations in spatial frequency transfer are largely suppressed, which greatly facilitates the quantitative HRTEM image interpretation<sup>[157]</sup>. Furthermore, a gain in spatial resolution is achieved.

The so far discussed imaging conditions all use parallel illumination (specific  $\mathbf{k}_0$ ). In the following, convergent beam techniques (range of  $\mathbf{k}$ -vectors) will be considered. In the case of convergent beam electron diffraction (CBED), the electron beam is converged by several mrad in TEM imaging mode and focused onto the sample. The obtained diffraction patterns show extended diffraction disks rather than localized diffraction spots. Furthermore, for sufficiently thick samples (in the range of several tens of nanometers), the disks show intensity modulations due to dynamical diffraction conditions. For low-indexed zone axes, these modulations contain a wealth of information, such as absolute crystal polarity of non-centrosymmetric crystals<sup>[159]</sup>. Theoretical CBED patterns for comparison can be simulated easily using TEM simulation packages such as JEMS<sup>[160]</sup>. Due to the spatial resolution of the probe of several nanometers, this method is suited for the polarity determination of GaN nanostructures.

In scanning transmission electron microscopy (STEM), a convergent electron beam is scanned over the sample, much like in the case of SEM, however,

the beam direction with respect to the optical axis of the microscope is unchanged during scanning. This is required to maintain the beam incident direction with respect to the specimen, in order to avoid varying image contrast by changing the scattering conditions. The great advantage of the STEM mode is the use of a fine probe (can be below 1 nm spatial resolution) and a variety of detectors, that allow to characterize the specimen chemically and structurally on the nanoscale. The circular STEM bright field detector is surrounded by a ring-shaped annular dark field (ADF) detector, which is again surrounded by a high-angle annular dark field (HAADF) detector. The first dark field detector collects electrons scattered through angles of around 10 to 50 mrad, the latter  $> 50$  mrad with respect to the optical axis. Since electrons scattered under such high angles have been subject to Rutherford scattering, HAADF images are mainly<sup>2</sup> sensitive to chemical contrast, while ADF images are rather sensitive to diffraction contrast.

Similar to SEM-CL, cathodoluminescence experiments can be performed in STEM mode. Due to the small sample thickness in the range of some tens of nanometers, the volume which contributes to CL is mainly dominated by the incident electron beam spread and the excited free carrier diffusion length. The beam spread in thin samples in STEM-CL is proportional to  $E_0^{-1}$ <sup>[158]</sup>, which is in contrast to the  $E_0^{1.67}$ -dependency<sup>[156]</sup> in the case of thick samples in SEM-CL. The resulting beam spread in the case of a 150 nm thick GaN TEM lamella which is illuminated by 80 keV electrons is around 30 nm. In the case of a thick GaN sample which is illuminated by 3 keV electrons, the penetration depth is around 90 nm. Thus, for thin STEM-CL samples, the spatial resolution due to the smaller excitation volume can be significantly enhanced as compared to SEM-CL, by an increase of acceleration voltage. The absolute spatial resolution for the detected CL intensity in STEM-CL is determined by the beam diameter (spread) and the free carrier diffusion length.

### 5.2.5 Raman spectroscopy

Raman spectroscopy is a contactless and non-destructive technique for the investigation of the structural properties of solids<sup>[161]</sup>. A focused laser beam irradiates the sample, where elastic or inelastic scattering of the light occurs. The latter scattering process is referred to as Raman scattering. The incident photons can excite or absorb a phonon. In the optical spectrum, this results in the occurrence of a low- and high-frequency sideband with respect to the laser line frequency, respectively. These bands are termed Stokes and Anti-Stokes lines. Mainly phonons close to  $\Gamma$  ( $k = 0$ ) are excited; thus, for semiconductors, the optical phonon dispersion relation typically dictates the spectral peak position within Raman spectra. Raman selection rules

<sup>2</sup> Due to channeling effects also diffraction contrast may be observed.

determine the appearance of specific phonon modes in the spectra and take into account the scattering geometry, i.e. direction and polarization of the laser light. Ref.<sup>[161]</sup> summarizes Raman selection rules, spectral positions, as well as atomic displacements of optical phonon modes in wurtzite III nitrides. Shifts in the spectral position of phonon modes with respect to predicted spectral positions can be for example used to evaluate the strain state of the specimen. Furthermore, Raman spectra are sensitive to atomic arrangement disorder which correlates with the phonon spectral peak width<sup>[161]</sup>.





Part II

RESULTS



---

TOWARDS SELECTIVE AREA GROWTH

---

*Figure 6.1* shows representative images of selective area growth of GaN nanocolumns which have been obtained by the use of thin regularly patterned Mo masks on GaN template. This section explains the routines which have been used in this thesis to achieve the selective area growth. Investigation of the growth mechanism and characterization of the nanocolumns follows in the next chapters.

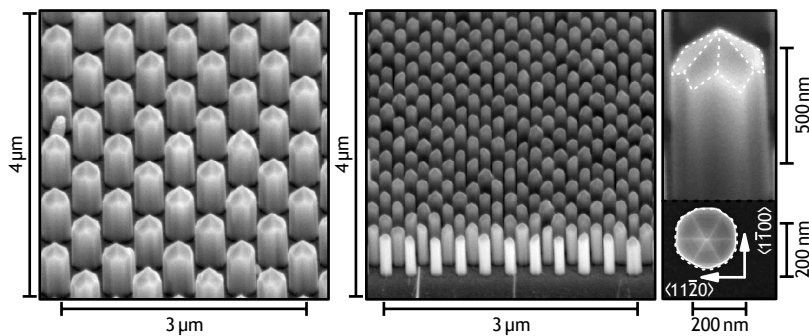


**Figure 6.1:** Bird's eye view SEM micrographs of SAG GaN nanocolumns (NCs) with different NC diameters and aperture pitches. To the right, bird's eye view and top-view SEM micrographs of the typical pyramidal tip morphology are shown, which corresponds to semipolar GaN surfaces. Crystallographic orientations are given. *Samples G1225 and G1253.*

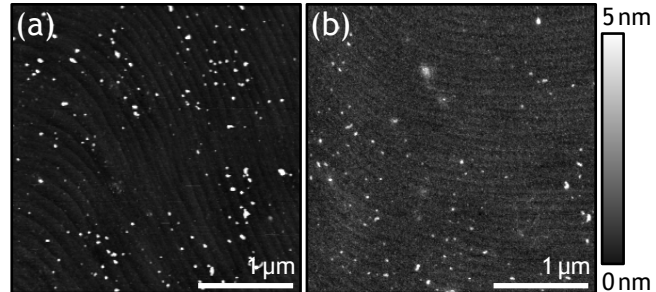
### 6.1 PATTERNING OF SAG ARRAYS

This section describes the patterning of thin molybdenum layers for the fabrication of arrays for selective area growth. All relevant process parameters are summarized in [Section A.1](#). Commercially available GaN templates<sup>1</sup> have been used.

<sup>1</sup> 3.5 μm thick MOCVD-grown Ga-polar GaN(0001) on Al<sub>2</sub>O<sub>3</sub> from LUMILOG with a dislocation density of 4 · 10<sup>8</sup> cm<sup>-2</sup>.

First, 10 or 20 nm thin Mo layers were deposited on  $10 \times 10 \text{ mm}^2$  GaN templates by electron beam evaporation for patterning by electron beam lithography (EBL) or pulsed laser ablation. A deposition rate of about  $1 \text{ \AA s}^{-1}$  resulted in smooth layers. Figure 6.2 shows AFM images of a GaN(0001) surface after standard cleaning procedure and after deposition of 10 nm Mo.

**Figure 6.2:** AFM topography micrographs of the surface of a GaN(0001) template before (a) and after (b) deposition of 10 nm Mo.



In the case of the degreased GaN surface, some residues can be observed which appear as white spots. These are possibly remains due to wafer dicing. Furthermore, atomic steps with a height which corresponds to the  $c$  lattice constant can be observed. After deposition of Mo, the steps can still be observed, which indicates the smoothness of the Mo layer. For the clean GaN surface, and the sample covered with Mo, the root mean square ( $rms$ ) roughness for  $1 \times 1 \mu\text{m}^2$  regions is comparable with values of about 0.2 and 0.3 nm, respectively.

Two different patterning techniques have been used in this thesis for the fabrication of SAG arrays. Electron beam lithography allows to vary the design of the array to a large degree. The drawback however, is the time consumption of this method. Pulsed laser ablation on the other hand, is a high-throughput method. The drawback in this case, is the limited possibility to vary array design parameters. Mainly two array designs were used throughout this thesis. These are schematically shown in Figure 6.3 and 6.4.

To study the *SAG mechanism*, SAG array patterning on small sample areas was performed by EBL and the array design is termed *M*. The arrays consist of circular apertures in hexagonal arrangement.

In order to obtain GaN nanostructures on a large scale for the fabrication of *arrayed, semipolar GaN templates*, patterning was performed by pulsed laser ablation. This sample design is termed *T*. In this case, the array geometry is given by circular apertures in quadratic arrangement.

The obtained SAG arrays will be characterized in the following sections. Precise EBL, pulsed laser ablation, and reactive ion etching (RIE) process parameters, as well as experimental setups are given in Section A.1 and Section A.2.

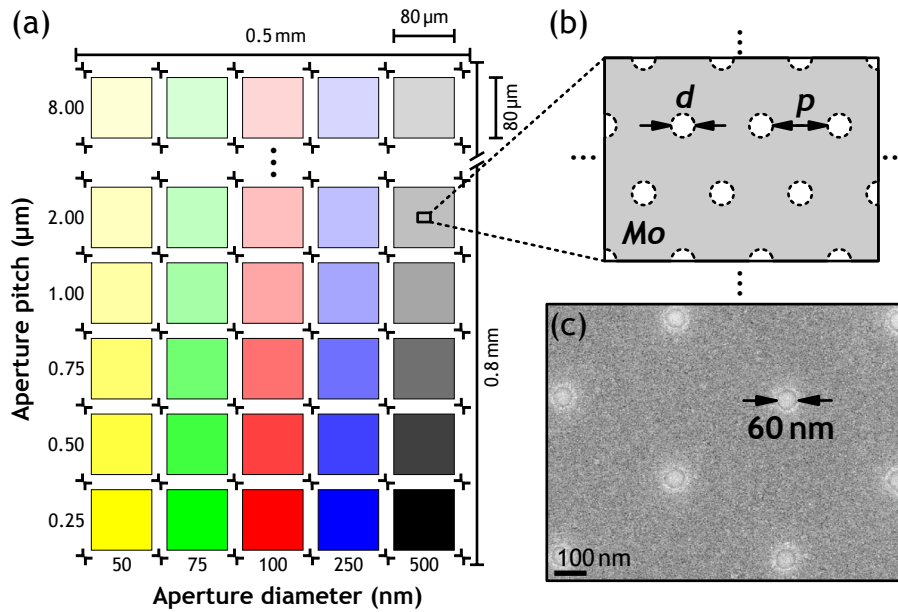


**Figure 6.3:** (a) Schematic layout of the array design  $M$  for patterning by electron beam lithography. The color coding identifies constant aperture diameter  $d$ , the color tone represents constant aperture pitch  $p$ . The individual arrays are positioned in between  $10 \times 10 \mu\text{m}^2$  large markers. Typically, the aperture pitch was varied between 2, 4, 6 and  $8 \mu\text{m}$  for the design region which was spared. The hexagonal arrangement of the apertures is shown in (b). A top-view SEM micrograph of apertures with 60 nm diameter is shown in (c).

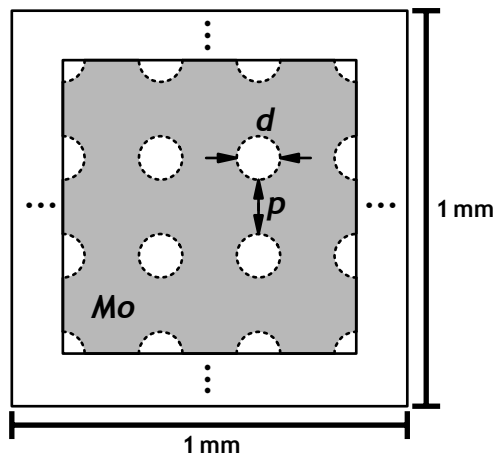


**Figure 6.4:** Schematic layout of the array design  $T$  obtained by pulsed laser ablation. Aperture diameter and nearest neighbor pitch are around 650 and 800 nm, respectively.

### 6.1.1 Electron beam lithography

10 nm thin Mo layers were deposited on the samples for EBL patterning. After e-beam exposure and development of the resist, the patterns were transferred by a selective reactive ion etching step into the Mo layer. Finally, the e-beam resist was stripped by an organic remover. Figure 6.5 shows a representative AFM image of a SAG array which was obtained by EBL. Furthermore, an unpatterned region on the same sample is shown.

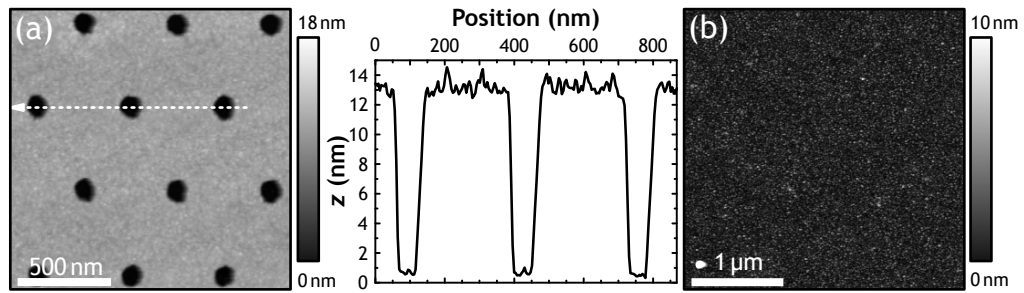


**Figure 6.5:** (a) AFM topography micrograph of a SAG array with aperture diameters of around 50 nm. The height profile along the dashed arrow is shown to the right. An unpatterned region on the same sample is shown in (b).

The aperture depth is in good agreement with the initially deposited Mo thickness of around 10 nm. This shows, that the Mo layer is etched down to the GaN template. It is worth noting, that the used standard RIE procedure does not etch the GaN surface (see [Section A.1](#)). To analyze the surface roughness after electron beam lithography patterning, an unpatterned region on the sample was investigated (b). Although the Mo surface was protected by the EBL resist, the *rms* value ( $1 \times 1 \mu\text{m}^2$ ) increased to about 1.1 nm as compared with the initial Mo surface roughness. Furthermore, no atomic steps are visible. The increase in surface roughness is possibly caused by the EBL resist remover.

Each array consisted of a  $80 \times 80 \mu\text{m}^2$  large area, with the complete pattern covering a  $0.8 \times 0.6 \text{mm}^2$  large region which was located at the center of the samples. Thus, for all the arrays, identical growth conditions can be assumed.

### 6.1.2 Pulsed laser ablation

Pulsed laser ablation for the patterning of regular SAG arrays on a large scale was performed by J.-H. Klein-Wiele and P. Simon in collaboration with the Laser Laboratorium Göttingen e.V.. As in the case of patterning by electron beam lithography, the final thickness of the Mo mask was 10 nm. However, the processing procedure for pulsed laser ablation is slightly different and will be explained in the following: After deposition of 20 nm Mo onto the cleaned GaN templates, the samples were patterned by pulsed laser ablation. SEM analysis after the laser ablation processing showed incomplete ablation in the aperture region and redeposition of Mo onto the mask ([Figure 6.6\(a\)](#)). A higher ablation efficiency can be obtained by increasing the laser power; however, due to the low ablation threshold of GaN, also the substrate material was removed. Defect formation at the GaN template surface may occur and the former are expected to propagate in the growing NCs. Therefore, after laser ablation the Mo layer was etched down to 10 nm by RIE. [Figure 6.6\(b\)](#) shows that the RIE process provides

apertures free of Mo. The surface roughness ( $1 \times 1 \mu\text{m}^2$ ) of the Mo layer after laser ablation and RIE was measured by AFM (not shown) and is around 0.8 nm. The edge of the apertures is less sharp than obtained on similar structures by e-beam lithography. Figure 6.6(c) shows a representative SEM top-view micrograph of the final array.

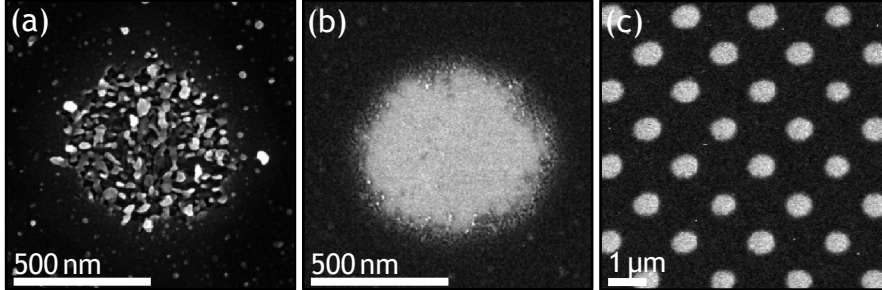


**Figure 6.6:** SEM top-view micrographs of the apertures prepared by pulsed laser ablation. The aperture morphology after laser ablation is shown in (a), after the RIE treatment in (b), and on a larger scale in (c).

For pulsed laser ablation, the maximal size of an individual array was  $1 \times 1 \text{ mm}^2$ . To obtain a large scale SAG array, the patterning process was repeated after shifting the sample by 1 mm with respect to the previous pattern area. In this approach a centered sample region of  $5 \times 5 \text{ mm}^2$  was patterned. Since MBE growth conditions are expected to vary spatially over such large areas, all following analyses of NC morphology and growth rates were performed at the center of the samples.

## 6.2 FLUX CALIBRATION

Growth parameters such as substrate temperature  $T$ , beam equivalent pressures  $p_{\text{BEP}}$  of the effusion cells, nitrogen flow through the plasma source  $F_{\text{N}_2}$  and plasma excitation power  $P$  are no well-defined parameters, in such manner, that the same growth conditions in a different MBE system according to these parameters would yield the same results. This is due to differences in chamber geometry, temperature measuring methods and various other factors. An approach for the determination of absolute substrate temperature is described in Ref.<sup>[53]</sup>. For this thesis, the growth temperature value according to the thermocouple temperature reading of the radiative substrate heater was used. Concerning material supply parameters, in the case of GaN layers, it is accepted to express supply fluxes in terms of GaN(0001) layer growth rates. These are for example calibrated by measuring *ex situ* film thicknesses<sup>[162,163]</sup>. Note, that these supply rates explicitly include desorption, since effective fluxes at the sample surface are measured if the reference samples are fabricated at typical growth temperatures. In addition, *in situ* growth rate determination can be performed by analyzing RHEED

intensity oscillations. Assuming that the respective element limits the layer growth rate, one can calibrate the typically given supply parameters of Ga (beam equivalent pressure) and N (nitrogen flow rate and plasma excitation power) in terms of GaN layer growth rates in  $\text{nm min}^{-1}$ .

In the case of NCs, the analogous, direct growth rate determination by RHEED is not possible. This is due to the three-dimensional geometry of the NCs with respect to the RHEED incident electron beam, i.e. the electron beam is transmitted through the crystal and thus RHEED surface sensitivity is lost. Furthermore, due to the non-compact columnar morphology, *ex situ* film thickness analysis is not suited for flux calibration.

To overcome these problems, a calibration approach is used, which is based on layer growth rates determined by RHEED intensity oscillations and the ratio of the beam equivalent pressures. Figure 6.7(a) shows a typical growth diagram for GaN layers grown by MBE.

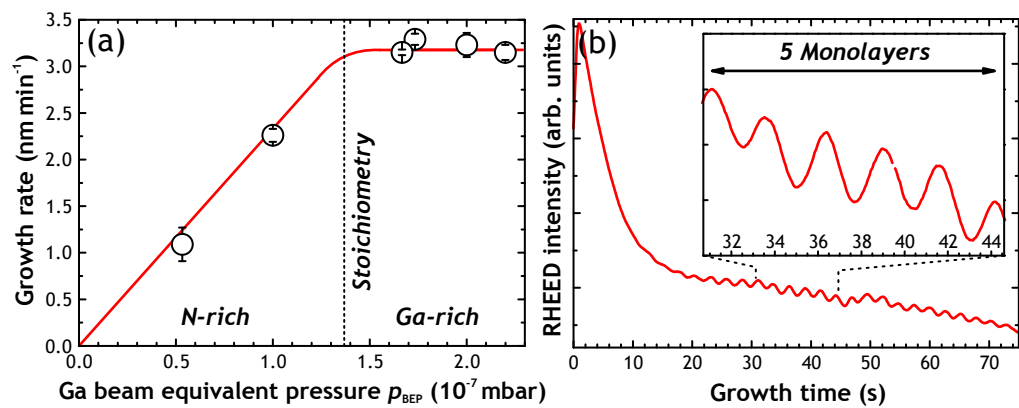


**Figure 6.7:** (a) GaN growth diagram for specific nitrogen plasma conditions ( $P = 300 \text{ W}$ ,  $F_{\text{N}_2} = 0.5 \text{ sccm}$ ). The substrate temperature of the GaN template (LUMILOG) was  $775 \text{ }^\circ\text{C}$ . Growth regimes are indicated, the solid line guides the eye. Data according to Ref.<sup>[53]</sup>. (b) RHEED intensity oscillations of a GaN(0001) layer grown under slightly Ga-rich conditions. Substrate temperature and plasma parameters were equivalent to typically used SAG conditions. One period corresponds to the deposition of a complete monolayer.

Given is the GaN(0001) layer growth rate as function of Ga beam equivalent pressure  $p_{\text{BEP}}$  for specific nitrogen plasma conditions. For stoichiometric growth conditions, the ratio of effective Ga and N supply at the sample surface is unity. If the Ga beam equivalent pressure is increased by raising the Ga effusion cell filament temperature, the Ga flux at the sample surface increases accordingly. However, the growth rate remains constant. This is due to the fact that the nitrogen supply limits the growth rate in this regime. Consequently, the term Ga-rich or N-limited growth conditions are used. Reducing the Ga flux with respect to stoichiometry, the growth rate decreases linearly with the Ga supply and approaches zero for a Ga beam



equivalent pressure of about zero. Analogously, this regime is termed N-rich or Ga-limited.

Figure 6.7(a) is now further used for the calibration of the Ga and N fluxes: For this purpose a GaN(0001) layer on GaN template was grown under the very same nitrogen supply parameters and substrate temperature as used for standard SAG (see Section 6.3). The Ga effusion cell temperature was adjusted until slightly Ga-rich growth conditions were reached. Under these conditions, the growth proceeds layer-by-layer and the growth rate at the sample surface can be measured via RHEED intensity oscillations. This behavior is shown in Figure 6.7(b).

Since slightly Ga-rich conditions were used, immediately follows that the effective nitrogen flux is given by  $F_N = w_{\text{stoichio}}$ , where  $w_{\text{stoichio}}$  is the stoichiometric growth rate. The Ga effusion cell temperature was then slightly lowered in order to obtain the Ga beam equivalent pressure  $p_{\text{BEP}}^{\text{stoichio}}$  which corresponds to stoichiometric growth conditions. These conditions are recognized by a rather constant RHEED intensity during growth. The growth rate remains unchanged; for further Ga supply reduction, the growth rate depends linearly on the Ga supply. In the N-rich regime, the growth rate  $w$  will be thus given by the product of stoichiometric growth rate and the ratio of reduced and stoichiometric Ga flux:

$$w = w_{\text{stoichio}} \frac{p_{\text{BEP}}^{\text{N-rich}}}{p_{\text{BEP}}^{\text{stoichio}}} \quad (6.1)$$

Due to the N-rich growth conditions, Ga limits the growth rate and the Ga beam equivalent pressure  $p_{\text{BEP}}^{\text{N-rich}}$  can be calibrated in  $\text{nm min}^{-1}$  according to

$$F_{\text{Ga}} = w_{\text{stoichio}} \frac{p_{\text{BEP}}^{\text{N-rich}}}{p_{\text{BEP}}^{\text{stoichio}}} \quad (6.2)$$

The right side of the equation describes the extrapolated GaN(0001) layer growth rate under N-rich conditions. Therefore, this expression is termed layer equivalent growth rate. Considering NCs, the axial growth rate of the NCs will typically exceed this value due to enhanced growth along the  $c$ -direction. However, the maximum total growth rate, i.e. the NC ensemble volume growth rate, is given by the layer equivalent growth rate due to mass conservation (neglecting the possibility of different desorption rates for layers and nanocolumns). The nitrogen flux  $F_N$  is consequently calibrated in  $\text{nm min}^{-1}$  via

$$F_N = w_{\text{stoichio}} \quad (6.3)$$

Again, it has to be noted, that this approach explicitly includes desorption. In order to give the *incoming* Ga or N flux  $F^+$  in  $\text{nm min}^{-1}$ , a sample with significantly reduced substrate temperature has to be grown, for which desorption can be neglected.

## 6.3 STANDARD SELECTIVE AREA GROWTH CONDITIONS

The most important task for the MBE crystal grower is a proper adjustment of the growth temperature<sup>[52]</sup>. This is due to the fact that important surface processes for crystal growth are thermally activated.

Self-induced GaN NCs on Si(111) have been grown in the used MBE system (not shown), using nitrogen plasma parameters of  $F_{N_2} = 1$  sccm and  $P = 400$  W. Therefore, as starting point for the investigation of SAG of GaN NCs by MBE, the very same plasma parameters were chosen. The corresponding effective fluxes and N/Ga ratio were  $F_N = 6.2$  nm min<sup>-1</sup>,  $F_{Ga} = 0.7$  nm min<sup>-1</sup> and  $F_N/F_{Ga} = 8.9$ . Several samples have been grown at different substrate temperatures in order to adjust the proper growth temperature, as shown in [Figure 6.8](#).

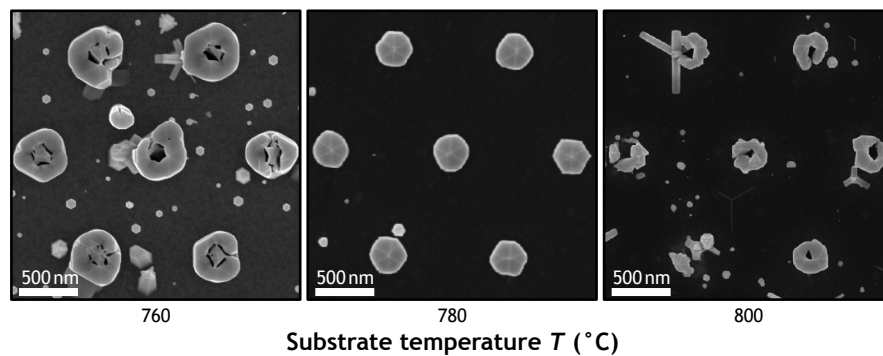


**Figure 6.8:** Top-view SEM micrographs of SAG GaN crystal morphology after 3 h of growth. *M* arrays were used, nominal design parameters are  $d = 250$  nm and  $p = 750$  nm. Samples *G1233*, *G1225*, and *G1223* from left to right.

At a substrate temperature of 760 °C, growth of GaN nanostructures in the apertures was observed. However, the morphology of the structures is inhomogeneous and nucleation of GaN on the Mo layer occurred. By raising the temperature to 780 °C, the radial growth rate was reduced and well-aligned GaN NCs were growing in the apertures. Furthermore, the density of self-induced GaN NCs on the Mo layer was strongly reduced. At 800 °C or above (not shown), GaN begins to decompose with significant decomposition rates. This resulted in a pronounced inhomogeneity of the SAG GaN NC morphology. Furthermore, the thermal lift-off of the Mo layer and a very rough GaN surface morphology was observed for the exposed regions. Therefore, the growth of SAG GaN NCs was performed at a substrate temperature of 780 °C throughout the entire thesis.

The standard SAG procedure after SAG array patterning is summarized in the following:

First, the samples were cleaned for 2 min in acetone, methanol and deionized water, as described in more detail in [Section A.1](#). Each step was

performed once, without the use of an ultrasonic bath, in order not to damage the thin Mo layer on the template. Afterwards, the samples were heated in the MBE intro chamber for 10 min at 200 °C to reduce organic contaminants and water. Outgassing at 600 °C for the same duration occurred subsequently in the buffer chamber. In the growth chamber, the samples were ramped ( $25\text{ °C min}^{-1}$ ) to growth temperature and a substrate rotation of 10 rpm was used. Shortly before reaching growth temperature, the nitrogen valve was opened and the plasma was ignited and stabilized. Indications for an increasing density of self-induced NCs on the Mo mask were observed for prenitridated Mo layers as compared to unintentionally nitridated Mo layers (not shown). Therefore, in contrast to Ti layers (see [Section 4.2](#)), the Mo layers were not prenitridated and nitrogen was introduced into the growth chamber only around 2 min prior to growth. At stable plasma conditions, the N and Ga shutters were opened simultaneously and growth occurred under *standard SAG conditions* with following parameters:

$T$ (°C)	$F_N$ (nm min <sup>-1</sup> )	$F_{Ga}$ (nm min <sup>-1</sup> )	$t$ (h)
780	6.2	0.7	3

**Table 6.1:** Standard SAG conditions. The conversion factor from  $\text{nm min}^{-1}$  to  $\text{atoms cm}^{-2} \text{s}^{-1}$  is  $7.42 \cdot 10^{13}$ .

Deviating conditions will explicitly be mentioned. Calibrated nitrogen flux values which correspond to specific plasma source parameters are summarized in [Table A.2](#).



---

## SELECTIVE AREA GROWTH OF GAN NANOCOLUMNS BY MBE

---

*Crystal growth is generally understood in the framework of thermodynamics. For MBE however, the growth proceeds at untypically low substrate temperatures, and kinetics plays an important role. This chapter will present results on the position-controlled homoepitaxial selective area growth of GaN nanocolumns by molecular beam epitaxy, using thin patterned Mo layers. First, the growth will be discussed in a kinetic description which is based on a Ga diffusion assisted growth mechanism. The concept of selective area growth is then adapted for the growth of columns with diameters close to one micron. Such columns are suitable candidates for the fabrication of arrayed, semipolar GaN templates. The effect of Ga diffusion on the effective local growth conditions will be discussed in the last section of the kinetic description. The second section focuses on the identification of the semipolar facets which form at the tip of the nanocolumns. Furthermore, the polarity of the selectively grown and the self-induced nanocolumns will be determined and corroborated by various methods. The last section discusses thermodynamic aspects which may become relevant for the understanding of selective area growth of GaN nanocolumns by MBE.*

### 7.1 KINETIC DESCRIPTION

#### 7.1.1 Ga adatom surface processes

In order to investigate the SAG of GaN NCs within the Ga adatom diffusion assisted growth mechanism, as described in [Section 4.1](#) and [4.2](#), a representative SAG NC sample with array design **M** was investigated by SEM after growth. Standard SAG conditions have been used. Statistical analysis of NC height and diameter as function of aperture pitch allowed for interpretation of the growth scheme. In the following, only the results on NCs which were grown in apertures with diameters of 50, 75 and 100 nm

are shown. Larger apertures have been prepared as well, however due to resist overexposure these NCs show a hollow core (see Section A.2) and are not included for quantitative analysis. Some SEM micrographs of the investigated sample are exemplarily shown in Figure 7.1.

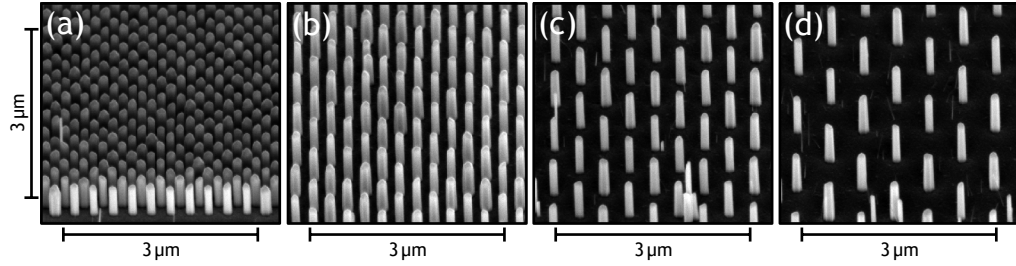


**Figure 7.1:** SEM bird's eye view micrographs of SAG GaN NC arrays with different pitch. The average diameter of the NCs is about 150 nm. The measured pitch is about 150 (a), 400 (b), 670 (c), and 940 nm (d). The nominal aperture diameter was 50 nm. *Sample G1225.*

Before the results of the statistical analysis will be presented, some important considerations will be repeated for clarity:

In **regime I**, the growth of the NCs is expected to be driven mainly by Ga adatom diffusion on the substrate with a diffusion length  $\lambda_s$ , and by the direct impingement  $F_{\text{Ga}}$  on the aperture area. This regime is valid, when the NC height  $h$  is much smaller than the Ga adatom diffusion length on the NC sidewalls,  $h \ll \lambda_f$ . For aperture pitches  $p$  smaller than twice the Ga adatom diffusion length on the substrate (**competitive regime**,  $p < 2\lambda_f$ ), NCs within ordered arrays are expected to compete for Ga adatoms from the substrate. For aperture pitches larger than twice the Ga adatom diffusion length on the substrate (**isolated regime**,  $p > 2\lambda_f$ ), NCs within ordered arrays are expected to be isolated from each other and do not compete for Ga adatoms from the substrate. In **regime II**,  $h \gg \lambda_f$ , the growth is expected to be driven mainly by Ga adatom diffusion on the NC sidewalls (adsorbed Ga adatoms due to direct impingement) and the direct impingement on the NC tip area.

In typical growth experiments, the NC height and diameter are evaluated *ex situ* and the different growth regime contributions are not easy to decouple. Therefore, first the Ga adatom diffusion length on the Mo layer will be estimated. According to this estimation, the results can be interpreted in a first approach. Following up on this, the diffusion length on the NC sidewalls will be discussed.

For the investigated sample, the growth of SI NCs on the Mo mask in between the SAG NCs was observed for pitch values  $\gtrsim 1 \mu\text{m}$ . However, around each nanocolumn a denuded area almost free of any self-induced NCs is observed, as shown in Figure 7.2. The width of this circular area is typically attributed to the Ga diffusion length on the substrate<sup>[76,122]</sup>. In the presented case, it is about 400 nm.

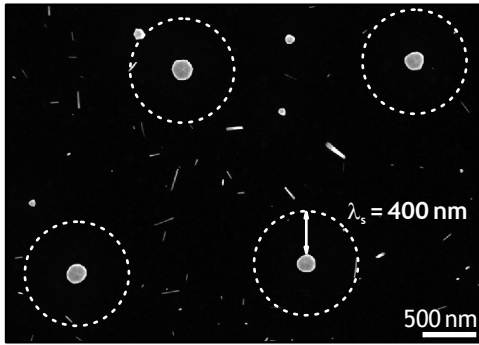


**Figure 7.2:** SEM top-view micrograph of SAG GaN NCs with diameter and pitch of 200 nm and 2  $\mu\text{m}$ , respectively. Dashed circles indicate areas where GaN nucleation was suppressed. Features in between correspond to SI NCs. The nominal aperture diameter was 100 nm. *Sample G1225.*

**Figure 7.3** presents the results of the statistical analysis of SEM micrographs<sup>1</sup> obtained in top-view (NC diameter) and bird's eye view (NC height) geometry. For the SAG NCs, it was observed that the nucleation of GaN is delayed for smaller apertures as compared to larger ones. This is due to a size-dependent incubation time (see [Section A.4](#)). For samples with constant aperture diameter and pitch (*T* design), the corresponding incubation time was measured by RHEED (see [Section A.4](#)). However, due to variable aperture diameters, this was not possible for this sample. Therefore, the NC height and diameter are reported, instead of the growth rates.

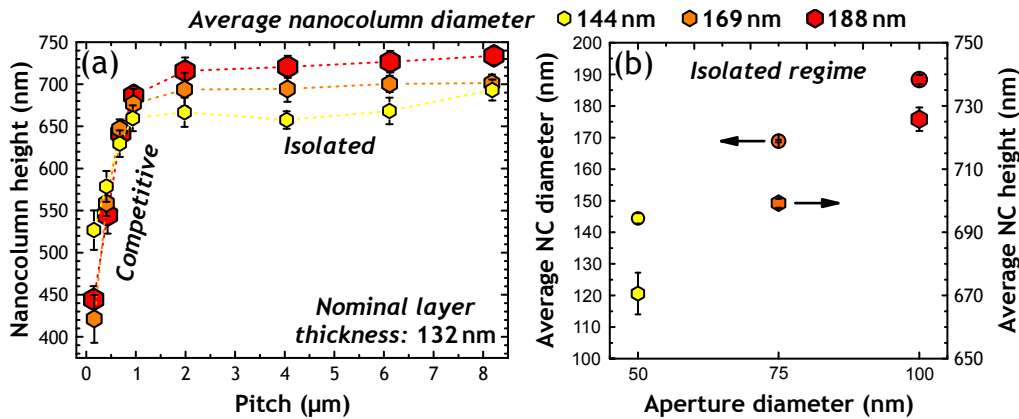


**Figure 7.3:** (a) Average nanocolumn height as function of aperture pitch. The correction of the NC height due to the sample tilt during SEM analysis was taken into account. The error bars are given by the standard deviation, dashed lines guide the eye. Growth regimes have been indicated (see text). The average NC diameter and height for the isolated regime are shown for different aperture diameters in (b). The nominal aperture diameters were 50, 75, and 100 nm. *Sample G1225.*

The nanocolumn height increases with pitch and saturates for pitch values larger than approximately 1  $\mu\text{m}$ . Comparison of the saturated NC height with the nominal layer thickness<sup>2</sup> shows a higher growth rate of the NCs by a factor of around 5 to 6. The nominal layer thickness is simply given by the

<sup>1</sup> About  $\leq 20$  NCs for each array.

<sup>2</sup> This value describes the thickness of a compact two-dimensional layer, if under SAG conditions all the supplied Ga was incorporated into the layer.

product of effective Ga flux and total growth time. In the saturation regime, the nanocolumn height is clearly function of diameter and increases with the latter. This behavior is shown in [Figure 7.3\(b\)](#). The increase of NC height with aperture diameter in the saturation regime could be interpreted to result from the size-dependent incubation time, i.e. a height offset due to delayed nucleation is maintained during growth. Also, a diameter-dependent NC axial growth rate due to size-dependent desorption fluxes (see [Section 3.2.3](#)) cannot be ruled out. In the transient regime of [Figure 7.3\(a\)](#), the NC height as function of diameter follows no clear trend. This is possibly due to the larger standard deviations as compared to the saturation regime.

The NC diameter as function of pitch follows qualitatively the aperture diameter. No influence of the aperture pitch on the NC diameter was observed (not shown). However, the average NC diameter exceeds the aperture diameter, as shown in [\(b\)](#). For the used growth conditions, radial growth of the NCs was therefore not completely suppressed.

An enhanced NC axial growth rate as compared to the radial one was explained in Ref.<sup>[141]</sup> solely by the geometric arrangement of the NCs with respect to the Ga effusion cell. Neglecting diffusion, the ratio of NC height and diameter  $h/d$  was predicted to be simply given by  $\pi/\tan \alpha$ . Using  $\alpha = 33^\circ$  for the inclination of the Ga effusion cell of the used MBE system, a value of 4.8 is obtained. Using the average NC heights and average NC diameters from [Figure 7.3\(b\)](#), a value of about 7.8 is obtained. Thus, the enhancement of the NC axial growth rate as compared to the layer growth rate, and the denuded zone around the NCs ([Figure 7.2](#)) evidences an additional material supply by diffusion, which contributes to growth.

In order to understand the decrease of the NC height for  $p \lesssim 1 \mu\text{m}$  in [\(a\)](#), the nanocolumn layer equivalent thickness was evaluated. This parameter describes the thickness of a compact two-dimensional layer, if the material was not deposited in the form of NCs, but in a layer (note, that this parameter is different from the nominal layer thickness). It is given by the product of average NC density  $\sigma_{\text{NC}}$  in the arrays and the NC volume  $V_{\text{NC}}$ . For ease of calculation, the NCs were treated cylindrically and the pyramidal tip volume was converted into an equivalent cylindrical volume. [Figure 7.4](#) shows the comparison of the nanocolumn layer equivalent thickness and the nominal layer thickness for the discussed regime.

The NC layer equivalent thickness decreases with increasing pitch. However, for the smallest pitch value, the NC layer equivalent thickness is observed to be close to the nominal layer thickness. This result can be interpreted, if the substrate area (per NC) which was directly exposed to the Ga beam from the effusion cell is calculated. For this calculation, the NC diameter and height, the pitch, and the inclination of the Ga effusion cell by  $33^\circ$  with respect to the substrate normal were taken into account (see [Section A.5](#) and [Equation A.2](#)). Only the results for NCs with an average diameter of 188 nm are shown; the results for NCs with smaller diameter



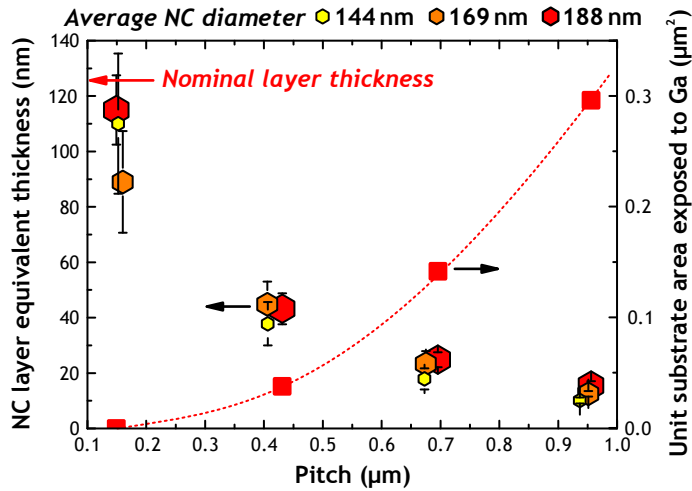


**Figure 7.4:** Comparison of the nanocolumn layer equivalent thickness and the nominal layer thickness. The errors were calculated according to Gaussian error propagation. Furthermore, the substrate area (per NC) which was exposed to the Ga beam from the effusion cell is shown exemplarily for the NCs with diameter of 188 nm. The dashed line guides the eye. *Sample G1225.*

only differ negligibly. The trend of the data is qualitatively opposite to the behavior of the NC layer equivalent thickness: For the smallest pitch, the dense arrangement of the NCs results in complete shadowing of the Mo mask (at the time of investigation; during the early stages of growth this is not true). For larger pitches, the mask is however directly exposed to the Ga beam. Since the Ga diffusion length on the Mo layer was estimated to be around 400 nm, it is expected that the growth of the NCs proceeded in the *competitive regime* for Figure 7.4. If the Ga adatom diffusion length on the NC sidewalls is smaller than the NC height, i.e. *regime II*, the Ga adatoms which diffuse on the Mo mask will desorb or contribute to radial growth. The decrease of the nanocolumn layer equivalent thickness with increasing pitch is therefore interpreted to be due to Ga desorption from the Mo mask. For the smallest pitch—for which the NC layer equivalent thickness is close to the nominal layer thickness—, only the upper part of the NCs (around 230 nm, see Equation A.1 and Table A.3) was directly exposed to the Ga beam from the effusion cell. This indicates that the Ga diffusion length on the NC sidewalls is at least on the order of this value. For the second smallest pitch of around 400 nm, the NC heights are about 650 nm. According to Table A.3, it becomes clear that the complete surface of the NCs was exposed to the Ga beam from the effusion cell. The discrepancy of the NC layer equivalent thickness and the nominal layer thickness for this data set allows to estimate an upper limit for the Ga diffusion length on the NC sidewalls, which is simply given by the NC height, i.e.  $230 \text{ nm} < \lambda_f < 650 \text{ nm}$ .

The fact that for the smallest pitch, the nanocolumn layer equivalent thickness is close to the expected value of the nominal layer thickness shows

that in this case, the total NC growth rate is comparable to layers. The slight discrepancy in the nominal layer and NC layer equivalent thickness for smallest pitch, can be due to Ga desorption from the Mo mask during the early stage of growth (when the mask was directly exposed to the Ga beam) or due to slightly higher Ga desorption from the NC sidewalls as compared to  $c$ -plane GaN (layers).

The increase of the NC height with increasing pitch in Figure 7.3(a), is consequently concluded to be due to the transition from the *competitive* to the *isolated regime*. The average Ga diffusion length on the Mo mask was then estimated by the intersection of these regimes. In the case of the competitive regime a linear fit was used, while for the isolated regime the average NC height was chosen (not shown). An average value of

$$\lambda_s = 435 \pm 29 \text{ nm} \quad (7.1)$$

was deduced. The error was calculated according to Gaussian error propagation.

### Discussion

The homoepitaxial SAG of GaN NCs on GaN template using Mo masks was consistently discussed according to the nanocolumn growth mechanism concepts which were reviewed in Section 4.1 and 4.2. The growth is driven by Ga adatom diffusion on the Mo mask and the NC sidewalls. The Ga diffusion length on Mo was estimated to be about 435 nm. The Ga diffusion length on the NC sidewalls could not be estimated precisely; a value in the range of about 230 to 650 nm seems plausible. The used growth conditions were similar to the ones reported in Ref.<sup>[106]</sup>. In this publication a Ga diffusion length on the NC  $m$ -plane sidewalls of 45 nm was obtained. For the SAG NCs, the sidewalls are however of  $a$ - and  $m$ -plane (see Figure 6.1). Taking into account the Ga adatom diffusion anisotropy along the  $c$ -direction on GaN  $a$ - and  $m$ -surfaces<sup>[80]</sup>, in fact, a larger diffusion length on the  $a$ -surface is expected (assuming constant diffusion lifetimes for  $a$ - and  $m$ -plane). The next section will present a more precise estimation for the Ga diffusion length on the NC sidewalls.

The investigation of the NC height as function of diameter revealed an anomalous behavior which is typically not predicted in diffusion assisted growth models. As discussed in Section 4.1, an axial growth rate inversely proportional to the NC radius is expected. It has to be noted, that such a behavior was not only found in this thesis, but also for other works which investigated SAG of GaN NCs by MBE<sup>[76,124]</sup>. Two effects which seem plausible for the explanation of this behavior have already been mentioned: On the one hand, size-dependent Ga desorption fluxes from GaN might be causing this behavior (see Section 3.2.3). On the other hand, size-dependent incubation times for the nucleation of GaN in apertures of different size

were observed (see [Section A.4](#)). Thus, the delayed nucleation of GaN in smaller apertures as compared to larger ones might explain the fact, that the NC axial growth rate increases with NC diameter. Note, that these effects may be related.

### 7.1.2 Towards arrayed, semipolar GaN templates

[Figure 6.1](#) showed that for the SAG GaN NCs, stable semipolar surfaces form at the NC tip. In order to obtain larger areas of semipolar GaN per nanocolumn, the aim of the following investigation was the technology transfer of the SAG process to the growth of columns with diameters in the range of about one micron. For convenience, the acronym NC will be used further on. Regular arrangement of these columns on the large scale is expected to be suited for the fabrication of GaN templates for the growth of GaN-based semipolar heterostructures.

SAG array design *T* was used, with aperture diameter and pitch around 700 and 800 nm, respectively. The estimated value of  $\lambda_s$  for standard SAG conditions was shown to be around 435 nm. It is thus expected, that the growth of the NCs proceeds in the transition region of competitive and isolated regime. To verify the applicability of the SAG process and to further elaborate the growth mechanism, a series of samples has been grown with increasing growth time. This allowed to easily study the time evolution of the SAG NC morphology due to the large diameter of these NCs, as compared to the previous section. Furthermore, axial and radial growth rates as function of growth duration were analyzed quantitatively. In contrast to the previous section, this was possible due to constant aperture diameters and consequently due to a constant incubation time. [Figure 7.5](#) shows the NC morphology evolution with growth time  $t$ , the elaboration of the experiment by AFM is shown in [Figure 7.6](#).

[Figure 7.5\(a\)](#) shows that during the early stage of growth, multiple GaN nuclei were formed in the center of the apertures and coalesced. The outermost part of the aperture shows a transition region with a width of about 50 – 75 nm, where GaN was nucleating differently as compared to the inner part of the aperture. This is possibly due to residues of Mo on the GaN surface at the edge of the apertures (see [Section 6.1.2](#)). The coalescence was then completed for growth durations longer than 20 min and a compact pedestal was formed ([b](#)). With increasing growth time, semipolar facets were formed, starting at the pedestal edges. The facets grow from the outside of the NC inwards ([c – e](#)). For a growth duration of 120 min, growth of self-induced NCs on the Mo mask was observed ([e'](#)). This is expected to occur, once the Ga diffusion length on the NC sidewalls is exceeded by the NC height. The Ga adatoms which diffuse on the NC sidewalls and do not reach the tip, contribute to radial growth or desorb to vacuum or are readsorbed by the Mo layer. The latter effect is expected to increase the net

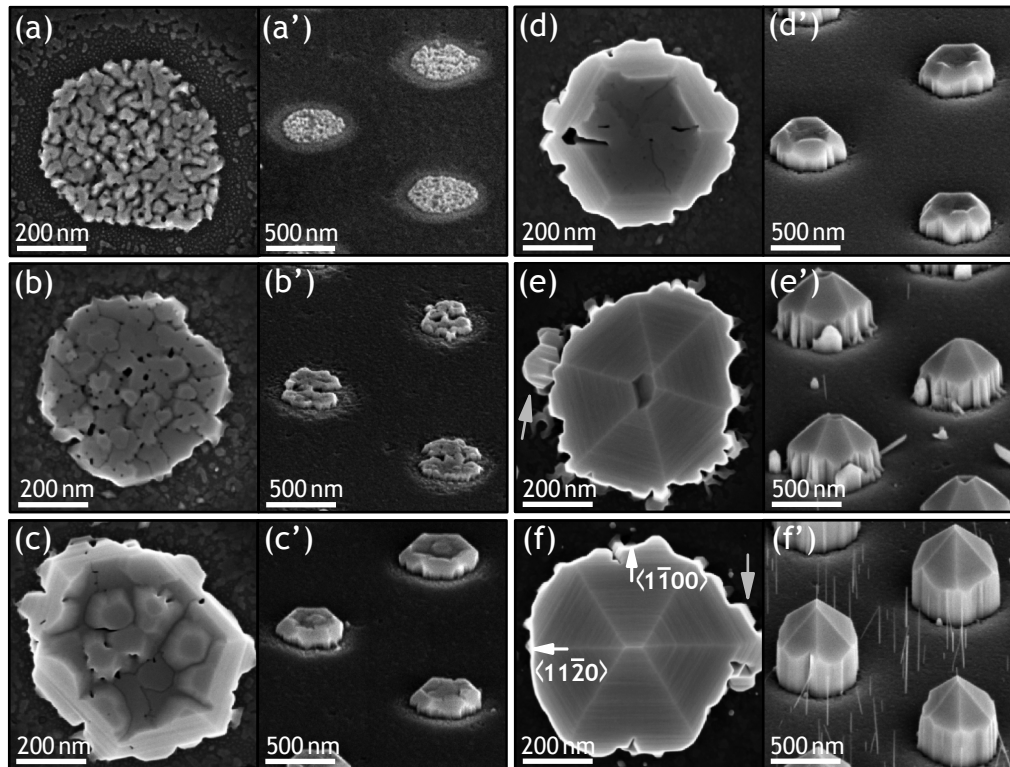


**Figure 7.5:** SEM top-view (a – f) and bird’s eye view (a’ – f’) micrographs of SAG GaN NCs with diameters in the range of 500 to 700 nm. The growth times are  $t = 10, 20, 40, 60, 120,$  and  $180$  min for (a – f), respectively. Crystallographic directions are given in (f). Gray arrows indicate non-uniform radial overgrowth (see text). *Samples G1309, G1270, G1304, G1269, G1302, and G1267* for (a – f) respectively.

Ga adatom concentration on the Mo mask, i.e. the supersaturation. This is similar to the situation of lowering the substrate temperature (Figure 6.8), for which the growth of SI NCs on the mask was observed due to insufficient Ga desorption from the mask. Note, that the SI NCs grow on the Mo mask and not in randomly arranged imperfections of the mask, e.g. holes; see Section A.6. Eventually, the semipolar facets have coalesced and formed fully developed pyramidal structures on a pedestal, with almost hexagonal (0001) cross section (f). Due to the rough edges of the apertures (Section 6.1.2), also the sidewalls revealed a certain roughness. The density of self-induced NCs significantly increased for this growth time. The diameter of the self-induced NCs was typically in the range of  $d = 10 - 100$  nm and the tip showed  $c$ -plane morphology (shown in Section 7.2.2). The morphological differences of the SAG and self-induced NCs will be discussed in Section 7.3 considering thermodynamic arguments.

The morphology of SAG NCs with diameters close to one micron is qualitatively the same as for the NCs with much smaller diameter (see Figure 6.1).

From a morphological point of view, the adaption of the SAG process was successful. To further elucidate the selective area growth mechanism, axial and radial NC growth rates have been evaluated quantitatively. This allowed to estimate the Ga diffusion length on the Mo layer, as well as on the NC sidewalls.

Figure 7.6(a) shows the differential axial growth rate  $\Delta h/\Delta t$  as function of nanocolumn height; the average radial and axial growth rates  $w_{\text{rad}}$  and  $w_{\text{ax}}$  of the SAG NCs as function of growth time are presented in 7.6(b). The axial growth rates were determined by quantitative analysis of the AFM data, the radial growth rate by quantitative analysis of the SEM top-view micrographs. To derive these values, certain approximations and corrections have been used, which will be explained in the following. First, an incubation time for nucleation of  $t_{\text{inc}} = 6$  min, as observed by RHEED during growth (see Section A.4), was taken into account. Note, that this time can be directly correlated to the incubation time of GaN in the apertures, due to a constant aperture diameter and SAG patterning on large areas of the samples. Therefore, the effective growth time reads  $t_{\text{eff}} = t - t_{\text{inc}}$ .

The geometry of the NCs was approximated by a cylindrical geometry. Since the tip morphology of the NCs changed during growth from rather flat to pyramidal, the axial growth rates had to be corrected for quantitative comparison: Firstly, the NC height was measured by AFM. Secondly, top-view SEM micrographs were evaluated to determine the average NC radius. In the cylindrical approach, the radius is given by  $r = \sqrt{A_{\text{NC}}/\pi}$ , where  $A_{\text{NC}}$  is the contact area of the NC to the template. By measuring the height ratio  $h_{\text{base}}/h_{\text{tip}}$  of NC base and tip from bird's eye view SEM micrographs, the volume of the non-cylindrical tip was converted into an equivalent cylindrical volume  $V_{\text{tip}}^{\text{cyl}}$ . For this calculation, the measured NC diameter and the tip inclination (see Section 7.2.1) was used. The height of the pyramidal tip which was converted into the cylindrical equivalent, is then given by  $h_{\text{tip}}^{\text{cyl}} = V_{\text{tip}}^{\text{cyl}} / (\pi r^2)$ . The total height of the NC in the cylindrical approximation is given by  $h_{\text{tot}} = h_{\text{base}} + h_{\text{tip}}^{\text{cyl}}$ , and the average axial growth rate accordingly by  $w_{\text{ax}} = h_{\text{tot}}/t_{\text{eff}}$ . The differential axial growth rate  $\Delta h/\Delta t$  is given by  $\Delta h_{\text{tot}}/\Delta t$ . The variation of growth time from one sample to the next is given by  $\Delta t$ , the variation in total (cylindrical) NC height by  $\Delta h_{\text{tot}}$ . The average radial growth rates were deduced by calculating the increase of the NC radius as a function of growth time and taking as reference the average radius value  $r_0$  which was obtained for shortest growth, i.e.  $w_{\text{rad}} = (r - r_0) / t_{\text{eff}}$ . Since for  $r_0$  a reference is missing, the corresponding radial growth rate cannot be calculated. However, due to the short growth time ( $t_{\text{eff}} = 4$  min), negligible radial growth was assumed.

The NC growth rates can now be compared quantitatively and the nominal Ga supply  $F_{\text{Ga}}$  is given for comparison:

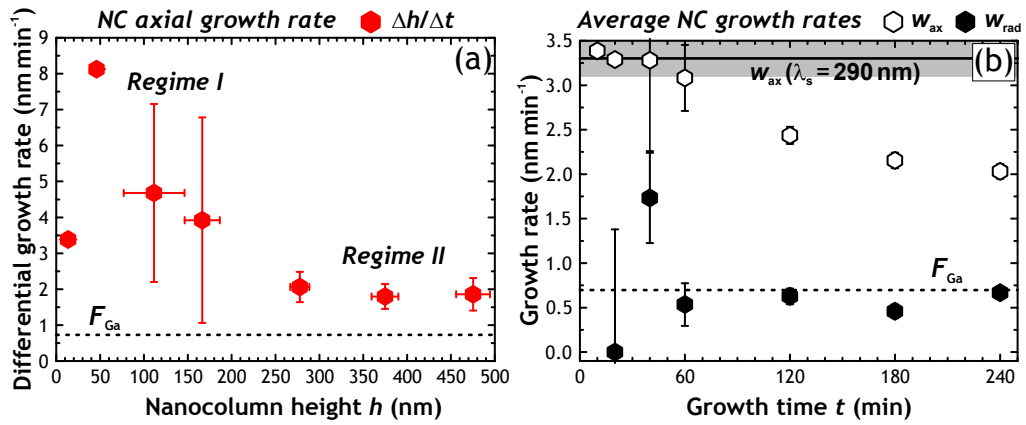


**Figure 7.6:** (a) Differential axial growth rate as function of NC height. (b) Average axial and radial growth rates of the SAG GaN NCs as function of growth duration. The solid line shows the enhanced axial growth rate due to Ga diffusion on the Mo mask (see text). The gray shaded region represents the error of the enhanced axial growth rate due to the error of the Ga diffusion length. The dashed lines indicate the nominal Ga flux (layer equivalent growth rate). Errors were calculated according to Gaussian error propagation and the standard deviations. Data from Samples G1309, G1270, G1304, G1269, G1302, G1267, and G1306 (increasing growth time).

For Figure 7.6(a), two different regimes can be distinguished, which qualitatively resemble the predicted growth rate behavior of Figure 4.1(a): For NC heights below 200 nm (*regime I*), a varying axial growth rate is observed. The general trend is a growth rate which decreases for increasing NC height. For *regime II*, a constant growth rate of 1.9(1) nm min<sup>-1</sup> is reached, which is larger than the Ga supply of 0.7 nm min<sup>-1</sup>. The transition from *regime I* to *II* occurs at a NC height of about 200 to 250 nm. Consequently, the Ga diffusion length on the NC sidewalls is estimated to be  $\lambda_f \lesssim 250$  nm. Fitting the data according to Equation 4.1 and 4.2 is refrained from, due to several factors: The theoretical growth model assumes a hexagonal NC with  $c$ -plane tip and constant diameter. In the experiment however, radial growth is not suppressed and the NC radii vary for the different samples. Besides, the observed NC geometry with pyramidal tips differs from the assumption of  $c$ -plane NC tips. Furthermore, the model depends on the driving forces for the diffusion of Ga adatoms to the NC top<sup>[106]</sup>. Especially for *regime I*—for which the uncertainty of the data is large or the data deviates<sup>3</sup> from the predicted behavior—the model contains three independent fit parameters. Therefore, in the following, only the estimation for  $\lambda_f$  will be used. The

3 The first data point in Figure 7.6(a) is in contradiction to the predicted behavior. According to the model, a significantly increased axial growth rate is expected. This discrepancy is possibly due to slight variations in the incubation time which was not measured for this specific sample. For small NC heights and short growth durations, an underestimation of the incubation time will significantly reduce the obtained differential growth rate.



Ga diffusion length  $\lambda_s$  on the Mo layer will be estimated according to a geometric model.

In the case of the average growth rates (Figure 7.6(b)), a rather constant axial growth rate is observed for *regime I*. This value is enhanced by a factor of about 5 as compared to the nominal effective Ga flux. The axial growth rate then decreases in *regime II*. The radial growth rate  $w_{\text{rad}}$  is constant within the accuracy of the measurements. For longer growth times, non-uniform radial overgrowth occurred on the Mo mask (Figure 7.5(e, f)) and the radial growth rate for these samples is thus underestimated.

The maximal NC height for growth durations  $t \leq 40$  min is about 125 nm. Using the estimated value for  $\lambda_f$  of about 250 nm, the condition  $h \ll \lambda_f$  is valid. According to Equation 4.1, the axial growth rate will therefore be determined mainly by the direct impingement on the aperture area ( $F_{\text{Ga}}$ ) and a diffusion term of Ga atoms from the Mo mask. Neglecting material contribution from the sidewalls,  $\lambda_s$  can be estimated from simple geometrical arguments. For each NC, a circular Ga adatom reservoir area which does not overlap with the nearest neighbor area (the aperture pitch was expected to be in the transition region of competitive and isolated regime) was assumed. The diffusion enhanced average axial growth rate then simply reads

$$w_{\text{ax}} = F_{\text{Ga}} \frac{(r + \lambda_s)^2}{r^2}. \quad (7.2)$$

From the average NC radius<sup>4</sup>  $\bar{r} = 245$  nm and the measured value  $w_{\text{ax}}$  for *regime I*, a Ga diffusion length of

$$\lambda_s = 290 \pm 16 \text{ nm} \quad (7.3)$$

is obtained. The error was calculated according to Gaussian error propagation.

The decrease of the axial growth rate for *regime II* is explained by taking into account the Ga adatom diffusion length  $\lambda_f$ : For  $h \gg \lambda_f$ , the axial growth rate does not depend on  $\lambda_s$ . Averaging over the total growth time results in a decreasing average axial growth rate with increasing growth time. The Ga adatoms that diffuse on the NC sidewalls and do not reach the tip will contribute to radial growth or desorb. An increase of the NC radial growth rate was not observed, however, this effect is likely to manifest itself in the non-uniform radial overgrowth for longer growth times. Furthermore, the observation of self-induced NCs which grow on the Mo mask for longer growth times is consistent with this explanation.

It is worth noting, that in crystal growth, the facet with the slowest growth rate will eventually determine the crystal shape. Thus, the growth rate of the semipolar surfaces is smaller than the axial growth rate. Besides the

<sup>4</sup> The measured NC radius has been used instead of the aperture radius, since for *regime I*, a discrepancy between both values was observed.

reduction of the axial growth rate due to decoupling the axial growth from the contribution of the substrate, the growth rate is expected to decrease also due to the formation of the semipolar surfaces.

### Discussion

The obtained Ga adatom diffusion length on the Mo mask is about 100 nm smaller as compared to the value obtained in [Section 7.1.1](#). The surface roughness of the Mo layers patterned by EBL and pulsed laser ablation are similar. It is therefore expected, that different patterning procedures are not the cause for this deviation. The Ga diffusion length was calculated according to [Equation 7.2](#) which is function of the average NC radius and the effective Ga flux. The latter was determined by RHEED directly at the GaN surface of a reference sample. However, it is expected that the Ga desorption rate from the Mo surface is larger than from GaN(0001) (see [Figure 7.4](#)). This was not taken into account for the estimation of  $\lambda_s$ . If one uses exemplarily  $\lambda_s = 435$  nm (see [Section 7.1.1](#)) and calculates the corresponding effective flux  $F_{\text{Ga}}^{\text{Mo}}$  on the Mo layer according to [Equation 7.2](#), i.e.  $F_{\text{Ga}}$  on the GaN aperture area, and  $F_{\text{Ga}}^{\text{Mo}}$  on the Mo surface, a value of about  $F_{\text{Ga}}^{\text{Mo}} = 0.4 \cdot F_{\text{Ga}}$  is obtained. Determination of the Ga desorption kinetics from the Mo surface by RHEED was hampered due to the polycrystallinity of the Mo layer. Therefore, it is not clear, whether such high desorption rates from the Mo surface are appropriate. Studies of the Ga adatom desorption kinetics from Mo surfaces are expected to further refine the understanding of the selective area growth mechanism. A suited method is for example quantitative line-of-sight mass spectrometry<sup>[164]</sup>. In this approach, the partial pressure of desorbed Ga can be detected in direct line of sight to the sample.

The distribution of SI NCs on the Mo mask in between the SAG arrays and outside of the arrays, supports the underestimation of  $\lambda_s$  in this geometric approach: For growth durations up to 60 min, the growth of self-induced NCs on the Mo mask in between the SAG NCs was suppressed; see [Figure 7.5\(d'\)](#). However, on the Mo layer outside of the array, the growth of SI NCs was observed (*Sample G1269*, not shown). The desorption rate inside and outside the arrays is assumed to be identical, therefore, the Ga adatom diffusion length on the Mo layer is expected to be at least in the range of  $p/2$ . Otherwise, growth of self-induced NCs would also have been observed in between the arrays. The correction of the diffusion length to  $\lambda_s \gtrsim p/2 \sim 400$  nm is in agreement with the result of [Section 7.1.1](#).

In conclusion, the SAG process in the case of NCs with diameters close to one micron, was successfully adapted. No pronounced deviations from the selective area growth mechanism as discussed in [Section 7.1.1](#) were observed. Furthermore, the Ga diffusion length on the NC sidewalls could be narrowed down to about 250 nm.



### 7.1.3 Dynamical growth conditions

As shown in the previous [Sections 7.1.1](#) and [7.1.2](#), the SAG mechanism is similar or even equivalent for a wide range of NC diameters. The consequence of a Ga adatom diffusion assisted growth mechanism is the variation of local growth conditions as function of aperture or NC diameter, and NC height. In the following, the effective Ga supply in the aperture  $F_{\text{Ga}}^{\text{ap}}$ , and the effective Ga supply at the NC tip  $F_{\text{Ga}}^{\text{tip}}$ , due to Ga diffusion will be calculated, to estimate the magnitude of these variations. The estimated Ga diffusion lengths of about  $\lambda_s = 400$  nm and  $\lambda_f = 250$  nm will be used. In principle, [Equation 4.1](#) and [4.2](#) are suited for this purpose. However, these expressions are function of the driving forces for the diffusion of Ga adatoms to the NC top, which have not been deduced in this work. Therefore, a geometric approach without the use of a sophisticated growth model was chosen:

The supply in the aperture is solely given by the nominal Ga supply, and by an additional contribution due to Ga diffusion on the Mo mask. The supply at the tip is assumed to be due to the nominal Ga flux, and due to the contribution of Ga diffusion on the NC sidewalls. Transient regimes, for which both diffusion lengths have to be taken into account were not considered. Furthermore, Ga desorption from the Mo layer or from the NC sidewalls was not included. For ease of calculation, a cylindrical NC shape with *c*-plane tip is assumed. From geometric considerations one obtains for the *isolated regime*

$$F_{\text{Ga}}^{\text{ap}} = F_{\text{Ga}} \left( 1 + 4 \frac{\lambda_s}{d} + 4 \frac{\lambda_s^2}{d^2} \right) \quad \text{and} \quad (7.4)$$

$$F_{\text{Ga}}^{\text{tip}} = F_{\text{Ga}} \left( 1 + \frac{4}{\pi} \frac{\lambda_f}{d} \tan \alpha \right). \quad (7.5)$$

The nanocolumn diameter is given by  $d$ , the inclination of the Ga effusion cell with respect to the substrate normal by  $\alpha = 33^\circ$ . The first term in the brackets is due to the direct impingement, the latter terms are due to Ga diffusion in both cases. According to these equations, the N/Ga ratio ( $F_{\text{N}}/F_{\text{Ga}}^{\text{ap,tip}}$ ) in the aperture or at the NC tip was calculated for different diameters and nitrogen supplies. The results are shown in [Figure 7.7](#).

The nominal N/Ga ratio at the sample surface for standard SAG conditions was about 9, which corresponds to highly nitrogen-rich conditions. [Figure 7.7\(a\)](#) suggests a significant change of the local growth conditions at the beginning of growth. For aperture diameters of about  $d = 50 - 250$  nm, the N/Ga ratio is smaller than unity (stoichiometry), which results in locally Ga-rich growth conditions. The growth is therefore expected to proceed in the N-limited regime which is typically used for the growth of high-quality GaN layers<sup>[70]</sup>. Even for apertures with diameters  $d > 500$  nm, a significant change of the nominal growth conditions is predicted. The effective growth

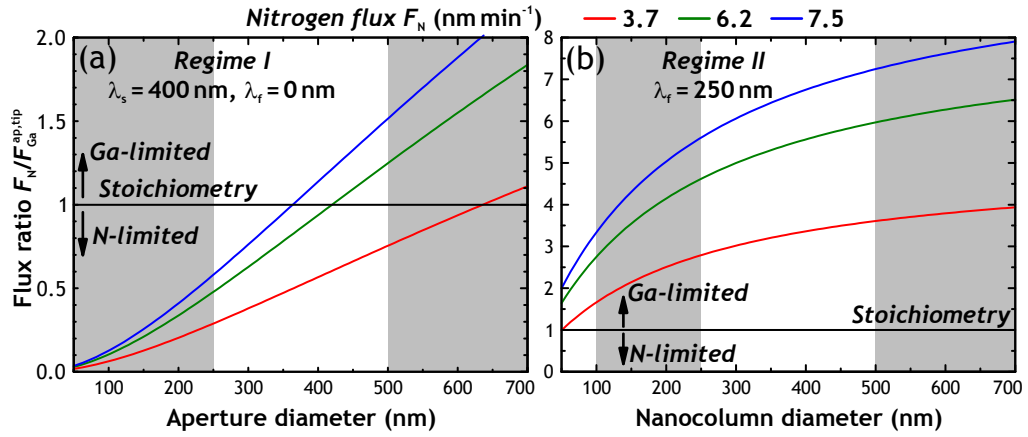


**Figure 7.7:** Calculated N/Ga ratio in the aperture (a) and at the NC tip (b) due to Ga diffusion for the *isolated regime*. An effective Ga flux of  $F_{\text{Ga}} = 0.7 \text{ nm min}^{-1}$  was used for calculation. Gray shaded regions indicate the experimentally assessed aperture(NC) diameter range. Note, that due to radial growth slightly different diameter(NC) ranges are covered for (a) and (b). Arrows indicate N- and Ga-limited growth regimes.

conditions may be shifted towards the slightly N-rich regime or even to the slightly Ga-rich regime for the lowest nitrogen supply.

The situation is expected to be different once the growth of the NCs occurs in *regime II* (Figure 7.7(b)). Although a Ga diffusion length on the NC sidewalls of 250 nm shifts the growth conditions in direction of stoichiometry, the Ga-rich regime is not reached. Therefore, for the experimentally assessed NC diameters and nitrogen supplies, always nitrogen-rich growth conditions are expected for *regime II*.

As discussed in the beginning, more sophisticated models should be used for a precise quantitative prediction of the local growth conditions. Nevertheless, the presented calculations show trends which are expected to be valid, independent of the exact model which has been used. For sufficient small aperture(NC) diameter the local growth conditions are expected to start in the Ga-rich regime and to dynamically evolve towards the N-rich regime for increasing NC height. Static growth conditions will only occur at the NC tip, when the growth has proceeded to *regime II*.

In order to validate these trends, the effect of nitrogen supply variation on the axial growth rate of NCs with different diameter was investigated. The N supply was varied between 3.7 and 8.1  $\text{nm min}^{-1}$ . SAG arrays of *M* and *T* design were used, the growth duration was 3 h for all samples. The plasma composition<sup>5</sup> was monitored during growth and kept constant. This is of importance due to the variation of plasma composition with nitrogen flux and plasma excitation power<sup>[55]</sup>, and the major contribution of atomic

<sup>5</sup> Ratio of excited atomic to excited molecular nitrogen.

nitrogen to the GaN growth rate in MBE<sup>[165]</sup>. The average axial growth rate was determined by SEM and is shown in Figure 7.8 for different NC diameters and nitrogen supplies. Note, that for each series only NCs with approximately constant diameter were compared, since the axial nanocolumn growth rate was observed to be function of NC diameter (see Section 7.1.1). Furthermore, only NCs of the isolated regime were investigated, such that the axial growth rate was no function of pitch. A shift of stoichiometric growth conditions occurred between<sup>6</sup> the series of different NC diameters. This resulted in the use of different effective Ga fluxes. Accordingly, the growth rates of the two series (small and large NC diameter) cannot be compared quantitatively.

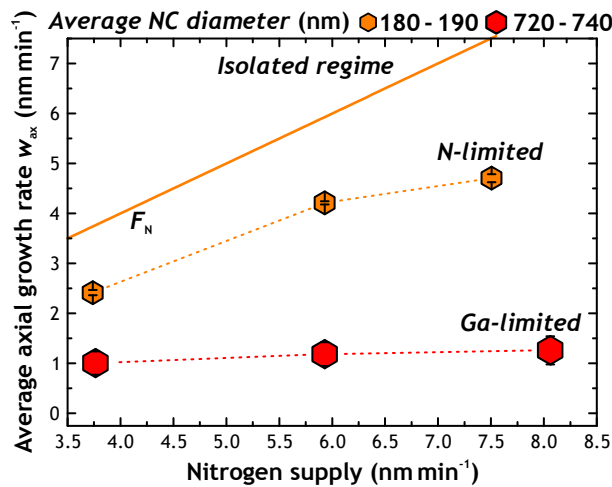


Figure 7.8: NC average axial growth rate for the *isolated regime* as function of nitrogen supply. Error bars are given by standard deviations, the growth duration was 3 h. Dashed lines guide the eye and have been assigned to different growth conditions (see text). The solid curve  $F_N$  indicates the supplied N flux. Samples G1253, G1255, G1256 and G1411, G1409, G1416.

For NCs with diameters around 180 – 190 nm, the axial growth rate is clearly function of nitrogen supply and increases sublinearly with the latter. For NC diameters around 720 – 740 nm, the axial growth rate is constant within the accuracy of the measurement. In both cases, the layer equivalent growth rate (nominal Ga flux) is exceeded. The used Ga fluxes  $F_{Ga}$  were 0.7 and 0.4 nm min<sup>-1</sup> for samples with small and large aperture diameter, respectively.

For the following discussion, only the effect of local Ga supply variations in *regime I* will be considered to cause growth rate variations. Once the growth proceeds to *regime II*, static Ga-limited growth conditions are expected and an increase of nitrogen supply is not assumed to affect the axial growth rate<sup>7</sup>.

<sup>6</sup> Maintenance of the MBE chamber.

<sup>7</sup> This assumption will be topic of discussion at the end of this section.

According to [Figure 7.7\(a\)](#), growth conditions around stoichiometry are expected for apertures with diameters of about 700 nm and an N supply of  $3.7 \text{ nm min}^{-1}$ . For larger N supplies, the local growth conditions are predicted to be Ga-limited and a constant NC axial growth rate is expected for increasing N supply. The data in [Figure 7.8](#), which corresponds to this diameter range resembles such a behavior.

For apertures in the range of 200 nm, one expects an increase of the axial growth rate for increasing nitrogen supply in *regime I*, according to [Figure 7.7\(a\)](#). No transition from N-limited to Ga-limited growth conditions is expected. The axial growth rate of the NCs which correspond to this diameter range indeed qualitatively follows the nominal nitrogen supply in [Figure 7.8](#). The fact that the growth rate is smaller than the nominal N supply is attributed to the fact that the total axial growth rate averages over *regimes I* and *II*. Only in the former case, the axial growth rate is expected to depend on the nitrogen supply.

### Discussion

An increase of the SAG GaN NC axial growth rate for increasing N supply was already observed by Kishino *et al.*<sup>[122]</sup>. The diameters of the nanocolumns were about 200 nm, and thus comparable to the presented results. The authors varied the nitrogen flow through the N plasma source and observed that the axial growth rate increased sublinearly for increasing nitrogen flow. However, the nitrogen supply was not calibrated in  $\text{nm min}^{-1}$  and the exact dependence of the axial growth rate on the N supply is therefore unknown. Nevertheless, the authors concluded, that the SAG occurred under N-limited growth conditions. It was suggested, that the Ga desorption rate was reduced for increasing N supply. Experimentally, a reduced Ga diffusion length on the mask was observed for increasing N supply. This was attributed to a reduction of Ga desorption. However, the Ga desorption rate as function of nitrogen supply was not monitored. Nevertheless, changes of Ga adatom diffusion lengths induced by variations of the N supply are conceivable: For the Ga-rich regime, an increase of N supply is expected to result in an increased probability of GaN to nucleate on the Mo mask, as well as on the NC sidewalls. Thus, both diffusion lengths are expected to decrease with increasing N supply. In the N-rich regime however, an increase of N supply is expected to result in an increased rate of  $\text{N}_2$  formation, which effectively reduces the probability of GaN nucleation. This would bring about an increase of diffusion lengths. The width of the denuded zone around the SAG NCs was measured by SEM for the different N supplies (not shown) in order to investigate the influence of N supply on  $\lambda_s$ . This width is an estimate for the Ga adatom diffusion length on the Mo layer. No significant change of  $\lambda_s$  was observed within the accuracy of the measurement. It is concluded, that changes of the Ga diffusion length on the Mo layer as function of N

supply are not the reason for the observed behavior of the growth rate in Figure 7.8. The effect of the variation of N supply on  $\lambda_f$  was not investigated. However, since  $\lambda_s$  was not affected under the specific growth conditions, it is assumed that this is true for  $\lambda_f$ .

It is therefore concluded, that the increase of the SAG NC axial growth rate for increasing N supply is due to locally Ga-rich growth conditions in *regime I* for sufficiently small NC diameters. These experimental results support the hypothesis, that the growth conditions at the tip of the NCs are in fact dynamical and do not have to follow the nominal growth conditions. Depending on the exact values of the Ga diffusion lengths and the array design, they may cover a wide range from the N-rich to the Ga-rich regime. Only in *regime II*, static growth conditions are expected. However, also in this case, deviations from the nominal growth conditions are expected.

## 7.2 EXCURSUS: MORPHOLOGY AND POLARITY

The following sections will investigate and discuss the morphology and polarity of the SAG GaN NCs. In the case of the morphology, attention will be paid particularly to the tip region of the nanocolumns. In the case of the polarity, also self-induced nanocolumns will be investigated. The polarity of the selectively grown and the self-induced NCs will be compared. Furthermore, an approach for polarity inversion of SAG GaN NCs will be presented.

### 7.2.1 Semipolar surfaces at the nanocolumn tip

In the following section, the semipolar facet family which forms the SAG NC tip will be identified and discussed. Due to the use of GaN templates, the GaN NCs have a homoepitaxial relationship to the template. Immediately,  $\langle 1\bar{1}00 \rangle_T \parallel \langle 1\bar{1}00 \rangle_{NC}$  and  $\langle 11\bar{2}0 \rangle_T \parallel \langle 11\bar{2}0 \rangle_{NC}$  follows. Subscripts T and NC denote GaN template and NC, respectively. This relation was confirmed by TEM investigation of the interface region of NCs and GaN template (not shown). The crystallographic orientation of the GaN template with respect to the array design is known<sup>8</sup>. From SEM top-view micrographs (see e.g. Figure 6.1), the sidewalls of the NCs are identified as *a*-  $\{11\bar{2}0\}$  and  $\{1\bar{1}00\}$  *m*-surfaces. The semipolar surfaces at the tip are terminated at the *m*-plane sidewalls. Accordingly, the family of the pyramidal tip can be reduced immediately to  $\{2\bar{2}0n\}$ . This observation holds for the complete NC diameter range investigated in this thesis. *n* is an integer number  $n = 1, 2, 3, \dots$ <sup>9</sup>, which increases for decreasing semipolar plane inclination

8 For GaN templates on Al<sub>2</sub>O<sub>3</sub>, the wafer flat typically identifies  $\{1\bar{1}00\}$ .

9 Note, that e.g.  $(1\bar{1}01)$  and  $(2\bar{2}02)$  are equivalent concerning their angles with  $(0001)$ , however their interplanar spacing differs. Therefore, the planes will be named according

with respect to the  $c$ -plane. For convenience, the reader is referred to [Figure 2.1](#), and furthermore some family members and their theoretical angles with respect to the  $c$ -plane are listed again in [Table 7.1](#).

Miller-Bravais index	$\angle((0001), (hkil))$	Nomenclature
$(1\bar{1}00)$	$90.0^\circ$	$m$ -plane
$(2\bar{2}01)$	$75.1^\circ$	
$(1\bar{1}01)$	$62.0^\circ$	$s$ -plane
$(2\bar{2}03)$	$51.4^\circ$	
$(1\bar{1}02)$	$43.2^\circ$	$r$ -plane

**Table 7.1:** Inclinations of GaN( $2\bar{2}0n$ ) surfaces.

The identification of the exact family was performed by TEM. Cross sectional TEM lamellae have been prepared by focused ion beam in  $[11\bar{2}0]$  zone axis geometry (see [Section A.7](#)). Since the view direction is in-plane with two facets of the  $\{2\bar{2}0n\}$  family, the measured angles of the tip with respect to the  $c$ -axis can be directly used to identify the value of  $n$ . [Figure 7.9](#) shows exemplarily TEM micrographs of SAG NCs with diameters of about 600 and 200 nm, which were grown under standard SAG conditions.

The majority of the investigated NCs show  $r$ -plane facets at the very tip. However, for some NCs—especially those which show a high basal plane stacking fault density—a large variety of semipolar planes in the range of [Table 7.1](#) and even larger values of  $n$  are observed.

To investigate a possible influence of the aperture diameter on the tip facet inclination, as suggested by Bengoechea-Encabo *et al.*<sup>[11,125]</sup>, a SAG NC sample was grown, for which the SAG aperture diameter was varied from 50 nm to 1  $\mu\text{m}$ . The pitch was 1  $\mu\text{m}$  and standard SAG growth conditions have been used. To reduce the density of SI NCs on the Mo mask, a growth time of 2 h was used. As discussed in the sections before, with a pitch of 1  $\mu\text{m}$ , the growth proceeded in the isolated regime. Therefore, the apertures were subject to the maximal possible Ga flux. A SEM bird's eye view micrograph and the analysis of the average semipolar facet inclination as function of NC diameter is shown in [Figure 7.10](#).

Similar to the results presented in [Section 7.1.2](#), it is observed, that the formation of semipolar facets at the tip and axial growth are not occurring in sequence, i.e. for NCs with diameters larger than 500 nm, the coalescence of the pyramidal tip has not completed and a rough layer-like morphology at the apex is present. This can be attributed to the N-rich growth conditions

---

to the Miller index convention, i.e. 1 being the greatest common divisor of the  $(hkil)$  quadruple.

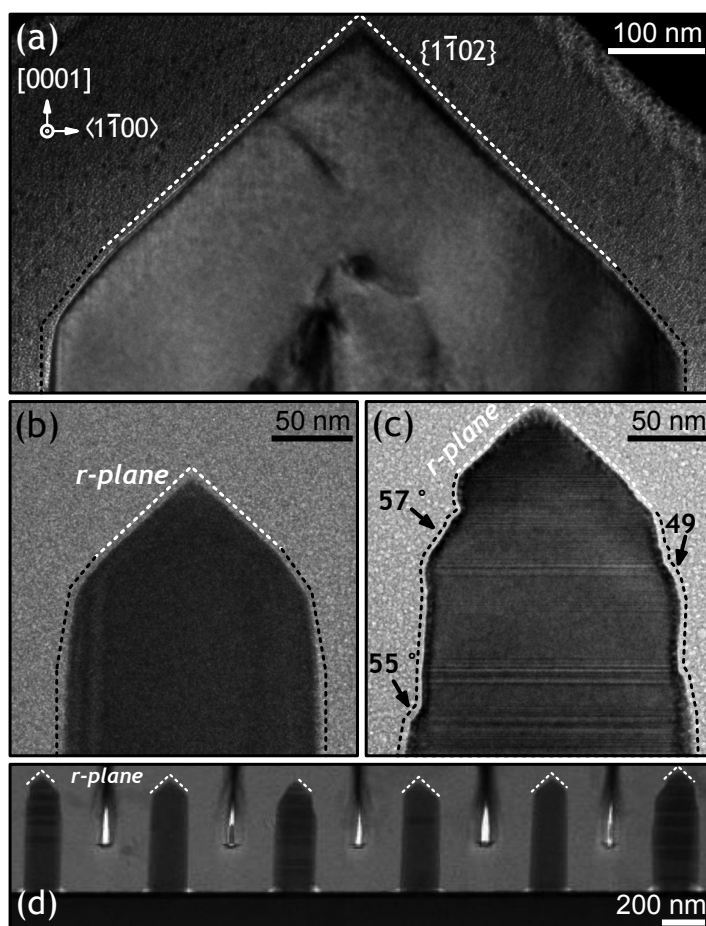


**Figure 7.9:** TEM micrographs of the tip area of single SAG NCs with diameters of around 600 (a) and 200 nm (b, c). The inclination of the tip facets is shown by dashed lines. Bright segments correspond to *r*-planes. For black segments in (c), the measured inclination is given. An annular dark field STEM micrograph of six NCs on the GaN template is shown in (d). The NC diameter is about 200 nm. Horizontal contrasts in (c, d) correspond to extended defects, e.g. basal plane stacking faults. *Samples G1267 (a), G1253 (b, c) and G1225 (d).*

at the tip in *regime II*, which strongly reduces the Ga diffusion length on polar GaN surfaces<sup>[67]</sup>. It is expected, that if the growth had been performed for longer durations, the semipolar facets would have coalesced further, such that eventually the pyramidal tip morphology would be obtained for all NCs in the shown diameter range.

In contrast to the previously shown results, this sample shows mainly *s*-plane facets at the NC tip. A possible explanation might be the fact that the nitrogen plasma source was subject to degradation<sup>10</sup> at the end of this thesis, when this sample was grown.

Despite the observation of a different inclination than usual, no clear evidence for a diameter-dependence was observed. The data scatter among

<sup>10</sup> The plasma state became unstable for the typically used conditions.



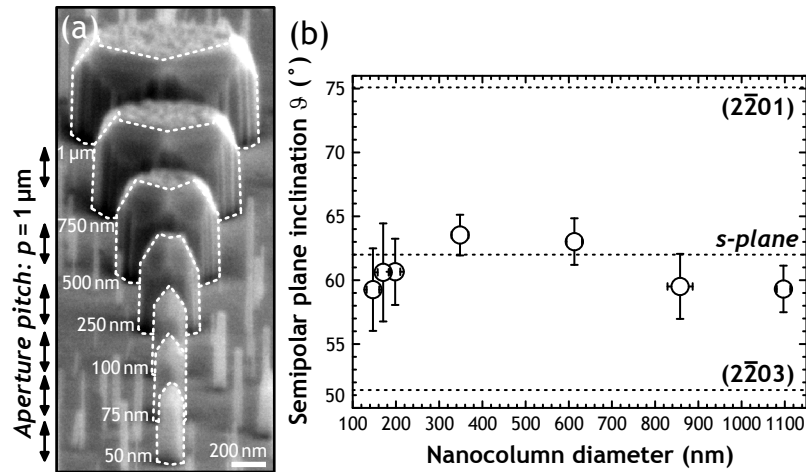


**Figure 7.10:** (a) Bird's eye view SEM micrograph of a row of SAG NCs with different diameter. Dashed lines trace the NC morphology and the tip inclination. The nominal aperture diameter is indicated. The pitch was  $1 \mu\text{m}$  for all apertures. (b) Average NC tip inclination with respect to the  $c$ -plane as function of NC diameter. Dashed lines denote theoretical inclination angles as labeled. The measured inclination was corrected, taking into account the sample tilt of  $15^\circ$  with respect to the substrate normal. Error bars are given by standard deviations. *Sample G1502.*

the inclination expected for  $s$ -plane, a change of  $n$  towards the next lower- or higher-indexed plane is not observed.

### Discussion

The authors of Refs.<sup>[11,125]</sup> demonstrated homoepitaxial SAG of GaN NCs by MBE. Depending on the exact growth conditions, the NC tip morphology could be altered from semipolar to  $c$ -plane. This behavior was related to the local growth conditions in the apertures. In contrast to these results, no correlation of aperture diameter and semipolar plane inclination at the NC tip was observed for standard SAG conditions in this thesis.

In the discussed publications, the incoming Ga and N fluxes  $F^+$  are given in GaN(0001) growth rates. The reported nominal supply ratios, for which  $c$ -plane NCs have been obtained, were always Ga-rich. However, due to the high substrate temperature, the effective fluxes at the sample surface remained unknown and the authors expect a shift towards lower Ga fluxes<sup>[11]</sup>. Nevertheless, it was concluded, that the growth of  $c$ -plane SAG GaN NCs requires a local Ga-rich environment in the apertures<sup>[125]</sup>. As discussed in [Section 7.1.3](#), such conditions are also expected to have occurred for the nominally N-rich standard SAG conditions in this thesis, due to Ga diffusion on the mask. However, in *regime II*, N-rich growth conditions were restored. The absence of SAG NCs with  $c$ -plane tips, even for the smallest aperture diameter, is therefore interpreted to be due to the N-rich growth conditions in *regime II*. These conditions seem to stabilize  $\{2\bar{2}0n\}$  semipolar GaN



surfaces.

The consequent hypothesis in order to obtain SAG GaN NCs with purely  $c$ -plane tips, i.e. without the formation of semipolar segments, is the need of a local Ga-rich environment at the NC tip during the entire growth process. This refines the suggestion of Refs.<sup>[125]</sup>, that a local Ga-rich environment is only needed in the apertures.

From a kinetics point of view, the Ga adatom diffusion barriers on the nonpolar, semipolar and polar surfaces (and at edges) have to be considered to understand the formation of the tip facets. However, diffusion barriers on semipolar GaN surfaces are scarcely calculated. One surface which has been treated is the  $(11\bar{2}2)$  surface<sup>[83]</sup>. For the specific surface reconstruction which is predicted to be thermodynamically stable under N-rich growth conditions<sup>[61]</sup>, a Ga adatom diffusion barrier of 1.2 eV was found. This value is 4 to 6 times higher than lowest Ga adatom diffusion barriers on the nonpolar surfaces<sup>[80]</sup>. On the other hand, it is smaller by a factor of around 0.7 as compared to the Ga adatom diffusion barrier on GaN(0001)<sup>11</sup> surfaces under N-rich conditions. Although diffusion barriers for  $\{2\bar{2}0n\}$  have not been calculated, the results of the  $(11\bar{2}2)$  surface might indicate lower diffusion barriers for semipolar GaN surfaces as compared to polar ones. This could in principle explain the different surface roughness of the semipolar tip facets (smooth) and the  $c$ -plane layer-like apex (rough) which is observed for NCs with larger diameters.

The stabilization of semipolar or  $c$ -plane GaN at the NC tip will be discussed in the framework of equilibrium thermodynamics in [Section 7.3](#).

### 7.2.2 Polarity determination and control of SAG GaN NCs

Several methods can be used to experimentally determine the polarity of GaN NCs<sup>[12]</sup>. Since each technique has its advantages and disadvantages, various methods were used in this thesis, to determine and consolidate the polarity of the NCs. Wet chemical etching, aberration corrected high resolution transmission electron microscopy (HRTEM) in combination with image simulations, and convergent beam electron diffraction (CBED) were applied, to obtain a consistent picture of the GaN NC polarity. The last paragraph of this section is devoted to the polarity control of SAG GaN NCs.

#### 7.2.2.1 Wet chemical etching

KOH is known to etch preferentially the N-face of bulk GaN<sup>[166]</sup>. The selective etching originates from the bonding configuration of nitrogen at

---

<sup>11</sup> The fact that the SAG GaN NCs show Ga-polarity will be proved in the next section.

the surface<sup>[167]</sup>. In the case of GaN(0001), the first Ga layer is dissolved in KOH by formation of gallium oxide Ga<sub>2</sub>O<sub>3</sub>. The potassium hydroxide solution works as a catalyst. After this step, the OH<sup>-</sup> ions encounter a N-terminated surface with three occupied dangling bonds of nitrogen. These effectively repulse the hydroxide ions. For GaN(000 $\bar{1}$ ), only one dangling bond per N atom is facing the hydroxide ions, and the repulsion is weaker. The hydroxide ions can attack the bonds of the tetrahedrally coordinated Ga atoms and dissolve them in solution. The initially N-terminated surface with one dangling bond per N atom is restored, and the cycle is repeated.

To study the nanocolumn polarity, SAG NCs with fully developed pyramidal morphology and self-induced NCs which grow on the unpatterned region of the Mo layer were etched for 10 min in a saturated solution of KOH at room temperature. The morphology prior to and after KOH etching is presented for both types of NCs in Figure 7.11.

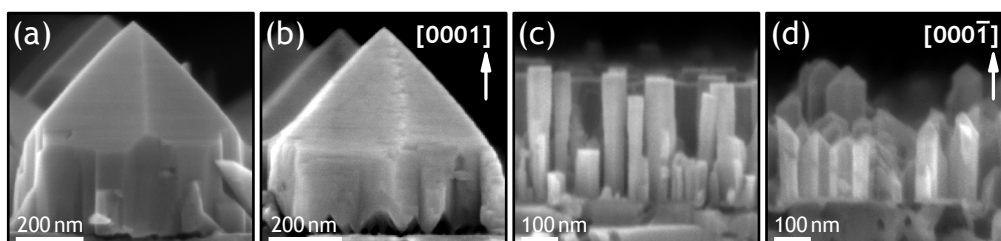


**Figure 7.11:** SEM side-view micrographs of SAG (a) and self-induced (c) GaN NCs prior to KOH etching. The SI NCs were grown on the Mo layer on the GaN template. At the tip of the SI NCs, AlN marker insertions have been grown, however, the typical morphology of the NCs was not altered. The NC morphology after KOH treatment is shown in (b) and (d), for the SAG and the self-induced case, respectively. The polarity of the NCs is assigned in (b) and (d). *Samples G1348, G1288* for SAG, and SI NCs, respectively.

In the case of the selectively grown columns (a, b), the NC base region at the interface to the Ga-polar substrate is etched. This indicates Ga-polarity of the NCs, at least for the base region. Due to the lack of *c*-plane GaN at the tip, information on the polarity of the tip region cannot be directly deduced by this method.

The tips of the self-induced NCs (c, d) are etched, which indicates N-polarity.

### Discussion

In the case of the SI NCs, AlN insertions at the tip were introduced as markers for following TEM analysis (not shown). The typical morphology of the *c*-plane tip was however not changed. Since N-face AlN is also preferentially etched by KOH<sup>[168]</sup>, these results are consistent with KOH etching experiments performed on N-polar self-induced GaN NCs, which show qualitatively the same morphology before and after KOH treatment<sup>[138,144]</sup>. Furthermore,

it was shown that in the case of MBE-grown GaN NCs which contain AlN heterostructures, the polarity of the GaN NC determines the polarity of the AlN cap (and shell)<sup>[143]</sup>. Thus, it is concluded, that the AlN insertions did not influence the experimental outcome of polarity determination.

It has to be noted, that in the case of the SAG NCs, the vicinal step structure at the tip is enhanced after etching by KOH. This is especially pronounced at the edges of the pyramidal tip facets, where the local atomic (and dangling bond) configuration is expected to be different as compared to the configuration at the surface. The partial instability against KOH for the crystal edges at the tip is therefore rather attributed to changes in the local binding configuration, than to a change of polarity. This argumentation is plausible, since no particular care was taken to change the polarity during growth. The final discussion at the end of this section will pick up the importance of the initial polarity of the substrate for the polarity of the NCs.

#### 7.2.2.2 *Aberration corrected high resolution transmission electron microscopy*

To corroborate the obtained results and to extend the polarity determination in the case of the SAG NCs to the tip region, spherical aberration ( $C_s$ ) corrected high resolution transmission electron microscopy in combination with image simulations was performed. As discussed,  $C_s$  correction may suppress the formation of imaging artifacts, which complicate direct image interpretation.

The measurements were performed using a Titan TEM at 300 kV in  $[11\bar{2}0]$  zone axis geometry. For this arrangement of the specimen, the polarity can be easily imaged, due to a zigzag arrangement of the GaN dumbbells along  $\langle 0001 \rangle$ . TEM lamellae for the investigation of SAG NCs have been prepared by focused ion beam (FIB). The procedure is described in [Section A.7](#). SI NCs have been prepared conventionally by embedding the sample in epoxy adhesive, subsequent mechanical thinning, and  $\text{Ar}^+$  ion polishing. HRTEM image simulations were performed using the JEMS software<sup>[160]</sup>. Titan microscope parameters are given in [Table A.4](#). Simulated images for different defoci and sample thickness in  $[11\bar{2}0]$  projection are shown in [Figure 7.12](#). The experimental HRTEM micrographs of SAG and SI GaN NCs are shown in [Figure 7.13](#).

The simulation shows, that bright features are expected for the Ga and N atomic column position for thin sample thickness and for the used defocus values. The different contrast in the HRTEM micrographs can therefore be used to identify the orientation of the GaN dumbbell. However, it is observed that for very thin sample thicknesses and a defocus value of  $\Delta f = 0$  nm, the interpretation of the images may be difficult, since the features attributed to Ga and N atomic columns are very similar. In the case of underfocus with  $\Delta f = -5$  nm, the orientation of the GaN dumbbell is difficult to determine

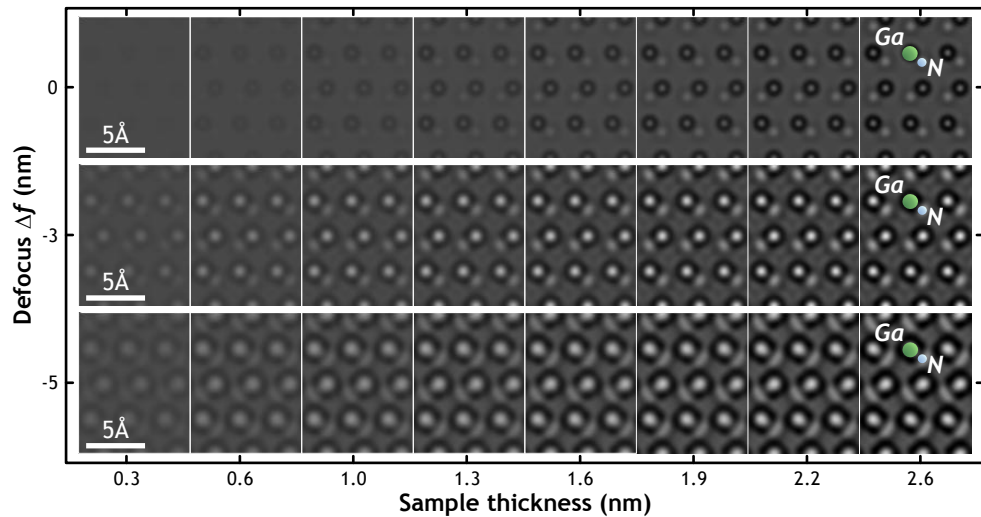


**Figure 7.12:** Simulated HRTEM images of Ga-polar GaN in  $[11\bar{2}0]$  zone axis geometry. The sample thickness and defocus was varied. A spherical aberration of  $C_s = 0$  mm was used. Variation of the spherical aberration within the error interval ( $\sigma_{C_s} = \pm 1.584 \mu\text{m}$ ) affects the simulated images only negligibly. Atomic positions of Ga and N columns are denoted by big and small spheres, respectively.

due to the delocalized intensity at the N column position. For a defocus value of  $-3$  nm however, the GaN dumbbell orientation can be clearly assigned for various sample thicknesses. Therefore, this defocus value was chosen for experimental imaging conditions.

**Figure 7.13(a)** shows an experimental HRTEM micrograph obtained in the pyramidal tip region of a SAG GaN NC<sup>12</sup>. The exact specimen position—an overview image was not recorded—was at the interface of the semipolar GaN(AlN) surface and the amorphous protective  $\text{Si}_3\text{N}_4$  layer, in which the NCs were embedded. The silicon nitride layer can be observed in the upper right corner. For the investigated sample position, the silicon nitride was almost completely removed by the  $\text{Ar}^+$  polishing procedure. The sample thickness for the investigated region is therefore expected to be only a few unit cells, and thus comparable to the simulated sample thickness. The individual atomic columns could not be resolved. However, the GaN dumbbell orientation can be determined: The bright contrast is interpreted to be due to the Ga atomic columns, whereas the faint contrast which elongates the whole pattern in a zigzag fashion antiparallel to the growth direction, is interpreted to be due to the N atoms. Therefore, the orientation of the GaN dumbbells with respect to the growth direction is Ga-polar. Thus, in addition to the NC base of the SAG NCs, also the tip is Ga-polar.

The HRTEM overview and close-up micrographs of a thin SI NC are shown in **Figure 7.13(b, c)**. The NC was grown on the unpatterned region of

12 In this case, a semipolar AlN/GaN multi-quantum well (3 AlN barriers) was grown at the tip. This is however not expected to influence the polarity in the tip region<sup>[143]</sup>, as discussed in the section before.

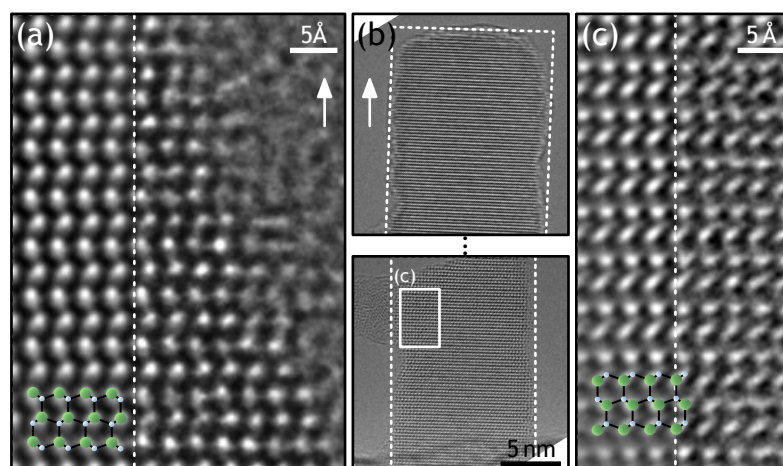


**Figure 7.13:** Experimental HRTEM micrographs ( $\Delta f = -3$  nm) obtained in thin regions at the tip of a SAG NC (a) and for a SI NC (grown on the unpatterned region of the Mo layer) close to the NC sidewall (b, c). The overview image (b) shows the  $c$ -plane tip of the NC. The middle section of the NC was damaged by the electron beam and is not shown. To improve the visibility of GaN dumbbell orientation, a fast Fourier transform filtered image is shown in the left part of (a) and (c). White arrows denote the growth direction in both cases. Ga- and N-polar atomic arrangements are schematically shown. *Samples G1290 and G1306* for SAG and SI NCs, respectively.

the Mo layer. The NC shows a  $c$ -plane tip and a diameter of around 10 nm, which is typical for the SI NCs, as discussed in [Section 7.1.2](#). Due to the high acceleration voltage and the thin specimen thickness, a part of the NC was dissociated during measurement. This undesirable side effect allowed for the investigation of a very thin region, comparable to the previous case. The elongation of the GaN dumbbell contrast in [Figure 7.13\(c\)](#) is reversed with respect to [7.13\(a\)](#). Thus, again N-polarity is concluded for the self-induced NCs.

### Discussion

Comparison of simulated and experimental HRTEM images requires correct adjustment of the defocus conditions. Experimentally, this was achieved by adjusting the focus to Gaussian focus, for which minimal contrast is observed for amorphous specimen regions. The defocus was set to zero and subsequently adjusted to  $\Delta f = -3$  nm. This implies, that the correct choice of the Gaussian focus is crucial for adjusting the appropriate defocus conditions. Since both samples contained amorphous material in the very vicinity of the investigated specimen region, the correct choice of Gaussian focus (or at least similar deviations relative to this focus) is expected to have been fulfilled. Furthermore, if the simulations were carried out for larger underfocus values (not shown), the geometry of the simulated intensity

distribution significantly deviated from the experimental images. Therefore, the reversal of the GaN dumbbell orientation for the experimental images is concluded to be due to opposite crystal polarity of the SAG and SI NCs. The slightly different shape of the dumbbells for the two experimental HRTEM images is due to slight deviations from the perfect alignment of the samples with respect to  $[11\bar{2}0]$ .

### 7.2.2.3 Convergent beam electron diffraction

Convergent beam electron diffraction patterns show extended diffraction disks, rather than localized diffraction spots. The intensity of the disks is modulated due to dynamical diffraction conditions and contains for example information on the absolute crystal polarity of non-centrosymmetric crystals<sup>[159]</sup>. As crystal edges are discussed to affect the appearance of the CBED disks<sup>[169]</sup>, the experiment is not straight forward for thin NCs, and results have to be evaluated carefully with respect to influences of the specimen geometry. The diameter of the SAG NCs is however much larger as compared to SI NCs, and polarity determination by CBED is more convenient in the SAG case. Therefore, CBED experiments for polarity determination were only performed on SAG NCs.

The measurements were performed in  $[1\bar{1}00]$  zone axis geometry at 200 kV using the CM200 TEM. The nominal probe diameter was 6.5 nm. SAG NCs with an average diameter of about 300 nm have been thinned to around 100 nm thickness by FIB. Polishing by Ar<sup>+</sup> ion afterwards was skipped. This left the thickness and the geometry of the lamella unchanged. Consequently, the sample resembled a slice geometry for which edge effects due to the initial hexagonal cross section of the NCs are expected to be negligible. The calculated beam spread<sup>[158]</sup> for the estimated thickness of the lamella is about 7 nm. The spatial resolution can be estimated by the average value of the nominal beam diameter and the beam spread<sup>[158]</sup>. The experimental resolution is thus expected to have been on the order of around 10 nm. This allowed to locally obtain polarity information from small specimen regions of the SAG NCs.

In order to compare the CBED patterns of the NCs with the pattern of a reference sample with known polarity, first, the CBED pattern of the Ga-polar template was recorded. This allowed the identification of the  $(0002)$  and  $(000\bar{2})$  reflections in the diffraction pattern: (1) The convergence angle of the electron beam was determined by measuring the diameter of the CBED disks and the distance from the center of the direct beam (central disk) to the center of the  $(hki\bar{l})$  reflection<sup>[158]</sup> (see Section A.8). The convergence angle and known microscope parameters (see Table A.4) were then used to simulate CBED patterns for different GaN sample thicknesses with the JEMS software<sup>[160]</sup>. (2) The comparison of the experimental patterns from the template with the simulated patterns allowed to determine the relationship



of Ga- and N-polar orientations in the diffraction pattern (reciprocal space) with respect to the real space orientation, i.e. whether the  $(0002)$  reflection is oriented parallel or antiparallel to the normal vector of the template surface. (3) The polarity of the NCs was then determined according to the orientation of the CBED pattern from the NCs with respect to the pattern of the Ga-polar template. The NC is Ga-polar for  $(0002)_T \parallel (0002)_{NC}$  and N-polar for  $(0002)_T \parallel (000\bar{2})_{NC}$ . Subscripts T and NC denote template and NC, respectively. The results and the scheme (1 – 3) for the determination of the polarity is shown in Figure 7.14.

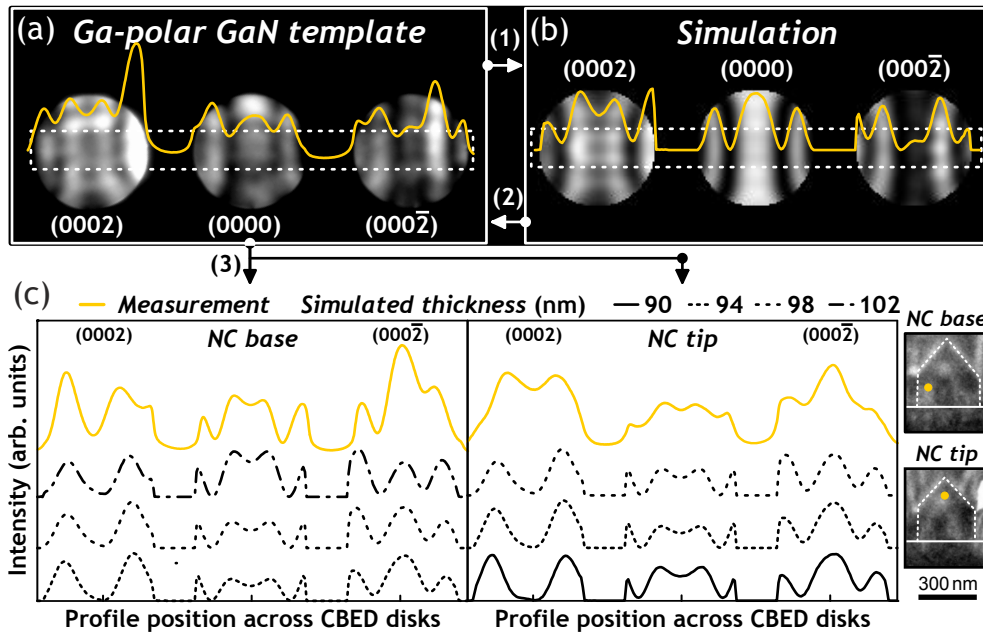


**Figure 7.14:** Experimental CBED pattern of the Ga-polar template (a) and a simulated pattern for a thickness of 130 nm (b), together with intensity profiles across the CBED disks. The profile width is indicated as dashed rectangles. The arrows indicate the flow diagram for NC polarity determination as described in the text. The zone axis was  $[1\bar{1}00]$ . Intensity profiles across the CBED disks for the NC base and tip region are shown in (c). TEM micrographs to the right show the regions from which the CBED patterns have been obtained. *Sample G1290*.

In the case of the NC base, the intensity profile across the CBED disks is in good agreement with a sample thickness of around 102 nm and Ga-polarity. In the case of the NC tip, in general all the recorded CBED disks appeared distorted. This is attributed to the fact that at the tip a semipolar AlN/GaN multi-quantum well (3 AlN barriers) was grown. TEM investigation of a reference lamella from the same sample revealed considerable densities of basal plane stacking faults for the tip region (see Figure 8.9). These defects introduce intensity contributions in the CBED disks, which are related to zinc blende GaN. Nevertheless, the experimental profile for the NC tip in Figure 7.14(c) can be qualitatively reproduced for a simulated sample thickness of around 100 nm and Ga-polarity. The thickness of the GaN

template at the investigated position was about 130 nm. Consequently, the lamella thickness increases going from the NCs to the template. This is consistent with the wedge shape of the TEM lamella which results from the FIB procedure.

The CBED measurements confirm Ga-polarity for the SAG NC base region and suggest identical polarity for the tip region.

#### 7.2.2.4 Discussion

In summary, KOH etching, aberration corrected HRTEM and CBED measurements have been applied to determine the polarity of homoepitaxial SAG GaN NCs grown by MBE. Consistently, Ga-polarity was concluded for the NC base and tip region for all techniques. In contrast, the polarity of self-induced nanocolumns was shown to be N-polar.

Considering homoepitaxial growth of GaN, the polarity of the epistucture is not influenced by N/Ga supply ratios during growth<sup>[170,171]</sup> and is thus conserved, if no particular procedure for polarity inversion is carried out. The inversion of Ga-polar GaN to N-polarity during growth requires e.g. Mg<sup>[172]</sup> or Si<sup>[173]</sup>  $\delta$ -doping.

The SAG NCs were homoepitaxially grown on the GaN template and the polarity of the NCs will thus be induced by the Ga-polar substrate. Obtaining Ga-polar SAG NCs on Ga-polar GaN template is therefore a direct consequence of the polarity of the substrate.

Due to the polycrystallinity of the  $\text{Mo}_x\text{N}_y$  layer which forms at the interface, no polarity information from the template can be transferred to the self-induced NCs. These conditions resemble the self-induced growth of N-polar NCs on  $\text{Si}_x\text{N}_y/\text{Si}(111)$ <sup>[138,140]</sup>, for which typically N-polarity is observed.

These results indicate, that the initial polarity conditions during MBE are the key to control the polarity of GaN NCs. At first glance, this might appear to be in contradiction with the conclusion of Ref.<sup>[139]</sup>, that growth of Ga-polar GaN NCs by MBE is not possible. However, it has to be noted, that another key element is the selectivity mechanism during growth. Combination of both approaches allows for the growth of Ga-polar NCs on Ga-polar template. In the case of initial N-polarity<sup>[145]</sup>, as well as for the case that no restriction on the initial polarity exists, a N-polar NC is favored. This demonstrates, that the initial polarity before growth is certainly a control parameter, however, not the fundamental physical property which dictates the polarity of GaN NCs. [Section 7.3](#) will pick up this discussion in the framework of equilibrium thermodynamics.



### 7.2.2.5 Controlling the polarity of SAG GaN NCs

Besides the position-controlled selective area growth of GaN NCs on GaN template, also the SAG of GaN NCs on silicon carbide SiC(0001) substrate<sup>13</sup> was achieved. The cleaning procedure of the substrates, the patterning of the SAG arrays by e-beam lithography, and the growth conditions were similar to the approaches which were used for the GaN templates. The native oxide at the surface of the SiC substrate was removed prior to growth (see Section A.1). Analogous to Section 7.2.2.1, the NCs were etched by KOH to determine the polarity (saturated solution of KOH; etch duration 7.5 min; room temperature). An array of SAG GaN NCs on SiC is exemplarily shown in Figure 7.15, together with the results of the polarity determination.

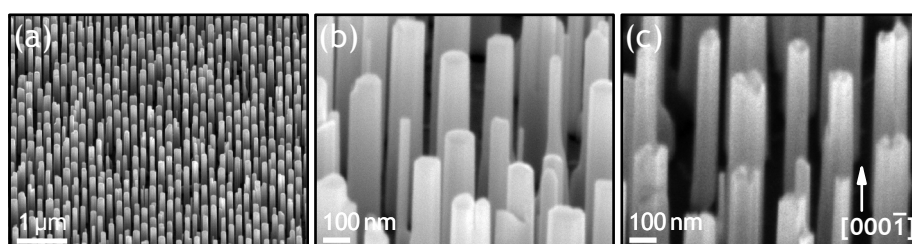


**Figure 7.15:** (a, b) Bird's eye view SEM micrographs of SAG GaN NCs on SiC(0001). The regular arrangement of the NCs on a large scale is shown in (a). The morphology of the tips of the NCs before and after KOH treatment (7.5 min) is shown in (b) and (c), respectively. *Samples G1237* (a) and *G1236* (b, c). The growth temperatures were 800 and 820 °C for (a) and (b, c), respectively. Apart from that, standard SAG conditions were used. Aperture diameter and pitch are 100 and 250 nm, respectively.

In Figure 7.15(b), distinct differences to the SAG GaN NCs on GaN template can be observed: First, no semipolar facets have been formed at the tip of the NCs, but mainly *c*-plane tips. Second, the maximal diameter of the nanocolumns was limited to about 100 nm. For apertures of this diameter, the growth of a single NC per aperture was observed. For the next larger investigated aperture diameter of 250 nm, multiple NCs with diameters of about 100 nm or below have been grown within a single aperture. According to the previous sections, from a morphological point of view, these results indicate N-polarity. In fact, this was confirmed by KOH etching, as shown in Figure 7.15(c). In agreement with the previous results, the *c*-plane tips were etched, which confirms N-polarity of the SAG GaN NCs on SiC(0001). In the case of GaN layers, which are grown heteroepitaxially on Si-polar SiC(0001) substrates by MBE, typically Ga-polar layers are obtained<sup>[174]</sup>. This is attributed to the stronger bonds of Si–N, as compared to Si–Ga<sup>[175]</sup>. The fact, that N-polar GaN NCs were grown on the Si-polar SiC substrates

13 340 μm thick chemical mechanical polished 6H-SiC(0001) substrates from PAM-XIAMEN with a micropipe density of 3 cm<sup>-2</sup> and a Si-face surface roughness *rms* of 0.2 nm.

is attributed to the atomic surface configuration of the SiC substrate at the initial stage of growth, the exact mechanism however remained unknown.

To investigate the possibility of polarity inversion of GaN NCs by modifying the atomic surface configuration of the SiC substrate, some monolayers (MLs) liquid Ga were predeposited prior to growth, and especially prior to ignition of the N plasma source: Before igniting the plasma source at growth temperature,  $\sim 6.5$  MLs Ga were predeposited. During the ignition of the plasma source (shutters closed), again  $\sim 6.5$  MLs Ga were deposited, to compensate Ga desorption. Afterwards, the sample was nitridated for 2 min using the standard nitrogen flux. Then, the Ga shutter was additionally opened. The impact on the morphology of the nanocolumns was striking: Mainly pyramidal GaN nanostructures were grown within the apertures. At the same growth temperature without Ga predeposition, NCs with *c*-plane tips and a significantly larger axial growth rate have been grown (*Sample G1240*, not shown). After the KOH treatment, only the base region of the nanostructures was partly etched<sup>14</sup>, similar to the Ga-polar case which was presented in [Figure 7.11](#). The etching behavior, the morphology of the nanocolumns, and the reduced growth rate are consistent with polarity inversion from N-polarity to Ga-polarity. The results are presented in [Figure 7.16](#). Note, that similar to these results, the trend of a reduced growth rate of Ga-polar MBE-grown GaN layers as compared to their N-polar counterparts was observed in Ref.<sup>[176]</sup>.

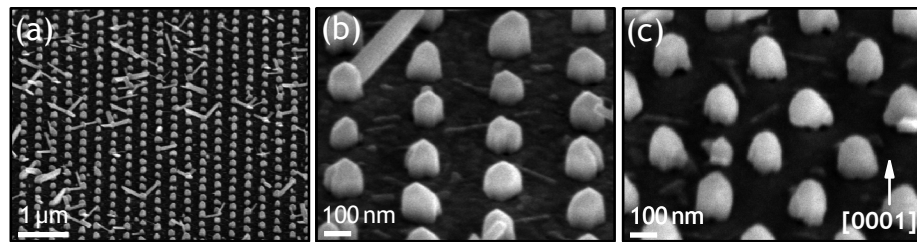


**Figure 7.16:** (a, b) Bird's eye view SEM micrographs of SAG GaN NCs on SiC(0001) substrate after Ga predeposition (see text). The regular arrangement of the NCs on a large scale is shown in (a). The morphology of the tips of the NCs before and after KOH treatment (7.5 min) is shown in (b) and (c), respectively. The substrate temperature was 829 °C. Apart from that, standard SAG conditions were used. Aperture diameter and pitch are 100 and 250 nm, respectively. *Sample G1239*.

Accordingly, it is expected that the Ga predeposition resulted in a Ga-polar surface, which promoted the growth of Ga-polar GaN NCs. The binding energy of C–Ga was calculated to be larger as compared to Si–Ga<sup>[175]</sup>, and therefore, the interchange of Ga and Si is expected to have occurred at the surface, which resulted in the preparation of a Ga terminated, Ga-

<sup>14</sup> Note, that after additional KOH treatment for 7.5 min, the NCs have been almost completely etched from the NC base towards the tip (not shown).

polar surface of the SiC substrate. The polarity of the NCs was therefore predefined and the selective area growth resulted in Ga-polar GaN NCs.

This experiment confirms that the initial polarity conditions during MBE are the key to control the polarity of GaN NCs. The next section will address the distinct morphology of Ga- and N-polar NCs in the framework of equilibrium thermodynamics.

### 7.3 THERMODYNAMIC DESCRIPTION

If kinetic processes during crystal growth become important, the equilibrium surface structure is certainly a useful starting point<sup>[56]</sup>. This becomes clear, if one has a look at smooth GaN(0001) layers which are grown under slightly Ga-rich conditions. The growth rates of such layers are directly determined by the incoming fluxes and thus described in a kinetic framework. The experimentally observed atomic surface structure (laterally contracted Ga bilayer) however, is derived from calculations in the framework of thermodynamics<sup>[70]</sup>.

In general, high growth temperatures and low growth rates will bring the system closer to thermodynamic equilibrium<sup>[56]</sup>. As shown in [Section 6.3](#), the growth of SAG GaN NCs takes place close to the decomposition temperature of GaN. In addition, [Section 7.1.1](#) and [7.1.2](#) proved that the NC axial growth rates (although enhanced by Ga diffusion) are considerably smaller (in the range of  $2 \text{ nm min}^{-1}$  in *regime II*) as compared to smooth GaN(0001) layers (about  $4 \text{ nm min}^{-1}$ ). These arguments motivate the discussion of the characteristic morphologies which are observed for Ga- and N-polar NCs (pyramidal and flat tips, respectively) in a thermodynamic picture.

In thermodynamic equilibrium, the shape of a crystal will be given by the configuration which minimizes the total surface energy, while conserving the volume. This means, that in principle one should calculate the surface energies for various GaN surfaces and compare them quantitatively. However, the fact that for the typically used approach<sup>[57]</sup>, absolute surface energies can only be obtained for *a*- and *m*-plane GaN complicates matters. Furthermore, for comparison of the calculations with experiment, the MBE growth conditions have to be expressed as the difference of the Ga chemical potentials (see [Section 3.2.2](#)). This is especially difficult due to the deviations from the nominal supply, which are caused by the contribution of Ga diffusion. Nevertheless, it is worth to mention, that recently an *ab initio* approach was developed, which allows to study reconstruction, adsorption, and incorporation mechanisms on GaN surfaces as function of growth parameters, such as substrate temperature or Ga beam equivalent pressure<sup>[177]</sup>.

Since the surface energy is equal as a first approximation to the sum of energies of the broken bonds per unit area<sup>[51]</sup>, in the following approach a simple broken bond model will be used: The GaN crystal is cut at some arbitrary plane and the broken bond density  $\sigma_{\text{bb}}$  for the two created surfaces

can be easily calculated. Then, these densities will be compared to estimate which GaN surfaces are expected to be energetically more favorable. The specific chemical environment, surface reconstructions or edge effects were not taken into account. However, the surface termination of the outermost surface atoms depends here on the exact cleavage position as exemplarily shown in Figure 7.17.

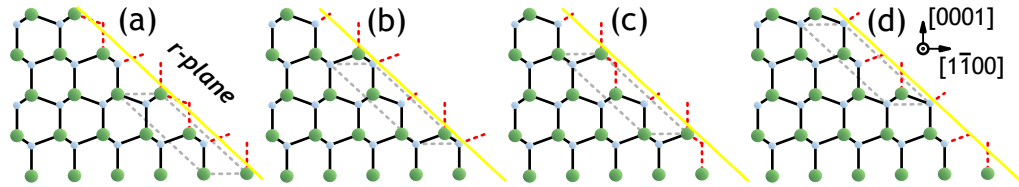


**Figure 7.17:** Ball-and-stick model of cleaved  $r$ -surfaces of Ga-polar GaN. Big and small spheres denote Ga and N atoms, respectively. Dashed red lines at the surface indicate broken bonds, the dashed parallelograms indicate in-plane  $(11\bar{2}0)$  unit cells.

As discussed in Section 3.2.2, in general, cation adatom stabilized semipolar surface reconstructions are favored for a wide range of growth conditions. To reflect this trend in the broken bond model, semipolar surface configurations with maximal Ga coverage were considered. Furthermore, the opposite extreme of maximal N coverage was considered, to take into account possible stabilization of such surfaces due to the N-rich growth conditions. In addition, the overall lowest broken bond densities (arbitrary surface termination) have been evaluated. It is worth mentioning, that the exact surface configuration is not influencing the conclusion which was drawn from the broken bond model. For sake of completeness however, the different cases are presented. Note furthermore, that the broken bond density of a (semi)polar surface with maximal Ga coverage and Ga-polarity is identical to the N-polar counterpart with maximal N coverage of the surface. In contrast, the polar GaN surfaces are expected to show kinetically stabilized N adatom surface reconstructions under N-rich growth conditions<sup>[67]</sup>. Therefore, for the GaN(0001) and GaN(000 $\bar{1}$ ) surfaces, kinetic stabilization of N termination was assumed for the model due to the nominally N-rich SAG conditions. Furthermore, the broken bond densities of the nonpolar surfaces have been calculated. These are always stoichiometric. Figure 7.18 shows the broken bond densities of various surfaces for Ga- and N-polar GaN.

For the nonpolar  $m$ - and  $a$ -surfaces,  $\sigma_{bb}$  is independent on the polarity. As explained, this is not the case for the semipolar and polar surfaces. The  $m$ - and  $a$ -surfaces have the lowest broken bond densities with only small differences. Taking into account the bond energy of 2.17 eV per bond in GaN<sup>[59]</sup>, the broken bond densities translate to surface energies of around 131 and 151 meV  $\text{\AA}^{-2}$  for  $(1\bar{1}00)$  and  $(11\bar{2}0)$ , respectively. The trend of the absolute values is consistent with the calculated surface energies of the stoichiometric nonpolar surfaces<sup>[59]</sup>.

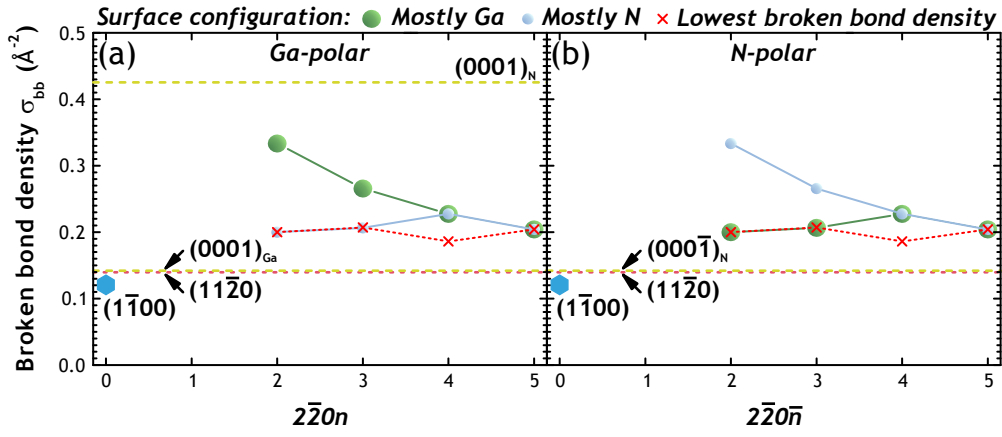


**Figure 7.18:** Calculated broken bond densities of various GaN surfaces. The N terminated polar surfaces (subscript N) are shown for the Ga-polar and N-polar case in (a) and (b), respectively. The Ga terminated (subscript Ga) GaN(0001) surface is shown only for Ga-polarity. The values for the stoichiometric  $m$ - and  $a$ -surfaces are valid for both plots.

For *Ga-polar* GaN, the broken bond densities of the semipolar surfaces are larger by factors in the range of 1.5 to 2.4 as compared to the nonpolar surfaces, depending on the exact surface which is considered and its termination. The broken bond density of the N terminated GaN(0001) surface is the largest one,  $\sigma_{bb}^{c, N \text{ terminated}} = 0.425 \text{ \AA}^{-2}$ . Thus, one finds

$$\sigma_{bb}^m \lesssim \sigma_{bb}^a < \sigma_{bb}^{\text{semipolar}} < \sigma_{bb}^{c, N \text{ terminated}}. \quad (7.6)$$

For *N-polar* GaN, the N terminated (0001 $\bar{1}$ ) surface has a broken bond density almost equal to that of the  $a$ -surface. For the semipolar surfaces, the broken bond densities of Ga and N termination are reversed as compared to the Ga-polar case. Therefore the broken bond densities follow the relation:

$$\sigma_{bb}^m \lesssim \sigma_{bb}^a \approx \sigma_{bb}^{c, N \text{ terminated}} < \sigma_{bb}^{\text{semipolar}}. \quad (7.7)$$

In the following, a possible explanation for the observed NC morphologies under N-rich growth conditions will be discussed. For a growth direction parallel to [0001] (Ga-polar), the NC sidewalls will be stabilized by  $m$ - and  $a$ -surfaces with the lowest values of  $\sigma_{bb}$ . The broken bond density of the semipolar planes  $\sigma_{bb}^{\text{semipolar}} < \sigma_{bb}^{c, N \text{ terminated}}$ , and therefore, the crystal tends to form the semipolar surfaces at the top, which are then terminated at the sidewalls. As described in [Section 7.2.2](#), this morphology was experimentally observed for the Ga-polar SAG NCs. Note, that especially for the surface configuration which corresponds to the lowest broken bond density, the appearance of  $r$ -plane surfaces is predicted. These surfaces were typically observed at the tip of the SAG NCs (see [Section 7.2.1](#)).

Discussing the N-polar case requires the assumption that the growth direction of N-polar GaN NCs is [0001 $\bar{1}$ ]. This is not straight forward, since N-polar NCs are not only observed for epitaxial growth on N-polar substrates,

but also for self-induced growth on polycrystalline substrates—the Mo layer in this case—for which no epitaxial relation is given. Without this assumption, the growth of the NCs could proceed either in  $a$ - or in  $\bar{c}$ -direction due to the very similar broken bond densities of the corresponding surfaces, according to Figure 7.18(b). The formation of semipolar surfaces can be excluded here due to their large broken bond densities as compared with the  $a$ -,  $m$ - and N terminated  $\bar{c}$ -surfaces. Therefore, the crystal will form the nonpolar sidewalls and the polar surface at the tip of the NC. Accordingly, this morphology was experimentally observed for N-polar GaN NCs (see Section 7.2.2).

If the two polarities are compared among each other, the N terminated GaN(000 $\bar{1}$ ) surface is expected to be energetically favored as compared to the Ga-polar semipolar surfaces, as well as compared to the N terminated GaN(0001) surface. Accordingly, if no restriction to the polarity exists—such as for polycrystalline or amorphous thin layers on which self-induced NCs grow—and growth proceeds along  $\langle 0001 \rangle$ , the system will adopt N-polarity in the framework of equilibrium thermodynamics to minimize the total number of broken bonds. In fact, for self-induced GaN NCs on thin amorphous silicon nitride layers, typically N-polarity is observed<sup>[138,140]</sup>.

Interestingly, paying attention to rather untypical growth conditions for GaN NCs, the broken bond model predicts changes in the morphology of the nanocolumns: For Ga-rich growth conditions, the stabilization of Ga terminated GaN surfaces is expected. In the broken bond model, the broken bond density of N terminated N-polar GaN and Ga terminated Ga-polar GaN are identical. Therefore, the ordering of the densities for the Ga terminated Ga-polar case of Figure 7.18(a) changes to:

$$\sigma_{bb}^m \lesssim \sigma_{bb}^a \approx \sigma_{bb}^{c, \text{Ga terminated}} < \sigma_{bb}^{\text{semipolar}}. \quad (7.8)$$

The model thus suggests, that the morphology of the NC tip of Ga-polar NCs which are grown under Ga-rich conditions is equivalent to the  $c$ -plane tip morphology of N-polar NCs grown under N-rich conditions. In fact, such a behavior was presumably observed in Refs.<sup>[11,125]</sup>. The polarity of the NCs was not reported, however, similar to this thesis, the authors used GaN(0001) templates from LUMILOG. Consequently, it is assumed, that the polarity of the SAG GaN NCs from the literature references was Ga-polar. The authors observed a change of the morphology of the NC tips, from semipolar to  $c$ -plane, if the growth was carried out under presumably locally Ga-rich conditions.

Repeating the analogous discussion for N-polar NCs grown under Ga-rich conditions, the model suggests the stabilization of semipolar facets at the tip of the NCs, instead of  $c$ -plane. Unfortunately, up to my best knowledge, experiments on the growth of N-polar NCs under such conditions have not been reported so far. However, the applicability of this model is not restricted to NCs, but can be used for GaN layers as well. In fact, in Ref.<sup>[178]</sup> the growth of a rough (pyramidal surface morphology) N-polar GaN(0001)



layer on sapphire grown under Ga-rich conditions by MBE was reported, while the Ga-polar GaN(0001) layer which was grown under the same growth conditions showed a smooth  $c$ -plane surface.

The selective area growth of GaN NCs on N-polar and Ga-polar GaN templates under Ga-rich conditions may verify these predictions.

To further examine the description of the morphology of the NCs in a thermodynamics framework, the ratio of the average segment lengths of  $m$ - and  $a$ -plane sidewalls per NC in  $[0001]$  projection was evaluated by SEM. This analysis was performed for several NCs with different diameters in the range of  $1\ \mu\text{m}$  to 200 nm and is exemplarily shown in Figure 7.19. The expected ratio of  $m$ - and  $a$ -plane segment lengths for GaN crystals with equilibrium shape can be determined by the Wulff construction. Neglecting surface reconstructions and energy contributions due to edges, the theoretical value is 1.8 (see Section 3.2.2).

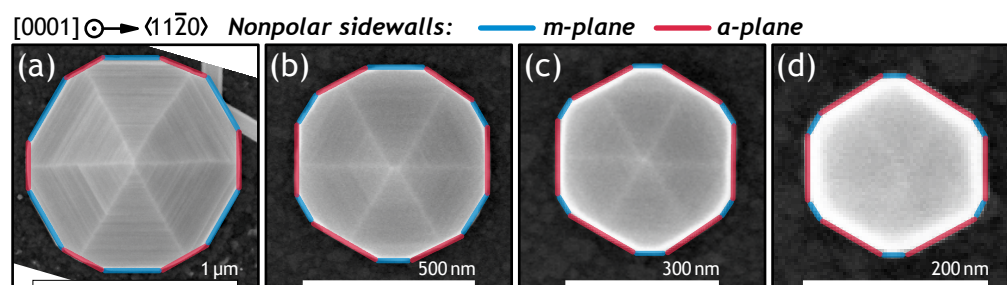


**Figure 7.19:** SEM top-view micrographs of SAG GaN NCs with smooth segments of  $m$ - and  $a$ -plane sidewalls. The average  $m$ - to  $a$ -plane segment length ratios are  $2.2 \pm 0.4$  (a),  $0.5 \pm 0.2$  (b),  $0.4 \pm 0.1$  (c), and  $0.3 \pm 0.2$  (d). The samples were grown under standard SAG conditions, for (a), a growth time of 4 h was used. *Samples G1306* (a) and *G1253* (b – d).

For the NCs with the largest diameter (about  $1\ \mu\text{m}$ ), from the experiment an average ratio of  $2.2 \pm 0.4$  (error given by standard deviations and Gaussian error propagation) was obtained. For NCs with smaller diameter ( $< 600\ \text{nm}$ ), however, a significant decrease of this ratio is observed, which is as low as  $0.3 \pm 0.2$  for the NCs with diameter of about 200 nm. For these NCs, the formation of  $a$ -plane sidewalls is strongly favored as compared to  $m$ -plane sidewalls.

Due to the significant deviation from the equilibrium ratio of  $m$ - and  $a$ -plane segment length for NCs with diameters smaller than 600 nm, it is concluded that the NC sidewall configuration is not related to equilibrium crystal shape as derived by the Wulff construction. Nevertheless, it is worth to note, that this construction only considers surface energies; edge energies, which may become important for crystallites with small diameter<sup>[179]</sup>, are neglected. This suggests, that one actually expects deviations from the equilibrium shape which is derived from the Wulff construction, once the

structures become small enough that edge energies must be taken into account. The magnitude of these deviations is however unknown due to the absence of estimations for purely  $a$ -plane, purely  $m$ -plane, and  $a$ -/ $m$ -plane edge energies. For columns with diameters around  $1\ \mu\text{m}$ , it is not clear, whether the ratio of  $m$ - and  $a$ -plane in the range of the expected equilibrium value is due to an increase of the structure size, such that these edge energies can be neglected for equilibrium shape considerations. If one rather assumes that the sidewall configuration for NCs grown under SAG conditions is related to kinetics, the surface configuration will change with growth time due to different growth rates of the  $m$ - and  $a$ -surface. Thus, the evaluation of the segment lengths may have been performed at such time, that the sidewall configuration accidentally resembled the equilibrium configuration, although it is dictated by kinetics. As discussed, the equilibrium shape is independent of growth time.

### *Discussion*

The importance of adatom kinetics for the growth of GaN NCs by MBE was already discussed and experimentally verified in [Chapter 4](#) and [Section 7.1](#), respectively. This section on the other hand, discussed the morphology of Ga-polar SAG GaN NCs with semipolar faceted tips in the framework of equilibrium thermodynamics. In addition, the morphology of N-polar SI and SAG NCs was of debate. Particularly, for the tip of the NCs, a consistent picture was obtained, which suggests that surface energies, i.e. surface thermodynamics, govern the shape of the tip of GaN NCs grown by MBE. Note however, that this description explicitly included the kinetic stabilization of N terminated GaN(0001) and GaN(000 $\bar{1}$ ) surfaces due to the nominally N-rich growth conditions.

Interestingly, the distinct morphology of the tip of Ga- and N-polar NCs resembles the morphology of bulk GaN platelets which have been grown from a solution of atomic nitrogen in liquid gallium under high nitrogen pressures of up to 20 kbar (HPS, see [Section 2.2](#))<sup>[180]</sup>. These crystals have been grown at temperatures of around  $1/2$  to  $2/3$  of the melting temperature of GaN. Revisiting [Figure 2.7\(a\)](#), it becomes clear that the growth of such platelets is likely to proceed close to thermodynamic equilibrium. For these platelets, the N-polar growth front was reported to show a very smooth  $c$ -plane surface morphology, while the Ga-polar side was rough with the presence of pyramids (semipolar surfaces). The morphology of these bulk GaN platelets is in agreement with the morphology of the GaN NCs grown by MBE. Consequently, it is suggested that the growth of SAG (and SI) GaN NCs by MBE is not exclusively related to kinetics, but rather to a concurrent interplay of thermodynamics and kinetics. In fact, the nucleation stage of SI NCs has already been discussed to be rather related to thermodynamics,



than to kinetics<sup>[90]</sup>. In addition, the conclusion that surface thermodynamics, rather than anisotropic adatom kinetics have to be considered for the understanding of the large aspect ratio of SI NCs (which show exclusively  $m$ -plane sidewalls)<sup>[80]</sup> corroborates this conclusion.

The sidewall configuration of these SAG NCs however revealed significant deviations from the expected crystal equilibrium shape.

In order to understand whether the sidewall configuration of SAG GaN NCs is dominated to larger extends by kinetics or thermodynamic equilibrium, following experiments and estimations are suggested to be performed: From experimental side, the ratio of  $m$ - and  $a$ -surfaces has to be evaluated for various growth times and various NC diameters. The difficulty in appropriate experimental realization is the fact that local growth conditions over the NC sidewalls are not allowed to vary for the different samples. Firstly, this implies that growth conditions have to be reproducible with high accuracy, and secondly, the growth has to proceed in *regime II*, such that Ga diffusion from the substrate has no effect on the local growth conditions at the NC sidewalls (at least for the region of the NC, which is separated from the substrate by more than the diffusion length  $\lambda_f$ ). Changes of the configuration of the NC sidewalls as function of growth duration (for NCs with comparable diameter) are related to kinetics. Variation of the NC diameter may shed some light on the relevance of edge energy contributions. Theoretical calculations on the magnitude of these energies can be used to refine the Wulff construction including edge configurations. The equilibrium crystal shape will then be related to minimization of the sum of total surface energy and total edge energy, while conserving the volume of the crystallite.



---

## STRUCTURAL PROPERTIES OF SAG GAN NANOCOLUMNS

---

*This chapter will discuss the structural properties of selectively grown GaN nanocolumns. In the first section, dislocations and extended defects in selectively grown GaN nanocolumns are investigated by transmission electron microscopy. The second section presents investigations on the crystal quality by means of Raman spectroscopy. In the last section, the growth of semipolar AlN/GaN heterostructures at the tip of the nanocolumns is investigated by transmission electron microscopy.*

### 8.1 DISLOCATIONS AND EXTENDED DEFECTS

This section will focus on the structural imperfections of SAG GaN NCs. First, threading dislocations (TDs) will be investigated by transmission electron microscopy (TEM). In the second part, possible correlations of extended defects and the morphology of the NCs will be discussed. The identification of extended defects according to their optical emission characteristics will be performed in [Chapter 9](#).

#### 8.1.1 Threading dislocations

Thin GaN nanocolumns are considered as candidates for the growth of defect-free GaN due to their large aspect ratio and small contact area to the substrate<sup>[12,86]</sup>. Typically, the Ga-polar SAG NCs have a larger diameter than self-induced NCs and it is questionable whether these arguments also apply in the SAG case. In the following, the behavior of threading dislocations in SAG NCs will be discussed and conclusions concerning the growth of SAG GaN NCs free of any threading dislocations will be drawn.

In general, for arbitrary TEM imaging conditions, most of the dislocations present in crystals are observed. If however specific excitation conditions<sup>1</sup> are chosen, these defects may become invisible. TEM invisibility criteria for dislocations are given in Section A.8. For the following analysis, the  $[11\bar{2}0]$  zone axis without the selection of a specific diffraction vector was used. Therefore, all dislocations possible to image in this geometry are visible. Figure 8.1 shows TEM micrographs of SAG GaN NCs with diameters of about 200 and 600 nm.

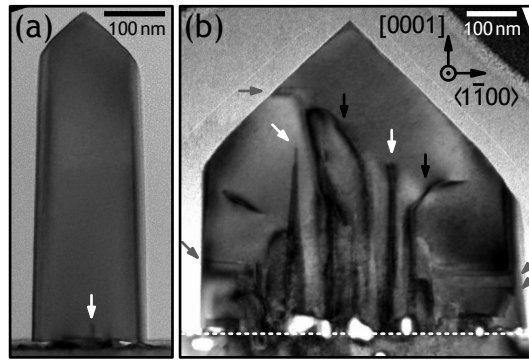


**Figure 8.1:** TEM micrographs of SAG NCs with diameters around 200 (a) and 600 nm (b) in  $[11\bar{2}0]$  geometry. The dashed line marks the interface in (b). White and black arrows denote bending of TDs towards  $\langle 11\bar{2}0 \rangle$  and  $\langle 1\bar{1}00 \rangle$ , respectively (see text). Gray arrows denote basal plane stacking faults which do not extend through the entire NC. Samples G1253 (a) and G1267 (b).

For both type of NCs, one or more threading<sup>2</sup> dislocations are introduced in the vicinity of the interface to the GaN template. It is stressed, that these are not due to propagating dislocations which originate from the GaN template. Due to the limited number of investigated NCs, the density of the TDs was not measured quantitatively. However, from qualitative comparison, it is obvious that the density of the TDs is higher for the NC with diameter around 600 nm as compared to the NC with diameter of about 200 nm. This behavior was observed for all investigated NCs for the discussed range of diameter.

The homoepitaxial growth is expected to proceed without the introduction of misfit dislocations at the interface. It is therefore concluded, that the formation of these TDs is due to the coalescence of GaN nuclei in the beginning of growth, as discussed in Section 7.1.2. In addition, basal plane stacking faults may be introduced during coalescence. In general, basal plane stacking faults in the vicinity of the GaN template interface were only observed in the case of the thicker NCs, as shown in Figure 8.1(b). Smooth (layer-by-layer) and rough (islands) GaN layers are grown on GaN template

1 Centering an aperture around a spot in the diffraction pattern selects the corresponding diffraction vector  $\mathbf{g}$ .

2 Misfit dislocations are not expected to be introduced due to the homoepitaxial growth.

under slightly Ga-rich and N-rich conditions, respectively. The different defect densities at the interface therefore support the conclusion, that NCs with smaller diameters are grown in *regime I* under a locally more Ga-rich environment as compared to NCs with larger diameters (see Section 7.1.3). For the sake of completeness, it has to be noted, that the different techniques for SAG array patterning (electron beam lithography for Figure 8.1(a) and pulsed laser ablation for (b)) yield different surface morphologies of the GaN template within the apertures. In the case of pulsed laser ablation, the surface of the GaN template is not as smooth as compared to electron beam lithography patterning (AFM measurements not shown). Therefore, independent of the NC diameter, in general, a higher density of TDs is expected for NCs which are grown in SAG arrays patterned by pulsed laser ablation as compared to arrays patterned by electron beam lithography.

Further inspection of Figure 8.1 shows that for the thinner NC, the TD appears to be terminated after propagation along the  $c$ -axis of less than 50 nm. For the thicker NC, the length of propagation along  $[0001]$  until the TDs appear to be terminated, is significantly longer. Furthermore, bending of TDs towards  $[1\bar{1}00]$  is observed. Since a termination of an isolated TD inside any crystal is not possible<sup>[181]</sup>, termination of TDs along  $[0001]$  is interpreted as bending towards  $[11\bar{2}0]$ , and subsequent termination at the surface of the NC<sup>[23]</sup>.

Not endeavoring to discuss the mechanism for bending of TDs, it is nevertheless fruitful to have a closer look at the behavior of TDs in SAG GaN NCs, since the prospect of growing defect-free GaN is tempting.

Hersee *et al.* studied the behavior of TDs in GaN NCs grown by MOCVD on GaN template. The vertical  $[0001]$  length of the TDs was investigated as function of (projected) radial distance of the TD from the nanocolumn sidewalls. The authors observed, that the vertical length of the TDs increased for increasing distance from the NC sidewalls<sup>[23]</sup>. The schematic description and the reported data is shown in Figure 8.2.

Following this approach, the TD  $[0001]$  length  $l_{TD}$  in the SAG NCs was evaluated from TEM analysis: When bending of TDs towards  $[1\bar{1}00]$  and termination at the NC sidewalls occurred, the  $[0001]$  length of the threading dislocation was measured. Furthermore, the (projected) radial distance of the TD from the NC sidewalls was measured. For bending of TDs towards  $[11\bar{2}0]$  (in view direction), the projected radial distance along  $[11\bar{2}0]$  cannot be measured and these TDs have been neglected<sup>3</sup>. Note, that due to the cross sectional slice geometry of the lamellae and TEM being a projection technique, the exact errors for dislocation length and radial distance from the NC sidewalls are difficult to determine. Since the lamellae have been

3 In first approximation, it is expected that bending always occurs towards the facet in closest proximity.

prepared for HRTEM analysis, for which the thickness of the specimens is typically only a few nanometers, both error values were estimated to be 10 nm. Furthermore, if reaction of dislocations which originated at different radial positions and subsequent bending occurred, an average value for the radial position was chosen. In this case, the corresponding error was calculated according to Gaussian error propagation. Several NCs with different diameters from different samples were investigated. In all cases, standard SAG conditions were used. The results are shown in Figure 8.2(b).

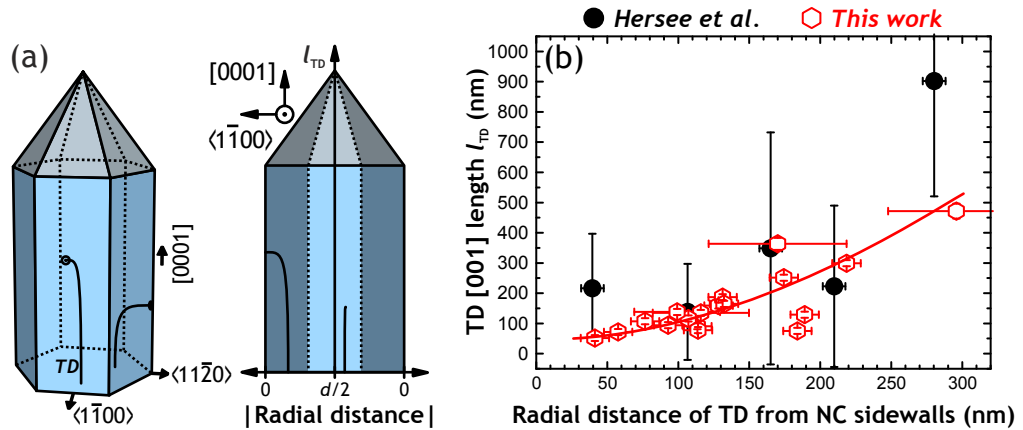


**Figure 8.2:** (a) Schematic of bending of TDs towards  $[11\bar{2}0]$  and  $[1\bar{1}00]$  in dimensional and projected view as observed in TEM. The vertical TD  $[0001]$  length as function of (projected) radial distance from the NC sidewalls is shown in (b). Solid data was taken from Ref.<sup>[23]</sup>. The solid line guides the eye along the data of this thesis. *Samples G1225, G1253, and G1267.*

The trend which was observed by Hersee *et al.* is confirmed: The results indicate, that bending of TDs occurs more easily, the closer the TD is located to a NC sidewall. It has to be noted, that bending of TDs will only occur if the NC height exceeds a critical value. The lower limit for this critical value is the  $[0001]$  length of the dislocation.

Regardless of the relevant mechanism for bending of TDs to occur, important conclusions concerning the growth of SAG GaN NCs free of any threading dislocations can be drawn. Since the incorporation of TDs occurs at the interface to the template, a GaN NC which contains TDs will grow free of any further, once these are annihilated at the NC surface. Taking into account that the NCs are never perfectly symmetric and furthermore assuming, that the TDs are not stabilized within the NCs due to a perfectly centered position<sup>[182]</sup>, the critical height  $h_c$ , for which all TDs should be eliminated, can be estimated as function of NC diameter: For NCs with diameters around 150 to 300 nm, one obtains  $h_c \sim 100 - 200$  nm. In the case of NCs with diameters around 600 nm, bending of a centered TD is expected to occur at  $h_c \sim 500$  nm.

The presented data of [Figure 8.2\(b\)](#) can thus be used as orientation for the necessary NC height as function of diameter in order to obtain SAG GaN NCs free of any TDs in the upper region of the NCs.

### *Discussion*

Bending of TDs and annihilation at the NC sidewalls can reduce the TD density in the upper part of the SAG GaN NCs virtually to zero. This enables the growth of GaN free of any threading dislocations. Since the critical height is smaller for thinner NCs as compared to thicker ones, the growth durations in the latter case have to be significantly longer to reach this specific NC height. In the case of NCs with diameters around 150 to 300 nm, a growth duration of about 1 h under standard SAG conditions is sufficient to overcome the estimated critical NC height. For NCs with diameters around 600 nm, the typically used growth durations of about 3 h are necessary. With the aim of growing semipolar GaN-based heterostructures, such growth durations are furthermore required to ensure complete coalescence of the NC tip, in order to maximize the semipolar GaN surface area (see [Figure 7.5](#) and [7.10](#)). Such structures will be discussed in [Section 8.3](#).

#### 8.1.2 *Extended defects*

To investigate extended defects, such as basal plane stacking faults (BSFs) and cubic inclusions, TEM analysis in  $[11\bar{2}0]$  zone axis geometry was performed. For this imaging condition, all BSF types are visible. Note, that for the other commonly used geometry  $[1\bar{1}00]$ , all types will be invisible. Again, excitation of specific diffraction vectors can be used to enhance or diminish defect-related contrast. Thus, dark field images selecting  $\mathbf{g} = (1\bar{1}00)$  (and  $\mathbf{g} = (0002)$ , not shown<sup>4</sup>) have been recorded to enhance the visibility of the BSFs. Note, that the extrinsic type and the theoretically predicted BSF of type  $I_3$  will become invisible under such conditions. For convenience, the reader is referred to [Section A.8](#) which summarizes invisibility criteria for BSFs in TEM.

The SAG NCs could be classified into three categories. [Figure 8.3](#) summarizes the results for SAG NCs with diameters of around 200 nm.

The NCs can be classified<sup>5</sup> according to their density of BSFs into:

1. *defect-free* ([Figure 8.3\(a\)](#)),
2. *low defect density* ([Figure 8.3\(b\)](#)), and
3. *high defect density* ([Figure 8.3\(c\)](#)).

<sup>4</sup> In agreement with the invisibility criteria for BSFs, no contrast related to extended defects was observed for this imaging condition.

<sup>5</sup> This classification neglects any defects other than BSFs.

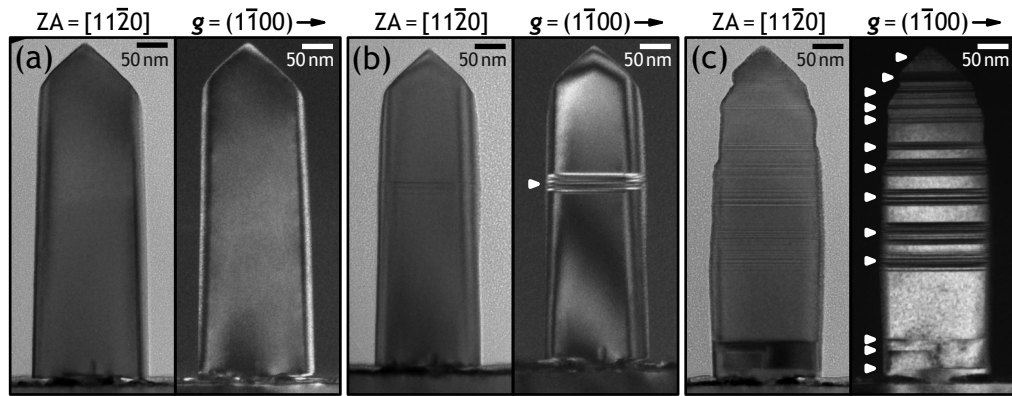


**Figure 8.3:** TEM micrographs of SAG GaN NCs in  $[11\bar{2}0]$  zone axis (ZA) geometry. White arrows in the dark field images denote BSFs. The NCs were grown under standard SAG conditions, the pitch is  $0.5\ \mu\text{m}$ . The lamella was prepared by focused ion beam. *Sample G1253*.

The defect-free NC shows smooth sidewalls. Despite a monotonous decrease of the diameter towards the tip, no modulation of the diameter is observed. In the case of the low defect density NC, a similar behavior is observed, however, a slight increase in diameter is observed in the vicinity of the BSFs. For the high defect density NC—which shows agglomeration of BSFs—, significant changes in diameter are found in the vicinity of the BSFs. The NC shows an asymmetric shape and deviations from the typically observed semipolar  $r$ -surfaces are observed.

Small variations in diameter can be simply explained considering the atomic structure of extended BSFs, which actually require changes of the diameter of the NC on an atomic scale (see [Figure 2.2](#)). Since the nonpolar surfaces are not expected to be perfectly atomically flat, BSFs can cause diameter variations on the nanoscale. To gain insight into the variation of the inclination of the facets, the tip of the high defect density NC was further analyzed. [Figure 8.4](#) shows an overview micrograph and a higher magnification from a region, where a change of facet inclination was observed. Fast Fourier transforms (FFTs) were recorded for regions with different surface inclination.

Analyzing the FFT of the region, where an inclination in agreement with  $r$ -plane GaN is observed, shows as expected wurtzite crystal structure. For the region with a surface inclination of about  $56^\circ$ , the FFT corresponds to zinc blende GaN. The change of inclination can be easily explained, comparing the two different crystal structures. The projected wurtzite and zinc blende structure according to the TEM view direction is shown in [Figure 8.5](#).

Considering low-indexed zinc blende crystallographic planes, a theoretical inclination of  $54.7^\circ$  with respect to the wurtzite basal plane is expected for GaN(001). This value is in agreement with the experimentally observed



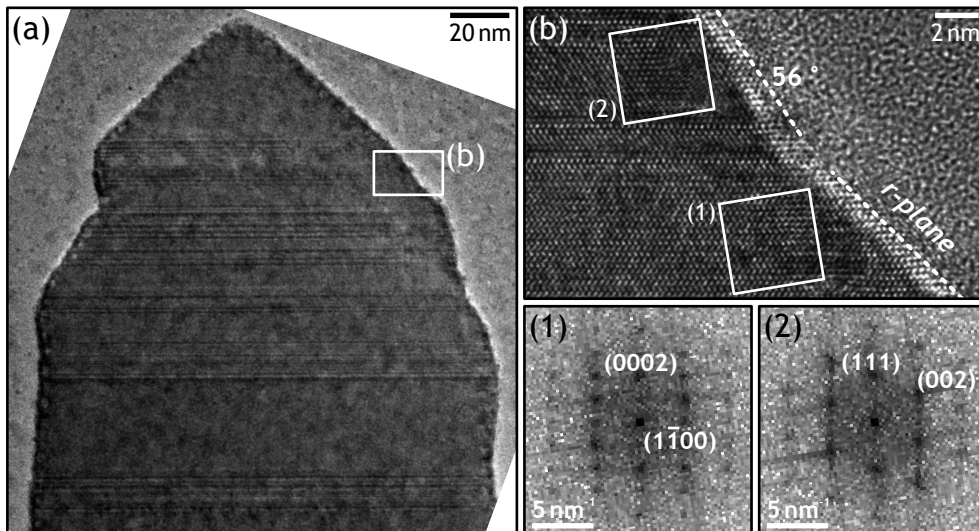


**Figure 8.4:** (a) HRTEM micrograph of the high defect density tip region of the NC shown in Figure 8.3(c). A higher magnification is shown in (b). Dashed lines indicate facet inclinations. Local FFTs from the white boxed regions are shown below. The FFT images have been rotated for clarity.

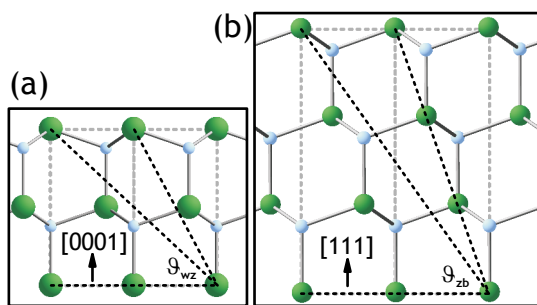


**Figure 8.5:** Wurtzite (a) and zinc blende (b) GaN projected along  $[11\bar{2}0]$ . Gray dashed lines show the conventional unit cells. Black dashed lines show low-indexed planes with non-perpendicular inclination angles  $\vartheta$  with respect to the growth direction.

angle of around  $56^\circ$ . For the zinc blende system, an inclination similar to  $r$ -plane ( $43.2^\circ$ ) can only be obtained, if higher-indexed surfaces are considered. It is expected however, that stabilization of low-indexed surfaces is generally favored.

The change of inclination is thus a direct consequence of changes of the crystal structure during growth. Due to the inclination mismatch of low-indexed crystallographic surfaces in the wurtzite and zinc blende phase, deviations from the initial surface inclination have to occur, once the crystal structure changes.

### Discussion

This section (and Section 7.2.1) showed, that for SAG NCs which show a homogenous diameter and exclusively  $r$ -plane facets at the tip, typically a low density of BSFs or no BSFs at all were observed. On the other hand, for SAG NCs which showed a large variety of semipolar plane inclinations, a

much higher density of BSFs was found. It was shown that inclusions of zinc blende segments during the growth of wurtzite SAG GaN NCs are partially the cause for changes of the crystal surface inclination. Since a single extended BSF locally promotes the formation of a few<sup>6</sup> monolayers zinc blende GaN, it is expected that these defects correlate with the variation of semipolar surface inclination as well. However, the question of causality—i.e. whether the formation of semipolar facets promotes the incorporation of BSFs, or vice versa—cannot be answered in a satisfactory manner.

Crystal phase polytypism in III–V NCs grown by MBE or MOVPE by the VLS approach has been extensively studied and allows precise tailoring of alternating sequences of wurtzite and zinc blende phases<sup>[183]</sup>. Key parameters which determine the prevalent crystal phase are the growth temperature, the NC diameter, and the V/III ratio. It has to be noted, that the thermodynamically stable phase of most III–V bulk crystals is the zinc blende phase<sup>[16]</sup>. For NCs, the wurtzite phase is predicted to be stabilized due to surface energy contributions which play an important role for NCs with small diameters<sup>[184,185]</sup>. In contrast, for the III nitrides, the wurtzite phase is predicted to be thermodynamically stable, independent of the NC diameter<sup>[184]</sup>. Therefore, it is not clear, whether similar concepts for the control of the density of BSFs also apply in the case of GaN NCs. Nevertheless, if this was the case, the first key parameter can be ruled out for this work due to the constant growth temperature for the NCs on the very same area of the sample. An influence of the NC diameter on the density of BSFs cannot be ruled out. In fact, photoluminescence experiments showed that the luminescence band related to extended defects decreases for increasing NC diameter (see [Section A.9](#)). However, the fact that the diameter of the presented SAG NCs, for which a varying density of BSFs was observed, was relatively constant, shows that the NC diameter was not the key parameter. Therefore, only the local N/Ga ratio remains as possible control parameter. If one takes into account, that the growth is assisted by Ga diffusion from the NC sidewalls to the tip, the local N/Ga ratio might be influenced by diffusion barriers which are expected to vary on the different semipolar surfaces. However, Ga adatom diffusion barriers on semipolar surfaces are largely unknown. Nevertheless, the effect of the nominal N/Ga ratio on the density of BSFs in SAG GaN NCs can be easily verified experimentally. Furthermore, the diameter of the NCs can be varied in order to investigate the effect of this parameter on the density of BSFs. It is therefore expected, that TEM (or STEM-CL, see [Chapter 9](#)) investigations of SAG GaN NCs with different diameter, and which have been grown under varying N/Ga ratio may shed some light into this question. Furthermore, the answer to the interesting question, whether a self-induced incorporation mechanism is present, i.e. whether the incorporation of a BSF increases the

---

<sup>6</sup> The number of zinc blende units depends on the type of basal plane stacking fault.

incorporation probability of another BSF, was beyond this thesis. Again, detailed TEM investigations in order to analyze the statistical distribution of BSFs, and the correlation of the densities of BSFs with the appearance of specific semipolar facets, are expected to lead towards the answer of this question.

## 8.2 RAMAN SPECTROSCOPY

Micro-Raman measurements have been performed to complement structural analysis of the SAG GaN NCs. The experiments were carried out by E. Secco, N. Garro, and A. Cantarero in a collaboration with the University of Valencia, Spain. Non-resonant Raman spectroscopy was performed with an excitation wavelength of 514 nm at room temperature in backscattering geometry  $z(y, -)z$ . The spectral resolution was about  $1 \text{ cm}^{-1}$ , the diameter of the focused laser beam about  $1 \mu\text{m}$ .

Different SAG arrays from a standard SAG sample with  $M$  design were investigated. The smallest pitch value was about 150 nm. For this specific pitch, the number of SAG NCs which contributed to the Raman spectrum is calculated to be about 9. With increasing pitch, this value rapidly decreases to about one column per excitation area for  $p = 0.75 \mu\text{m}$ . Due to the growth of self-induced NCs for larger pitch values, the corresponding Raman spectra originate from SAG and self-induced NCs. Typical Raman spectra expected to result solely from SAG NCs or mainly from self-induced NC are shown in Figure 8.6. Furthermore, the contribution of the template is shown.

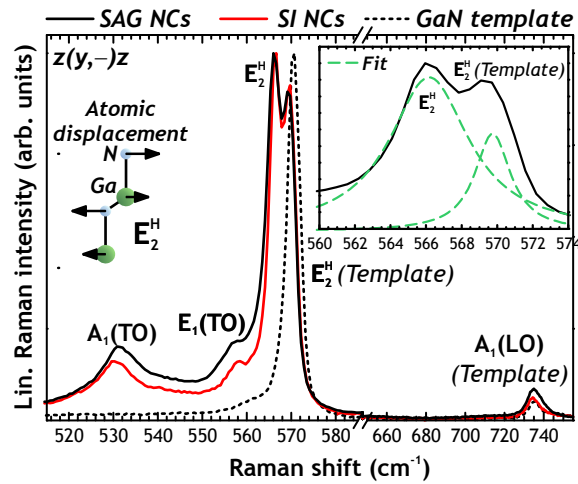


**Figure 8.6:** Raman spectrum of about 9 SAG NCs ( $d = 144 \text{ nm}$ ,  $p = 150 \text{ nm}$ ) and of mainly self-induced NCs (same aperture diameter,  $p = 6110 \text{ nm}$ ) at room temperature. The Raman signal from the template is shown as dashed line. The inset shows Lorentzian peak fits of the  $E_2^H$  modes of the SAG NCs and the GaN template. The atomic displacement for the  $E_2^H$  phonon mode is schematically depicted. *Sample G1225.*

In backscattering configuration, Raman selection rules allow the  $A_1(\text{LO})$  and  $E_2^{\text{H}}$  mode<sup>[161]</sup>. The peak at  $570\text{ cm}^{-1}$  is attributed to the  $E_2^{\text{H}}$  mode of the GaN template on sapphire. Being slightly larger than the theoretically predicted and experimentally reported values for bulk GaN ( $565\text{--}568\text{ cm}^{-1}$ )<sup>[161,186,187]</sup>, the template is compressively strained. This is due to differences in thermal expansion coefficients of GaN and sapphire<sup>[188]</sup>. The dominant sharp peak at  $566\text{ cm}^{-1}$  can be attributed to the  $E_2^{\text{H}}$  mode of the nanocolumns. The corresponding full width at half maximum (FWHM) is about  $5\text{ cm}^{-1}$ . The spectral position is in agreement with values reported for bulk GaN and self-induced GaN NCs grown by MBE<sup>[103,119,143,189,190]</sup>, which are considered to be free of internal strain. Since the  $E_2^{\text{H}}$  mode is most sensitive to in-plane strain, as schematically depicted, it is concluded that also the SAG NCs are free of internal strain.

The  $A_1(\text{LO})$  mode of the GaN template is observed around  $734\text{--}741\text{ cm}^{-1}$ . Due to the refraction of the incident laser light at the pyramidal facets of the NCs, deviations from the backscattering geometry occurred. In addition, the high refractive index of GaN causes multiple internal reflections which furthermore altered the scattering geometry. Therefore, the  $A_1(\text{TO})$  and  $E_1(\text{TO})$  modes became allowed for the used scattering configuration. These are observed at  $531\text{ cm}^{-1}$  and  $558\text{ cm}^{-1}$ , respectively.

In order to compare the crystal quality of the SAG and SI NCs, the FWHM of the  $E_2^{\text{H}}$  mode as function of pitch was evaluated. The result is shown in Figure 8.7.

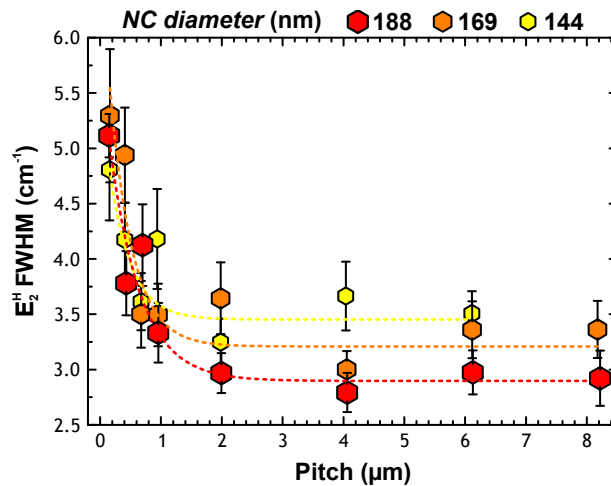


**Figure 8.7:** Evolution of the full width at half maximum of the  $E_2^{\text{H}}$  mode of GaN NCs. The average diameter of the SAG NCs is given. Dashed lines guide the eye. The error bars are given by the error of the Lorentzian peak fit centered around  $566\text{ cm}^{-1}$ . *Sample G1225.*

It is observed, that the FWHM decreases for increasing pitch from around  $5$  to  $3\text{ cm}^{-1}$ , suggesting, that also the crystal quality improves with pitch. However, for pitches larger than  $0.75\text{ }\mu\text{m}$ , the density of SI NCs on the Mo

mask significantly increased (see [Section 7.1.1](#)). At maximum, only one SAG NC contributed to the spectra for such pitch values. It is thus concluded, that for pitch values  $p < 0.75 \mu\text{m}$ , mainly SAG NCs contributed to the spectra, while for larger pitch values, mainly self-induced NCs contributed to the spectra. Thus, the decrease of the FWHM is related to a change of NC type which contributed to the Raman signal. This implies, that the atomic arrangement disorder is slightly lower for the self-induced NCs as compared to the SAG NCs. Comparison of the SAG NCs among each other ( $p < 0.75 \mu\text{m}$ ) showed no clear trend of improving crystal quality as function of diameter.

### *Discussion*

At the date of writing this thesis, Raman reports on GaN NCs from literature paid more attention to self-induced NCs as compared to selectively grown ones. Therefore, the (micro-) Raman results on self-induced GaN NCs from literature were taken as reference for comparison.

The FWHM of the  $E_2^H$  mode is slightly larger for the SAG NCs as compared to the SI NCs. Nevertheless, comparison with literature values which have been obtained from ensemble measurements on MBE-grown SI NCs ( $2.8 - 5 \text{ cm}^{-1}$ )<sup>[119,189,190]</sup> proves the excellent crystal quality of the SAG NCs.

Dense NC arrays are expected to be model cases for the observation of surface optical phonon modes. These modes are vibrations of the free surface of polar semiconductors. Due to the high surface-to-volume ratio, NCs are suited candidates for the investigation of such modes. Theoretically, the interaction between the NC and the electromagnetic wave can be described according to the effective medium theory, i.e. considering the NC ensemble as homogeneous material and defining an appropriate effective dielectric function<sup>[191]</sup>. The frequency of the surface optical mode then mainly<sup>7</sup> depends on the fill factor which describes the coverage of the substrate surface by NCs.

In the case of GaN SI NC ensembles, the observation of surface optical phonon modes was reported in literature<sup>[189,191]</sup>. In Ref.<sup>[191]</sup>, it was concluded that for fill factors in the range of 0.3 to 0.8, a surface optical mode occurred at frequencies in the range of  $655$  to  $715 \text{ cm}^{-1}$ . The authors analyzed ensembles of SI NCs which were reported to be tilted with respect to the substrate normal. For the investigated sample of this thesis, a pitch value of  $150 \text{ nm}$  corresponds to a fill factor of around 0.3. However, as shown in [Figure 8.6](#), for the SAG GaN NCs, no surface optical mode in the reported frequency range was observed. This discrepancy is expected to result from the perfect perpendicular(parallel) alignment of the SAG NCs with respect to

<sup>7</sup> Also NC shape and size effects may affect the frequency.

the substrate(incident laser light). It is therefore assumed, that the coupling of the laser light to the NC surface was much more efficient for the SI NCs. In order to analyze the behavior of surface optical modes in SAG NC arrays, it is expected that the excitation with the laser light perpendicular or not perfectly parallel to the NC growth direction will result in the excitation of surface optical phonon modes as well.

### 8.3 TOWARDS SEMIPOLAR III NITRIDE HETEROSTRUCTURES

Section 8.1.1 showed that bending of threading dislocations significantly reduces the defect density for the tip region of SAG GaN NCs. In addition, with an inclination of about  $43^\circ$  with respect to the basal plane, almost no total polarization discontinuity was predicted at the interface of  $r$ -plane  $\text{In}_x\text{Ga}_{1-x}\text{N}/\text{GaN}$  heterostructures<sup>[43]</sup>.

Therefore, the SAG GaN NCs have been used as templates to examine their feasibility for the growth of high-quality semipolar GaN-based heterostructures. However, the growth of  $\text{In}_x\text{Ga}_{1-x}\text{N}$  is already demanding in the case of layers and requires careful optimization of growth conditions<sup>[53]</sup>. On the other hand, the growth conditions of GaN and AlN resemble each other. Therefore, as a first approach, AlN/GaN multi-quantum wells (MQWs) were grown. After standard<sup>8</sup> selective area growth, semipolar AlN barriers and GaN QWs were grown at the NC tips, using the typical N/III ratio of about 9. This ratio corresponded to an effective metal (Ga, Al) supply of about  $F_{\text{III}} = 0.7 \text{ nm min}^{-1}$ . Analogously, substrate temperature and nitrogen supply were not varied. For the presented sample, the growth duration of the MQW (AlN/GaN/AlN/.../GaN NC) was 14/10/10/6/6 min, where the longest growth duration corresponds to the AlN cap. Figure 8.8 shows the morphology of the SAG NCs after growth.

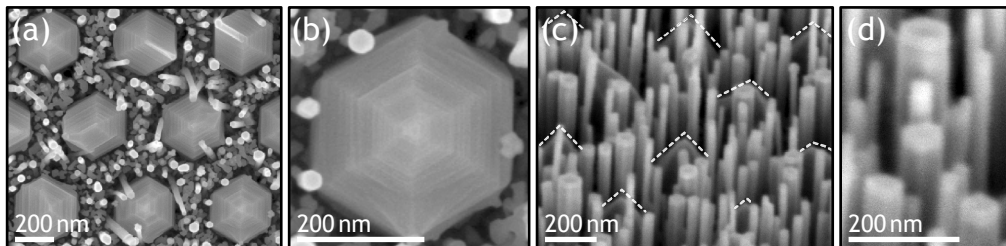


**Figure 8.8:** SEM top-view (a, b) and bird's eye view (c) micrographs of SAG GaN NCs after the growth of AlN/GaN MQWs at the tips. The magnification of SI NCs from (c) is shown in (d). Sample design *M* was used. The nominal aperture pitch and diameter were 250 nm, respectively. The dashed lines indicate the tips of the SAG NCs in between the SI NCs. *Sample G1290*.

<sup>8</sup> To suppress growth of SI NCs on the Mo mask, a reduced growth time compatible with Figure 8.2(b) was chosen.



For the SAG NCs with AlN/GaN MQWs, an enhancement of the vicinal step structure at the semipolar faceted tips was observed as compared to SAG GaN NCs without heterostructures (see Figure 6.1 and 7.5). In addition, the density of SI NCs on the Mo mask significantly increased (see Figure 7.1, 7.2, and 7.5). Note, that this behavior was observed for all investigated samples for which AlN insertions have been grown. These self-induced NCs show  $c$ -plane tips, which resulted in the growth of polar AlN/GaN MQWs. The latter can be resolved by SEM as shown in Figure 8.8(d).

A considerable number of SI NCs must have been grown on the Mo mask prior to growth of the AlN barriers, otherwise, no AlN barriers would be observed at the SI NC tips. Nevertheless, the significantly increased density of SI NCs can be explained by assuming a much smaller diffusion length of Al on the Mo layer, as compared to Ga. This leads to the nucleation of AlN on Mo. The nucleation of AlN in return will reduce the effective Ga diffusion length due to an increased probability of GaN nucleation on AlN. This leads to the growth of GaN SI NCs, similar to the growth of GaN NCs at the edges of AlN islands on Si<sup>[117]</sup>. A smaller diffusion length of Al as compared to Ga was also reported for diffusion on GaN NC sidewalls<sup>[105]</sup>. In the case of SI NCs, AlN insertions are commonly used as markers for growth rate analysis. Due to the strong influence of Al on the growth kinetics, this is however not possible for SAG GaN NCs grown under such conditions. A similar approach to study SAG NC growth rates and morphology evolution by marker layers might be Si  $\delta$ -doping<sup>[192]</sup>.

In order to investigate the structural quality of the MQWs and to gain insight into the semipolar growth rates, TEM lamellae have been prepared by focused ion beam in cross sectional geometry. TEM overview micrographs of SAG and SI NCs are presented in Figure 8.9.

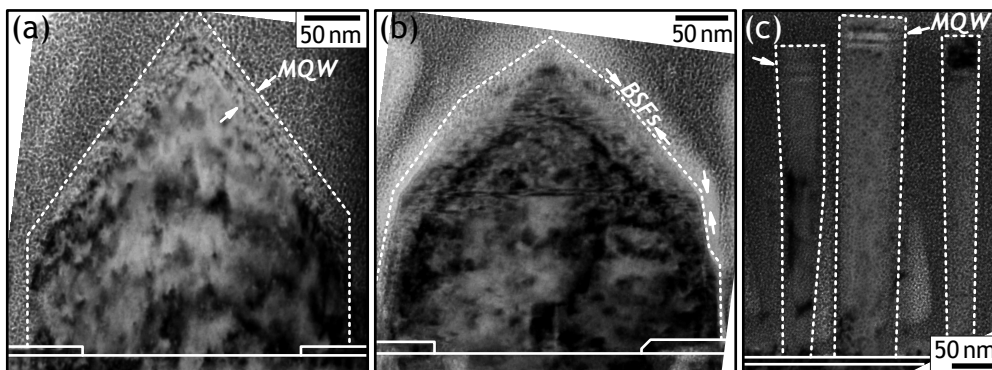


**Figure 8.9:** TEM micrographs of SAG (a, b) and SI (c) NCs with semipolar and polar AlN/GaN MQWs at the tip, respectively. Solid lines mark the interface to the GaN template and Mo layer. Dashed lines indicate the NC morphology. Note, that the NCs of (a) and (b) are not identical. The zone axis for (b) is  $[11\bar{2}0]$ . In the case of (a) and (c), deviations from this orientation are present. Important features are marked by arrows and have been labeled. *Sample G1290.*

The unsatisfying quality of the micrographs is due to ion beam-induced damage and Ga contamination, since for these lamellae no argon plasma treatment was carried out. Nevertheless, the semipolar and polar MQWs can be observed in Figure 8.9(a) and (c), respectively. In these cases, the zone axis orientation deviates from the typically used  $[11\bar{2}0]$  geometry towards  $[1\bar{1}00]$ . As discussed in Section 8.1.2, BSF-related contrast diminishes for this orientation. Investigation in  $[11\bar{2}0]$  zone axis geometry (b) revealed the presence of a considerable density of BSFs for the tip region of the NC. The average tip inclination for this sample was about  $53^\circ$ . This value is in agreement with  $\text{GaN}\{2\bar{2}03\}$  which shows a theoretical inclination of  $51.4^\circ$ .

High resolution micrographs of the semipolar and polar MQWs are presented in Figure 8.10.

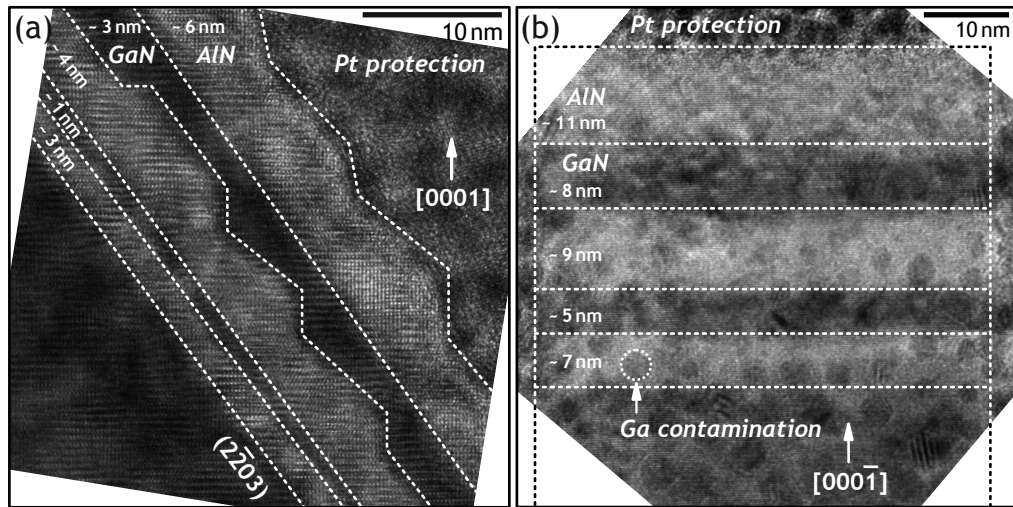


**Figure 8.10:** HRTEM micrographs of a semipolar (a) and polar (b) AlN/GaN MQW. Approximate layer thicknesses are given, the dashed lines guide the eye along the interfaces. The zone axis for (a) was  $[11\bar{2}0]$ , for (b) a sample tilt towards  $[1\bar{1}00]$  was present. Polarity and important features are labeled. *Sample G1290.*

The HRTEM micrograph of the semipolar MQW reveals rather smooth AlN/GaN interfaces, whereas the GaN/AlN interface or AlN cap surface shows a pronounced step structure. In the case of the polar MQW, much smoother interfaces are observed. Although Ga and Al supplies were estimated to be equal for both MQW structures, the thicknesses of the AlN barriers are found to be slightly larger than their GaN counterparts which were grown for the same duration. Furthermore, it is observed that the polar growth rates exceed the semipolar ones.

Due to the lattice mismatch of GaN and AlN, the inclinations  $\vartheta_{\text{GaN}}$  and  $\vartheta_{\text{AlN}}$  of the  $(2\bar{2}0n)$  planes with respect to the basal plane are slightly different. In the case of  $(2\bar{2}03)$ , the plane inclination with respect to the  $c$ -axis is about  $0.5^\circ$  steeper for GaN. On the one hand, it is assumed, that the observed step structure of the AlN barriers is related to slight variations in the plane inclination angles. On the other hand, stabilization of different



semipolar surfaces in the case of GaN and AlN might have been occurred. Furthermore, non-vanishing strain components for semipolar GaN-based heterostructures ( $\varepsilon_{zz}$  and  $\varepsilon_{yz}$ , see Section 2.1.5) might result in relaxation mechanisms, which could lead to such a step structure.

Concerning MQW growth rates, the height of the SAG and SI NCs is in the range of the Ga diffusion length on the NC sidewalls (see Section 7.1). The growth of the MQWs is thus expected to have proceeded in the transition of *regime I* and *II*. However, due to the high density of SI NCs, the contribution of Ga diffusion from the substrate to the axial growth will have been significantly reduced. Taking into account the inclination of the semipolar surfaces, and the fact that the slant height of the NC tip is of the same order as  $\lambda_f$ , the growth rate  $w_{(2\bar{2}03)}$  perpendicular to the semipolar plane is expected to have been given mainly by the direct impingement:  $w_{(2\bar{2}03)} = F_{\text{III}} \cdot \cos \vartheta = 0.45 \text{ nm min}^{-1}$ , where  $\vartheta_{(2\bar{2}03)}^{\text{GaN}} = 51.4^\circ$ . Quantitative investigation of the growth rates (layer thicknesses evaluated by TEM, not shown) revealed, that the GaN and AlN semipolar growth rates follow this behavior with deviations of about  $-0.1$  and  $+0.1 \text{ nm min}^{-1}$ , respectively. For the SI NCs with *c*-plane tip and diameters smaller than SAG NCs, also material contribution due to diffusion from the NC sidewalls has to be taken into account. Consistently, the axial growth rates exceed the supplied metal fluxes:  $w_{\text{ax}} \sim 0.9 - 1.0 \text{ nm min}^{-1} > F_{\text{III}}$ .

In the case of AlN, both the semipolar and polar growth rates were slightly higher as compared to GaN. It is not clear, whether this is related to different growth kinetics of GaN and AlN, or related to uncertainties in the determination of the Al supply by RHEED, or related to uncertainties in the evaluation of the QW thickness by TEM.

### Discussion

The semipolar tip region of SAG GaN NCs was discussed to be suited for the growth of high-quality semipolar GaN-based heterostructures. However, the preceding section revealed difficulties in obtaining high-quality semipolar AlN/GaN MQWs.

This is expected to be particularly due to the lattice mismatch of AlN and GaN. As discussed in Section 2.1.5, uniaxial strain along the *c*-direction ( $\varepsilon_{zz}$ ) and shear strain within the *m*-planes along  $[0001]$  ( $\varepsilon_{yz}$ ) are expected to occur in semipolar GaN-based heterostructures. This may give rise to higher densities of BSFs of type  $I_2$  (or  $I_3$ )<sup>9</sup> for the tip region of SAG GaN NCs which contain (M)QWs, as compared to their homostructural counterparts. In fact, photoluminescence (PL) experiments on SAG NCs with AlN/GaN MQWs showed a significant increase in the PL intensity of the luminescence

<sup>9</sup> Only these types of BSFs can be formed during deformation. The types  $I_1$  and  $E$  are exclusively related to growth<sup>[25]</sup>.

band which was related to BSFs (*Sample G1352*, not shown).

Nevertheless, the growth of semipolar MQWs at the tips of SAG GaN NCs was achieved and quantum well morphology, as well as crystal quality are expected to improve going towards low alloy concentrations in semipolar  $\text{Al}_y\text{Ga}_{1-y}\text{N}$  and  $\text{In}_x\text{Ga}_{1-x}\text{N}$  heterostructures.

The semipolar QW growth rates will be given in *regime II* mainly by the nominal supply due to the large surface area of the semipolar facets—especially for SAG NCs with diameters in the range of one micron—and can thus be controlled precisely. In addition, it is expected that the coalescence mechanism of the semipolar facets (see [Section 7.1.2](#)) and fine-tuning of growth conditions towards the Ga-rich regime<sup>[125]</sup> allow for the growth of polar and semipolar QWs within the same nanostructure by MBE, similar to approaches already established in the MOVPE process<sup>[10,193–195]</sup>. This may pave the way towards quantitative comparison of polarization induced effects on the optical emission properties of polar and semipolar QWs grown under nominally identical growth conditions.

---

## CORRELATION OF OPTICAL AND STRUCTURAL PROPERTIES

---

*Chapter 8 discussed the structural properties of SAG GaN NCs, which included a microscopic investigation of crystal structure and defects by transmission electron microscopy. This chapter will present the optical properties which were assessed by cathodoluminescence spectroscopy. This technique allows direct correlation of optical and structural properties on the nanoscale in the case of single SAG NCs, and on the micron scale in the case of ensembles of SAG NCs. First, single NCs will be investigated. Afterwards, the optical properties of the ensembles will be investigated and interpreted on the basis of the conclusions from single NCs.*

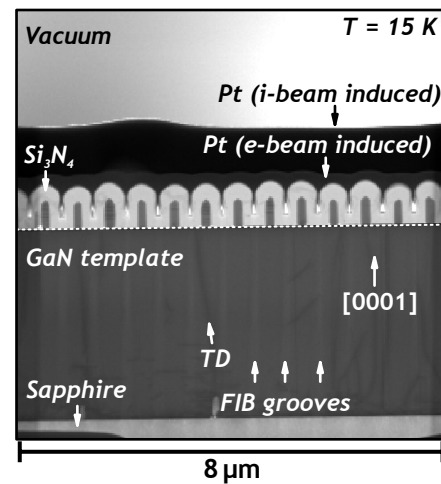
Scanning transmission electron microscopy (STEM) and scanning electron microscopy (SEM) cathodoluminescence (CL) measurements have been performed by M. Müller, G. Schmidt, S. Metzner, P. Veit, T. Hempel, F. Bertram, C. Karbaum, and J. Christen in a collaboration with the Otto-von-Guericke-University Magdeburg, Germany. In the case of STEM-CL, measurements were performed at a temperature of 15 K at 80 kV. A retractable parabolic mirror was suited for initial STEM-CL measurements (mirror inserted) and subsequent structural analysis of the very same sample position with improved spatial resolution (mirror retracted). The samples for STEM-CL have been prepared in cross sectional TEM lamellae geometry by the optimized preparation approach by focused ion beam. Details on the experimental setups are given in [Section A.1](#). SEM-CL measurements on as-grown SAG NC ensembles were performed at a temperature of 6 K in bird's eye view sample geometry (sample tilt of 45° with respect to the template normal) at 3 kV. For convenience, the reader is referred to [Table 2.3](#) for nomenclature and spectral positions of common optical transitions in GaN .

## 9.1 SINGLE SAG NANOCOLUMNS

To correlate the optical emission characteristics with the structural properties on the nanoscale, single SAG GaN NCs were investigated by STEM-CL. For this experiment, an optimized cross sectional preparation approach by focused ion beam (FIB) was developed. Due to this approach, ion beam-induced damage and consequent quenching of the cathodoluminescence<sup>[196,197]</sup> was largely circumvented. This allowed to assess the optical properties of single NCs which showed strong variations in the density of extended defects.

In general, STEM micrographs have been recorded using the annular dark field (ADF) and high angle annular dark field (HAADF) detector; the first shows mainly diffraction contrast, the latter mainly chemical contrast (see Section 5.2.4). Figure 9.1 shows an ADF micrograph of the investigated sample which was prepared in cross sectional geometry for low temperature STEM-CL.

**Figure 9.1:** ADF micrograph of the investigated TEM lamella. Distinct features have been labeled, the dashed line marks the interface to the GaN template. The view direction is close to  $[11\bar{2}0]$ . The sample was grown under standard SAG conditions. The NC diameter is about 200 nm, the pitch is about 430 nm (*M* design). *Sample G1225*.



The SAG GaN NCs with diameter of around 200 nm are perfectly arranged in the TEM lamella. The thickness of the lamella before the final low-energy  $\text{Ar}^+$  ion treatment was estimated to be around 250 nm. The lamella therefore presents a single row of NCs with diameter in the range of the TEM lamella. The NCs have been embedded in  $\text{Si}_3\text{N}_4$  before FIB preparation. Due to different FIB milling yields for GaN and  $\text{Si}_3\text{N}_4$ , etching grooves parallel to the NC growth direction are observed. Furthermore, threading dislocations (TDs) are observed in the substrate. These are filtered at the Mo interface due to the small contact area of the SAG NCs to the template. A higher magnification of around 14 NCs in (HA)ADF contrast together with a panchromatic CL intensity (CLI) image is shown in Figure 9.2.

In the NCs, extended bright (HAADF), and dark (ADF) contrasts perpendicular to the growth direction reveal extended defects, such as basal plane stacking faults (BSFs) and zinc blende inclusions (see Section 8.1.2). The panchromatic CLI image shows dominant emission exclusively from the NCs, only low emission from the GaN template and the sapphire substrate (not

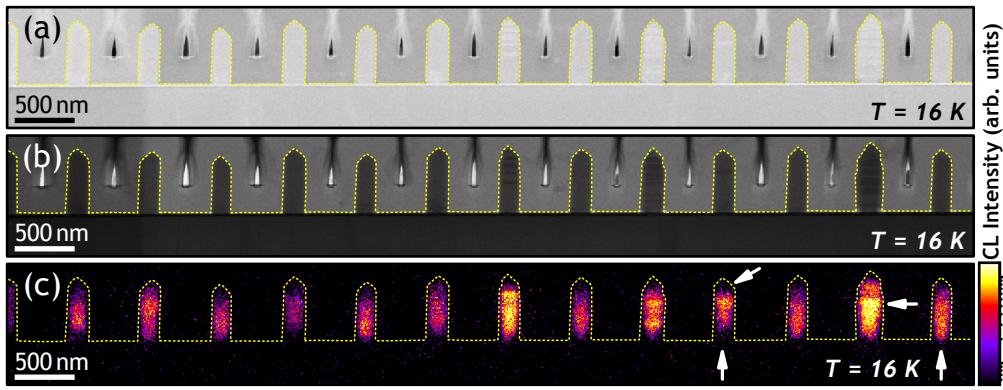


**Figure 9.2:** HAADF (a), ADF (b), and panchromatic CLI (c) images of SAG GaN NCs. The dashed lines guide the eye along the NCs and the surface of the Mo layer. Arrows label distinct features (see text) in the CLI image which is shown on a logarithmic scale. *Sample G1225.*

shown) was observed. For the NC base region of some NCs, the emission extends up to the interface of the GaN template, for some NCs it is quenched in the vicinity of the interface. For all NCs, a reduction of the CL intensity in growth direction towards the NC tip is observed. Furthermore, a modulation of the CL intensity is observed for NCs which contain a high density of extended defects.

The dominant peak of the corresponding ensemble spectrum of these 14 NCs ( $T = 16$  K, spectral resolution  $\sim 0.3$  nm, spectrum not shown) is located at 3.485 eV and is attributed to  $D^0X$ -related emission. The blue shift of 13 meV with respect to the expected position of 3.472 eV of unstrained GaN is most likely due to compressive strain of the surrounding  $\text{Si}_3\text{N}_4$  matrix (compare with Section 9.2). Note, that the spectral resolution is expected to have been just sufficient to resolve  $D^0X_A$  and  $D^0X_B$ . However, to avoid ambiguity, the identification with  $D^0X$  will be used in the following. Since already this spectrum of only 14 NCs showed a broad luminescence band in the range of 3.0 – 3.5 eV, in the following single SAG GaN NCs will be investigated. According to Section 8.1.2, three different types of NCs were observed in the samples; *defect-free*, *low defect density* and *high defect density* NCs. All types will be studied in the next sections.

#### 9.1.1 Defect-free nanocolumn

Figures 9.3(a – c) show the (HA)ADF and panchromatic CLI images of a SAG NC. All images show a homogenous distribution of the corresponding signal along the NC. This suggests that the NC is free of extended defects. The CL intensity extends to the close vicinity of the GaN template and the typical decrease of the CL intensity along the NC towards the tip is observed.

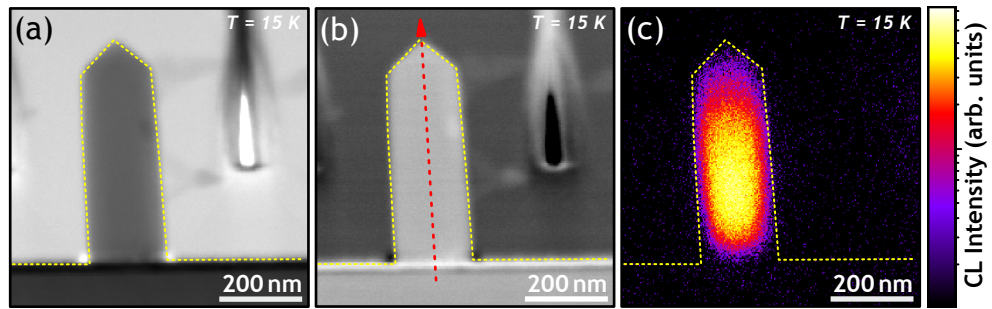


**Figure 9.3:** ADF (a), HAADF (b), and panchromatic CLI (c) images of a defect-free NC. The spectral evolution along the NC, as indicated by the arrow in (b), is shown in [Figure 9.4](#). *Sample G1225*.

In the spectrum (not shown), the dominant emission related to  $D^0X$  is observed around 3.481 eV. This is in agreement with the STEM-CL ensemble spectrum (also not shown). The full width at half maximum of  $D^0X$  is around 10 meV. This value is significantly larger as compared to PL linewidths of about 1 meV, which were reported for single free-standing SI GaN NCs<sup>[36]</sup>. Note, that comparable linewidths as observed in STEM-CL, were also observed in photoluminescence experiments which were performed on the SAG GaN NC ensembles (5 meV, see [Section A.9](#)). The reason for this behavior was not understood up to the date of writing this thesis, a possible explanation might be the presence of surface excitons<sup>[36]</sup>. To investigate the spectral evolution of the CL intensity, a centered linescan along the NC was recorded. The result is shown in [Figure 9.4](#).

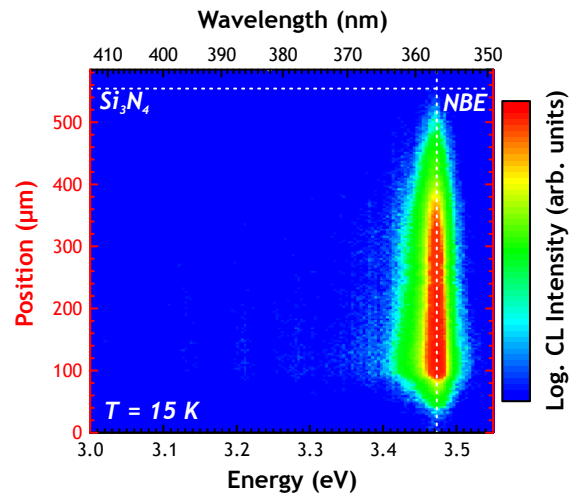


**Figure 9.4:** Spectral evolution of the CL intensity along the NC, as indicated in [Figure 9.3\(b\)](#). Dashed lines indicate relevant features. The linescan was recorded with a spectral resolution of  $\sim 1.5$  nm. *Sample G1225*.

Exclusively GaN near-band-edge (NBE<sup>1</sup>; i.e. X and  $D^0X$ ) emission at 3.472 eV is observed, which decreases towards the tip. The discrepancy concerning the NBE-related peak position with respect to the previously mentioned peak position at 3.481 eV is due to different spectral resolutions of linescan and spectrum ( $\sim 1.5$  and  $\sim 0.3$  nm, respectively).

<sup>1</sup> A possible observation of acceptor-bound exciton emission is ruled out (see [Section 2.1.4](#)).

This result shows that the NC is in fact free of any extended defects. The decrease in CL intensity towards the tip may be due to a reduction of the sample thickness which is caused by the pyramidal geometry of the tip, or due to enhanced non-radiative surface recombination at the semipolar surfaces as compared to the nonpolar ones.

### 9.1.2 Low defect density nanocolumns

In the following, two different NCs which show disperse defect-related optical properties will be discussed.

#### 9.1.2.1 BSF $I_1$ signature

Figures 9.5(a, b) show the presence of three extended defects with narrow contrast signature in a NC. Two are separated by around 45 nm and are located in the region which is confined by nonpolar sidewalls; one defect is located in the region of the tip and separated by the lower defect by around 95 nm. Otherwise, no extended defects are observed.

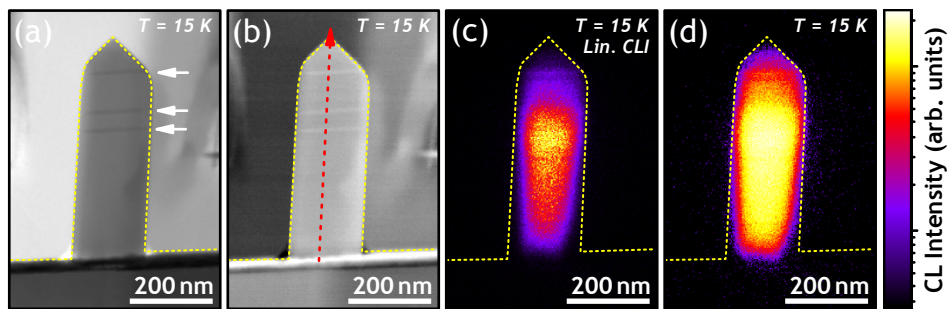


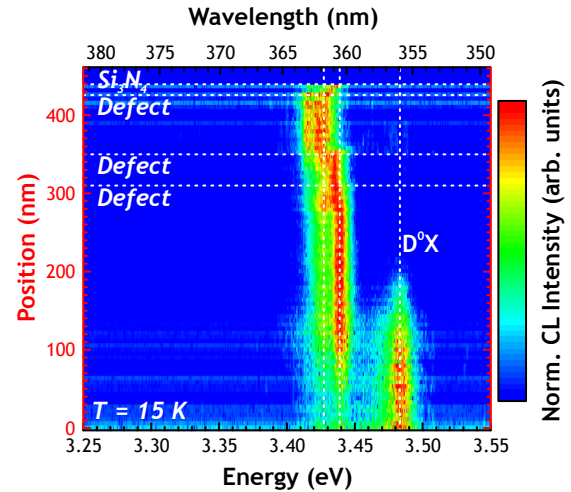
**Figure 9.5:** ADF (a), HAADF (b), and panchromatic CLI images on a linear (c) and logarithmic (d) scale of a NC which contains three extended defects. These are marked by arrows. The spectral evolution along the NC, as indicated by the dashed arrow in (b), is shown in Figure 9.6. *Sample G1225.*

The panchromatic CLI images (c, d) will be discussed sampling the NC from base to tip: The CL intensity in the NC base extends to the very vicinity of the GaN template. Moving along the NC, an increase of intensity is observed, which has a localized maximum in the region of the first defect. Moving towards the tip, the typically observed decrease of the CL intensity is detected. Note however, that for the last defect, again a local intensity maximum parallel to the defect is observed. The spectral evolution along the NC is shown in Figure 9.6.

Following the linescan from NC base to tip, several emission lines are observed. In the very base region, mainly  $D^0X$  emission at 3.484 eV is observed. After around 100 nm, another line at 3.438 eV is observed and the emission of  $D^0X$  is quenched after around 200 nm. The distance along  $[0001]$  between the position where the  $D^0X$  emission is quenched, and the first



**Figure 9.6:** Spectral evolution of the CL intensity along the NC, as indicated in Figure 9.5(b). Dashed lines indicate relevant features. The linescan was recorded with a spectral resolution of  $\sim 0.3$  nm. *Sample G1225*.



of the three defects, is about 100 nm. Subsequently, solely defect-related emission is observed. In general, in the vicinity of the defects, the line at 3.438 eV is redshifted and furthermore, another line at 3.428 eV is observed.

As discussed, the blueshift of  $D^0X$  with respect to the expected value of unstrained GaN is expected to be caused by compressive strain of the  $\text{Si}_3\text{N}_4$  matrix. Assuming the same relation for the defect-related luminescence lines, the defect-related peak positions are revised to 3.426 and 3.416 eV. These values are in excellent agreement with literature reports of the luminescence band attributed to BSFs of type  $I_1$  in GaN<sup>[28,31]</sup>.

It is thus concluded, that three BSFs of type  $I_1$  were observed in the NC. The fact that the  $D^0X$  emission is completely quenched around 100 nm before the electron beam excites the first defect, as well as the complete quenching between the upper defects, shows that free carrier effective diffusion lengths are of the same order. Furthermore, the localized CL intensity maxima around the BSFs, and the related quenching of the  $D^0X$  emission shows that BSFs are favored recombination sites for free carriers. This can be understood by the local QW-like type-II band alignment around these defects<sup>[26]</sup>. The exact reason for the redshift in the vicinity of the defects remains unclear and needs further investigation for a complete understanding. However, possible explanations are different strain distributions for the defects which are confined by non- or semipolar surfaces, as well as coupling effects of carriers confined in the QW-like potentials of adjacent BSFs<sup>[198]</sup>.

#### 9.1.2.2 BSF E signature

Figures 9.7(a, b) show a NC with the presence of one extended defect with broad contrast signature, which is confined by nonpolar sidewalls. Furthermore, a TD is observed in the NC at the interface to the GaN template. After propagation of around 150 nm, it interacts with another defect (probably non-extended BSF) and is terminated.



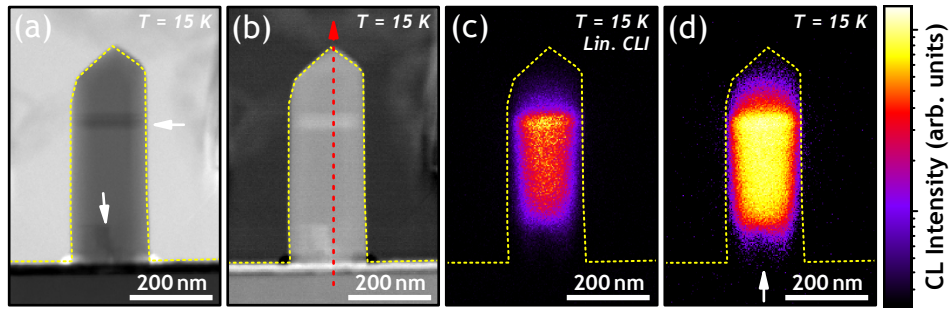


**Figure 9.7:** ADF (a), HAADF (b), and panchromatic CLI images on a linear (c) and logarithmic (d) scale of a NC which contains one extended defect which is marked by a horizontal arrow. Further relevant features are indicated by arrows as well (see text). The spectral evolution along the NC, as indicated by the dashed arrow in (b), is shown in [Figure 9.8](#). *Sample G1225*.

The panchromatic CLI images (c, d) show qualitatively some differences to the previous case. Similarly, a localized CL intensity maximum is observed at the position of the extended defect, parallel to the defect. Furthermore, sampling the NC towards the tip, the typical decrease of the CL intensity is observed. In contrast however, is the behavior of the CL intensity in the vicinity of the GaN template and the TD. The CL intensity is quenched in a wing-shape and centered around the position, where the TD is terminated. Therefore, the CL intensity in the NC base does not extend to the GaN template. The spectral evolution of the CL intensity along the NC is shown in [Figure 9.8](#).

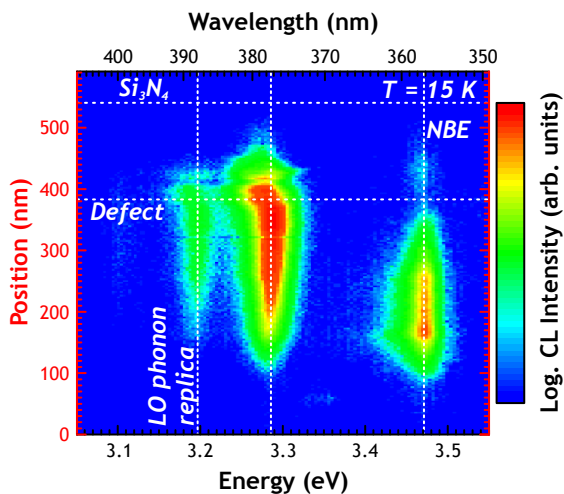


**Figure 9.8:** Spectral evolution of the CL intensity along the NC, as indicated in [Figure 9.7\(b\)](#). Dashed lines indicate relevant features. The linescan was recorded with a spectral resolution of  $\sim 1.3$  nm. *Sample G1225*.

Sampling the NC from base to tip along the linescan, first, no emission is observed. Crossing the position where the TD is terminated, several emission lines are observed at 3.473, 3.289, and 3.196 eV. The first is attributed to NBE emission and is most intense in the beginning. A decrease of the NBE emission intensity is related to an increase of the defect-related intensity (3.289 eV), which becomes the most dominant peak at a distance of around

150 nm from the defect. At the defect position, a slight redshift in the defect-related emission is observed; the line at 3.196 eV follows qualitatively the just described behavior. Subsequently, the NBE emission is quenched almost completely.

The energy difference of the defect-related peak positions is 93 meV. Furthermore, the line at lower energy shows qualitatively the same behavior as the line at higher energy. Therefore, the line at 3.196 eV is attributed to a LO phonon replica of the defect-related line at 3.289 eV. The latter is in excellent agreement with literature reports of the luminescence band attributed to BSFs of type *E* in GaN<sup>[31]</sup>. Considering the spectral resolution of around 1.3 nm (and the corresponding spectral uncertainty of around 10 meV), possible emission due to BSF(s) of type *I*<sub>2</sub> ( $\gtrsim$  3.32 eV) or zinc blende GaN inclusions (3.27 eV) are less probable. However, it has to be noted, that due to the broad contrast of the defect in the (HA)ADF images, unambiguously exclusion of these extended defects is not possible.

Again, the onset of intense defect-related emission around 150 nm before the extended defect is actually excited by the electron beam, is a rough estimate for the effective diffusion length of the free carriers. Furthermore, the presence of a TD in the NC base, and the local CL intensity distribution around the dislocation, allow to explain the dispersive CL behavior at the interface of the NCs to the GaN template, which was observed in [Figure 9.2\(c\)](#). The fact that for the presented single NC, in the vicinity of the TD, no NBE emission or emission due to a BSF<sup>2</sup> was observed, shows that TDs are non-radiative recombination sites. This is in agreement with literature<sup>[199]</sup>. If no TDs are present, free carriers which are generated in the NC base, can diffuse towards the template, given that the distance is smaller than their effective diffusion length. There, mainly non-radiative recombination occurs. Approaching the interface of the GaN template, the CL emission therefore spatially decreases. Directly at the interface, abrupt quenching of the CL intensity is observed. If however a TD is present, electron-hole pairs recombine non-radiatively at the TD which extends into the base of the NCs. Therefore, the CL intensity is quenched already significantly inside the base of the NC and a region of reduced CL emission is wrapped around the TD. Thus, besides ADF images, which show mainly diffraction contrast, also panchromatic CLI images of the interface of the NCs and the GaN template can be used as indicator for the presence of TDs in the NCs.

### 9.1.3 High defect density nanocolumn

The HA(ADF) micrographs in [Figures 9.9\(a, b\)](#) show a SAG NC with the presence of a high density of extended defects. These are observed as dark (ADF) and bright (HAADF) contrasts perpendicular to the growth direction.

---

<sup>2</sup> The latter is expected to occur due to the interaction of the TD with a non-extended BSF.

Due to the broad contrast signature and the relatively large sample thickness (which causes a low spatial resolution in the STEM images), it is not clear, whether these are bundles of BSFs or cubic inclusions. Besides the high defect density, an inhomogeneous NC diameter and the formation of semipolar surfaces with varying inclination are observed. Similar to the previous single NCs, the panchromatic CL intensity is modulated. Local intensity maxima occur at positions which are related to extended defects.

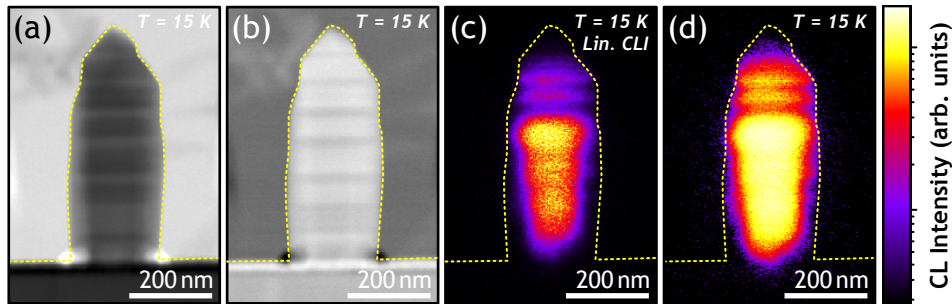


**Figure 9.9:** ADF (a), HAADF (b), and panchromatic CLI images on a linear (c) and logarithmic (d) scale of a NC which contains a high density of extended defects. *Sample G1225.*

The spectrum in [Figure 9.10](#) shows various peaks, the one at highest energy (3.479 eV) is related to  $D^0X$ . Distinct features at lower energy occur at 3.435, 3.323, 3.293, and 3.244 eV. The most intense peak is observed at 3.293 eV, however, each of the other mentioned peaks is higher in intensity as compared to the  $D^0X$  emission. The optical emission properties of the NC are therefore dominated by defect-related emission.

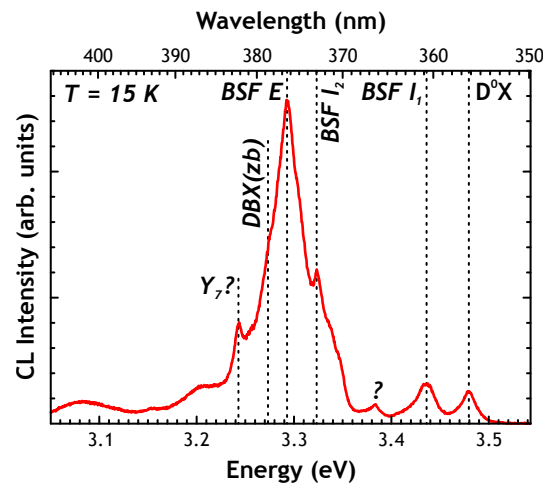


**Figure 9.10:** CL spectrum ( $\sim 0.3$  nm resolution) of the high defect density NC. Dashed lines indicate relevant features (see text). *Sample G1225.*

Correcting all peak energies according to the strain-induced blueshift (see arguments before), the defect-related emission lines are revised to 3.428,

3.316, 3.286, and 3.237 eV. The first three lines are in good agreement with BSFs of type  $I_1$ <sup>[31]</sup>,  $I_2$ <sup>[29,30]</sup>, and  $E$ <sup>[31]</sup>, respectively. The latter is possibly related to the  $Y_7$  line in GaN. Note, that also extended cubic inclusions are expected. Closer investigation of the line which is related to BSFs of type  $E$ , reveals the presence of a shoulder towards lower energy. Fitting the peaks with Lorentzian curves (not shown), the peak position of the low-energy shoulder occurs at 3.273 eV. Taking into account the energy correction due to strain, the value is revised to 3.266 eV which is in excellent agreement with the donor-bound exciton (DBX) emission of zinc blende GaN. This line is expected at 3.27 eV. Note, that none of the observed peaks can be explained by GaN LO phonon replica.

## 9.2 ENSEMBLES OF SAG NANOCOLUMNS

Investigation of the optical properties of single NCs revealed the presence of a NC free of any extended defects. In low defect density NCs, the optical fingerprints of BSFs of type  $I_1$  and presumably a single BSF of type  $E$  were observed. In the case of a high defect density NC, optical transitions in agreement with the presence of BSFs of type  $I_1$ ,  $I_2$ , and  $E$ , as well as zinc blende inclusions were found. The presence of BSFs effectively reduced the GaN NBE emission in favor of the defect-related lines.

These results will now be used for the interpretation of the optical properties of SAG GaN NC ensembles, which were assessed by SEM-CL. Besides identification of dominant optical transitions, the ensemble measurements allow to analyze homogeneity of the NCs concerning their optical properties. [Figure 9.11](#) shows a SEM micrograph of the SAG NCs, together with panchromatic CLI images. The sample represents an as-grown SAG NC sample with  $M$  design, which was grown under standard SAG conditions.

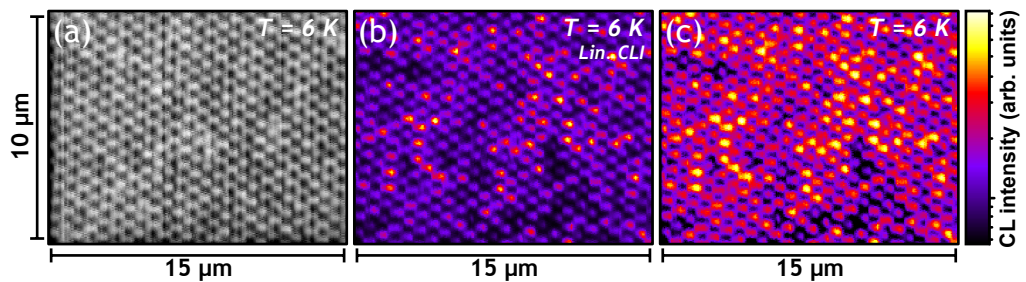


**Figure 9.11:** (a) SEM micrograph of a SAG GaN NC array (the average NC diameter is about 180 nm, nominal aperture diameter and pitch were 100 and 500 nm, respectively) and the corresponding panchromatic CLI images on a linear (b) and logarithmic (c) scale to enhance visibility of low intensity contributions. The sample tilt was digitally corrected to plan view geometry. *Sample G1284*.

The SEM micrograph clearly shows the position of the SAG NCs as bright contrasts. The simultaneously recorded panchromatic CLI image (b) shows

intense localized CL intensity which correlates with the spatial position of the SAG NCs in the SEM micrograph. However, it is observed that the most intense CL intensity is inhomogeneously distributed among the NC ensemble. Displaying the CLI image on a logarithmic scale (c), shows a clear modulation of the CL intensity with minima corresponding to NC interstitial positions. On the one hand, this is due to the Mo mask, which covers possible emission from the template. However, on the other hand, also for an unpatterned region of a reference sample on GaN template (*Sample G1408*, not shown), only low emission was observed from the GaN template. This evidences that the most intense CL emission is due to the SAG NCs. This is in agreement with the result from the STEM-CL measurements. [Figure 9.12](#) shows the corresponding CL spectra which cover different spectral ranges.

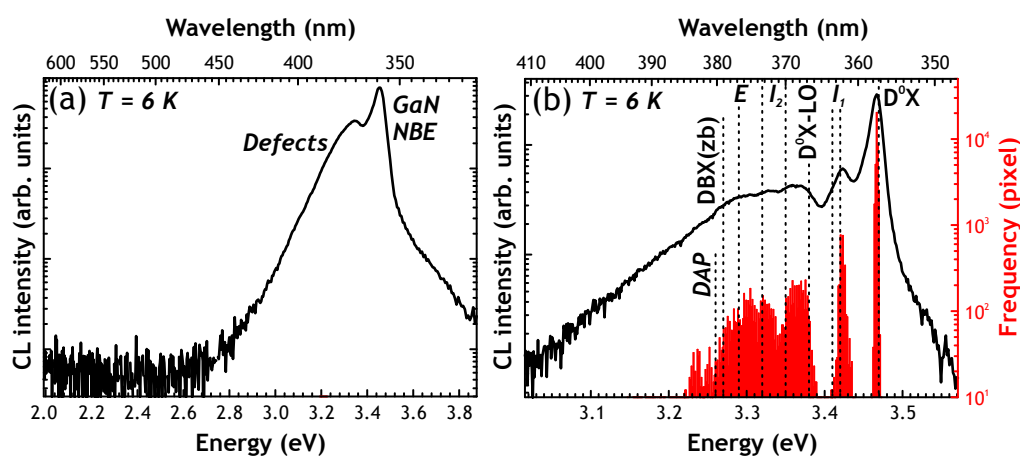


**Figure 9.12:** CL spectra with a spectral resolution of  $\sim 1.5$  nm (a) and  $\sim 0.8$  nm (b). For (b), the peak energy histogram is shown (see text). In addition, common optical transitions in GaN according to [Table 2.3](#) are indicated in (b). The presence of BSFs of type  $I_1$ ,  $I_2$ , and  $E$  was presumably observed in [Section 9.1](#). *Sample G1284*.

The spectrum [9.12\(a\)](#) shows the dominant emission peak at around 3.46 eV, which is attributed to GaN NBE emission. Furthermore, a broad luminescence band in the range of 2.80 – 3.42 eV is observed. Typically, this spectral range is mainly correlated with structural imperfections in wurtzite GaN ( $Y_1 - Y_{10}$  lines)<sup>[15]</sup> and thus assumed to be due to the occurrence of defects in the SAG GaN NCs. Interestingly, no yellow luminescence is observed in the energy range between 2.0 – 2.6 eV. The latter fact will be discussed at the end of this section.

[Figure 9.12\(b\)](#) shows the interesting wavelength region at a higher spectral resolution. Furthermore, the histogram is shown, which gives the frequency of a specific peak energy(wavelength). This was obtained from a CL wavelength image, in which the spatial distribution of the peak wavelength is visualized (corresponding to [Figure 9.11](#), not shown). The CL spectrum reveals the dominant emission line at 3.467 eV, which is in agreement with the expected position of  $D^0X_A$  at 3.472 eV in unstrained GaN. Due to the limited spectral



resolution, again, rather the identification with  $D^0X$  will be used in the following. Furthermore, the next dominant peak at 3.422 eV is in good agreement with the experimentally reported spectral position for BSFs of type  $I_1$  at 3.41 – 3.42 eV<sup>[28,31]</sup>. Comparison of the predicted spectral positions of the luminescence lines at lower energy with the observed spectral positions in the histogram shows slight discrepancies. This is due to the contribution of around 350 NCs to the spectrum, each of them showing slightly different emission characteristics, as observed in Section 9.1 and reported in literature<sup>[36]</sup>. To investigate the spatial occurrence and spatial homogeneity of different CL emission wavelengths, monochromatic CLI images limited to a small spectral range were evaluated. These were created by applying spectral filters to the mapping which corresponds to the spectrum 9.12(b). Such images are shown for various energy ranges in Figure 9.13.

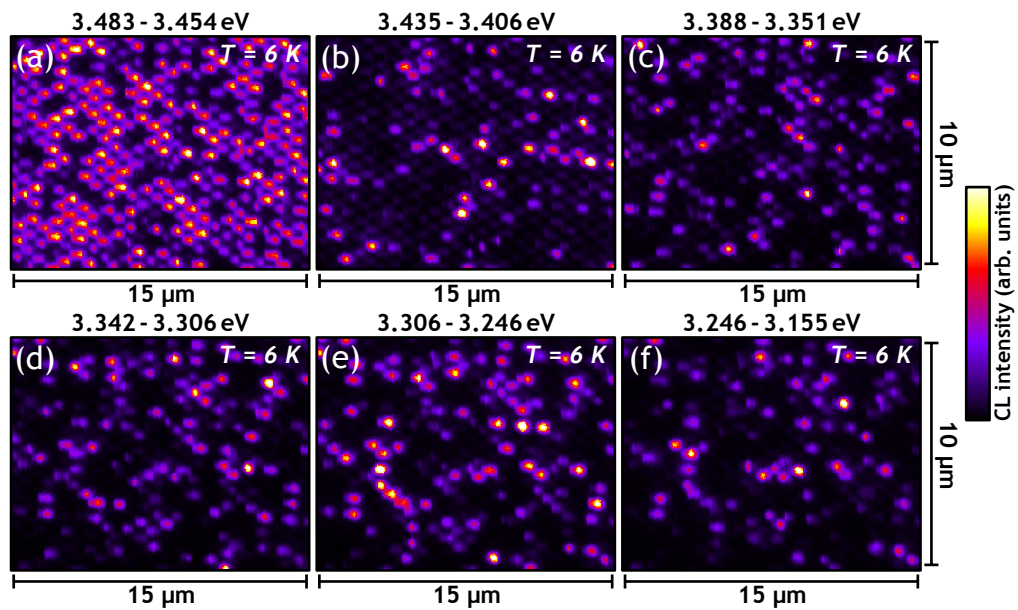


**Figure 9.13:** Monochromatic CL intensity images. Energy ranges correspond to luminescence presumably due to (see text): (a) NBE, (b) BSF  $I_1$ , (c) BSF  $I_2$ , (d) BSF  $I_2$ , (e) BSF  $E$  and DBX(zb), (f) structurally-related. The intensity scale is identical for all images. *Sample G1284*.

First, the different energy ranges will be discussed. According to Table 2.3, the image (a) corresponds to GaN NBE emission and possibly TES. The previous Section 9.1 showed a good agreement of the luminescence of extended defects with literature reports of BSFs of types  $I_1$ ,  $I_2$ ,  $E$ , and zinc blende inclusions. Accordingly, image (b) is in the energy range of BSFs of type  $I_1$ , (c) in the range of BSFs of type  $I_2$ . Note, that slightly different spectral positions are reported for the BSFs of type  $I_2$  and therefore, the energy window (d) may correspond to  $I_2$  as well. For (e), a DAP-related transition, the BSF type  $E$ , and the DBX of zinc blende GaN are possible. In the case of (f), a structural-bound exciton ( $Y_7$ ) or DAP-related transition

in zinc blende GaN may be considered. In addition, phonon replica peaks may be observed for several energy windows. Note, that for the single GaN NCs (see Section 9.1), as well as for local spectra from the investigated NC ensemble (not shown), no clear evidence for DAP emission was found. Furthermore, photoluminescence spectra (not shown) from a GaN MBE reference layer which was grown on truly bulk GaN substrate<sup>3</sup> in the same MBE system only several days after the investigated sample, showed also no DAP-related emission. Therefore, emission related to DAP transitions are ruled out. The possible contribution of a  $D^0X - LO$  phonon replica to (c) is expected to be low in comparison with the emission related to BSFs for considerable densities of these defects<sup>[28,30]</sup>. This argument is again supported by PL measurements on the reference GaN layer, for which an intensity ratio of  $10^{-3}$  for  $D^0X_A - LO$  and  $D^0X_A$  was found.

According to these arguments, the energy windows (b – e) can presumably be narrowed down to extended defects; BSFs of type  $I_1$ ,  $I_2$ , and  $E$ , as well as possibly zinc blende inclusions. Revisiting the histogram of Figure 9.12(b), the most frequent occurrence of emission related to BSFs of type  $I_1$  among these extended defects is in agreement with theoretical calculations which predict the lowest formation energy for type  $I_1$  as compared to the types  $I_2$  and  $E$ <sup>[26]</sup>. Figures 9.13(a – f) show that intense NBE emission is observed for the majority of the SAG NCs. The spatial position, from which NBE emission is observed, is statistically distributed. In the following, the spatial coincidence of the different defect types, as well as the spatial coincidence of NBE emission and defect-related emission will be investigated. For this purpose, RGB (red, green, blue) spatial correlation images of the SAG NC ensemble have been analyzed. In these images, the monochromatic images from Figure 9.13 were color coded using additive color mixing (red, green, blue). The results are presented in Figure 9.14.

Figure 9.14(a) shows the spatial correlation of BSFs of type  $I_1$ ,  $I_2$ , and  $E$  (together with DBX of zinc blende GaN). For convenience, only the BSFs will be named in the following. Red, green, and blue areas correspond to emission from BSFs of type  $I_2$ ,  $I_1$ , and  $E$ , respectively. Additive mixed colors indicate spatial overlap of different energy windows. Consequently, yellow, cyan, and magenta are related to spatial coincidence of the luminescence from  $I_1$  and  $I_2$ ,  $I_1$  and  $E$ , and  $I_2$  and  $E$ , respectively. The most prevalent colors are green and magenta. This indicates that the exclusive formation of BSFs of type  $I_1$  is favored. In the case of the BSFs of type  $I_2$  and  $E$ , the image however suggests, that the formation of these defects often occurs in the same NC.

Figure 9.14(b) shows the spatial correlation of NBE emission with the energy range related to BSFs of type  $I_1$ , and  $E$ . Green areas correspond to the spatial position of NBE emission, red, and blue to BSFs of type  $I_2$ ,

<sup>3</sup> Sample G1289: 50 nm MBE GaN grown under slightly Ga-rich conditions on AMMONO GaN(0001) substrate.

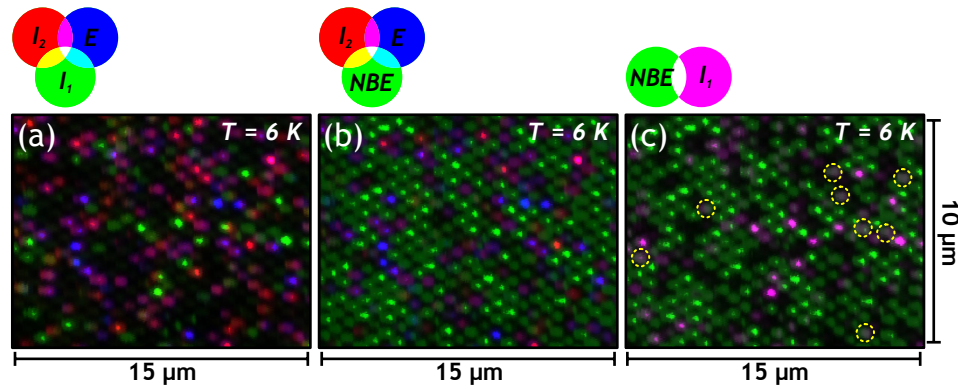


**Figure 9.14:** Additive RGB color images for the investigation of the spatial coincidence of CL emission. The labeling identifies the color coding of the monochromatic CL intensity images, which have been assigned to NBE emission and different BSF types (see Figure 9.13). Some whitish features in (c) have been marked by dashed circles (see text). *Sample G1284.*

and  $E$ , respectively. In general, spatially separated emission of NBE (green) and of the defects (red, blue, magenta) is observed. Furthermore, almost no regions are present, from which no emission occurs. This shows that the presence of BSFs of type  $I_2$  and  $E$  locally reduces the NBE emission in favor of the defect-related emission, as already observed in Figure 9.9.

Figure 9.14(c) correlates NBE (green) and BSFs of type  $I_1$  (magenta). In this case, a different behavior as compared to the previous case is observed: Mainly green and magenta, as well as whitish features (marked for clarity), and dark regions (no emission) are observed. As indicated in the color coding, whitish features are due to spatial coincidence of emission related to NBE and BSFs of type  $I_1$ . This shows that the reduction of the NBE emission due to the presence of BSFs of type  $I_1$  is not as pronounced as in the case of BSFs of type  $I_2$  and  $E$ .

Section 9.1 showed that the presence of BSFs in SAG GaN NCs in general reduced the NBE emission. However, in order that such a reduction can occur, one has to take into account, that free carriers which are excited not directly at the defect position have to diffuse to the extended defects. Consistently, the location of the individual BSFs was observed to affect the reduction of the NBE emission. If the density and distribution of the BSFs in the NCs is such, that the mean distance between the defects is smaller than the free carrier effective diffusion length of around 100 to 150 nm, mainly defect-related emission will be observed. For low defect density NCs, the position of the BSF(s) with respect to the optically dead layers (GaN template, TDs, tip region with semipolar facets) is furthermore of importance. Thus, it is suggested that the observation of spatially separated emission related to NBE and related to BSFs of types  $I_2$  and  $E$  (and zinc blende inclusions) is due to a high density of those defects in the individual NCs. On the other hand, the partial spatial agreement of emission related to NBE



and BSFs of type  $I_1$ , is suggested to be due to a lower defect density in the NCs; i.e. mean distance of the BSFs larger than the effective diffusion length of the free carriers.

## DISCUSSION

In summary, intense GaN near-band-edge cathodoluminescence from the NCs was observed, whereas the GaN template showed minor emission. Investigation of the optical properties of single NCs revealed the presence of a NC free of any extended defects. Furthermore, no yellow luminescence from the NCs was observed. PL experiments (not shown) which were performed on MBE-grown GaN reference layers on GaN template<sup>4</sup> or truly bulk GaN<sup>5</sup>, showed the presence, and absence of yellow luminescence, respectively. The first layer is slightly strained, the latter unstrained. These layers were grown within a short period after the investigated NC samples. Raman experiments (see Section 8.2) revealed the strain-free nature of the SAG NCs. Theory suggests that Ga vacancies<sup>[34]</sup> or substitutional carbon impurities on N sites<sup>[35]</sup> are the cause for yellow luminescence in GaN. However, at typical MBE working conditions, i.e. substrate and effusion cells at typically used temperatures, no molecular masses related to carbon were detected by quadrupole mass spectrometry in the residual gas (not shown). Therefore, the unintentional incorporation of C is ruled out. Thus, the absence of yellow luminescence in the case of strain-free SAG NCs, as well as for layers on bulk GaN, suggests that the unintentional incorporation of Ga vacancies was suppressed due to the strain-free nature of the crystal.

Besides intense GaN NBE emission, a broad defect-related luminescence band in the energy range of 2.80 – 3.42 eV was observed for the SAG NC ensemble. In single NCs with low defect density, the optical fingerprints of three BSFs of type  $I_1$ , and presumably a single BSF of type  $E$  were observed. In the case of a high defect density NC, optical transitions in agreement with the presence of BSFs of type  $I_1$ ,  $I_2$ , and  $E$ , as well as zinc blende inclusions were found. As discussed in Section 8.1.2, it is not clear, whether a self-induced incorporation mechanism of BSFs in SAG GaN NCs with semipolar faceted tips is present. However, the presented results indeed suggest, that the incorporation of BSFs of types  $I_2$  and  $E$  might be correlated.

Due to the relatively small diameter of the NCs, mainly extended BSFs were observed. This circumvents the appearance of additional luminescence features—e.g. due to partial dislocations—which are observed in GaN layers which contain non-extended BSFs<sup>[28]</sup>. Furthermore, due to the varying

4 *Sample G1286*: 70 nm MBE GaN grown under slightly Ga-rich conditions on Oxford Instruments-TDI GaN(0001) template on sapphire.

5 *Sample G1289*: 50 nm MBE GaN grown under slightly Ga-rich conditions on AMMONO GaN(0001) substrate.

density of the defects, which is in the range of single BSFs to agglomeration of BSFs, the SAG NCs are a model case for the investigation of the luminescence characteristics of single extended defects, as well as for the investigation of possible defect-interactions and the consequences on the luminescence properties.

Part III

CONCLUSION



---

## SUMMARY AND OUTLOOK

---

This work investigated the homoepitaxial selective area growth (SAG) of gallium nitride (GaN) nanocolumns (NCs) by molecular beam epitaxy (MBE). Comprehensive studies of the selective area growth mechanism, the structural properties of the NCs, as well as the correlation of optical and structural properties are presented. Besides the precise position control of the regularly arranged NCs in arrays—which is prerequisite for future NC-based device processing—the SAG approach allowed for the analysis of single GaN nanocolumns concerning their structural and optical properties.

The growth of ordered GaN columns with diameters in the range of one hundred nanometer up to the micron scale was achieved by regular patterning of thin Mo layers on GaN(0001) template by electron beam lithography or pulsed laser ablation. It has been well-established in literature, that the growth of GaN NCs by MBE is assisted by Ga diffusion. This kinetic description was adapted and experimentally verified for the investigated diameter range. Analysis of the axial growth rate as function of array design parameters or NC height allowed to estimate Ga adatom diffusion lengths on the Mo layer and on the sidewall surfaces of the GaN NCs for the used growth conditions. These parameters are of major importance for fine-tuning of NC growth rates, as well as for the understanding of local dynamical growth conditions. Experimental evidence was given that the growth of SAG NCs with sufficiently small diameter proceeded in the beginning of growth in the N-limited growth regime, despite the fact that nominally nitrogen excess conditions were used.

A property of wurtzite GaN NCs, which is controversially discussed in literature is the crystal polarity. It describes the orientation of the Ga–N dimer along [0001] and determines for example the direction of internal electric fields in GaN-based heterostructures. Well-established techniques for the determination of the polarity of GaN have been used in this work to assess and consolidate the Ga-polarity of the SAG GaN NCs which were grown on Ga-polar GaN templates. In addition, the polarity of self-induced NCs which have been grown mainly on areas of the unpatterned Mo layer was determined. In this case, N-polarity was found. A method to control the polarity of the SAG GaN NCs is the choice of the substrate. Using silicon carbide 6H-SiC(0001) substrates instead of GaN templates,

the selective area growth of N-polar SAG GaN NCs was achieved. In addition, an approach for the polarity inversion of these SAG GaN NCs was presented. The Ga-polar SAG NCs possess a distinct morphology with nonpolar sidewalls ( $\{1\bar{1}00\}$ , as well as  $\{11\bar{2}0\}$  surfaces) and semipolar surfaces at the pyramidal tip. This is in contrast to the N-polar NCs which show  $c$ -plane (0001) tip morphology.

The distinct morphology of the Ga-polar and N-polar GaN NCs was discussed in a thermodynamic picture. A simple model which counts the number of bonds which have to be broken to create a specific GaN surface by cleavage was used to estimate the relative energetic favorability of various GaN surfaces. The experimentally observed NC morphology was consistently explained with this model for both polarities. This work therefore suggests, that the growth of SAG (and self-induced) GaN NCs by MBE is not exclusively related to kinetics as often suggested, but rather to a concurrent interplay of thermodynamics and kinetics.

Dislocations in single Ga-polar NCs were investigated by transmission electron microscopy (TEM). Threading dislocations were shown to be generated only at the interface of the NCs and the template. These defects are detrimental to the optical properties and have to be avoided, if the GaN NCs are considered for future optoelectronic device applications. Dislocation bending is known to effectively reduce the dislocation density in nanostructures. The propagation length until bending of such dislocations occurred was investigated. Based on these experimental data, this thesis provides criteria which can be used as estimate for the required NC height and diameter, in order to reduce the density of threading dislocations virtually to zero in the tip region of these NCs.

The majority of the SAG GaN NCs showed the presence of  $r$ -plane  $\{1\bar{1}02\}$  surfaces at the tip. Such semipolar surfaces are promising candidates for the realization of GaN-based heterostructures for optoelectronic devices with reduced internal electric field as compared to conventional heterostructures, for which the growth surface is the  $c$ -plane. Feasibility of Ga-polar SAG GaN NCs for the growth of such semipolar heterostructures was investigated by the growth of AlN/GaN multi-quantum wells at the tip of the NCs. Although this was achieved, TEM investigations revealed that there is still room for improvement of the homogeneity and crystal quality of the heterostructures.

An important step towards the improvement of the structural properties of such semipolar GaN-based heterostructures is the understanding of the incorporation mechanism of extended defects, such as basal plane stacking faults (BSFs) and zinc blende inclusions in the NCs, especially in the tip region. SAG GaN NCs with dispersive density of BSFs were found by TEM: Firstly, NCs free of any extended defects were observed; secondly, NCs with only a few isolated BSFs were observed; and thirdly, NCs with a much higher density of BSFs and the inclusion of zinc blende segments were

found. The exact origin of such a dispersive defect incorporation behavior however remained unclear.

Micro-Raman spectroscopy revealed that the GaN NCs are free of internal strain. Comparison of the linewidth of the  $E_2^H$  phonon mode showed that the crystal quality of the self-induced GaN NCs with typical diameters in the range of 100 nm and below is slightly superior to the one of the SAG NCs with diameters in the range of 150 nm. Nevertheless, a linewidth of about  $5\text{ cm}^{-1}$  in the case of the SAG NCs, is comparable to results reported in literature for ensembles of self-induced GaN NCs.

In the last part of this work, the optical properties of the nanocolumns were assessed by scanning transmission electron microscopy cathodoluminescence (STEM-CL) and scanning electron microscopy cathodoluminescence (SEM-CL).

To correlate the optical emission characteristics with the structural properties on the nanoscale, single SAG GaN NCs were investigated by STEM-CL. For this experiment, an optimized cross sectional preparation approach by focused ion beam (FIB) was developed. Due to this approach, focused ion beam-induced damage and consequent quenching of the cathodoluminescence was largely circumvented. This allowed to assess the optical properties of single NCs which showed strong variations in the density of extended defects. In the case of a NC free of any extended defects, exclusively GaN near-band-edge (NBE) luminescence was observed. For a GaN NC with one isolated extended defect, the optical fingerprint of a BSF of type  $E$  was observed in addition to the NBE luminescence. Another NC with three extended defects showed luminescence characteristics which were attributed to BSFs of type  $I_1$  and GaN NBE. A plethora of luminescence lines energetically positioned below NBE emission was observed for a NC with a significantly higher density of extended defects. In this case, presumably luminescence due to BSFs of type  $I_1$ ,  $I_2$ ,  $E$  and zinc blende inclusions was observed.

The optical properties of ensembles of SAG GaN NCs were assessed by SEM-CL experiments. Intense GaN NBE luminescence at 3.46 eV was observed from the NCs. A further indication of the high crystal quality of the NCs is the fact that no yellow luminescence was observed from the SAG NCs. This broad luminescence band in the energy range of 2.0 – 2.6 eV is commonly observed in GaN layers and attributed to the incorporation of point defects, such as vacancies or impurities. This suggests that the strain-free nature of the NCs suppressed the formation of these point defects. However, the NBE luminescence among the NC ensemble was observed to be spatially inhomogeneously distributed and locally reduced in favor of defect-related luminescence. The insight which was gained from the investigation of single NCs was used to further interpret the SEM-CL ensemble measurements. The spatial coincidence of various luminescence lines among the NC ensemble was investigated. Evidence was found that for the Ga-polar SAG GaN NCs,



the formation of BSFs of types  $I_2$  and  $E$  within the same NC often occurs, while in the case of the BSFs of type  $I_1$ , the exclusive formation of this defect type is favored.

#### 10.1 OUTLOOK

This thesis provides a solid foundation for future research activities on the selective area growth of GaN nanocolumns by molecular beam epitaxy.

From a technological point of view, switching to a high-throughput, high-resolution patterning technique for the fabrication of the SAG arrays is highly recommended. A compatible method is nanoimprint lithography which is based on mechanical deformation of an imprint resist by a mold. This allows for an immense reduction in the processing time, as well as for enhanced reproducibility of the SAG arrays.

Concerning the selective area growth mechanism, the diameter-dependent growth rate of the nanocolumns, which is in contradiction to growth models based on Ga diffusion, requires further investigation. Analysis of the size-dependent incubation time for the nucleation of GaN, as well as *in situ* growth rate analysis by the introduction of Si markers are promising experiments to further refine the understanding of the growth mechanism.

Concerning the defect-related optical properties, the GaN nanocolumns are a model case for the study of the luminescence properties of individual basal plane stacking faults, as well as possible coupling effects in the case of higher defect densities.

With regard to GaN-based optoelectronic devices based on dense arrays of GaN columns with semipolar surfaces at the tip, following issues have to be addressed: First, the incorporation behavior of basal plane stacking faults in the nanocolumns and possible correlations with the inclination of the semipolar surfaces have to be investigated. Possible factors which influence the incorporation probability are the NC diameter and the growth conditions. TEM investigations in combination with variation of these parameters are expected to shed some light into this topic which is of major importance for the reduction of the density of extended defects. Second, the growth of semipolar  $\text{In}_x\text{Ga}_{1-x}\text{N}/\text{GaN}$  heterostructures at the tip of these columns, and the incorporation behavior of In has to be investigated. Spectroscopic methods, such as photo- or cathodoluminescence, in combination with transmission electron microscopy are suited methods for these investigations. In fact, this topic is currently addressed in the research group.

The widespread field of research which covers fundamental research, as well as application-oriented research, motivates further activities on the selective area growth of GaN nanocolumns by molecular beam epitaxy.

# A

---

## APPENDIX

---

### A.1 EXPERIMENTAL SETUPS, ROUTINES, AND PROCEDURES

The following list describes the experimental setups and procedures which were used in this thesis. If possible, the appropriate order was chosen according to the appearance in this thesis.

- **Wafer dicing saw:** *DAD320* from DISCO Corp.. The 2-inch wafers were cut into  $10 \times 10 \text{ mm}^2$  pieces.

- **Sample cleaning after dicing:** To remove dicing remains and to degrease the GaN templates, they were treated in an ultrasonic bath (power 2) using acetone, methanol, and deionized water. Each step was 2 min, the first two steps have been repeated. The used solvent was rinsed with new solvent over the old beaker and a new beaker was used for each step. Afterwards, the samples were blown dry thoroughly with dry nitrogen.

In the case of SiC, the same approach without the use of an ultrasonic bath was used for cleaning.

- **Mo deposition:** *Univex 350* from Oerlikon Leybold Vacuum. Onto the cleaned samples, 10 to 20 nm Mo were deposited by electron beam evaporation of solid Mo. To guarantee deposition uniformity, the sample holder was rotated with 10 rpm. Furthermore, the sample holder was cooled during deposition to room temperature. The electron beam acceleration voltage was 7 kV and the power (i.e. beam current) was manually adjusted, such that a deposition rate of  $1 \text{ \AA s}^{-1}$  was achieved. For typical crucible Mo fill levels, this translates to a power value of around 25 % (internal parameter). Deposition occurred at a background pressure of  $p \leq 10^{-5}$  mbar.

- **E-beam resist (positive):** *950PMMA A2* from MicroChem Corp.. For details, see [Section A.2](#).

- **Spin coater:** *OPTIspin SB20* from SSE Sister Semiconductor Equipment GmbH. For details, see [Section A.2](#).

- **Electron beam lithography unit:** *e-LiNE* from Raith GmbH. The processing for electron beam lithography is explained in detail in [Section A.2](#).

- **E-beam developer:** *1:3 MIBK:IPA* (methylisobutylketone:isopropanol). For details, see [Section A.2](#).

- **E-beam resist remover:** *AR 300-70* from ALLRESIST GmbH. For details, see [Section A.2](#).
- **Pulsed laser ablation:** Pulsed laser ablation setup of the Laser Laboratorium Göttingen e.V.. A picosecond solid state laser *Hyperrapid 50* from Lumera Laser GmbH (Coherent, Inc.) and a wavelength of  $\lambda = 355$  nm (3rd harmonic) was used. The pulse duration was 10 ps. In the image plane of a Schwarzschild-type reflective objective, the laser beam is splitted by a diffractive phase mask (cross grid) into multiple beams. Out of these beams, a specific set is selected (here: the first 4 diffraction orders) and constructively interfered on the sample surface. Details can be found in Ref.<sup>[155]</sup>.
- **Reactive ion etching:** *PlasmalabSystem100* from Oxford Instruments. In the first step, the empty fluoride chamber was cleaned for 30 min using the recipe *Clean (CH3)*. To establish a defined composition of the residual gas in the chamber, a GaN dummy sample was then etched for around 45 s using the recipe *Mo@ch2*. This recipe uses a mixture of SF<sub>6</sub> (20 sccm) and Ar (10 sccm) gases at a process pressure of 60 mTorr. In the next step, the samples were etched with the same recipe. In the beginning of the thesis, a plasma forward power of  $P = 50$  W (13.56 MHz) and a DC bias  $U = 90$  V were used. The corresponding etch rate was  $3 \text{ \AA s}^{-1}$ . Due to a change of the plasma generator, stable plasma conditions changed to  $P = 35$  W,  $U = 65$  V, which corresponded to an etch rate of  $10 \text{ \AA s}^{-1}$ . Besides the nominal change of the etch rate, an inhomogeneous etching behavior was observed, which resulted in a reduced etch rate for aperture diameters in the range of 50 nm and below. In the case of electron beam lithography patterned samples, the nominal etch depth was chosen to be around 15 nm. This ensured, that the apertures in the Mo layer were etched down to the GaN template. In the case of pulsed laser ablation patterned samples, a nominal etch depth of 10 nm was chosen to reduce the as-deposited Mo thickness (20 nm) exactly to 10 nm.

It is worth noting, that after standard RIE treatment on clean GaN template, atomic steps were still visible. Thus, it is concluded that for the used RIE conditions, exclusively Mo is etched and the sputter rate for GaN due to Ar<sup>+</sup> ions is negligible.

- **Sample cleaning right before growth:** Prior to insertion into the MBE system, the patterned samples were cleaned for 2 min in acetone, methanol, and deionized water and blown dry with dry nitrogen. Each step was performed only once without the use of an ultrasonic bath in order not to damage the thin Mo layer on the samples. Directly after this step, the GaN templates were inserted into the MBE. In the case of SiC, the samples were treated for 2 min in hydrofluoric acid (HF 48%) and rinsed for 2 min in deionized water to remove the native oxide at the surface. After this step, the SiC substrates were inserted into the MBE.

- **Atomic force microscope:** *5600LS* from Agilent Technologies. AFM cantilevers *Tap300Al-G* from BudgetSensors with a resonant frequency of around 300 kHz were used. The tip radius is below 10 nm.
- **Molecular beam epitaxy:** *Mod GEN II* from Veeco Instruments GmbH. A Veeco *UNI-Bulb RF Plasma source* for nitrogen (6N) and a *Hot Lip SUMO Source* for Ga (7N) effusion were used. Before growth, the samples were heated in the MBE intro chamber for 10 min at 200 °C in order to reduce organic contaminants and water. Outgassing at 600 °C for the same duration occurred subsequently in the buffer chamber.
- **Scanning electron microscope:** *Leo Supra 35* from Carl Zeiss Microscopy GmbH. All micrographs were recorded using the In-Lens secondary electron detector.
- **Silicon nitride deposition:** *PlasmalabSystem100* from Oxford Instruments. In order to protect the samples for preparation of TEM lamellae by FIB, 200 nm Si<sub>3</sub>N<sub>4</sub> was deposited by plasma enhanced chemical vapor deposition (PECVD). The recipe *Si3N4 Dep mix RF LF Basic* was used, which supplies a mixture of N<sub>2</sub> (380 sccm), NH<sub>3</sub> (30 sccm), and 5% SiH<sub>4</sub>/Ar (400 sccm) gases. The temperature of the substrate holder was 300 °C. Further process parameters are: High frequency (HF) power  $P = 20$  W, low frequency (LF) pulse power  $P = 20$  W. Forward and reflected power were adjusted to 13 and 7 W, respectively. The deposition rate of around 3.6 nm min<sup>-1</sup> is low as compared to the rate of about 6.7 nm min<sup>-1</sup> which is achieved with the alternative recipe *Si3N4 Dep RF Only Basic* which does not use the low frequency pulses. However, in the former case, the deposited layers show reduced film stress and improved film quality.
- **Focused ion beam:** Dual beam *Nova 600 NanoLab* from FEI. The preparation of TEM lamellae by FIB is explained in detail in [Section A.7](#).
- **Ar<sup>+</sup> ion etching:** *PIPS* (Precision Ion Polishing System) from Gatan, Inc.. For details, see [Section A.7](#).
- **Transmission electron microscopes:** *CM200-FEG-UT* from Philips and *Titan ETEM G2* from FEI. Microscope parameters are given in [Table A.4](#).
- **Raman spectroscopy:** Non-resonant micro-Raman scattering setup of the University of Valencia, Spain. An Ar laser *Innova 70C* from Coherent, Inc. with an excitation wavelength of 514.5 nm and a 100x microscope objective was used to focus the laser onto the sample in backscattering geometry. The spectral and spatial (laser beam diameter) resolution were about 1 cm<sup>-1</sup> and 1 μm, respectively. The light was dispersed using a *T64000 spectrometer* and detected by a CCD *CCD-3000V*, both from HORIBA Yobin-Yvon. Measurements were performed at room temperature.
- **Scanning transmission electron microscopy cathodoluminescence spectroscopy:** STEM-CL setup of the University of Magdeburg, Germany. A *Tecnai F20 twin STEM* from FEI with HAADF and ADF detector (*Model 3000* from E.A. Fischione Instruments, Inc.) was used in combination with

a CL spectroscopic unit *MonoCL4* from Gatan, Inc.. A liquid He single tilt TEM-cryo-sample holder allowed for measurements at 15 K. The acceleration voltage was 80 kV. The preparation of TEM lamellae for STEM-CL by FIB is described in detail in [Section A.7](#).

- **Scanning electron microscopy cathodoluminescence spectroscopy:** SEM-CL setup of the University of Magdeburg, Germany. A *JSM 6400* SEM from JEOL was used. A liquid He cryo-sample holder allowed for measurements at 6 K. The light was collected by an ellipsoidal mirror, dispersed by a monochromator (*M270* from SPEX) and detected by a Si/InGaAs Reticon diode. The acceleration voltage was 3 kV.

- **Photoluminescence spectroscopy:**

(1) PL setup of the University of Valencia, Spain. An He-Cd laser from Kimmon Koha Co., Ltd. with an excitation wavelength of 325 nm and a 40x microscope objective was used to focus the laser onto the sample in backscattering geometry. The spectral resolution was below 1 meV, the diameter of the focused laser beam about 4  $\mu\text{m}$ . A liquid He cryostat allowed measurements at around 5 K. The spectrometer and detector setup was analogous to the Raman setup.

(2) PL setup of the Georg-August-University of Göttingen, Germany (results not shown). An He-Cd laser *IK3452R-F* from Kimmon Koha Co., Ltd. with an excitation wavelength of 325 nm was used. The light was detected by a CCD *LN/CCD1752PB/VISAR* from Princeton Instruments, Inc.. A liquid He cryostat allowed measurements at around 4 K.

## A.2 ELECTRON BEAM LITHOGRAPHY

After Mo deposition onto the cleaned substrates, the samples were treated on a hotplate for 1 min at 90 °C to remove possible remains of solvents. This step was left out, if the Mo layer was deposited right before further preparation. Reaching ambient temperature, three droplets e-beam resist (pipette volume of 45  $\mu\text{l}$ ) were deposited on the sample. This quantity completely wets the sample, resist creeping to the backside of the sample is however prevented due to the surface tension of the resist. The resist was then spin coated at 6000 rpm for 60 s which results in a film thickness of about 40 nm. The resist was hardened at a temperature of 180 °C for 5 min.

In order to achieve well-defined aperture diameters, optimal e-beam exposure doses were determined by dose testing in the first step. For this purpose an initial exposure dose  $D_i = I \cdot t_d \cdot s^{-2}$  is chosen. The beam current is given by  $I$ , the dwell time of the electron beam per pixel by  $t_d$  and the step width by  $s$ . For a test pattern which contained the relevant geometrical structures for the final array (in this case single pixels and circular areas), the exposure dose was varied via dose factors  $d_{\text{px}}$  and  $d_{\text{area}}$  for pixel and area exposure, respectively. The total exposure dose  $D$  is simply given by

$D_i \cdot d_{\text{px, area}}$  and the influence of exposure dose variation on the aperture diameter can be investigated. The dose factor for single pixels in a hexagonal arrangement in a  $5 \times 5 \mu\text{m}^2$  area was varied from  $d_{\text{px}} = 0.011 - 109$  in order to investigate the diameter of the apertures as function of exposure dose. The dose factor for areas was varied from  $d_{\text{area}} = 0.1 - 2$ . The layout for exposure dose testing, an enlargement of one of the single pixel arrays in hexagonal arrangement and the evaluation of the aperture diameter as function of exposure dose is shown in [Figure A.1](#).

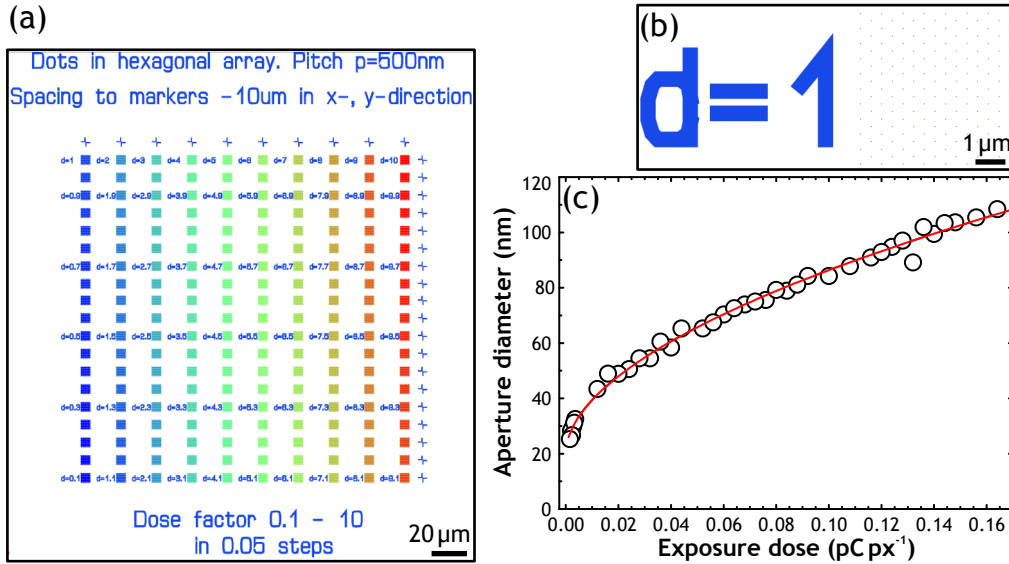


**Figure A.1:** (a) GDSII layout for pixel exposure dose testing. The color scale indicates minimal and maximal dose factors ranging from blue to red, respectively. Only the layout for a dose factor variation from 0.1 to 10 is shown. (b) Enlargement of the test layout for pixel exposure with a dose factor of  $d_{\text{px}} = 1.0$ . The obtained aperture diameter as function of exposure dose for single pixel exposure in hexagonal arrangement is shown in (c). The pitch was  $p = 500 \text{ nm}$ . Acceleration voltage  $U$  and aperture  $A$  were  $20 \text{ kV}$  and  $7.5 \mu\text{m}$ , respectively.

After exposure, the samples were developed for 30 s in the developer at  $4^\circ\text{C}$ , rinsed for 1 min in isopropanol and blown dry with  $\text{N}_2$ . The exposed pattern was then transferred into the Mo layer by RIE as described in [Section A.1](#). Afterwards, the remaining resist was stripped by keeping the samples for 30 min in a remover and subsequent spray-washing using a medical injection. The solvent was rinsed for 2 min in deionized water. The obtained apertures were investigated by AFM or SEM, which allowed for choosing the appropriate exposure doses in order to obtain aperture diameters  $d \geq 30 \text{ nm}$ .

Note, that fabrication of apertures with diameters  $\geq 100 \text{ nm}$  by pixel exposure is critical due to excessive resist exposure which results in overexposure, as shown in [Figure A.2](#).

**Figure A.2:** AFM topography micrographs of EBL patterned 10 nm thin Mo layers. A pixel exposure dose below (a) and above (b) the overexposure threshold was used.

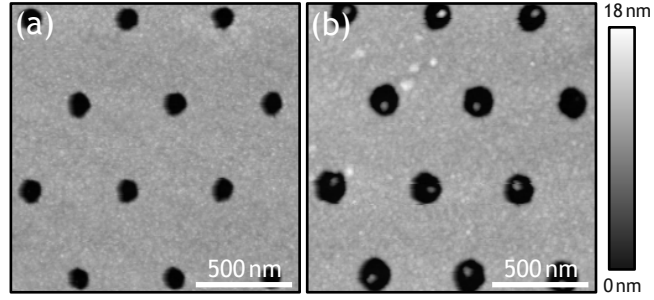


Figure A.2(a) shows a typical AFM image of SAG apertures which have been completely etched down to the GaN template. Overexposing each pixel (b) results in an chemical inertness of the resist with respect to the developer. The obtained apertures in the mask after RIE treatment were donut-shaped and resist residues remained in the apertures. SAG GaN NCs grown within such apertures will show a hollow core region. However, if the growth duration is long enough, this core will coalesce and the typical pyramidal SAG NC tip morphology is obtained (*Sample G1300*, not shown).

For this reason, area exposure is more suited for the fabrication of SAG apertures by EBL. Typical exposure parameters for area exposure are listed in Table A.1. Note, that for the different pitch values, slightly different dose factors were used to circumvent the proximity effect which results in an overexposure for small pitch values if constant dose factors are used.

Aperture pitch $p$ ( $\mu\text{m}$ )	Aperture diameter $d$ (nm)			
	50	75	100	$\geq 250$
0.25	1.780	1.430	1.359	1.00
0.5	1.661	1.470	1.470	1.297
$\geq 0.75$	1.774	1.494	1.494	1.268

**Table A.1:** Optimized electron beam lithography dose factors  $d_{\text{area}}$  at the end of this thesis for an area exposure dose  $D_{\text{area}} = 350 \text{ pC cm}^{-2}$ . An acceleration voltage of  $U = 20 \text{ kV}$ , an aperture size of  $A = 10 \mu\text{m}$  (typical beam currents in the range of  $30 - 45 \text{ pA}$ ), a beam speed  $v$  of around  $4 \text{ mm s}^{-1}$ , and a step size of  $s = 3.2 \text{ nm}$  was used. Suited pixel exposure doses  $D_{\text{px}}$  can be obtained from Figure A.1.

## A.3 NITROGEN FLUX CALIBRATION

Nitrogen flow $F_{\text{N}_2}$ (sccm)	Plasma source power $P$ (W)	Effective N flux $F_{\text{N}}$ (nm min <sup>-1</sup> )
0.5	360	3.7
1	400	6.2
1.35	450	7.5

**Table A.2:** Calibrated effective nitrogen flux for typically used nitrogen plasma source parameters according to [Section 6.2](#). The conversion factor from nm min<sup>-1</sup> to atoms cm<sup>-2</sup> s<sup>-1</sup> is  $7.42 \cdot 10^{13}$ .

## A.4 INCUBATION TIME DURING SAG

*Size-dependent incubation time*

To investigate the initial stage of growth during the SAG process, a set of samples was grown using standard SAG conditions. The growth time was varied between 30 and 52 min. SAG array design *M* was used for this analysis. Prior to growth, it was verified that the apertures of the SAG arrays were etched down to the GaN template (*Sample G1507*, AFM measurements not shown). After growth, the samples were investigated by SEM, as shown in [Figure A.3](#).

After 30 min of growth, almost no GaN nucleation is observed for apertures with  $d \leq 100$  nm. Some individual GaN nuclei are formed mainly at the edges of the apertures. This result is independent of the aperture pitch (not shown). For apertures with  $d = 250$  nm, centered nucleation of GaN is observed. For the investigated area, each aperture contained at least one nanostructure with hexagonal pyramidal morphology. This morphology corresponds to the formation of semipolar GaN surfaces. Increasing the growth time to 52 min, GaN nucleation was also observed for the apertures with  $d \leq 100$  nm. However, the nucleation was inhomogeneously distributed and only about 70 to 80% of the apertures contained a nanostructure. This value increased to slightly below 100% for a pitch of 500 nm. For a pitch of 750 nm, eventually all apertures—independent of diameter—contain at least one nanostructure (not shown).

The driving force for crystallization is supersaturation which is related to the effective flux at the sample surface (see [Section 3.2.1](#)). According to [Section 7.1.3](#), an increase of aperture pitch, while keeping the aperture diameter constant, will result in an increase of the effective Ga flux in the apertures and consequently in an increase of the supersaturation. Follow-



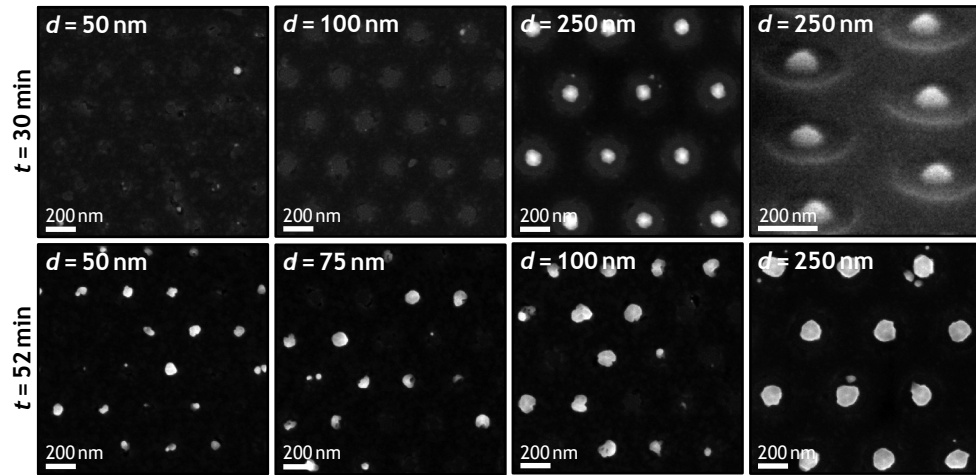


**Figure A.3:** SEM micrographs after 30 and 52 min of growth. The pitch is 250 nm for all images, the nominal aperture diameter is indicated. The topmost right image is a bird's eye view image, all other images were recorded in top-view geometry. The array with aperture diameter of 75 nm and growth time of 30 min is not shown. *Samples G1499 (30 min) and G1507 (52 min).*

ing this argumentation in the case of the sample grown for 30 min, the arrays with the smallest aperture diameter should locally be exposed to the highest supersaturation for constant pitch. Therefore, nucleation should occur especially for the smallest apertures. However, the opposite effect was observed.

This could indicate a size-dependent desorption flux from the nanostructures, as discussed in [Section 3.2.3](#).

Another explanation for the observed behavior might be variable heat dissipation for different aperture dimensions. Using radiative heaters<sup>1</sup> in MBE instead of solid heat conducting blocks behind the sample, it is well-established to cover the backside of the sample with a thin metal film to enhance absorption in the infrared<sup>[162,163,200]</sup>. In the case of patterned metal films on the sample surface, in principle, this could lead to a gradient temperature profile, e.g. the Mo mask having locally a higher temperature as compared to the GaN template. With decreasing aperture size, the local temperature will be mainly given by the surrounding Mo mask, and less by the GaN template. Since the desorption flux increases with temperature, one could expect in sum a lower supersaturation with decreasing aperture size.

Studies on the nucleation behavior are important for the understanding of the initial stage of selective area growth of NCs. This thesis however paid more attention to the elongation phase of the NCs. Nevertheless, in technical terms an important conclusion can be drawn from the presented results. In the case of SI NCs, the incubation time until nucleation occurs was reported to be function of Ga supply and substrate temperature<sup>[93]</sup>. For SAG

<sup>1</sup> Red to infrared range of the electromagnetic spectrum.

NCs, Figure A.3 indicates, that furthermore aperture diameter and pitch may influence the incubation times. For samples with constant aperture diameter and pitch (*T* design), the corresponding incubation time was measured by RHEED. However, for samples with different aperture diameters and pitches (*M* design), the corresponding incubation time(s) could not be measured individually. This is due to the fact that RHEED probes much larger sample surface areas as compared to the SAG array area.

#### Determination by RHEED

Figure A.4 shows the determination of the incubation time of GaN by RHEED for a SAG sample of *T* design. The electron beam incident was  $[11\bar{2}0]$ .

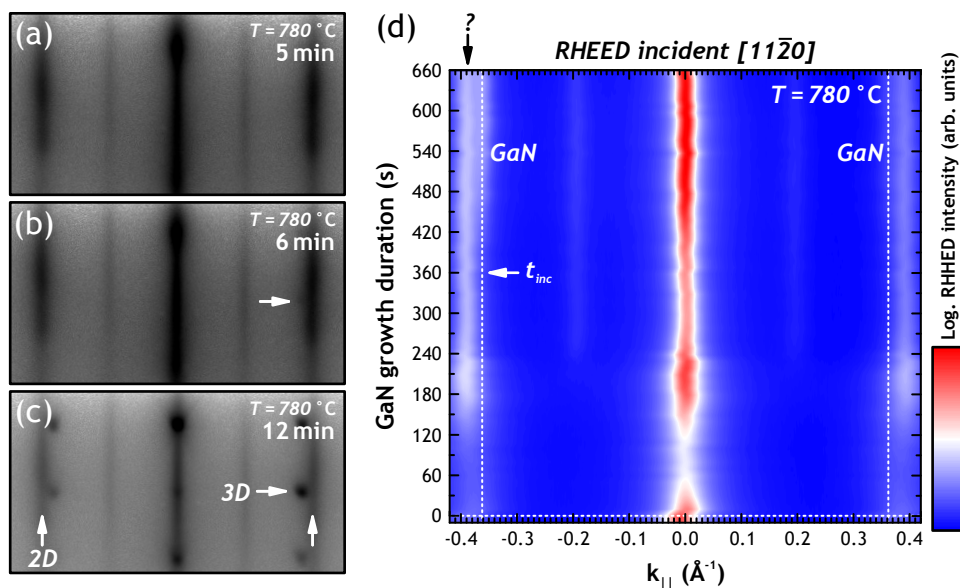


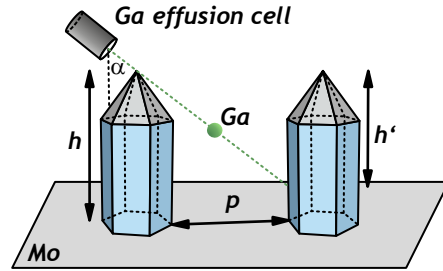
**Figure A.4:** RHEED images in  $[11\bar{2}0]$  incident for different growth time (a – c). The intensity is shown on a logarithmic scale to enhance weak intensity contributions. The time-resolved elaboration of the experiment is shown in (d). The horizontal line indicates the opening of the Ga and N shutters. The calibration of the reciprocal diffraction peak spacing was performed on a 400 nm thick GaN MBE layer grown under slightly Ga-rich conditions on GaN template (*Sample G0903*). Standard SAG conditions were used. *Sample G1302*.

After 5 min of GaN growth under standard SAG conditions, a streaky pattern is observed (a). The origin is however unknown (the diffraction pattern of molybdenum nitride showed polycrystalline diffraction rings, not shown). For 6 min growth duration, a faint, spotty pattern was observed, which is attributed to three-dimensional GaN (b). After 12 min of growth, the spotty pattern can be clearly observed (c). The corresponding time-resolved evolution of the diffraction pattern is shown in (d).

## A.5 SHADOWING EFFECTS

This paragraph discusses shadowing effects during the SAG of NCs. In the following, an ordered array of NCs with height  $h$ , diameter  $d$ , and pitch  $p$  will be considered as shown in Figure A.5. The Ga effusion cell is inclined by  $\alpha = 33^\circ$  with respect to the substrate normal. The Ga diffusion length on the NC sidewalls  $\lambda_f$  is about 250 nm (see Section 7.1.2).

Figure A.5: Schematic description for shadowing effects during the SAG of NCs by MBE.



The segment length  $h'$  of the NCs, which is directly exposed to the Ga beam from the Ga effusion cell can be calculated from geometrical considerations:

$$h' = \frac{p}{\tan \alpha} = 1.54 \cdot p. \quad (\text{A.1})$$

Table A.3 lists the average NC height, diameter, and pitch, as well as the calculated segment length  $h'$  in the *competitive regime* for *Sample G1225* which was investigated in Section 7.1.1.

$d_{\text{nom}}$ (nm)	$d$ (nm)	$p$ (nm)	$h$ (nm)	$h'$ (nm)
100	212(10)	149	445(16)	230
100	201(12)	431	545(22)	664
75	176(16)	160	421(28)	246
75	189(17)	406	559(15)	625
50	157(17)	152	527(23)	235
50	160(17)	407	579(18)	626

Table A.3: Nominal aperture diameter  $d_{\text{nom}}$ , measured nanocolumn diameter  $d$ , pitch  $p$ , and height  $h$  for the *competitive regime* after 3 h of growth. For comparison, the segment length  $h'$  was calculated, which was directly exposed to the Ga beam from the Ga effusion cell. Values in brackets denote standard deviations. *Sample G1225*.

Several conclusion can be obtained from Table A.3:

1. Shadowing of one NC by another adjacent NC ( $h' < h$ ) must be taken into account for the arrays with pitch of around 150 nm. However, a segment

length of  $h' \sim \lambda_f$  at the NC tip is directly exposed to the Ga beam. Therefore, also for the most dense arrays, growth is expected to have proceeded in *regime II* as if no shadowing occurred.

2. For all arrays with larger pitch, the complete sidewall length of the NCs was exposed to the Ga beam.
3. Complete shadowing of the Mo mask occurred (for a growth time of 3 h) only for the arrays with pitches of around 150 nm. Note, that for complete shadowing of the Mo mask, the conditions  $h' < h$  and  $d > p$  must be fulfilled.

The unit substrate area (per NC)  $A_{\text{Ga}}$ , which was exposed to the Ga beam can be calculated according to Equation A.2. For simplicity, a *c*-plane tip of the NCs was assumed.

$$A_{\text{Ga}} = \frac{\sqrt{3}}{4} p^2 \cos \alpha - \frac{h d}{2} \sin \alpha \quad (\text{A.2})$$

#### A.6 WET CHEMICAL ETCHING OF MO

The fact that the self-induced NCs grow on the Mo mask and not in randomly arranged imperfections of the mask, e.g. holes, was confirmed by wet chemical removal of the mask. GaN is chemically stable against nitric acid, while Mo is not<sup>[168,201]</sup>. Treatment of the samples in 65% HNO<sub>3</sub> at room temperature for 1 min (estimated etch rate about 20 nm min<sup>-1</sup>) was sufficient to remove the Mo mask. SEM and energy dispersive X-ray analysis showed that the Mo layer was removed completely (*Sample G1248*, not shown). After removal of the Mo mask, the self-induced NCs were lying on the GaN template due to detachment from their substrate.

#### A.7 OPTIMIZED CROSS SECTIONAL FOCUSED ION BEAM PREPARATION

FIB milling was used for the preparation of cross sectional TEM lamellae of SAG NCs. Due to the ordered growth of the NCs, the ion beam-induced damage of the samples can be reduced, once the diameter of the NCs is in the range of the thickness of the lamella. The following section describes the preparation method, the individual steps are shown in Figure A.6.

Prior to FIB, a 200 nm thick amorphous Si<sub>3</sub>N<sub>4</sub> layer was deposited on the samples via PECVD (a). The sample was transferred to the FIB and a 200 nm thick rectangular electron beam-induced Pt layer was deposited on a region of interest (b). The size of the rectangle was 12 × 1.5 μm<sup>2</sup>, acceleration voltage and beam current were 5 kV and 1.6 nA, respectively. Afterwards, a 2 μm thick ion beam-induced Pt layer was deposited onto the same area. Acceleration voltage and beam current were in this case 30 kV

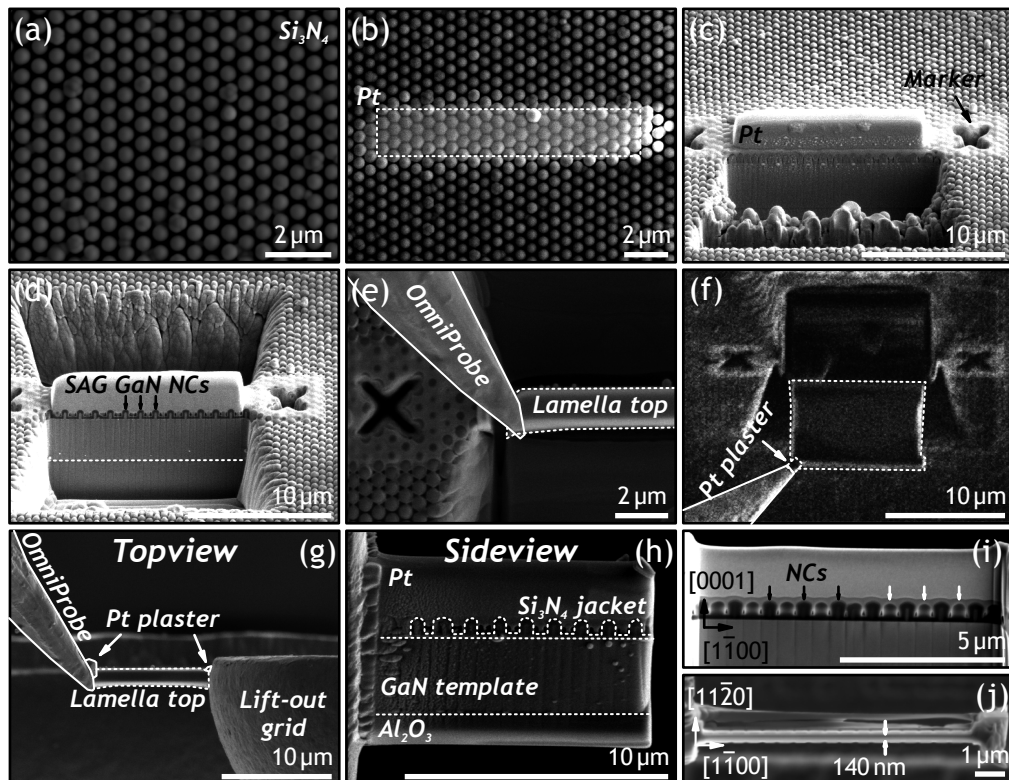


**Figure A.6:** SEM and scanning ion microscopy (f) micrographs which show different steps during the optimized cross sectional focused ion beam preparation of SAG GaN NC TEM lamellae. White arrows in (i) indicate the silicon nitride jacket of the adjacent NC row. Top-view images are (a, b, e, g, j), bird's eye view images are (c, d, f) and cross sectional side-view images are (h, i). The side- and top-view of the final lamella is shown in (i) and (j), respectively.

and 0.3 nA, respectively. Afterwards, two trenches of  $14 \times 14 \mu\text{m}^2$  size and depth of about  $10 \mu\text{m}$  were milled next to the Pt protection (c, d), using the recipe *VR-Vorpraep-schnell*. The milling direction was parallel to the growth direction of the NCs. Alternatively, this step can be performed manually using an acceleration voltage of 30 kV and an ion beam current of 7 nA. The lamella is removed with the help of the OmniProbe. For this step, the contact to the substrate is removed on one side of the lamella by ion milling. Then, the lamella is contacted mechanically to the Omniprobe and fixed by the deposition of a small Pt plaster (e). The remaining contact of the lamella to the substrate is milled and the lamella which is attached to the Omniprobe can be retracted (f). Fixing the lamella at an Omniprobe lift-out grid (g) occurs again by the deposition of Pt plasters. The contact of the lamella to the Omniprobe is milled (h) and the lamella can be thinned:

The ion beam incident direction with respect to the lamella sidewalls (NC growth direction) was  $1.2^\circ$ , such that a wedge-shape specimen geometry is obtained after milling. Iterative milling of the front- and backside of the lamella was *in situ* monitored using the e-beam setup. In the first step, an

ion beam current of 0.3 nA was used and reduced to 0.1 nA for the second step. For the third step, an ion beam inclination of  $0.7^\circ$  with respect to the lamella sidewalls and a beam current of 30 pA was used. For all the steps, the ion beam acceleration voltage was 30 kV. Due to monitoring of the milling procedure, the thinning process can be stopped precisely, such that the cross sectional lamella contains only a single row of SAG NCs which are centered along the lamella (i). As shown in Figure A.6(i) for the NC interstitial positions, the  $\text{Si}_3\text{N}_4$  jackets which correspond to the adjacent row of NCs (already milled) can be observed. For the typically investigated SAG NCs with diameters in the range of 200 nm, the thickness of the lamella at that step was accordingly about 250 nm. However, for NCs with smaller or larger diameter, the thickness of the lamella can be varied, according to the needs of the reader. To remove amorphous surface layers, the lamella was cleaned using an acceleration voltage of 5 kV, an ion beam current of 29 pA, and a beam inclination with respect to the NC growth direction of  $1.5^\circ$ . Note, that for the preparation of STEM-CL specimens, this procedure should be followed, i.e. the lamella thickness should be larger than the NC diameter in order not to damage the NCs. For HRTEM specimen preparation, the thickness of the lamella can be reduced to about 100 nm (j).

In the next step, the lamellae were polished in the PIPS system by low-energy  $\text{Ar}^+$  ions. The acceleration voltage was subsequently reduced from 2 kV to 1 kV to 0.5 kV. The corresponding ion beam currents were about 20, 10 and  $0.5 \mu\text{A}$ . Etch durations of 1, 5, and 15 min, respectively, resulted in an estimated reduction of the TEM lamellae thickness (material and procedure as described above) of about 50 nm.

## A.8 TRANSMISSION ELECTRON MICROSCOPY

### *TEM convergence angle*

The electron beam convergence angle  $\alpha$  was measured according to  $\alpha = \Theta_B \cdot a/b$ <sup>[158]</sup>.  $\Theta_B = \arcsin(\lambda \cdot g_{hkil}/2)$  is the Bragg angle,  $\lambda$  the relativistic de Broglie electron wavelength, and  $g_{hkil}$  the absolute value of the reciprocal lattice vector. The diameter of the CBED disks is given by  $a$ . The distance from the center of the (0000) reflection to the (hkil) reflection is given by  $b$ .

### *TEM parameters*

Table A.4 lists the transmission electron microscope parameters. For HRTEM multislice image simulation (JEMS software), the parameters of the Titan microscope were used (except  $C_s = 0 \text{ mm}$ ). For CBED Blochwave image



simulation (JEMS software), the parameters of the CM200 microscope have been used.

Quantity	Titan	CM200
Focus spread $\Delta$ (nm)	2.93	4
Semiconvergence angle $\alpha$ (mrad)	0.1	0.2
Semiconvergence angle $\alpha$ (mrad) (CBED)		3.6
Acceleration voltage $U$ (kV)	300	200
Spherical aberration $C_s$	$-0.273 \pm 1.584 \mu\text{m}$	0.49 mm
Information limit $q_{\text{info}}$ ( $\text{nm}^{-1}$ )	12.5	8

**Table A.4:** Transmission electron microscope parameters.

### *Defect visibility criteria in TEM*

According to diffraction contrast theory<sup>[158]</sup>, threading dislocations are invisible in the TEM for  $\mathbf{g} \cdot \mathbf{b} = 0$  and  $\mathbf{g} \cdot \mathbf{b} \times \mathbf{u} = 0$ .  $\mathbf{g}$  is the diffraction vector,  $\mathbf{u}$  the line direction of the dislocation. Two beam conditions selecting  $\mathbf{g} = (0002)$  and  $\mathbf{g} = (1\bar{1}00)$  can be used to characterize the TDs according to the invisibility criteria above. Dislocations imaged with  $\mathbf{g} = (1\bar{1}00)$  are of  $\mathbf{a}$ - or mixed type. Imaging with  $\mathbf{g} = (0002)$  identifies  $\mathbf{c}$ - or mixed type dislocations. The aperture diameter in the CM200 is slightly too large to solely select the  $\mathbf{g} = (1\bar{1}00)$  reflection and contribution from the direct beam is present. Thus, faint contrast from  $\mathbf{c}$ -type dislocations may be observed in the  $\mathbf{g} = (1\bar{1}00)$  dark field images.

In the case of stacking faults, diffraction contrast theory predicts invisibility of stacking faults in the TEM for  $\mathbf{g} \cdot \mathbf{R} = n$ . Here,  $n$  is an integer number. Furthermore, due to the atomic arrangement of the wurtzite structure, BSFs can only be observed in  $[11\bar{2}0]$  zone axis geometry. This implies, that for  $\mathbf{g} = (1\bar{1}00)$ , BSFs of type  $E$  and  $I_3$  are invisible due to their displacement vector which is aligned along  $\langle 0001 \rangle$ . For  $\mathbf{g} = (0002)$ , all BSFs will become invisible. The displacement vectors of BSFs are listed in [Section 2.1.2](#).

### A.9 PHOTOLUMINESCENCE

Photoluminescence (PL) experiments have been performed to complement the analysis of the optical properties of the SAG GaN NCs, as well as to complement the correlation of structural and optical properties. The experiments were carried out by E. Secco, N. Garro, and A. Cantarero in a collaboration with the University of Valencia, Spain. PL spectroscopy was performed with an excitation wavelength of 325 nm at liquid He temperature.

The spectral resolution was below 1 meV, the diameter of the focused laser beam about  $4\ \mu\text{m}$ .

Different SAG arrays from a standard as-grown SAG sample with  $M$  design were investigated. Figure A.7 shows PL spectra of SAG NCs with different diameter.

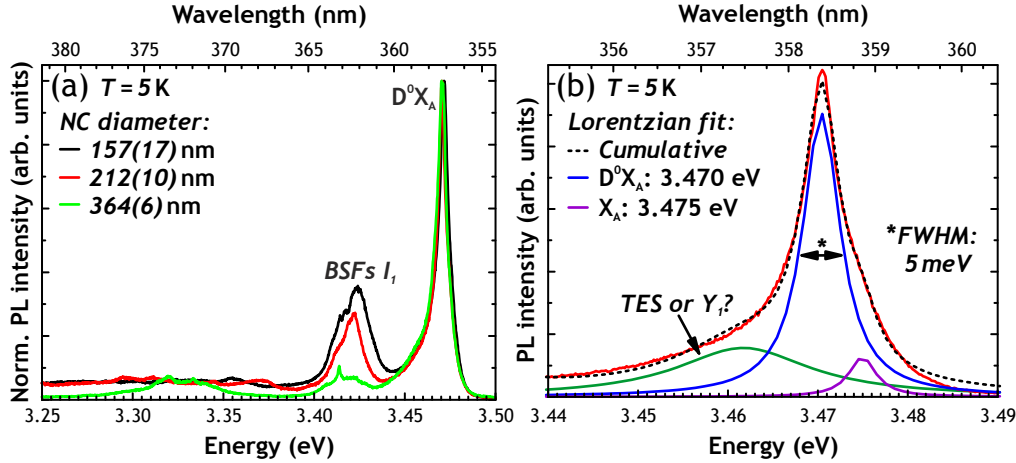


**Figure A.7:** (a) Normalized PL spectra of SAG GaN NCs with different diameters; the brackets denote standard deviations. The pitch was  $\sim 400\ \text{nm}$  for NCs with diameter of about  $360\ \text{nm}$ , and  $\sim 150\ \text{nm}$  for the NCs with smaller diameters. (b) PL spectrum in the energy range of GaN NBE emission for the NCs with diameter of about  $212\ \text{nm}$ . The spectrum was deconvoluted according to Lorentzian peak fits. *Sample G1225.*

Figure A.7(a) shows that the intensity of the luminescence band which is related to BSFs of type  $I_1$ , decreases for increasing NC diameter. The penetration depth of the laser light in GaN is about  $83\ \text{nm}$ <sup>[202]</sup>. Accordingly, only the tips of the NCs contributed to the PL spectra. This indicates, that the diameter of the NCs affects the incorporation probability of BSFs of type  $I_1$  in the tip region of the NCs. The number of SAG NCs which contributed to the spectra was calculated to be about 24, 111, and 151 for decreasing diameter.

Figure A.7(b) shows the deconvolution of the GaN NBE emission. The peaks at  $3.470\ \text{eV}$  and  $3.475\ \text{eV}$  are attributed to  $D^0X_A$  and the free exciton  $X_A$ , respectively. These values are in good agreement with the expected positions in unstrained GaN, see Table 2.3. The peak attributed to  $D^0X_A$  has a linewidth (FWHM) of about  $5\ \text{meV}$ .

#### A.10 HOOKE'S LAW FOR WURTZITE SYMMETRY

In wurtzite symmetry, the fourth ranked elastic tensor  $c_{ijkl}$  can be reduced to a  $6 \times 6$  matrix in Voigt notation and Equation 2.9 reads<sup>[41,43]</sup>:



$$\begin{pmatrix} \sigma_{xx} \\ \sigma_{yy} \\ \sigma_{zz} \\ \sigma_{yz} \\ \sigma_{xz} \\ \sigma_{xy} \end{pmatrix} = \begin{pmatrix} c_{11} & c_{12} & c_{13} & 0 & 0 & 0 \\ c_{12} & c_{11} & c_{13} & 0 & 0 & 0 \\ c_{13} & c_{13} & c_{33} & 0 & 0 & 0 \\ 0 & 0 & 0 & c_{44} & 0 & 0 \\ 0 & 0 & 0 & 0 & c_{44} & 0 \\ 0 & 0 & 0 & 0 & 0 & \frac{c_{11}-c_{12}}{2} \end{pmatrix} \begin{pmatrix} \varepsilon_{xx} \\ \varepsilon_{yy} \\ \varepsilon_{zz} \\ 2\varepsilon_{yz} \\ 2\varepsilon_{xz} \\ 2\varepsilon_{xy} \end{pmatrix}, \quad (\text{A.3})$$

where  $c_{ij}$  are the elastic coefficients of GaN.

---

## BIBLIOGRAPHY

---

- [1] J. S. Speck and S. F. Chichibu. Nonpolar and Semipolar Group III Nitride-Based Materials. *MRS Bull.*, 34:304–12, 2009.
- [2] S. P. DenBaars, D. Feezell, K. Kelchner, S. Pimputkar, C.-C. Pan, C.-C. Yen, S. Tanaka, Y. Zhao, N. Pfaff, R. Farrell, M. Iza, S. Keller, U. Mishra, J. S. Speck, and S. Nakamura. Development of gallium-nitride-based light-emitting diodes (LEDs) and laser diodes for energy-efficient lighting and displays. *Acta Mater.*, 61:945–51, 2013.
- [3] H. Masui, S. Nakamura, S. P. DenBaars, and U. K. Mishra. Nonpolar and Semipolar III-Nitride Light-Emitting Diodes: Achievements and Challenges. *IEEE T. Electron. Dev.*, 57:88–100, 2010.
- [4] M. T. Hardy, D. F. Feezell, S. P. DenBaars, and S. Nakamura. Group III-nitride lasers: a materials perspective. *Mater. Today*, 14:408–415, 2011.
- [5] J. Wu. When group-III nitrides go infrared: New properties and perspectives. *J. Appl. Phys.*, 106:011101, 2009.
- [6] F. Scholz. Semipolar GaN grown on foreign substrates: a review. *Semicond. Sci. Technol.*, 27:024002, 2012.
- [7] K. Fujito, S. Kubo, and I. Fujimura. Development of Bulk GaN Crystals and Nonpolar/Semipolar Substrates by HVPE. *MRS Bull.*, 34:313–7, 2009.
- [8] H. Sekiguchi, K. Kishino, and A. Kikuchi. Emission color control from blue to red with nanocolumn diameter of InGaN/GaN nanocolumn arrays grown on same substrate. *Appl. Phys. Lett.*, 96:231104, 2010.
- [9] K. A. Bertness, A. W. Sanders, D. M. Rourke, T. E. Harvey, A. Roshko, J. B. Schlager, and N. A. Sanford. Controlled Nucleation of GaN Nanowires Grown with Molecular Beam Epitaxy. *Adv. Funct. Mater.*, 20:2911–5, 2010.
- [10] W. Bergbauer, M. Strassburg, Ch. Kölper, N. Linder, C. Roder, J. Lähne-  
mann, A. Trampert, S. Fündling, S. F. Li, H.-H. Wehmann, and A. Waag. Continuous-flux MOVPE growth of position-controlled N-face GaN nanorods and embedded InGaN quantum wells. *Nanotechnology*, 21: 305201, 2010.

- [11] A. Bengoechea-Encabo, F. Barbagini, S. Fernandez-Garrido, J. Grandal, J. Ristic, M. A. Sanchez-Garcia, E. Calleja, U. Jahn, E. Luna, and A. Trampert. Understanding the selective area growth of GaN nanocolumns by MBE using Ti nanomasks. *J. Cryst. Growth*, 325: 89–92, 2011.
- [12] S. Li and A. Waag. GaN based nanorods for solid state lighting. *J. Appl. Phys.*, 111:071101, 2012.
- [13] R. Calarco, T. Stoica, O. Brandt, and L. Geelhaar. Surface-induced effects in GaN nanowires. *J. Mater. Res.*, 26:2157–68, 2011.
- [14] H. Morkoç. *Handbook of Nitride Semiconductors and Devices: Materials Properties, Physics and Growth*, volume 1. WILEY-VCH Verlag GmbH & Co. KGaA, Weinheim, 2008.
- [15] H. Morkoç. *Handbook of Nitride Semiconductors and Devices: Electronic and Optical Processes in Nitrides*, volume 2. WILEY-VCH Verlag GmbH & Co. KGaA, Weinheim, 2008.
- [16] C.-Y. Yeh, Z. W. Lu, S. Froyen, and A. Zunger. Zinc-blende – wurtzite polytypism in semiconductors. *Phys. Rev. B*, 46:10086–97, 1992.
- [17] F. Bernardini, V. Fiorentini, and D. Vanderbilt. Spontaneous polarization and piezoelectric constants of III-V nitrides. *Phys. Rev. B*, 56: R10024–7, 1997.
- [18] J. F. Nicholas. The Simplicity of Miller-Bravais Indexing. *Acta Crystallogr.*, 21:880–1, 1966.
- [19] S. E. Bennett. Dislocations and their reduction in GaN. *Mater. Sci. Technol.*, 26(9):1017–28, 2010.
- [20] S. Gradečak, P. Stadelmann, V. Wagner, and M. Illegems. Bending of dislocations in GaN during epitaxial lateral overgrowth. *Appl. Phys. Lett.*, 85:4648–50, 2004.
- [21] J. K. Farrer and C. B. Carter. Defect structure in GaN pyramids. *J. Mater. Sci.: Mater. Electron.*, 41:779–92, 2006.
- [22] R. Colby, Z. Liang, I. H. Wildeson, D. A. Ewoldt, T. D. Sands, R. E. García, and E. A. Stach. Dislocation Filtering in GaN Nanostructures. *Nano Lett.*, 10:1568–73, 2010.
- [23] S. D. Hersee, A. K. Rishinaramangalam, M. N. Fairchild, L. Zhang, and P. Varangis. Threading defect elimination in GaN nanowires. *J. Mater. Res.*, 26:2293–8, 2011.

- [24] R. Datta and C. J. Humphreys. Mechanisms of bending of threading dislocations in MOVPE grown GaN on (0001) sapphire. *Phys. Status Solidi C*, 3:1750–3, 2006.
- [25] H. Blank, P. Delavignette, R. Gevers, and S. Amelinckx. Fault Structures in Wurtzite. *Phys. Status Solidi*, 7:747, 1964.
- [26] C. Stampfl and C. G. Van de Walle. Energetics and electronic structure of stacking faults in AlN, GaN, and InN. *Phys. Rev. B*, 57(24):R15052, 1998.
- [27] D. N. Zakharov, Z. Liliental-Weber, B. Wagner, Z. J. Reitmeier, E. A. Preble, and R. F. Davis. Structural TEM study of nonpolar a-plane gallium nitride grown on (11 $\bar{2}$ 0) 4H-SiC by organometallic vapor phase epitaxy. *Lawrence Berkeley National Laboratory*, pages 1–21, 2005. URL <http://www.escholarship.org/uc/item/1nr9x79t>.
- [28] R. Liu, A. Bell, F. A. Ponce, C. Q. Chen, J. W. Yang, and M. A. Khan. Luminescence from stacking faults in gallium nitride. *Appl. Phys. Lett.*, 86:021908, 2005.
- [29] I. Tischer, M. Feneberg, M. Schirra, H. Yacoub, R. Sauer, and K. Thonke.  $I_2$  basal plane stacking fault in GaN: Origin of the 3.32 eV luminescence band. *Phys. Rev. B*, 83:035314, 2011.
- [30] I. Tischer, M. Feneberg, M. Schirra, H. Yacoub, R. Sauer, K. Thonke, T. Wunderer, F. Scholz, L. Dieterle, E. Müller, and D. Gerthsen. Stacking fault-related luminescence features in semi-polar GaN. *Phys. Status Solidi B*, 248(3):611–5, 2011.
- [31] J. Lähnemann, O. Brandt, U. Jahn, C. Pfüller, C. Roder, P. Dogan, F. Grosse, A. Belabbes, F. Bechstedt, A. Trampert, and L. Geelhaar. Direct experimental determination of the spontaneous polarization of GaN. *Phys. Rev. B*, 86:081302, 2012.
- [32] C. G. Van de Walle and J. Neugebauer. First-principles calculations for defects and impurities: Applications to III-nitrides. *J. Appl. Phys.*, 95:3851, 2004.
- [33] T. Stoica and R. Calarco. Doping of III-Nitride Nanowires Grown by Molecular Beam Epitaxy. *IEEE J. Sel. Top. Quant.*, 17:859, 2011.
- [34] J. Neugebauer and C. G. Van de Walle. Gallium vacancies and the yellow luminescence in GaN. *Appl. Phys. Lett.*, 69:503–5, 1996.
- [35] J. L. Lyons, A. Janotti, and C. G. Van de Walle. Carbon impurities and the yellow luminescence in GaN. *Appl. Phys. Lett.*, 97:152108, 2010.

- [36] O. Brandt, C. Pfüller, C. Chèze, L. Geelhaar, and H. Riechert. Sub-meV linewidth of excitonic luminescence in single GaN nanowires: Direct evidence for surface excitons. *Phys. Rev. B*, 81:045302, 2010.
- [37] R. Resta. Macroscopic polarization in crystalline dielectrics: the geometric phase approach. *Rev. Mod. Phys.*, 66:899–915, 1994.
- [38] M. Grundmann. *The Physics of Semiconductors – An Introduction Including Devices and Nanophysics*. Springer-Verlag Berlin Heidelberg, 2006.
- [39] I. Vurgaftman and J. R. Meyer. Band parameters for nitrogen-containing semiconductors. *J. Appl. Phys.*, 94:3675, 2003.
- [40] F. Bernardini and V. Fiorentini. Spontaneous versus Piezoelectric Polarization in III–V Nitrides: Conceptual Aspects and Practical Consequences. *Phys. Status Solidi B*, 216:391–8, 1999.
- [41] J. F. Nye, editor. *Physical properties of crystals: Their representation by tensors and matrices*. Oxford University Press, New York, 1985.
- [42] ANSI/IEEE Standard 176-1987. IEEE Standard on Piezoelectricity. Technical report, The Institute of Electrical and Electronics Engineers, Inc., New York, 1988.
- [43] A. E. Romanov, T. J. Baker, S. Nakamura, and J. S. Speck. Strain-induced polarization in wurtzite III-nitride semipolar layers. *J. Appl. Phys.*, 100:023522, 2006.
- [44] T. Matsuoka. Progress in MOVPE-Growth of GaN to InN. In R. Sudharsanan and C. Jelen, editors, *Quantum Sensing and Nanophotonic Devices V*, volume 6900 of *Proc. of SPIE*, 2008.
- [45] W. Martienssen and H. Warlimont, editors. *Springer Handbook of Condensed Matter and Materials Data*. Springer Berlin Heidelberg, 2005.
- [46] S. Fernández-Garrido, G. Koblmüller, E. Calleja, and J. S. Speck. In situ GaN decomposition analysis by quadrupole mass spectrometry and reflection high-energy electron diffraction. *J. Appl. Phys.*, 104:033541, 2008.
- [47] O. Ambacher, M. S. Brandt, R. Dimitrov, T. Metzger, M. Stutzmann, R. A. Fischer, A. Miehr, A. Bergmaier, and G. Dollinger. Thermal stability and desorption of Group III nitrides prepared by metal organic chemical vapor deposition. *J. Vac. Sci. Technol. B*, 14:3532, 1996.

- [48] N. Grandjean, J. Massies, F. Semond, S. Yu. Karpov, and R. A. Talalaev. GaN evaporation in molecular-beam epitaxy environment. *Appl. Phys. Lett.*, 74:1854–6, 1999.
- [49] P. Gibart. Metal organic vapour phase epitaxy of GaN and lateral overgrowth. *Rep. Prog. Phys.*, 67:667–715, 2004.
- [50] J. A. Freitas Jr. Properties of the state of the art of bulk III–V nitride substrates and homoepitaxial layers. *J. Phys. D: Appl. Phys.*, 43:073001, 2010.
- [51] I. V. Markov. *Crystal Growth for Beginners*. World Scientific Publishing Co. Pte. Ltd., 2008.
- [52] M. A. Herman, W. Richter, and H. Sitter. *Epitaxy – Physical Principles and Technical Implementation*. Materials Science. Springer-Verlag Berlin Heidelberg, 2004.
- [53] D. Broxtermann. *Towards high electron mobility in GaN(0001) based InGaN and AlGaN heterostructures*. PhD thesis, Georg-August-Universität Göttingen, 2011.
- [54] Applied Epi. *Mod GEN II MBE System Operation Manual*. Applied Epi, Inc., 4900 Constellation Drive, St. Paul, MN. 55127 USA, REV.4.01 edition.
- [55] H. Hollermann. GaN-MBE growth under different N-plasma source conditions. Master's thesis, Georg-August-Universität Göttingen, 2010.
- [56] J. Neugebauer. Ab initio Analysis of Surface Structure and Adatom Kinetics of Group-III Nitrides. *Phys. Status Solidi B*, 227(1):93–114, 2001.
- [57] K. Rapcewicz, B. Chen, B. Yakobson, and J. Bernholc. Consistent methodology for calculating surface and interface energies. *Phys. Rev. B*, 57:7281, 1998.
- [58] F. Bechstedt. *Principles of Surface Physics*. Springer-Verlag Berlin Heidelberg, 2003.
- [59] J. E. Northrup and J. Neugebauer. Theory of GaN(10 $\bar{1}$ 0) and (11 $\bar{2}$ 0) surfaces. *Phys. Rev. B*, 53:R10477, 1996.
- [60] J. E. Northrup, L. T. Romano, and J. Neugebauer. Surface energetics, pit formation, and chemical ordering in InGaN alloys. *Appl. Phys. Lett.*, 74:2319–21, 1999.

- [61] T. Yamashita, T. Akiyama, K. Nakamura, and T. Ito. Surface Reconstructions on GaN and InN Semipolar  $(11\bar{2}2)$  Surfaces. *Jpn. J. Appl. Phys.*, 48:120201, 2009.
- [62] T. Yamashita, T. Akiyama, K. Nakamura, and T. Ito. Surface Reconstructions on GaN and InN Semipolar  $(20\bar{2}1)$  Surfaces. *Jpn. J. Appl. Phys.*, 49:018001, 2010.
- [63] T. Akiyama, D. Ammi, K. Nakamura, and T. Ito. Reconstructions of GaN and InN Semipolar  $(10\bar{1}1)$  Surfaces. *Jpn. J. Appl. Phys.*, 48:100201, 2009.
- [64] J. Kioseoglou, E. Kalesaki, L. Lymperakis, Th. Karakostas, and Ph. Komninou. Atomic scale morphology, growth behaviour and electronic properties of semipolar  $\{10\bar{1}3\}$  GaN surfaces. *J. Phys.: Condens. Matter*, 25:045008, 2013.
- [65] T. Akiyama, D. Ammi, K. Nakamura, and T. Ito. Surface reconstruction and magnesium incorporation on semipolar GaN  $(1\bar{1}01)$  surfaces. *Phys. Rev. B*, 81:245317, 2010.
- [66] A. R. Smith, R. M. Feenstra, D. W. Greve, J. Neugebauer, and J. E. Northrup. Reconstructions of the GaN  $(000\bar{1})$  Surface. *Phys. Rev. Lett.*, 79:3934–7, 1997.
- [67] T. Zywietz, J. Neugebauer, and M. Scheffler. Adatom diffusion at GaN  $(0001)$  and  $(000\bar{1})$  surfaces. *Appl. Phys. Lett.*, 73(4):487–9, 1998.
- [68] G. Wulff. Zur Frage der Geschwindigkeit des Wachstums und der Auflösung der Krystallflächen. *Z. Kristallogr.*, 34(5/6):449–530, 1901.
- [69] A. V. Davydov and T. J. Anderson. THERMODYNAMIC ANALYSIS OF THE Ga-N SYSTEM. In S. E. Mohny T. D. Moustakas and S. J. Pearton, editors, *III–V Nitride Materials and Processes III*, pages 38–49. The Electrochemical Society, Inc. Pennington, New Jersey, USA, 1998.
- [70] J. Northrup, J. Neugebauer, R. Feenstra, and A. Smith. Structure of GaN  $(0001)$ : The laterally contracted Ga bilayer model. *Phys. Rev. B*, 61(15):9932–5, 2000.
- [71] E. I. Givargizov. FUNDAMENTAL ASPECTS OF VLS GROWTH. *J. Cryst. Growth*, 31:20–30, 1975.
- [72] L. E. Fröberg, W. Seifert, and J. Johansson. Diameter-dependent growth rate of InAs nanowires. *Phys. Rev. B*, 76:153401, 2007.

- [73] V. G. Dubrovskii and N. V. Sibirev. General form of the dependences of nanowire growth rate on the nanowire radius. *J. Cryst. Growth*, 304: 504–13, 2007.
- [74] V. G. Dubrovskii, N. V. Sibirev, G. E. Cirlin, I. P. Soshnikov, W. H. Chen, R. Larde, E. Cadel, P. Pareige, T. Xu, B. Grandidier, J.-P. Nys, D. Stievenard, M. Moewe, L. C. Chuang, and C. Chang-Hasnain. Gibbs-Thomson and diffusion-induced contributions to the growth rate of Si, InP, and GaAs nanowires. *Phys. Rev. B*, 79:205316, 2009.
- [75] M. Tchernycheva, C. Sartel, G. Cirlin, L. Travers, G. Patriarche, J.-C. Harmand, L. S. Dang, J. Renard, B. Gayral, L. Nevou, and F. Julien. Growth of GaN free-standing nanowires by plasma-assisted molecular beam epitaxy: structural and optical characterization. *Nanotechnology*, 18:385306, 2007.
- [76] T. Gotschke. *Untersuchungen zum geordneten Wachstum von III-Nitrid Nanodrähten - Analyse der Nukleations-, Dekompositions- und Diffusionsmechanismen*. PhD thesis, Humboldt-Universität zu Berlin, 2011.
- [77] V. G. Dubrovskii, G. E. Cirlin, and V. M. Ustinov. Semiconductor Nanowhiskers: Synthesis, Properties, and Applications. *Semiconductors*, 43:1585–1628, 2009.
- [78] G. Bruno, M. Losurdo, T.-H. Kim, and A. Brown. Adsorption and desorption kinetics of Ga on GaN(0001): Application of Wolkenstein theory. *Phys. Rev. B*, 82:075326, 2010.
- [79] D. D. Koleske, A. E. Wickenden, R. L. Henry, W. J. DeSisto, and R. J. Gorman. Growth model for GaN with comparison to structural, optical, and electrical properties. *J. Appl. Phys.*, 84:1998–2010, 1998.
- [80] L. Lymperakis and J. Neugebauer. Large anisotropic adatom kinetics on nonpolar GaN surfaces: Consequences for surface morphologies and nanowire growth. *Phys. Rev. B*, 79:R241308, 2009.
- [81] N. Newman. The energetics of the GaN MBE reaction: a case study of meta-stable growth. *J. Cryst. Growth*, 178:102–12, 1997.
- [82] S. Guha, N. A. Bojarczuk, and D. W. Kisker. Surface lifetimes of Ga and growth behavior on GaN (0001) surfaces during molecular beam epitaxy. *Appl. Phys. Lett.*, 69(19):2879–81, 1996.
- [83] T. Akiyama, T. Yamashita, K. Nakamura, and T. Ito. Ab initio-Based Study for Adatom Kinetics on Semipolar GaN(11 $\bar{2}$ 2) Surfaces. *Jpn. J. Appl. Phys.*, 48:120218, 2009.



- [84] M. Yoshizawa, A. Kikuchi, M. Mori, N. Fujita, and K. Kishino. Growth of Self-Organized GaN Nanostructures on  $\text{Al}_2\text{O}_3(0001)$  by RF-Radical Source Molecular Beam Epitaxy. *Jpn. J. Appl. Phys.*, 36(4B):L459–62, 1997.
- [85] M. A. Sanchez-Garcia, E. Calleja, E. Monroy, F. J. Sanchez, F. Calle, E. Muñoz, and R. Beresford. The effect of the III/V ratio and substrate temperature on the morphology and properties of GaN- and AlN-layers grown by molecular beam epitaxy on Si(111). *J. Cryst. Growth*, 183:23–30, 1998.
- [86] K. A. Bertness, N. A. Sanford, and A. V. Davydov. GaN Nanowires Grown by Molecular Beam Epitaxy. *IEEE J. Sel. Top. Quant.*, 17: 847–58, 2011.
- [87] T. Stoica, E. Sutter, R. J. Meijers, R. K. Debnath, R. Calarco, H. Lüth, and D. Grützmacher. Interface and Wetting Layer Effect on the Catalyst-Free Nucleation and Growth of GaN Nanowires. *Small*, 4(6):751–754, 2008.
- [88] M. Knelangen, V. Consonni, A. Trampert, and H. Riechert. In situ analysis of strain relaxation during catalyst-free nucleation and growth of GaN nanowires. *Nanotechnology*, 21:245705, 2010.
- [89] C. Chèze, L. Geelhaar, A. Trampert, and H. Riechert. In situ investigation of self-induced GaN nanowire nucleation on Si. *Appl. Phys. Lett.*, 97: 043101, 2010.
- [90] V. Consonni, M. Knelangen, L. Geelhaar, A. Trampert, and H. Riechert. Nucleation mechanisms of epitaxial GaN nanowires: Origin of their self-induced formation and initial radius. *Phys. Rev. B*, 81:085310, 2010.
- [91] V. Consonni, M. Hanke, M. Knelangen, L. Geelhaar, A. Trampert, and H. Riechert. Nucleation mechanisms of self-induced GaN nanowires grown on an amorphous interlayer. *Phys. Rev. B*, 83:035310, 2011.
- [92] E. Galopin, L. Largeau, G. Patriarche, L. Travers, F. Glas, and J. C. Harmand. Morphology of self-catalyzed GaN nanowires and chronology of their formation by molecular beam epitaxy. *Nanotechnology*, 22:245606, 2011.
- [93] V. Consonni, A. Trampert, L. Geelhaar, and H. Riechert. Physical origin of the incubation time of self-induced GaN nanowires. *Appl. Phys. Lett.*, 99:033102, 2011.

- [94] O. Landré, C. Bougerol, H. Renevier, and B. Daudin. Nucleation mechanism of GaN nanowires grown on (111) Si by molecular beam epitaxy. *Nanotechnology*, 20:415602, 2009.
- [95] K. A. Bertness, A. Roshko, N. A. Sanford, J. M. Barker, and A. V. Davydov. Spontaneously grown GaN and AlGaN nanowires. *J. Cryst. Growth*, 287:522–7, 2006.
- [96] K. A. Bertness, N. A. Sanford, J. M. Barker, J. B. Schlager, A. Roshko, A. V. Davydov, and I. Levin. Catalyst-Free Growth of GaN Nanowires. *J. Electron. Mater.*, 35(4):576–80, 2006.
- [97] R. Calarco, R. J. Meijers, R. K. Debnath, T. Stoica, E. Sutter, and H. Lüth. Nucleation and Growth of GaN Nanowires on Si(111) Performed by Molecular Beam Epitaxy. *Nano Lett.*, 7(8):2248–51, 2007.
- [98] R. K. Debnath, R. Meijers, T. Richter, T. Stoica, R. Calarco, and H. Lüth. Mechanism of molecular beam epitaxy growth of GaN nanowires on Si(111). *Appl. Phys. Lett.*, 90:123117, 2007.
- [99] R. Songmuang, O. Landré, and B. Daudin. From nucleation to growth of catalyst-free GaN nanowires on thin AlN buffer layer. *Appl. Phys. Lett.*, 91:251902, 2007.
- [100] K. A. Bertness, A. Roshko, L. M. Mansfield, T. E. Harvey, and N. A. Sanford. Mechanism for spontaneous growth of GaN nanowires with molecular beam epitaxy. *J. Cryst. Growth*, 310:3154–8, 2008.
- [101] F. Furtmayr, M. Vielemeyer, M. Stutzmann, J. Arbiol, S. Estradé, F. Peirò, J. R. Morante, and M. Eickhoff. Nucleation and growth of GaN nanorods on Si(111) surfaces by plasma-assisted molecular beam epitaxy - The influence of Si- and Mg-doping. *J. Appl. Phys.*, 104:034309, 2008.
- [102] J. Ristić, E. Calleja, S. Fernandez-Garrido, L. Cerutti, A. Trampert, U. Jahn, and K. H. Ploog. On the mechanisms of spontaneous growth of III-nitride nanocolumns by plasma-assisted molecular beam epitaxy. *J. Cryst. Growth*, 310:4035–45, 2008.
- [103] A. P. Vajpeyi, A. Georgakilas, G. Tsiakatouras, K. Tsagaraki, M. Androulidaki, S. J. Chua, and S. Tripathy. Effect of substrate temperature on spontaneous GaN nanowire growth and optoelectronic properties. *Physica E*, 41:427–30, 2009.
- [104] C. Chèze, L. Geelhaar, B. Jenichen, and H. Riechert. Different growth rates for catalyst-induced and self-induced GaN nanowires. *Appl. Phys. Lett.*, 97:153105, 2010.

- [105] R. Songmuang, T. Ben, B. Daudin, D. González, and E. Monroy. Identification of III–N nanowire growth kinetics via a marker technique. *Nanotechnology*, 21:295605, 2010.
- [106] V. Consonni, V. G. Dubrovskii, A. Trampert, L. Geelhaar, and H. Riechert. Quantitative description for the growth rate of self-induced GaN nanowires. *Phys. Rev. B*, 85:155313, 2012.
- [107] N. V. Sibirev, M. Tchernycheva, G. E. Cirlin, G. Patriarche, J. C. Harmand, and V. G. Dubrovskii. Effect of Diffusion from a Lateral Surface on the Rate of GaN Nanowire Growth. *Semiconductors*, 46:838–41, 2012.
- [108] S. N. Mohammad. Substrate-mediated diffusion-induced growth of single-crystal nanowires. *J. Chem. Phys.*, 131:204703, 2009.
- [109] J.-C. Harmand, F. Glas, and G. Patriarche. Growth kinetics of a single  $\text{InP}_{1-x}\text{As}_x$  nanowire. *Phys. Rev. B*, 81:235436, 2010.
- [110] J. Johansson, C. P. T. Svensson, T. Mårtensson, L. Samuelson, and W. Seifert. Mass Transport Model for Semiconductor Nanowire Growth. *J. Phys. Chem. B*, 109:13567, 2005.
- [111] K. A. Bertness, A. Roshko, L. M. Mansfield, T. E. Harvey, and N. A. Sanford. Nucleation conditions for catalyst-free GaN nanowires. *J. Cryst. Growth*, 300:94–9, 2007.
- [112] L. Largeau, D. L. Dheeraj, M. Tchernycheva, G. E. Cirlin, and J. C. Harmand. Facet and in-plane crystallographic orientations of GaN nanowires grown on Si(111). *Nanotechnology*, 19:155704, 2008.
- [113] R. J. Meijers. *Growth and Characterisation of Group-III Nitride-based Nanowires for Devices*. PhD thesis, RWTH Aachen University, 2007.
- [114] V. G. Dubrovskii, N. V. Sibirev, G. E. Cirlin, A. D. Bouravleuv, Yu. B. Samsonenko, D. L. Dheeraj, H. L. Zhou, C. Sartel, J. C. Harmand, G. Patriarche, and F. Glas. Role of nonlinear effects in nanowire growth and crystal phase. *Phys. Rev. B*, 80:205305, 2009.
- [115] K. Tomioka, K. Ikejiri, T. Tanaka, J. Motohisa, S. Hara, K. Hiruma, and T. Fukui. Selective-area growth of III–V nanowires and their applications. *J. Mater. Res.*, 26:2127–41, 2011.
- [116] S. Ishizawa, A. Kikuchi, and K. Kishino. Selective growth of GaN nanocolumns on predeposited Al patterns by rf-plasma-assisted molecular-beam epitaxy. *Phys. Status Solidi C*, 5:1879–82, 2008.

- [117] S. Ishizawa, K. Kishino, and A. Kikuchi. Selective-Area Growth of GaN Nanocolumns on Si(111) Substrates Using Nitrided Al Nanopatterns by RF-Plasma-Assisted Molecular-Beam Epitaxy. *Appl. Phys. Express*, 1:015006, 2008.
- [118] E. Calleja, J. Ristić, S. Fernández-Garrido, L. Cerutti, M. A. Sánchez-García, J. Grandal, A. Trampert, U. Jahn, G. Sánchez, A. Griol, and B. Sánchez. Growth, morphology, and structural properties of group-III-nitride nanocolumns and nanodisks. *Phys. Status Solidi B*, 244(8): 2816–37, 2007.
- [119] L. Cerutti, J. Ristić, S. Fernández-Garrido, E. Calleja, A. Trampert, K. H. Ploog, S. Lazic, and J. M. Calleja. Wurtzite GaN nanocolumns grown on Si(001) by molecular beam epitaxy. *Appl. Phys. Lett.*, 88: 213114, 2006.
- [120] K. Kishino, T. Hoshino, S. Ishizawa, and A. Kikuchi. Selective-area growth of GaN nanocolumns on titanium-mask-patterned silicon (111) substrates by RF-plasma-assisted molecular-beam epitaxy. *Electron. Lett.*, 44(13):819, 2008.
- [121] H. Sekiguchi, K. Kishino, and A. Kikuchi. Ti-mask Selective-Area Growth of GaN by RF-Plasma-Assisted Molecular-Beam Epitaxy for Fabricating Regularly Arranged InGaN/GaN Nanocolumns. *Appl. Phys. Express*, 1:124002, 2008.
- [122] K. Kishino, H. Sekiguchi, and A. Kikuchi. Improved Ti-mask selective-area growth (SAG) by rf-plasma-assisted molecular beam epitaxy demonstrating extremely uniform GaN nanocolumn arrays. *J. Cryst. Growth*, 311:2063–68, 2009.
- [123] T. Gotschke, T. Schumann, F. Limbach, T. Stoica, and R. Calarco. Influence of the adatom diffusion on selective growth of GaN nanowire regular arrays. *Appl. Phys. Lett.*, 98:103102, 2011.
- [124] T. Schumann, T. Gotschke, F. Limbach, T. Stoica, and R. Calarco. Selective-area catalyst-free MBE growth of GaN nanowires using a patterned oxide layer. *Nanotechnology*, 22:095603, 2011.
- [125] S. Albert, A. Bengoechea-Encabo, P. Lefebvre, F. Barbagini, M. A. Sanchez-Garcia, E. Calleja, U. Jahn, and A. Trampert. Selective area growth and characterization of InGaN nano-disks implemented in GaN nanocolumns with different top morphologies. *Appl. Phys. Lett.*, 100: 231906, 2012.
- [126] A. Bengoechea-Encabo, S. Albert, M. A. Sanchez-Garcia, L. L. López, S. Estradé, J. M. Rebled, F. Peiró, G. Nataf, P. de Mierry, J. Zuniga-Perez, and E. Calleja. Selective area growth of  $a$ - and  $c$ -plane GaN

- nanocolumns by molecular beam epitaxy using colloidal nanolithography. *J. Cryst. Growth*, 354:1–4, 2012.
- [127] L. E. Jensen, M. T. Björk, S. Jeppesen, A. I. Persson, B. J. Ohlsson, and L. Samuelson. Role of Surface Diffusion in Chemical Beam Epitaxy of InAs Nanowires. *Nano Lett.*, 4(10):1961–4, 2004.
- [128] K. Xu and A. Yoshikawa. Effects of film polarities on InN growth by molecular-beam epitaxy. *Appl. Phys. Lett.*, 83:251, 2003.
- [129] D. N. Nath, E. Gür, S. A. Ringel, and S. Rajan. Molecular beam epitaxy of N-polar InGaN. *Appl. Phys. Lett.*, 97:071903, 2010.
- [130] L. K. Li, M. J. Jurkovic, W. I. Wang, J. M. Van Hove, and P. P. Chow. Surface polarity dependence of Mg doping in GaN grown by molecular-beam epitaxy. *Appl. Phys. Lett.*, 76:1740, 2000.
- [131] A. J. Ptak, L. J. Holbert, L. Ting, C. H. Swartz, M. Moldovan, N. C. Giles, T. H. Myers, P. Van Lierde, C. Tian, R. A. Hockett, S. Mitha, A. E. Wickenden, D. D. Koleske, and R. L. Henry. Controlled oxygen doping of GaN using plasma assisted molecular-beam epitaxy. *Appl. Phys. Lett.*, 79:2740, 2001.
- [132] S. F. Chichibu, A. Setoguchi, A. Uedono, K. Yoshimura, and M. Sumiya. Impact of growth polar direction on the optical properties of GaN grown by metalorganic vapor phase epitaxy. *Appl. Phys. Lett.*, 78:28, 2001.
- [133] H. M. Ng and A. Y. Cho. Investigation of Si doping and impurity incorporation dependence on the polarity of GaN by molecular beam epitaxy. *J. Vac. Sci. Technol. B*, 20:1217, 2002.
- [134] L. Macht, J. L. Weyher, P. R. Hageman, M. Zielinski, and P. K. Larsen. The direct influence of polarity on structural and electro-optical properties of heteroepitaxial GaN. *J. Phys.: Condens. Matter*, 14:13345–50, 2002.
- [135] N. A. Fichtenbaum, T. E. Mates, S. Keller, S. P. DenBaars, and U. K. Mishra. Impurity incorporation in heteroepitaxial N-face and Ga-face GaN films grown by metalorganic chemical vapor deposition. *J. Cryst. Growth*, 310:1124–31, 2008.
- [136] X. J. Chen, G. Perillat-Merceroz, D. Sam-Giao, C. Durand, and J. Eymery. Homoepitaxial growth of catalyst-free GaN wires on N-polar substrates. *Appl. Phys. Lett.*, 97:151909, 2010.
- [137] M. D. Brubaker, I. Levin, A. V. Davydov, D. M. Rourke, N. A. Sanford, V. M. Bright, and K. A. Bertness. Effect of AlN buffer layer properties

- on the morphology and polarity of GaN nanowires grown by molecular beam epitaxy. *J. Appl. Phys.*, 110:053506, 2011.
- [138] K. Hestroffer, C. Leclere, C. Bougerol, H. Renevier, and B. Daudin. Polarity of GaN nanowires grown by plasma-assisted molecular beam epitaxy on Si(111). *Phys. Rev. B*, 84:245302, 2011.
- [139] S. Fernández-Garrido, X. Kong, T. Gotschke, R. Calarco, L. Geelhaar, A. Trampert, and O. Brandt. Spontaneous Nucleation and Growth of GaN Nanowires: The Fundamental Role of Crystal Polarity. *Nano Lett.*, 12:6119–25, 2012.
- [140] X. Kong, J. Ristić, M. A. Sanchez-Garcia, E. Calleja, and A. Trampert. Polarity determination by electron energy-loss spectroscopy: application to ultra-small III-nitride semiconductor nanocolumns. *Nanotechnology*, 22:415701, 2011.
- [141] C. T. Foxon, S. V. Novikov, J. L. Hall, R. P. Campion, D. Cherns, I. Griffiths, and S. Khongphetsak. A complementary geometric model for the growth of GaN nanocolumns prepared by plasma-assisted molecular beam epitaxy. *J. Cryst. Growth*, 311:3423–7, 2009.
- [142] D. Cherns, L. Meshi, I. Griffiths, S. Khongphetsak, S. V. Novikov, N. R. S. Farley, R. P. Campion, and C. T. Foxon. Defect-controlled growth of GaN nanorods on (0001)sapphire by molecular beam epitaxy. *Appl. Phys. Lett.*, 93:111911, 2008.
- [143] M. de la Mata, C. Magen, J. Gazquez, M. I. B. Utama, M. Heiss, S. Lopatin, F. Furtmayr, C. J. Fernández-Rojas, B. Peng, J. R. Morante, R. Rurali, M. Eickhoff, A. Fontcuberta i Morral, Q. Xiong, and J. Arbiol. Polarity Assignment in ZnTe, GaAs, ZnO, and GaN-AlN Nanowires from Direct Dumbbell Analysis. *Nano Lett.*, 12:2579–86, 2012.
- [144] L. Largeau, E. Galopin, N. Gogneau, L. Travers, F. Glas, and J.-C. Harmand. N-Polar GaN Nanowires Seeded by Al Droplets on Si(111). *Cryst. Growth Des.*, 12:2724–9, 2012.
- [145] T. Kouno and K. Kishino. Well-arranged novel InGaN hexagonal nanoplates at the tops of nitrogen-polarity GaN nanocolumn arrays. *AIP Adv.*, 2:012140, 2012.
- [146] N. A. Fichtenbaum, C. J. Neufeld, C. Schaake, Y. Wu, M. H. Wong, M. Grundmann, S. Keller, S. P. DenBaars, J. S. Speck, and U. K. Mishra. MOCVD regrowth of InGaN on N-polar and Ga-polar pillar and stripe nanostructures. *Phys. Status Solidi B*, 244:1802–5, 2007.
- [147] S. F. Li, S. Fuendling, X. Wang, S. Merzsch, M. A. M. Al-Suleiman, J. D. Wei, H.-H. Wehmann, A. Waag, W. Bergbauer, and M. Strassburg.

- Polarity and Its Influence on Growth Mechanism during MOVPE Growth of GaN Sub-micrometer Rods. *Cryst. Growth Des.*, 11:1573–7, 2011.
- [148] K. Choi, M. Arita, and Y. Arakawa. Selective-area growth of thin GaN nanowires by MOCVD. *J. Cryst. Growth*, 357:58–61, 2012.
- [149] W. Bergbauer, M. Strassburg, Ch. Kölper, N. Linder, C. Roder, J. Lähmann, A. Trampert, S. Fündling, S. F. Li, H.-H. Wehmann, and A. Waag. N-face GaN nanorods: Continuous-flux MOVPE growth and morphological properties. *J. Cryst. Growth*, 315:164–7, 2011.
- [150] A. E. Grigorescu and C. W. Hagen. Resists for sub-20-nm electron beam lithography with a focus on HSQ: state of the art. *Nanotechnology*, 20:292001, 2009.
- [151] A. A. Tseng, K. Chen, C. D. Chen, and K. J. Ma. Electron Beam Lithography in Nanoscale Fabrication: Recent Development. *IEEE T. Electron. Pa. M.*, 26:141–9, 2003.
- [152] A. A. Tseng. Recent Developments in Nanofabrication Using Focused Ion Beams. *Small*, 1:924–39, 2005.
- [153] J. Gierak. Focused ion beam technology and ultimate applications. *Semicond. Sci. Technol.*, 24:043001, 2009.
- [154] T. C. Chong, M. H. Hong, and L. P. Shi. Laser precision engineering: from microfabrication to nanoprocessing. *Laser Photonics Rev.*, 4: 123–43, 2010.
- [155] J. Békési, J.-H. Klein-Wiele, and P. Simon. Efficient submicron processing of metals with femtosecond UV pulses. *Appl. Phys. A*, 76:355–7, 2003.
- [156] C. M. Parish and P. E. Russell. Scanning Cathodoluminescence Microscopy. *Adv. Imag. Elect. Phys.*, 147:1–135, 2007.
- [157] M. Haider, H. Rose, S. Uhlemann, B. Kabius, and K. Urban. Towards 0.1 nm resolution with the first spherically corrected transmission electron microscope. *J. Electron Microsc. (Tokyo)*, 47:395–405, 1998.
- [158] D. B. Williams and C. B. Carter. *Transmission Electron Microscopy – A Textbook for Materials Science*. Springer, New York, USA, 2nd edition, 2009.
- [159] J. Taftø and J. C. H. Spence. A Simple Method for the Determination of Structure-Factor Phase Relationships and Crystal Polarity Using Electron Diffraction. *J. Appl. Crystallogr.*, 15:60–4, 1982.

- [160] P. Stadelmann. Electron Microscopy Software Java Version (JEMS), 2004. URL <http://cimewww.epfl.ch/people/stadelmann/jemsWebSite/jems.html>.
- [161] H. Harima. Properties of GaN and related compounds studied by means of Raman scattering. *J. Phys.: Condens. Matter*, 14:R967–93, 2002.
- [162] J. S. Brown, G. Koblmüller, F. Wu, R. Averbeck, H. Riechert, and J. S. Speck. Ga adsorbate on (0001) GaN: In situ characterization with quadrupole mass spectrometry and reflection high-energy electron diffraction. *J. Appl. Phys.*, 99:074902, 2006.
- [163] B. Heying, R. Averbeck, L. F. Chen, E. Haus, H. Riechert, and J. S. Speck. Control of GaN surface morphologies using plasma-assisted molecular beam epitaxy. *J. Appl. Phys.*, 88:1855–60, 2000.
- [164] G. Koblmüller, R. Averbeck, H. Riechert, and P. Pongratz. Direct observation of different equilibrium Ga adlayer coverages and their desorption kinetics on GaN (0001) and (000 $\bar{1}$ ) surfaces. *Phys. Rev. B*, 69:035325, 2004.
- [165] J. Osaka, M. Senthil Kumar, H. Toyoda, T. Ishijima, H. Sugai, and T. Mizutani. Role of atomic nitrogen during GaN growth by plasma-assisted molecular beam epitaxy revealed by appearance mass spectrometry. *Appl. Phys. Lett.*, 90:172114, 2007.
- [166] M. Seelmann-Eggebert, J. L. Weyher, H. Obloh, H. Zimmermann, A. Rar, and S. Porowski. Polarity of (00.1) GaN epilayers grown on a (00.1) sapphire. *Appl. Phys. Lett.*, 71(18):2635, 1997.
- [167] D. Li, M. Sumiya, S. Fuke, D. Yang, D. Que, Y. Suzuki, and Y. Fukuda. Selective etching of GaN polar surface in potassium hydroxide solution studied by x-ray photoelectron spectroscopy. *J. Appl. Phys.*, 90:4219–23, 2001.
- [168] D. Zhuang and J. H. Edgar. Wet etching of GaN, AlN, and SiC: a review. *Mater. Sci. Eng. R*, 48:1–46, 2005.
- [169] A. Chuvilin and U. Kaiser. On the peculiarities of CBED pattern formation revealed by multislice simulation. *Ultramicroscopy*, 104: 73–82, 2005.
- [170] X. Wang and A. Yoshikawa. Molecular beam epitaxy growth of GaN, AlN and InN. *Prog. Cryst. Growth Charact. Mater.*, 48/49:42–103, 2004.



- [171] R. F. Davis, S. M. Bishop, S. Mita, R. Collazo, Z. J. Reitmeier, and Z. Sitar. Epitaxial Growth Of Gallium Nitride. In M. Skowronski, J. J. DeYoreo, and C. A. Wang, editors, *Perspectives on Inorganic, Organic, and Biological Crystal Growth: From Fundamentals to Applications*, volume 916 of *AIP Conf. Proc.*, pages 520–40. American Institute of Physics, 2007.
- [172] V. Ramachandran, R. M. Feenstra, W. L. Sarney, L. Salamanca-Riba, J. E. Northrup, L. T. Romano, and D. W. Greve. Inversion of wurtzite GaN(0001) by exposure to magnesium. *Appl. Phys. Lett.*, 75:808, 1999.
- [173] A. L. Rosa and J. Neugebauer. Polarity inversion of GaN(0001) surfaces induced by Si adsorption. *Surf. Sci.*, 600:335–9, 2006.
- [174] L. Liu and J.H. Edgar. Substrates for gallium nitride epitaxy. *Mater. Sci. Eng. R*, 37:61–127, 2002.
- [175] R. B. Capaz, H. Lim, and J. D. Joannopoulos. *Ab initio* studies of GaN epitaxial growth on SiC. *Phys. Rev. B*, 51:17755, 1995.
- [176] B. L. VanMil, H. Guo, L. J. Holbert, K. Lee, T. H. Myers, T. Liu, and D. Korakakis. High temperature limitations for GaN growth by rf-plasma assisted molecular beam epitaxy: Effects of active nitrogen species, surface polarity, hydrogen, and excess Ga-overpressure. *J. Vac. Sci. Technol. B*, 22:2149, 2004.
- [177] T. Ito, T. Akiyama, and K. Nakamura. *Ab initio*-based approach to reconstruction, adsorption and incorporation on GaN surfaces. *Semicond. Sci. Technol.*, 27:024010, 2012.
- [178] R. Dimitrov, M. Murphy, J. Smart, W. Schaff, J. R. Shealy, L. F. Eastman, O. Ambacher, and M. Stutzmann. Two-dimensional electron gases in Ga-face and N-face AlGa<sub>x</sub>N/GaN heterostructures grown by plasma-induced molecular beam epitaxy and metalorganic chemical vapor deposition on sapphire. *J. Appl. Phys.*, 87:3375–80, 2000.
- [179] R. Leitsmann and F. Bechstedt. Surface influence on stability and structure of hexagon-shaped III–V semiconductor nanorods. *J. Appl. Phys.*, 102:063528, 2007.
- [180] Z. Liliental-Weber, C. Kisielowski, S. Ruvimov, Y. Chen, J. Washburn, I. Grzegory, M. Bockowski, J. Jun, and S. Porowski. Structural Characterization of Bulk GaN Crystals Grown Under High Hydrostatic Pressure. *J. Electron. Mater.*, 25:1545–50, 1996.
- [181] F. R. N. Nabarro. Mathematical theory of stationary dislocations. *Adv. Phys.*, 1:269–394, 1952.

- [182] J. D. Eshelby. Screw Dislocations in Thin Rods. *J. Appl. Phys.*, 24: 176–9, 1953.
- [183] P. Caroff, J. Bolinsson, and J. Johansson. Crystal Phases in III–V Nanowires: From Random Toward Engineered Polytypism. *IEEE J. Sel. Top. Quant.*, 17:829–46, 2011.
- [184] T. Akiyama, K. Sano, K. Nakamura, and T. Ito. An Empirical Potential Approach to Wurtzite–Zinc-Blende Polytypism in Group III–V Semiconductor Nanowires. *Jpn. J. Appl. Phys.*, 45(9):L275–8, 2006.
- [185] M. Galicka, M. Bukala, R. Buczko, and P. Kacman. Modelling the structure of GaAs and InAs nanowires. *J. Phys.: Condens. Matter*, 20: 454226, 2008.
- [186] V. Yu. Davydov, Yu. E. Kitaev, I. N. Goncharuk, A. N. Smirnov, J. Graul, O. Semchinova, D. Uffmann, M. B. Smirnov, A. P. Mirgorodsky, and R. A. Evarestov. Phonon dispersion and Raman scattering in hexagonal GaN and AlN. *Phys. Rev. B*, 58:12899–907, 1998.
- [187] K. Kusakabe, A. Kikuchi, and K. Kishino. Overgrowth of GaN layer on GaN nano-columns by RF-molecular beam epitaxy. *J. Cryst. Growth*, 237–239:988–92, 2002.
- [188] T. Kozawa, T. Kachi, H. Kano, H. Nagase, N. Koide, and K. Manabe. Thermal stress in GaN epitaxial layers grown on sapphire substrates. *J. Appl. Phys.*, 77:4389, 1995.
- [189] K. Jeganathan, R. K. Debnath, R. Meijers, T. Stoica, R. Calarco, D. Grützmacher, and H. Lüth. Raman scattering of phonon-plasmon coupled modes in self-assembled GaN nanowires. *J. Appl. Phys.*, 105: 123707, 2009.
- [190] E. O. Schäfer-Nolte, T. Stoica, T. Gotschke, F. Limbach, E. Sutter, P. Sutter, and R. Calarco. Highly polarized Raman scattering anisotropy in single GaN nanowires. *Appl. Phys. Lett.*, 96:091907, 2010.
- [191] R. Mata, A. Cros, K. Hestroffer, and B. Daudin. Surface optical phonon modes in GaN nanowire arrays: Dependence on nanowire density and diameter. *Phys. Rev. B*, 85:035322, 2012.
- [192] F. Habel, P. Brückner, and F. Scholz. Marker layers for the development of a multistep GaN FACELO process. *J. Cryst. Growth*, 272:515–9, 2004.
- [193] V. Jindal, J. Grandusky, M. Jamil, N. Tripathi, B. Thiel, F. Shahedipour-Sandvik, J. Balch, and S. LeBoeuf. Effect of interfacial strain on the

- formation of AlGaN nanostructures by selective area heteroepitaxy. *Physica E*, 40:478–83, 2008.
- [194] T. Wunderer, M. Feneberg, F. Lipski, J. Wang, R. A. R. Leute, S. Schwaiger, K. Thonke, A. Chuvilin, U. Kaiser, S. Metzner, F. Bertram, J. Christen, G. J. Beirne, M. Jetter, P. Michler, L. Schade, C. Vierheilg, U. T. Schwarz, A. D. Dräger, A. Hangleiter, and F. Scholz. Three-dimensional GaN for semipolar light emitters. *Phys. Status Solidi B*, 248:549–60, 2011.
- [195] C.-H. Liao, W.-M. Chang, H.-S. Chen, C.-Y. Chen, Y.-F. Yao, H.-T. Chen, C.-Y. Su, S.-Y. Ting, Y.-W. Kiang, and C. C. Yang. Geometry and composition comparisons between *c*-plane disc-like and *m*-plane core-shell InGaN/GaN quantum wells in a nitride nanorod. *Opt. Express*, 20:15859, 2012.
- [196] K. Furuya and T. Saito. Determination of beam affected area and degradation of cathodoluminescence in GaAs induced by focused ion beam irradiation. *J. Appl. Phys.*, 80:1922, 1996.
- [197] T. Bever, G. Jäger-Waldau, M. Eckberg, E. T. Heyen, H. Lage, A. D. Wieck, and K. Ploog. Lateral spreading of focused ion-beam-induced damage. *J. Appl. Phys.*, 72:1858, 1992.
- [198] P. Corfdir and P. Lefebvre. Importance of excitonic effects and the question of internal electric fields in stacking faults and crystal phase quantum discs: The model-case of GaN. *J. Appl. Phys.*, 112:053512, 2012.
- [199] T. Sugahara, H. Sato, M. S. Hao, Y. Naoi, S. Kurai, S. Tottori, K. Yamashita, K. Nishino, L. T. Romano, and S. Sakai. Direct evidence that dislocations are non-radiative recombination centers in GaN. *Jpn. J. Appl. Phys.*, 37:L398–400, 1998.
- [200] G. D. Mahan and D. T. F. Marple. Infrared absorption of thin metal films: Pt on Si. *Appl. Phys. Lett.*, 42:219, 1983.
- [201] K. R. Williams, K. Gupta, and M. Wasilik. Etch Rates for Micromachining Processing – Part II. *J. Microelectromech. Syst.*, 12:761–78, 2003.
- [202] J. Zenneck. *Optische Eigenschaften von verdünnten magnetischen Halbleitern auf GaN-Basis*. PhD thesis, Georg-August-Universität Göttingen, 2007.

---

## PUBLICATIONS

---

Parts of this thesis have been published in:

### PUBLICATIONS

A. Urban, J. Malindretos, J.-H. Klein-Wiele, P. Simon, and A. Rizzi. Ga-polar GaN nanocolumn arrays with semipolar faceted tips. *New J. Phys.*, 15:053045, 2013.

### OTHER PUBLICATIONS

A. Urban, J. Malindretos, M. Seibt, and A. Rizzi. Structure and Elemental Distribution of (Ga,Mn)N Nanowires. *Nano Lett.* 11(2):398–401, 2011.

A. Bedoya-Pinto, C. Zube, J. Malindretos, A. Urban, and A. Rizzi. Epitaxial  $\delta$ -Mn<sub>x</sub>Ga<sub>1-x</sub> layers on GaN(0001): Structural, magnetic, and electrical transport properties. *Phys. Rev. B* 84:104424, 2011.

### CONFERENCES

MBE2010, Berlin, Germany. Mn Accumulation at the lateral Sidewalls of (Ga,Mn)N Nanowires grown on Si(111) by Molecular Beam Epitaxy. A. Urban, J. Malindretos, and A. Rizzi. Oral Session A1, Talk 5.

NWG2010, Rome, Italy. Selective area growth of GaN Nanostructures on Mo pre-patterned 6H-SiC(0001) by MBE. A. Urban, J. Malindretos, and A. Rizzi. Poster Session 3, Poster 4.

473. Wilhelm and Else Heraeus Seminar on III–V Nanowires – Growth, Properties, and Applications, 2011, Bad Honnef, Germany. Selective area growth of GaN nanostructures by MBE. A. Urban, J. Malindretos, and A. Rizzi. Poster.

ICNS2011, Glasgow, Scotland. Structural and optical properties of GaN nanostructures. A. Urban, E. Secco, J. Malindretos, N. Garro, A. Cantarero, and A. Rizzi. Poster Session 3, Poster 11.

NWG2012, St. Petersburg, Russia. Growth of semi-polar and polar AlN/GaN quantum wells in GaN nanocolumns. A. Urban, E. Secco, C. I. Oppo, J. Malindretos, N. Garro, A. Cantarero, and A. Rizzi. Poster Session 1, Poster 25.

MBE2012, Nara, Japan. Semipolar AlN/GaN QWs grown at the pyramidal tip of GaN NC arrays. A. Urban, E. Secco, J. Malindretos, N. Garro, A. Cantarero, and A. Rizzi. Oral Session WeA-2, Talk 5.

---

## ACKNOWLEDGMENTS

---

This part of this thesis is reserved to people who deserve my gratitude. In a variety of ways they enabled me to write this work as it appears in the final version; be it by offering a PhD position, support in the lab, performing measurements, proof-reading the thesis, providing a pleasant working atmosphere or encouraging me to finish this period of life.

My gratitude goes to Prof. Dr. Angela Rizzi for giving me the opportunity to work in her lab on epitaxy and nanostructuring and to learn about the exciting physics of the III nitrides. I would like to thank Prof. Dr. Michael Seibt who gave me the opportunity to work in the field of transmission electron microscopy and introduced me to the physics behind. I am thankful for fruitful scientific discussions with both of them, which allowed this thesis to evolve to its current state. I thank Dr. Bruno Daudin for the immediate willingness to act as second referee.

I deeply thank Dr. Jörg Malindretos for excellent assistance in the lab, proof-reading, scientific discussions and especially to have a sympathetic ear in all respects. Furthermore, I would like to thank especially all collaborators who spent a lot of time in the lab and in the office fabricating, characterizing and analyzing samples for me: Dr. Peter Veit and Marcus Müller, who performed STEM- and SEM-CL measurements, Dr. Núria Garro and Eleonora Secco, who performed Raman and PL spectroscopy, Jan-Hendrik Klein-Wiele and Peter Simon, who performed pulsed laser ablation patterning.

My gratitude goes to Dr. Christian Denker for teaching me e-beam lithography and for the fruitful discussions about the growth of nanocolumns, as well as to Henning Schuhmann for assistance at the TEM and related discussions. I thank Patrick Peretzki, Tobias Hildebrandt, and Carla Ivana Oppo for performing additional TEM, AFM, and PL experiments. Dr. Daniel Broxtermann is acknowledged for providing the style for this thesis, which saved me a lot of time. I thank Prof. Dr. Rainer G. Ulbrich for proof-reading and scientific discussions.

All members of the IV. Physikalisches Institut played a part in contributing to a harmonic working atmosphere and a social climate which I enjoyed. Especially, it was fun to share my office with Carla Ivana Oppo and Henning Hollermann. The Italian anecdotes and coffee delivery service made my day a lot of times. I enjoyed working in the lab together with Christian Zube, discussing the sense and nonsense of our work. I appreciated the relaxing

social climate in the working group; thanks, Dr. Jörg Malindretos, Christian Zube, Carla Ivana Oppo, Henning Hollermann, Thomas Lehmann, Bastian Henne, Johannes Schmidt, and all others who were part of the group, while I was.

Finally, I am deeply grateful to my family for their encouraging support to complete this work.

This research was partly supported by the Deutsche Forschungsgemeinschaft (SFB 602).

---

## LIST OF FIGURES

---

Figure 2.1	Model of the wurtzite crystal structure . . . . .	9
Figure 2.2	Atomic structure of basal plane stacking faults in GaN	12
Figure 2.3	Schematic representation of the $\Gamma$ point valence and conduction bands in GaN . . . . .	13
Figure 2.4	Schematic description of polarization effects in wurtzite GaN-based heterostructures . . . . .	17
Figure 2.5	Energy band profile in nonpolar and polar GaN-based heterostructures . . . . .	19
Figure 2.6	Scheme of the coordinate system for the semipolar GaN-based layer/template heterostructure, and the total polarization discontinuity in semipolar $\text{In}_x\text{Ga}_{1-x}\text{N}/\text{GaN}$ heterostructures . . . . .	20
Figure 2.7	Equilibrium $\text{N}_2$ vapor pressure between vapor and solid phases in the III nitride system, and GaN decomposition rates in vacuum and under active nitrogen exposure as function of temperature . . . . .	21
Figure 3.1	The Veeco GEN II MBE system . . . . .	24
Figure 3.2	Schematic of an MBE growth chamber . . . . .	25
Figure 3.3	Surface energies of nonpolar GaN surfaces . . . . .	28
Figure 3.4	Polar Wulff construction to determine the GaN equilibrium crystal shape in projection along $\langle 0001 \rangle$ . . .	30
Figure 3.5	Cubic model crystal for the schematic description of size effects during crystal growth . . . . .	31
Figure 3.6	Size-dependent Ga evaporation rate from a spherical GaN particle with isotropic surface energy . . . . .	33
Figure 4.1	Calculation of the NC axial growth rate as function of NC height and NC diameter according to the growth model from Ref. <sup>[106]</sup> . . . . .	40
Figure 6.1	SEM micrographs of SAG GaN NCs with different NC diameters and aperture pitches, and magnifications of the NC tip morphology . . . . .	59
Figure 6.2	AFM topography micrographs of a clean GaN(0001) template before and after deposition of 10 nm Mo . .	60
Figure 6.3	Schematic layout of the array design $M$ for patterning of the SAG masks by electron beam lithography	61
Figure 6.4	Schematic layout of the array design $T$ for patterning of the SAG masks by pulsed laser ablation . . . . .	61



Figure 6.5	AFM topography micrograph of a SAG array prepared by electron beam lithography, and an unpatterned region on the same sample . . . . .	62
Figure 6.6	SEM micrographs of a SAG array prepared by pulsed laser ablation . . . . .	63
Figure 6.7	GaN growth diagram, and RHEED intensity oscillations . . . . .	64
Figure 6.8	SEM micrographs for the determination of the optimal growth temperature for SAG GaN NCs . . . . .	66
Figure 7.1	SEM micrographs of SAG GaN NC arrays with different pitch for statistical analysis . . . . .	70
Figure 7.2	SEM micrograph for the estimation of the Ga diffusion length on Mo . . . . .	71
Figure 7.3	Statistical analysis of the NC height and diameter as function of pitch . . . . .	71
Figure 7.4	Comparison of the NC layer equivalent thickness and the nominal layer thickness . . . . .	73
Figure 7.5	SEM micrographs showing the morphology of SAG GaN NCs as function of growth duration . . . . .	76
Figure 7.6	NC growth rates as function of NC height and as function of growth duration . . . . .	78
Figure 7.7	Calculated N/Ga ratio in the aperture and at the NC tip due to Ga diffusion . . . . .	82
Figure 7.8	NC axial growth rate as function of nitrogen supply	83
Figure 7.9	TEM micrographs of the tip area of single SAG NCs	87
Figure 7.10	NC tip inclination as function of SAG NC diameter .	88
Figure 7.11	Determination of the NC polarity by KOH treatment	90
Figure 7.12	Simulated HRTEM images of Ga-polar GaN . . . . .	92
Figure 7.13	$C_s$ corrected HRTEM micrographs for the determination of the NC polarity . . . . .	93
Figure 7.14	CBED experiment for the determination of the polarity of the SAG NCs . . . . .	95
Figure 7.15	SEM micrographs of N-polar SAG GaN NCs on SiC(0001) before and after KOH treatment . . . . .	97
Figure 7.16	SEM micrographs of Ga-polar SAG GaN NCs on SiC(0001) before and after KOH treatment . . . . .	98
Figure 7.17	Ball-and-stick model of cleaved $r$ -surfaces of Ga-polar GaN . . . . .	100
Figure 7.18	Calculated broken bond densities of various GaN surfaces . . . . .	101
Figure 7.19	SEM micrographs of SAG GaN NCs with smooth segments of $m$ - and $a$ -plane sidewalls . . . . .	103
Figure 8.1	TEM micrographs of SAG NCs with diameters around 200 and 600 nm . . . . .	108

Figure 8.2	TEM analysis on bending of threading dislocations in SAG GaN NCs . . . . .	110
Figure 8.3	Classification of SAG GaN NCs according to the density of extended defects . . . . .	112
Figure 8.4	HRTEM micrograph of the high defect density tip region of a SAG GaN NC . . . . .	113
Figure 8.5	Wurtzite and zinc blende GaN projected along $\langle 11\bar{2}0 \rangle$	113
Figure 8.6	Raman spectrum of SAG NCs and of mainly self-induced NCs . . . . .	115
Figure 8.7	Evolution of the full width at half maximum of the $E_2^H$ mode of GaN NCs . . . . .	116
Figure 8.8	SEM micrographs of SAG GaN NCs after the growth of AlN/GaN MQWs at the tips . . . . .	118
Figure 8.9	TEM micrographs of SAG and SI NCs with semipolar and polar AlN/GaN MQWs at the tip . . . . .	119
Figure 8.10	HRTEM micrographs of a semipolar and polar MQW	120
Figure 9.1	ADF micrograph of the investigated TEM lamella . . . . .	124
Figure 9.2	HAADF, ADF, and panchromatic CLI images of 14 SAG GaN NCs . . . . .	125
Figure 9.3	ADF, HAADF, and panchromatic CLI images of a defect-free NC . . . . .	126
Figure 9.4	Spectral evolution of the CL intensity along the defect-free NC . . . . .	126
Figure 9.5	ADF, HAADF, and panchromatic CLI images of a NC which contains three extended defects . . . . .	127
Figure 9.6	Spectral evolution of the CL intensity along the NC which contains three extended defects . . . . .	128
Figure 9.7	ADF, HAADF, and panchromatic CLI images of a NC which contains one extended defect . . . . .	129
Figure 9.8	Spectral evolution of the CL intensity along the NC which contains one extended defect . . . . .	129
Figure 9.9	ADF, HAADF, and panchromatic CLI images of a NC which contains a high density of extended defects . . . . .	131
Figure 9.10	CL spectrum of the high defect density NC . . . . .	131
Figure 9.11	SEM micrograph of a SAG GaN NC array and the corresponding panchromatic CLI images . . . . .	132
Figure 9.12	CL spectra of an ensemble of SAG GaN NCs . . . . .	133
Figure 9.13	Monochromatic CL intensity images of an ensemble of SAG GaN NCs . . . . .	134
Figure 9.14	RGB color images for the investigation of the spatial coincidence of CL emission in SAG GaN NCs . . . . .	136
Figure A.1	Dose testing for pixel exposure by electron beam lithography . . . . .	149

Figure A.2	AFM topography micrographs of overexposed SAG arrays . . . . .	150
Figure A.3	SEM micrographs indicating size-dependent GaN incubation times . . . . .	152
Figure A.4	Determination of the incubation time by RHEED . . . . .	153
Figure A.5	Schematic description for shadowing effects during the SAG of NCs by MBE . . . . .	154
Figure A.6	Optimized cross sectional focused ion beam preparation	156
Figure A.7	PL spectra of SAG GaN NCs as function of diameter and evaluation of the linewidth related to $D^0X_A$ . . . . .	159

---

## LIST OF TABLES

---

Table 2.1	Lattice parameters of the III nitrides . . . . .	8
Table 2.2	Examples of semipolar planes in GaN . . . . .	10
Table 2.3	Luminescence characteristics of GaN . . . . .	15
Table 6.1	Standard SAG conditions . . . . .	67
Table 7.1	Inclinations of GaN( $2\bar{2}0n$ ) surfaces . . . . .	86
Table A.1	Optimized electron beam lithography dose factors . . . . .	150
Table A.2	Calibrated effective nitrogen flux for typically used nitrogen plasma source parameters . . . . .	151
Table A.3	Quantitative analysis of shadowing effects according to measured NC height and diameter . . . . .	154
Table A.4	Transmission electron microscope parameters . . . . .	158

# Arne Urban

## Curriculum vitae

Rosdorfer Weg 44  
37073 Göttingen

Date of birth: 11.02.1983

Place of birth: Bremen, Germany

Citizenship: German

### Doctoral studies

- 10/2009–11/2013 PhD student at the IV. Physikalisches Institut, Georg-August-Universität Göttingen
- 08/2009–09/2009 Research assistant at the IV. Physikalisches Institut, Georg-August-Universität Göttingen

### University education

- Degree Dipl.-Phys.
- 10/2003–05/2009 Study of Physics at the Georg-August-Universität Göttingen, Göttingen, Germany
- Diploma thesis at the IV. Physikalisches Institut: Molekularstrahl-epitaxie von (Ga,Mn)N Nanodrähten – Strukturelle, chemische und magnetische Untersuchungen

### Civil service

- 08/2002–06/2003 Integrationskindergarten Saarburger Straße, Bremen

### School education

- Graduation Abitur
- 07/1999–06/2002 Bilingual secondary school at Gymnasium Obervieland, Bremen
- 08/1995–07/1999 Bilingual secondary school at Schulzentrum Habenhausen, Bremen